Thesis for the degree of Doctor of Philosophy in Solid and Structural Mechanics

NUMERICAL METHODS AND MULTI-SCALE MODELLING FOR PHASE-FIELD FRACTURE

WITH APPLICATIONS IN LINEAR ELASTIC AND PORO-ELASTIC MEDIA

RITUKESH BHARALI

Division of Material and Computational Mechanics
Department of Industrial and Materials Science
CHALMERS UNIVERSITY OF TECHNOLOGY

Göteborg, Sweden, 2024

Doktorsavhandlingar vid Chalmers tekniska högskola, Ny series nr 5441
ISBN: 978-91-7905-975-0
ISSN: 0346-718X

Division of Material and Computational Mechanics
Department of Industrial and Materials Science
Chalmers University of Technology
SE-412 96, Göteborg, Sweden
Telephone +46 (0)31-772 1000

Cover image: A schematic of hydraulic fracturing and soil desiccation cracking with numerical experiment observations.

Typeset in `classicthesis` (André Miede and Ivo Pletikosić).

Printed by Chalmers Digitaltryck, Gothenburg, Sweden.

To my parents.

Scientific knowledge belongs to humanity.

— Alexandra Elbakyan

ABSTRACT

This thesis presents novel numerical methods and a multi-scale modelling framework tailored for advancing the phase-field fracture model with applications in linear elastic and poro-elastic media. In the realm of the numerical methods, the focus lies on devising computationally efficient and robust monolithic solution techniques. These techniques aim to solve non-convex fracture problems, while ensuring the irreversibility of fracture in a variationally consistent way. The multi-scale modelling framework seeks to incorporate microstructural heterogeneities (such as material constituents, voids, and defects) and fractures to derive engineering-scale mechanical responses.

Within the range of monolithic solution techniques proposed in this thesis, the fracture energy-based arc-length method and the Hessian scaling method stand out for their demonstrated computational efficiency and robustness on benchmark mechanical problems. Furthermore, to ensure the irreversibility of fracture in a variational context, a micromorphic variant of the phase-field fracture model is presented. The micromorphic variant not only allows a point-wise treatment of the fracture irreversibility constraint, but also demonstrates compatibility with the aforementioned arc-length method. Based on the computational efficiency and robustness proven by the arc-length method, this thesis presents a time-step computing variant of the method for hydraulic fracturing problems.

Furthermore, in the context of multiphysics fracture problems, a novel energy functional is proposed for soil desiccation cracking. The energy functional incorporates the part of the water pressure propagating into the solid skeleton in the fracture driving energy. Numerical experiments that utilize the integration point Hessian scaling method showcase the model's ability to capture experimentally observed phenomenon.

Finally, a hierarchical multi-scale phase-field fracture framework is developed using the variationally consistent homogenization technique. The framework allows the selective upscaling of micro-structural information to the engineering scale. The numerical multi-scale 'finite element squared' (FE^2) experiment conducted in this thesis successfully demonstrates the solvability of the engineering and fine-scale governing equations in a nested sequence.

The culmination of the novel numerical methods and the multi-scale framework represents a significant step towards robust, computationally efficient, and accurate modelling of fractures in engineering materials and structures.

Keywords: multiphysics, multiscale, phase-field, fracture, fracking, desiccation, solution techniques, solvers, finite element

PUBLICATIONS

A part of this thesis has been be re-cast into journals articles. They are listed below:

[1] Ritukesh Bharali et al. "Computational homogenisation of phase-field fracture." In: *European Journal of Mechanics - A/Solids* 88 (2021), p. 104247. ISSN: 0997-7538. DOI: 10.1016/j.euromechsol.2021.104247.

[2] Ritukesh Bharali et al. "Computational aspects of the weak micro-periodicity saddle point problem." In: *PAMM* 20.1 (2021), e202000259. DOI: 10.1002/pamm.202000259.

[3] Ritukesh Bharali et al. "A robust monolithic solver for phase-field fracture integrated with fracture energy based arc-length method and under-relaxation." In: *Computer Methods in Applied Mechanics and Engineering* 394 (2022), p. 114927. ISSN: 0045-7825. DOI: 10.1016/j.cma.2022.114927.

[4] Ritukesh Bharali et al. "A micromorphic phase-field model for brittle and quasi-brittle fracture." In: *Computational Mechanics* (Aug. 2023). ISSN: 1432-0924. DOI: 10.1007/s00466-023-02380-1.

[5] Ritukesh Bharali et al. "A time-step computing arc-length method for the phase-field hydraulic fracture model" (2024). *To be submitted*.

[6] Ritukesh Bharali et al. "Phase-field soil desiccation cracking modelling: Constitutive, numerical and statistical aspects" (2024). *To be submitted*.

Two open-source software packages are released as a part of this thesis. They are listed below:

[1] Ritukesh Bharali. "openFE2: A parallel multi-scale FE2 code based on COMSOL Multi-physics and MATLAB." In: *GitHub repository* (2021). URL: https://github.com/ritukeshbharali/openFE2.

[2] Ritukesh Bharali. "falcon: A C++ Finite Element Analysis software based on the Jem-Jive library." In: *GitHub repository* (2023). URL: https://github.com/ritukeshbharali/falcon.

PREFACE

The work in this thesis has been carried out from March 2019 until December 2023 at the Chalmers University of Technology, Sweden and at the Delft University of Technology (TU Delft), The Netherlands. The former as a doctoral student and the latter through a visiting researcher affiliation (Period: January 2023 to January 2024). Financial support for the research has been offered by the Swedish Research Council for Sustainable Development (FORMAS) under Grant 2018-01249 and the Swedish Research Council (VR) under Grant 2017-05192. The projects were titled 'Modeling of desiccation cracking in soils due to climate change' and 'Modeling and calculation based homogenization of a porous medium with fluid transport in a network of propagating fractures', respectively.

The computational framework developed for this thesis is based on the open-source Jem and Jive libraries from the Dynaflow Research Group, The Netherlands. Part of the research is also conducted using the commercial software COMSOL Multiphysics 5.5 licensed by Chalmers University of Technology. Computational resources from the Chalmers e-Commons (Vera cluster) and the Computational Mechanics group, TU Delft (HPC27 cluster) have been used to conduct numerical experiments.

ACKNOWLEDGMENTS

For the last five years, I've had the great privilege of being mentored by Prof. Prof. Ralf Jänicke (TU Braunschweig) and Prof. Fredrik Larsson in an intriguing research venture. I express a profound gratitude to my mentors for their unwavering belief in me, for fueling my curiosity, and for the generous support that allowed me boundless freedom to delve into diverse ideas. Thank you for creating the perfect atmosphere for an open scientific discussion, by the whiteboard, where we scribbled our equations and critically assessed them.

My gratitude extends to Prof. Minna Karstunen, Prof. Jelke Dijkstra, and Prof. Ayman Abed of the Geotechnics research group at Chalmers for their invaluable insights, constructive feedback, and expert guidance regarding porous media modeling. Their contributions have significantly enriched the depth and quality of my work in this area.

I extend a heartfelt thanks to Prof. Frans van der Meer for his instrumental role in facilitating the research visit to TU Delft, as well as for his vital support in conceptualizing and programming the hydraulic fracturing and desiccation cracking models within the Jem-Jive framework. Additionally, I am thankful to the staff and doctoral students at TU Delft for their warm welcome and lively discussions during our shared lunch and coffee gatherings.

I am grateful to the developers of the Jem-Jive framework, notably Erik Jan Lingen, whose guidance in C++ training and prompt assistance with my programming inquiries have been invaluable. My appreciation also extends to Frans van der Meer and Vinh Phu Nguyen from Monash University, whose foundational work laid the groundwork for my own codes. Furthermore, I am thankful to Joris Remmers and Britt Cordewener at TU Eindhoven for their support with the staggered solver and spectral decomposition split phase-field material, which greatly contributed to the advancement of my work.

I thank Somdatta Goswami, Cosmin Anitescu, and Prof. Timon Rabczuk at Bauhaus University for a great collaboration. Somdatta, your facilitation and insightful discussions on phase-field models, machine learning, and career aspects have been immensely valuable. Additionally, I express my thanks to Prof. Thomas Wick, Prof. Fadi Aldakheel, and Nima Noii at Leibniz University for the numerous discussions on solution techniques. Cheers to Jana Wolf, Patrick Schmidt and Lucianno Fissore for our first hackathon win.

I'm grateful to my MSc mentors, Prof. Bert Sluys from TU Delft, for introducing the world of computational mechanics, and Prof. Dan Givoli from Technion, who patiently taught me the intricacies of programming the finite element method. Additionally, I owe a debt of gratitude to Prof. Jayanta

Pathak and Prof. Palash Jyoti Hazarika at Assam Engineering College for instilling in me the foundational concepts crucial to understanding structural analysis.

Ahmet Semih Ertürk and Robert Auenhammer, I extend big thanks to both of you for meticulously proofreading this thesis with exceptional attention to detail. I also thank Prof. Christine Räisänen at Chalmers for the excellent 'Writing up for publication' course, from which this thesis greatly benefited.

The administrative team at the Department of Industrial and Materials Science has ensured a work environment conducive to research. I take this opportunity to extend my heartfelt appreciation to Jessica Twedmark for a seamless onboarding process. Paula Arhanto and Hanije Safakar, thank you for your invaluable assistance in countless administrative issues.

The past and present colleagues and friends at Chalmers hold the key to the vibrant and harmonious research environment and a bustling after-work environment. I am immensely grateful for the plethora of memories, from engaging fika and lunch table gossips to beers and Blutwurz, lunch football, apartment crawls, and the list goes on. Gothenburg has been a home away from home, thanks to you.

My mother has been my pillar of support, strength and inspiration. I am blessed to be her son, and I cannot thank her enough for the countless sacrifices, prayers and unwavering support through everything in life. I also owe a debt of gratitude to my extended family in Jorhat for their prayers and unconditional support. My friends at home, thank you for your calls and messages. Finally, I extend a heartfelt thanks to my best friend, Amrita for her relentless support through all the ups and downs, constantly finding ways to improve ourselves, and celebrating our tiny successes.

Ritukesh Bharali,
January, 2024.

CONTENTS

LIST OF TABLES

Part I

PROLOGUE

The need for computational modelling of fracture and relevant theoretical background.

1 INTRODUCTION

This chapter presents a background to the ever-increasing interest in the computational modelling of fracture(s) in engineering materials and structures. The relevant research gaps are identified and the chapter concludes with an outline of this thesis.

1.1 BACKGROUND

'*Why and how materials fracture?*' is a fundamental question in the design of engineered structures. Fracture is a common material failure mechanism, and is often associated with catastrophic consequences. One may think of infrastructure (such as, buildings, bridges, dams and embankments) collapsing due to severe earthquakes and winds [3–7]. Earthquakes and winds induce mechanical forces on these structures, leading to high stresses in the underlying material. This results in material fracture and eventual structural collapse. Fractures, however, may be induced by non-mechanical forces as well. For instance, earthen road/rail embankments, flood protection dykes and dams may crack due to high temperatures and low relative humidity, severely undermining their usefulness. This phenomenon is referred to as *drying-induced or desiccation cracking*. Desiccation cracks also appear in agricultural lands, resulting in nutrient shortage for crops [8], in turn affecting food security. Moving onto an energy security perspective, controlled fracturing of shale rocks is required to extract oil and natural gas, without creating undesirable artificial earthquakes and groundwater contamination. This process is known as *hydraulic fracturing*. The aforementioned examples pertaining to human habitation and safety, food and energy security stress the need for accurate fracture prediction models for different kinds of materials around us.

The study of the fracturing phenomenon in materials gained impetus following the breaking of the Liberty cargo ships due to hull and deck fractures in the 1940s [9]. Pioneering theoretical contributions were made by Griffith and Taylor [10], and Irwin [11], and following the advent of powerful computers in the past 50 years, the development of computational fracture models also gained momentum. Broadly, the computational fracture models can be categorized into discrete and diffused (smeared) fracture modelling techniques. In discrete fracture models, the fracture is explicitly represented using discontinuous surfaces. Examples of these models include the Cohesive Zone Model (CZM) [12–14], eXtended Finite Element Method (XFEM) [15–17], and intra-element (embedded) discontinuity approaches [18, 19]. The elegance of these models is the similarity in the representation of fractures with those observed in reality. However, the discrete fracture models involve a rather cumbersome and complex modelling process, often requir-

ing *a priori* knowledge of possible fracture propagation path and additional *ad hoc* criteria for complex fracture topologies (branching, kinking, merging of fractures). Other computational challenges include the ill-convergence of the solution techniques used to simulate the fracture of a material. Often, the solution techniques break-down even before the simulated material fractures.

In order to circumvent the challenges pertaining to discrete fracture models, one resorts to diffused fracture models. In these models, the fracture is represented by a band of finite width, where the material strength and stiffness properties are degraded. Examples of diffused fracture models include the phase-field model for fracture [20–22], gradient damage [23, 24], and peridynamics [25–27]. Among these models, the phase-field fracture model, conceived as a variational approach to Griffith and Taylor's brittle fracture theory [10], has grown in popularity in the past two decades. Based on a simple notion of minimizing the global energy of a structure/material, the phase-field fracture model circumvents the need for additional *ad hoc* criteria or *a priori* knowledge of the fracture propagation path. Complex topological features such as branching, merging and kinking of fractures can be simulated without *a priori* knowledge of the problem at hand. These desirable features offer the phase-field fracture model an edge over the discrete fracture models.

The phase-field fracture model, however, exhibits the notoriety of solution technique break-down, even before a fracture starts propagating in the simulated material. From a mathematical standpoint, this behaviour is attributed to the *non-convex* nature of the underling energy description, formally referred to as 'the energy functional'. A non-convex energy functional results in an ill-behaving Hessian, which impedes the convergence of conventional solution techniques, like the Newton-Raphson method. This has led to the development of alternative solution techniques, see De Lorenzis and Gerasimov [28] or Wick [29] for more details. Most of these alternative solution techniques have demonstrated mixed performance for the wide range of problems simulated so far. Thus, the development of robust solution techniques for the phase-field fracture model is still an active area of research. This leads to the first research objective of this thesis formulated as:

> **Research Objective 1:** Conduct an investigation into existing solution techniques for the phase-field fracture model, and propose novel computationally efficient monolithic solution technique(s).

A second computational challenge pertaining to the phase-field fracture model, arises from the notion of *fracture irreversibility*, i.e., a fracture is never allowed to heal. From a realistic standpoint, one might challenge the irreversibility notion as materials around us do exhibit some form of self-healing. Nevertheless, the engineering design of structures/materials follows a conservative approach, as such fractures are not allowed to heal computationally. The fracture irreversibility condition in the phase-field

fracture model does pose a challenge to computational frameworks, such as the finite element method [30, 31]. Traditionally, the finite element method is not developed to handle these irreversibility bounds/constraints. Therefore, researchers have opted to use constrained optimization techniques in conjunction with the finite element method to model fractures using the phase-field model. However, apart from the penalty method [32], techniques such as the primal-dual active set method [33, 34], interior-point method [35], and augmented Lagrangian method [36] are rather complex to implement. This is the reason why a rather simple notion of enforcing pointwise irreversibility of the fracture driving energy, the *history variable* approach [37] gained popularity. However, the history variable approach is variationally inconsistent. With this approach, starting from a set of strong or weak form phase-field fracture model equations, the energy functional cannot be retrieved. Furthermore, De Lorenzis and Gerasimov [28] reported an over-estimation of the diffused fracture bandwidth with the history variable approach. Motivated by the study, a second research objective of this thesis is formulated as:

> **Research Objective 2:** Propose a numerical method that allows pointwise treatment of fracture irreversibility, albeit in a variationally consistent fashion.

Assuming that a choice of fracture model is made, and pertinent computational challenges are addressed, one may tackle a wide range of problems involving single or several simultaneous physical phenomena in a material. The latter holds more appeal due to the inherent multiphysics nature of real-life processes/events. For instance, in hydraulic fracturing of shale rocks or desiccation cracking of soils, the underlying material comprises of a porous solid grain skeleton with interconnected pores/voids. These pores may contain different kinds of fluids (liquids and gases). Whenever a rock or a soil specimen is disturbed from its state of equilibrium, the mechanical response and the movement of fluids in the pores affect each other. When a fracture occurs, not only the porous skeleton loses strength, but also a channeled preferential path is created for the fluid flow. One can deduce that fluid flow through a fractured rock/soil specimen transitions from the laminar Darcian flow in the intact material to a Poiseuille-type fluid flow in the cracks. As such, computational fracture models are required to capture these fracture-induced responses.

Phase-field models for hydraulic fracture have been extensively developed over the past decade. They vary in the construction of the energy functional and fidelity w.r.t. representation of fluid flow in the diffused fracture region. However, most models involve either convexification measures [36, 38, 39] to circumvent minimizing a non-convex energy functional or computationally expensive alternate minimization solution techniques [40–42]. A robust and computationally efficient solution technique for hydraulic fracture is still elusive to the computational mechanics community.

In the context of desiccation cracking in soils, one observes a significant gap in the development of computational fracture models. Although, Irwin's Linear Elastic Fracture Mechanics (LEFM) theory [11] has been applied as early as in the 1960s [43], the focus was limited to obtaining analytical expressions for the crack depth and spacing. In later developments, the cohesive zone model was adopted within the framework of distinct element method [44–47]. Be it within a distinct element method or a finite element method framework, the cohesive zone model requires *a priori* knowledge of the fracture propagation path, which is undesirable. Phase-field desiccation cracking models [48–50] circumvent the undesirable features associated with 'discrete' cohesive zone models. However, so far, the phase-field models for desiccation cracking in soil have not achieved consensus in the construction of energy functional and in the introduction of fracture dependent material parameters to transition from a Darcian flow to Poiseuille-type flow upon fracturing. This motivates the need to investigate energy functional constructs and implement the transition from a Darcian flow to Poiseuille-type flow upon fracturing. Furthermore, similar to phase-field hydraulic fracture models, the desiccation models developed so far have relied on the computationally expensive alternative minimization solution techniques [48–51]. The use of monolithic solution techniques is still an open research question. Thus, a research objective is formulated based on the open-challenges associated with the phase-field hydraulic fracture and desiccation cracking models as:

Research Objective 3: Propose computationally efficient solution techniques and investigate possible fidelity enhancements for the phase-field hydraulic fracturing and desiccation cracking models.

In computational modelling of linear elastic or porous media (hydraulic fracturing, soil desiccation cracking), the governing equations are directly formulated at the engineering design scale. These governing equations are based on physical laws, such as the balance of linear momentum and the conservation of mass. The associated material properties and their evolution are described using phenomenological constitutive models/laws, based on select few experiments. As such, these constitutive material laws are empirical relationships with limited observations. Consequently, they do not cover the full range of material behaviour. Adopting an alternative approach, one may disregard the notion of constitutive laws, and directly model the material and its associated physical laws on a finer scale. Depending on the length-scale assumed for the fine scale, the material may comprise of atoms, molecules, grains or phases. Thereafter, an engineering scale material behaviour may be obtained from the fine scale information, a concept known as *multi-scale modelling of materials*.

Broadly, multi-scale modelling of materials may be categorized into resolved scale and upscaling/hierarchical methods. Resolved scale methods employ engineering scale and fine scale physics in different part of a specimen. At the interface between the scales, exchange of information is carried

out. Most phase-field multi-scale fracture models [52–55] have adopted the different variants of the resolved scale method. However, when the fine scale features (such as material phases, voids and defects) are several magnitudes smaller than that of the engineering scale, resolved scale methods become computationally expensive. In such cases, one resorts to upscaling/hierarchical multi-scale models. However, the hierarchical models [56, 57] developed so far, are restricted to upscaling elastic properties. The fractures on the fine scale are not accounted for. As such, the development of a variationally consistent hierarchical multi-scale phase-field fracture model accounting for fine scale fractures, is still an open question. This is addressed as the final research objective in this thesis.

Research Objective 4: Develop a variationally consistent hierarchical phase-field multi-scale framework for fracture in complex heterogeneous materials.

1.2 THESIS OUTLINE

This thesis comprises of several parts, aimed providing the foundational concepts and addressing the research objectives. In Part I, the background to this thesis has already been presented in the previous section. Chapter 2 provides the basic theoretical concepts, such as the finite element method, computational fracture models, poro-mechanics, and multi-scale modelling of materials. These concepts are later adopted to address the research objectives of this thesis.

Part II of this thesis is titled *Numerical methods for phase-field fracture*, and comprises of Chapters 3 and 4. They address research objectives 1 and 2 respectively. Chapter 3 presents a set of monolithic solution techniques for the '*non-convex*' phase-field fracture model. In Chapter 4, a variationally consistent way of enforcing fracture irreversibility is developed using a micromorphic theory. The efficacy of the numerical methods is investigated using benchmark numerical experiments.

Part III of this thesis is titled *Computational modelling of fractures in porous media*, and comprises of Chapters 5 and 6. They address research objective 3. A novel arc-length method is presented for the phase-field hydraulic fracturing model in Chapter 5. Chapter 6 presents a phase-field desiccation cracking model for clayey soil, where a novel energy functional is proposed and monolithic solution techniques developed in Chapter 3 are adopted for the numerical experiments.

Part IV of this thesis is titled *Multi-scale modelling of fractures*, and comprises of Chapter 7. Therein, a variationally consistent homogenization technique is adopted to develop a hierarchical multi-scale phase-field fracture framework. Additional concepts, such as selective upscaling/homogenization are introduced.

Part V concludes this thesis with new developments, conclusion, and future research directions in Chapter 8.

2

BASIC THEORETICAL CONCEPTS

This chapter presents the theoretical concepts used throughout this thesis. The finite element method is introduced for a generic (possibly nonlinear) continuum mechanics problem. It is followed by discussions on computational modelling of fracture, poro-mechanics, and multi-scale modelling of materials.

2.1 THE FINITE ELEMENT METHOD

The Finite Element Method (FEM) [30, 58, 59] is a general numerical technique that provides a formalism for generating discrete (finite) algorithms to approximate solutions of Partial Differential Equations (PDEs) on a certain geometry[1] [31]. To this end, a given geometry, for instance in Figure 2.1a is discretized (sub-divided) into a finite numbers of parts, as shown in Figure 2.1b. The smaller triangular parts referred to as *elements* and their vertices designated as *nodes* constitute a finite element *mesh*. The FEM, however, offers the flexibility in placing nodes anywhere inside an element or on its boundary. The solution of a PDE is typically computed at the nodes.

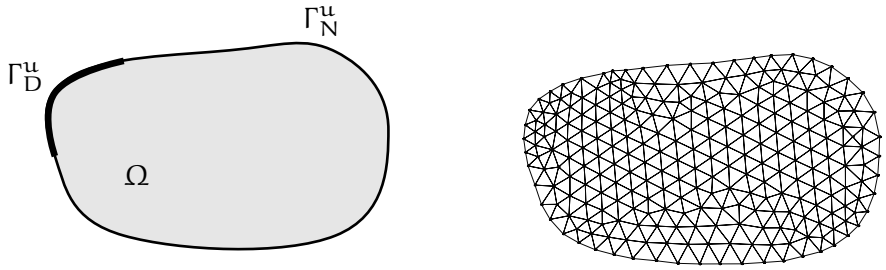

(a) A continuum $\Omega \in \mathbb{R}^2$ (b) Finite element mesh

Figure 2.1: Figure (a) presents a continuum $\Omega \in \mathbb{R}^2$ with Dirichlet and Neumann boundaries indicated as Γ^u_D and Γ^u_N respectively. The corresponding finite element discretized mesh in shown in Figure (b).

In the subsequent part of this section, the application of the FEM is presented for a generic continuum mechanics problem, involving the deformation of a two-dimensional solid geometry under mechanical forces.

A generic continuum mechanics problem

Let us assume a solid geometry $\Omega \in \mathbb{R}^2$ in Figure 2.1, subjected to mechanical forces. Its boundary Γ is additively decomposed into Dirichlet and Neumann boundaries, indicated as Γ^u_D and Γ^u_N respectively. The rate of the forces acting on Ω are assumed to be low enough to eliminate the dynamic

1 A geometry is a collection of points, lines, surfaces and/or volumes.

(inertia) effects. The potential energy functional for the solid geometry is then stated as

$$E(\mathbf{u}) = \underbrace{\int_\Omega \Psi(\boldsymbol{\epsilon}[\mathbf{u}])\,d\Omega}_{\text{internal energy}} - \underbrace{\int_{\Gamma_N^u} \mathbf{t}_p^u \cdot \mathbf{u}\,d\Gamma - \int_\Omega \mathbf{b}\cdot\mathbf{u}\,d\Omega}_{\text{externally applied energy}}, \tag{2.1}$$

where, $\Psi(\boldsymbol{\epsilon}[\mathbf{u}])$ is the strain energy density. It is a function of the strain $\boldsymbol{\epsilon}$, which is defined as the symmetric gradient of the displacement[2] $\mathbf{u}$,

$$\boldsymbol{\epsilon}[\mathbf{u}] = \frac{1}{2}(\boldsymbol{\nabla}\mathbf{u} + \boldsymbol{\nabla}\mathbf{u}^T). \tag{2.2}$$

In the subsequent integrals of the energy functional (2.1), $\mathbf{t}_p^u$ is an external traction acting on the Neumann boundary Γ_N^u, and $\mathbf{b}$ represents the body force. Examples of body forces include gravitational force and magnetic force.

The energy functional (2.1) is not used for generating discrete FEM algorithms to approximate solutions for the generic continuum mechanics problem. Instead, the *variational equation*[3] is used. The variational equation is obtained upon minimizing the energy functional (2.1) w.r.t. its primary unknown, the vector-valued displacement field $\mathbf{u}$. With appropriately defined test and trial Sobolev[4] spaces $H^1(\Omega)$, a complete variational problem statement is defined as:

Variational Problem 1. *Find* $\mathbf{u} \in \mathbb{U}$ *such that*

$$\begin{aligned} E'(\mathbf{u};\delta\mathbf{u}) = \int_\Omega \underbrace{\frac{\partial\Psi(\boldsymbol{\epsilon}[\mathbf{u}])}{\partial\boldsymbol{\epsilon}}}_{\boldsymbol{\sigma}(\boldsymbol{\epsilon}[\mathbf{u}])} : \boldsymbol{\epsilon}[\delta\mathbf{u}] - \int_{\Gamma_N^u} \mathbf{t}_p^u \cdot \delta\mathbf{u}\,d\Gamma \\ - \int_\Omega \mathbf{b}\cdot\delta\mathbf{u}\,d\Omega = 0 \quad \forall\,\delta\mathbf{u} \in \mathbb{U}^0 \end{aligned} \tag{2.3}$$

using pertinent time-dependent Dirichlet boundary conditions $\mathbf{u}^p$ *on* Γ_D^u *and Neumann boundary condition* $\mathbf{t}_p^u$ *on* Γ_N^u*. The trial and test spaces are defined as*

$$\mathbb{U} = \{\mathbf{u} \in [H^1(\Omega)]^{\dim} | \mathbf{u} = \mathbf{u}^p \text{ on } \Gamma_D^u\}, \tag{2.4a}$$

$$\mathbb{U}^0 = \{\mathbf{u} \in [H^1(\Omega)]^{\dim} | \mathbf{u} = \mathbf{0} \text{ on } \Gamma_D^u\}. \tag{2.4b}$$

■

2 adopting the small-strain or linearized kinematics assumption

3 also referred to as 'variational form', 'weak form', or 'Euler-Lagrange' equation

4 A function u for which $\int_\Omega (u)^2 + (\nabla u)^2 < \infty$, belongs to Sobolev space of degree one, denoted by $H^1(\Omega)$. For more on function spaces, the reader is referred to [31].

With reference to the Variational Problem 1, the definition of the Cauchy stress, $\boldsymbol{\sigma}(\boldsymbol{\epsilon}[\mathbf{u}])$ is introduced as the derivative of the strain energy density w.r.t. the strain,

$$\boldsymbol{\sigma}(\boldsymbol{\epsilon}[\mathbf{u}]) = \frac{\partial \Psi(\boldsymbol{\epsilon}[\mathbf{u}])}{\partial \boldsymbol{\epsilon}}. \tag{2.5}$$

Finite element discretized equations

Within the FEM framework, the Variational Problem 1 is assumed to operate on the discrete finite element mesh, shown in Figure 2.1b. Subsequently, the solution computed at the nodes is stored in a finite-dimensional vector $\tilde{\mathbf{u}}$. The solution vector for a particular element el, $\tilde{\mathbf{u}}_{el}$ is then extracted using an incidence/location matrix $\mathbf{L}_{el}$ as

$$\tilde{\mathbf{u}}_{el} = \mathbf{L}_{el}\tilde{\mathbf{u}}. \tag{2.6}$$

Thereafter, the continuous solution field $\mathbf{u}_{el}(\mathbf{x})$ inside the element el is computed using,

$$\mathbf{u}_{el}(\mathbf{x}) = \mathbf{N}_{el}(\mathbf{x})\,\tilde{\mathbf{u}}_{el}, \tag{2.7}$$

where, $\mathbf{N}_{el}$ is matrix of interpolation functions[5]. For a two-dimensional problem, the $\mathbf{N}_{el}$ matrix is given by

$$\mathbf{N}_{el}(\mathbf{x}) = \begin{bmatrix} N_1(\mathbf{x}) & 0 & N_2(\mathbf{x}) & 0 & \dots & N_n(\mathbf{x}) & 0 \\ 0 & N_1(\mathbf{x}) & 0 & N_2(\mathbf{x}) & \dots & 0 & N_n(\mathbf{x}) \end{bmatrix}, \tag{2.8}$$

where, an individual interpolation function $N_I(\mathbf{x})$ attains a value one at the I^{th} node and zero at other nodes. Adopting a Bubnov-Galerkin approach[6], the continuous test function for the element el is stated in a similar fashion as in (2.7),

$$\delta\mathbf{u}_{el}(\mathbf{x}) = \mathbf{N}_{el}(\mathbf{x})\,\delta\tilde{\mathbf{u}}_{el}. \tag{2.9}$$

The strain field inside element el follows from (2.2), and is given by

$$\boldsymbol{\epsilon}[\mathbf{u}] = \mathbf{B}_{el}(\mathbf{x})\tilde{\mathbf{u}}_{el} \quad \text{and} \quad \boldsymbol{\epsilon}[\delta\mathbf{u}] = \mathbf{B}_{el}(\mathbf{x})\delta\tilde{\mathbf{u}}_{el}, \tag{2.10}$$

where, the $\mathbf{B}_{el}$ matrix is defined as

5 also called basis functions or shape functions in the finite element method literature

6 Bubnov-Galerkin approach requires that test and trial functions come from the same finite-dimensional space.

$$\mathbf{B}_{el}(\mathbf{x}) = \begin{bmatrix} N_{1,x}(\mathbf{x}) & 0 & N_{2,x}(\mathbf{x}) & 0 & \dots & N_{n,x}(\mathbf{x}) & 0 \\ 0 & N_{1,y}(\mathbf{x}) & 0 & N_{2,y}(\mathbf{x}) & \dots & 0 & N_{n,y}(\mathbf{x}) \\ N_{1,y}(\mathbf{x}) & N_{1,x}(\mathbf{x}) & N_{2,y}(\mathbf{x}) & N_{2,x}(\mathbf{x}) & \dots & N_{n,y}(\mathbf{x}) & N_{n,x}(\mathbf{x}) \end{bmatrix}. \tag{2.11}$$

Note that the individual components of the $\mathbf{B}_{el}$ matrix are derivatives of the interpolation functions w.r.t. the argument after the comma. Furthermore, the last row in the $\mathbf{B}_{el}$ matrix is added to compute the shear strain, an essential component in the study of deformable solids.

Substituting (2.6), (2.7), (2.9), and (2.10) in the momentum balance equation (2.3), and assuming the resulting equation to hold for an arbitrary choice of the test function $\delta\tilde{\mathbf{u}}$ results in the discrete problem:

Discrete Problem 1. *Find* $\tilde{\mathbf{u}}$ *such that*

$$\mathbf{f}_{ext} - \mathbf{f}_{int}(\tilde{\mathbf{u}}) = \mathbf{0}, \tag{2.12}$$

where,

$$\mathbf{f}_{int}(\tilde{\mathbf{u}}) = \sum_{el=1}^{n_{el}} \mathbf{L}_{el}^{T} \int_{\Omega_{el}} \mathbf{B}_{el}^{T}\, \boldsymbol{\sigma}(\boldsymbol{\epsilon}[\tilde{\mathbf{u}}])\, d\Omega, \tag{2.13}$$

and

$$\mathbf{f}_{ext} = \sum_{el=1}^{n_{el}} \mathbf{L}_{el}^{T} \int_{\Gamma^{u}_{N,el}} \mathbf{N}_{el}^{T}\, \mathbf{t}_{p}^{u}\, d\Gamma + \sum_{el=1}^{n_{el}} \mathbf{L}_{el}^{T} \int_{\Omega_{el}} \mathbf{N}_{el}^{T}\, \mathbf{b}\, d\Omega, \tag{2.14}$$

respectively, and using pertinent Dirichlet boundary conditions $\tilde{\mathbf{u}}^{p}$ *on* Γ^{u}_{D}. *Note that* n_{el} *is the total number of elements in the finite element mesh.*

Without the loss of generality, the Discrete Problem 1 is assumed as a nonlinear problem. A nonlinear discrete problem may be solved using first-order optimization techniques (for e.g., fixed point method, gradient descent method, Wegstein's method [60]) or second-order optimization techniques (for e.g., Newton-Raphson method, quasi Newton-Raphson method). In the computational mechanics community, the Newton-Raphson method and its variants are often used to solve nonlinear problems. Being a second-order iterative solution technique, it requires both the gradient and the Hessian (stiffness matrix) of the functional which is minimized. In the context of the Discrete Problem 1, the energy functional $E(\mathbf{u})$ in (2.1) is minimized, its gradient in the discrete form expressed in (2.12), and the Hessian $\mathbf{K}$ is given by

$$\mathbf{K} = \frac{\partial \mathbf{f}_{int}(\tilde{\mathbf{u}})}{\partial \tilde{\mathbf{u}}}. \tag{2.15}$$

Given a solution $\tilde{\mathbf{u}}_k$ in the k^{th} iteration, the Newton-Raphson method computes the current $(k+1)^{th}$ solution as

$$\tilde{\mathbf{u}}_{k+1} = \tilde{\mathbf{u}}_k + \alpha \Delta \tilde{\mathbf{u}}_k, \quad \text{with} \quad \Delta \tilde{\mathbf{u}}_k = \mathbf{K}_k^{-1} \left[\mathbf{f}_{ext} - \mathbf{f}_{int,k}(\tilde{\mathbf{u}}) \right], \tag{2.16}$$

where, $\alpha \in (0, 1]$ is a scalar line-search parameter. When α is explicitly set to 1, the solution technique is referred to as the full Newton-Raphson (full-NR) method.

Remark 1. *The solution increment $\Delta \tilde{\mathbf{u}}_k$ in (2.16) is computed without computing the Hessian inverse $\mathbf{K}_k^{-1}$ explicitly. Using direct solvers (e.g., Umfpack [61], MUMPS [62], Pardiso [63, 64]), the action of the Hessian inverse on the vector $\left[\mathbf{f}_{ext} - \mathbf{f}_{int,k}(\tilde{\mathbf{u}}) \right]$ is computed using LU factorization of the Hessian, followed by forward and backward substitutions.*

2.2 COMPUTATIONAL MODELLING OF FRACTURE IN MATERIALS

The computational fracture modelling techniques can be broadly classified into two categories, the discontinuous (discrete) approach and the continuous (smeared) approach. In resemblance to the observed reality, the discontinuous modelling approach introduces the crack as a pair of surfaces in a continuum. Across these surfaces, the possible jump in the displacement field is computed. Examples of discontinuous modelling approaches include Cohesive Zone Model (CZM) [12–14], PUFEM [65], and XFEM [15, 16]. However, these models require changes to the finite element framework, which include adaptation of discontinuous displacement kinematic descriptions, dynamic tracking of the fracture front and mesh adaptivity. For complex fracture topologies (crack branching, merging and kinking), these changes may be prohibitively complex to incorporate in a computational model.

On the other hand, in continuous fracture modelling approaches, both the intact material and the fracture is modelled as a continuum. The fracture is viewed as weaker material with limited or no strength and stiffness, and is smeared over a finite band width. Although this representation of fracture departs from the observed reality, the modelling approach remains appealing from the finite element modelling perspective. Unlike the discontinuous modelling approaches, continuous models such as the gradient damage model [23, 24, 66] and the phase-field fracture model [20–22] circumvents the need for incorporating any discontinuity, tracking of the fracture front, and adaptive mesh refinement. The phase-field fracture model, developed over the last two decades, has shown its flexibility in modelling complex fracture topologies without any *ad hoc* criterion for different materials, as

reported by De Lorenzis and Gerasimov in [28]. As such, the phase-field fracture model is chosen as the fracture modelling approach in this thesis.

2.2.1 *The phase-field fracture model*

The phase-field fracture model emerged from the variational approach towards brittle fracture pioneered by Francfort and Marigo [20], and its regularized formulation proposed in [21, 22]. The model introduces an order parameter, a scalar continuous phase-field variable φ, as an approximation of a discrete crack. An illustration of this approximation is presented in Figure 2.2, where a continuum $\Omega \in \mathbb{R}^2$ embedded with a discrete crack is presented in (a), and its phase-field (φ) regularized counterpart is shown in (b). The phase-field $\varphi : \Omega \longrightarrow [0, 1]$ localizes into a band of finite width, l, where zero and one correspond to the intact and fully fractured material states, respectively.

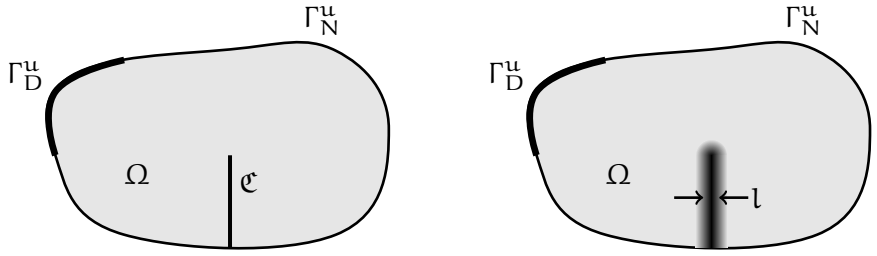

(a) discrete crack (b) diffused (smeared) crack

Figure 2.2: A solid $\Omega \in \mathbb{R}^2$ embedded with (a) discrete crack $\mathfrak{C}$ and (b) diffused (smeared) crack, with Dirichlet and Neumann boundaries indicated as Γ_D^u and Γ_N^u, respectively. Figure reproduced from [1].

The energy functional for the fracturing continuum in Figure 2.2a is expressed as

$$E(\mathbf{u}, \mathfrak{C}) = \Psi(\boldsymbol{\epsilon}[\mathbf{u}])\, d\Omega - \int_{\Gamma_N^u} \mathbf{t}_p^u \cdot \mathbf{u}\, d\Gamma - \int_{\Omega} \mathbf{b} \cdot \mathbf{u}\, d\Omega + G_c \int_{\mathfrak{C}} d\Gamma, \quad (2.17)$$

where, $\Psi(\boldsymbol{\epsilon}[\mathbf{u}])$ represents the strain energy density, and $\mathbf{t}_p^u$ and $\mathbf{b}$ indicate the surface traction and the body force, respectively. The fracture energy is contributed by the last integral, where G_c is the Griffith fracture toughness.

The phase-field fracture model [21, 22] incorporates an approximation of the discrete fracture energy using elliptic Ambrosio-Tortorelli function [67],

$$G_c \int_{\mathfrak{C}} d\Gamma \approx \int_{\Omega} \frac{G_c}{c_w} \left(\frac{w(\varphi)}{l} + l|\boldsymbol{\nabla}\varphi|^2 \right) d\Omega, \quad (2.18)$$

where, the phase-field $\varphi : \Omega \longrightarrow [0, 1]$ represents the fracture in a smeared (diffused) sense (see Figure 2.2b), c_w is a normalization constant linked with the choice of locally dissipated fracture energy $w(\varphi)$ [68]. Thereafter,

the phase-field energy functional for a fracturing continuum in Figure 2.2b is stated as

$$\begin{aligned} E(\mathbf{u},\varphi) = &\int_\Omega g(\varphi)\,\Psi^+(\boldsymbol{\epsilon}[\mathbf{u}])\,d\Omega + \int_\Omega \Psi^-(\boldsymbol{\epsilon}[\mathbf{u}])\,d\Omega - \int_{\Gamma_N^u} \mathbf{t}_p^u \cdot \mathbf{u}\,d\Gamma \\ &- \int_\Omega \mathbf{b}\cdot\mathbf{u}\,d\Omega + \int_\Omega \frac{G_c}{c_w}\left(\frac{w(\varphi)}{l} + l|\boldsymbol{\nabla}\varphi|^2\right) d\Omega, \end{aligned} \tag{2.19}$$

where, an additive decomposition of the strain energy density $\Psi(\boldsymbol{\epsilon}[\mathbf{u}])$ yields the fracture driving energy $\Psi^+(\boldsymbol{\epsilon}[\mathbf{u}])$ and the residual energy $\Psi^-(\boldsymbol{\epsilon}[\mathbf{u}])$. A degradation function $g(\varphi)$ is attached to $\Psi^+(\boldsymbol{\epsilon}[\mathbf{u}])$, accounting for the loss of strength and stiffness properties of the material upon fracture.

Choice of degradation and locally dissipated fracture energy functions

The phase-field fracture model offers flexibility in the construction of the degradation function $g(\varphi)$, albeit with the following restrictions,

- $g(0) = 1$ and $g(1) = 0$, since $\varphi = 0$ and 1 represent the intact and fully fractured material states, respectively,
- $g'(\varphi) < 0$, for a strictly decreasing monotone, and
- $g'(1) = 0$, in order to ensure that the energy converges to a finite value for a fractured material state.

The last criterion $g'(1) = 0$ ensures a zero crack driving force for a fully developed fracture, i.e., $\varphi = 1$. The zero crack driving force prevents the widening of localization band (see Figure 2.2b) in the direction orthogonal to the fracture.

> **Remark 2.** *A key difference between the phase-field fracture model and the gradient-enhanced continuum damage model [23] pertains to the fracture driving force. Unlike the phase-field fracture model, in gradient-enhanced damage models, the fracture driving force is constant. This results in the orthogonal widening of the localization band [24].*

Table 2.1 presents some of the popular degradation functions from the phase-field fracture literature. The quadratic function [22] and the cubic function [69] are adopted for modelling brittle fracture, whereas the rational fractions [2, 66] are a popular choice for modelling quasi-brittle fracture. Among the latter two, the rational fraction degradation function proposed by Wu [2] is adopted in this thesis. It involves additional material parameters (p, a_1, a_2, and a_3) which are calibrated from the different cohesive zone traction-separation relations. For a detailed derivation of these parameters, the reader is referred to Section 3 of [2]. Table 2.2 presents some of the

cohesive zone traction-separation relations adopted in phase-field fracture models. For all models, the parameter α_1 is computed as

$$\alpha_1 = \frac{4\, l_{ch}}{c_w\, l}, \tag{2.20}$$

where, l_{ch} is the Irwin's characteristic length, which governs the length of the fracture process zone. It is given by

$$l_{ch} = \frac{E_0\, G_c}{f_t^2}, \tag{2.21}$$

where, E_0 and f_t represent the Young's modulus and the tensile strength of the material, respectively.

$g(\varphi)$	Contribution
$(1-\varphi)^2$	Bourdin [22]
$3(1-\varphi)^2 - 2(1-\varphi)^3$	Borden et al. [69]
$\dfrac{(1-\varphi)^2}{(1-\varphi)^2 + \varphi + p\,\varphi^2}$	Lorentz and Godard [66]
$\dfrac{(1-\varphi)^p}{(1-\varphi)^p + \alpha_1\varphi + \alpha_1\alpha_2\varphi^2 + \alpha_1\alpha_2\alpha_3\varphi^3}$	Wu [2]

Table 2.1: Commonly used degradation functions in the phase-field fracture literature

Traction-separation relation	p	α_2	α_3
Linear	2	-0.5	0
Exponential	2.5	0.1748	0
Cornellisen et. al. [70]	2	1.3848	0.6567

Table 2.2: Cohesive zone traction-separation relations adopted in the phase-field fracture models [2].

Furthermore, the commonly used local dissipation fracture energy functions, $w(\varphi)$ are presented in Table 2.3. Here, AT and PFCZM are abbreviations for Ambrosio-Tortorelli [67] and Phase-Field regularized Cohesive Zone Model [2], respectively. In the cases of AT1 and PFCZM, an elastic stage precedes the onset of the phase-field fracture evolution. However, this elastic stage is missing from the AT2 model. The phase-field fracture evolves as soon as a specimen is loaded. In order to recover a pre-peak linear elastic behaviour for the AT2 model, Borden et al. [69] proposed a cubic degradation function (see Table 2.1).

Decomposition of the strain energy density

Within the phase-field fracture model, the strain energy density $\Psi(\boldsymbol{\epsilon}[\mathbf{u}])$ is additively decomposed into fracture driving $\Psi^+(\boldsymbol{\epsilon}[\mathbf{u}])$ and residual $\Psi^-(\boldsymbol{\epsilon}[\mathbf{u}])$ energies. The model offers flexibility in the choice of decomposition. Table

Abbreviated name	$w(\varphi)$	c_w
AT1	φ	$8/3$
AT2	φ^2	2
PFCZM	$2\varphi - \varphi^2$	π

Table 2.3: Commonly used local fracture energy functions in the phase-field fracture literature

2.4 provides the frequently used strain energy density decompositions in the phase-field fracture literature. In this context, K, λ and μ are material constants representing the bulk modulus, Lamé constant and shear modulus, respectively. The trace operator is given by tr, while $\langle\bullet\rangle_{\pm}$ represents the positive/negative Macaulay brackets. The latter is given by $0.5(\bullet \pm |\bullet|)$, where $|\bullet|$ indicates the absolute value of '$\bullet$'. Furthermore, $\boldsymbol{\epsilon}_{dev}$ is the deviatoric strain tensor, and $\boldsymbol{\epsilon}^{\pm}$ indicates the tensile/compressive strain tensors, obtained through spectral decomposition of the strain tensor.

Ψ^+	Ψ^-	Contribution
$\mu\,\boldsymbol{\epsilon}_{dev}\colon\boldsymbol{\epsilon}_{dev} + \frac{1}{2}Ktr^2(\boldsymbol{\epsilon})$	0	Bourdin [22]
$\mu\,\boldsymbol{\epsilon}_{dev}\colon\boldsymbol{\epsilon}_{dev}$	$\frac{1}{2}Ktr^2(\boldsymbol{\epsilon})$	Lancioni and Royer-Carfagni [71]
$\frac{1}{2}K\langle tr(\boldsymbol{\epsilon})\rangle_+^2 + \mu\,\boldsymbol{\epsilon}_{dev}\colon\boldsymbol{\epsilon}_{dev}$	$\frac{1}{2}K\langle tr(\boldsymbol{\epsilon})\rangle_-^2$	Amor, Marigo, and Maurini [72]
$\frac{1}{2}\lambda\langle tr(\boldsymbol{\epsilon})\rangle_+^2 + \mu\,\boldsymbol{\epsilon}^+\colon\boldsymbol{\epsilon}^+$	$\frac{1}{2}\lambda\langle tr(\boldsymbol{\epsilon})\rangle_-^2 + \mu\,\boldsymbol{\epsilon}^-\colon\boldsymbol{\epsilon}^-$	Miehe, Hofacker, and Welschinger [37]

Table 2.4: Frequently used strain energy density decompositions in the phase-field fracture literature

With reference to Table 2.4, it is observed that earlier research on the phase-field fracture model by Bourdin [22] did not consider any decomposition of strain energy density. In such a model, the total strain energy density, irrespective of its tensile or compressive nature, contributes to the evolution of the phase-field. As a consequence, the model exhibits (i) an unrealistic symmetric behaviour in terms of fracture propagation under tension and compression, and (ii) possible fracture interpenetration under compressive loading [73]. In a later research, Lancioni and Royer-Carfagni [71] proposed a deviatoric-volumetric split of the strain energy density for describing fracturing under shear loading. However, for most materials, fracturing is observed under tensile loading. This motivated the development of strain energy decomposition approaches by Amor, Marigo, and Maurini and Miehe, Hofacker, and Welschinger in [37, 72]. Amor, Marigo, and Maurini assumed a pure volumetric strain energy and the deviatoric energy as the fracture driving energy, while Miehe, Hofacker, and Welschinger opted for a tensile strain energy density, obtained through spectral decomposition of the strain.

Remark 3. *The tension-compression strain energy density decompositions proposed by Amor, Marigo, and Maurini [72] and Miehe, Hofacker, and Welschinger [37] have been used in this thesis. Their limitations and drawbacks are discussed by Li [74] and De Lorenzis and Maurini [73].*

2.2.1.1 *Variational equations*

The set of variational equations for the phase-field fracture model is derived upon minimizing the energy functional (2.19) w.r.t. its solution fields, the vector-valued displacement $\mathbf{u}$, and the scalar-valued phase-field φ. With appropriately defined test and trial Sobolev[7] spaces H^1 and the fracture irreversibility constraint $\dot{\varphi} \geqslant 0$, the complete variational problem assumes the form:

Variational Problem 2. *Find* $(\mathbf{u}, \varphi) \in \mathbb{U} \times \mathbb{P}$ *such that*

$$\begin{aligned} E'(\mathbf{u}, \varphi; \delta\mathbf{u}) = &\int_\Omega \left(g(\varphi) \frac{\partial \Psi^+(\boldsymbol{\epsilon}[\mathbf{u}])}{\partial \boldsymbol{\epsilon}} + \frac{\partial \Psi^-(\boldsymbol{\epsilon}[\mathbf{u}])}{\partial \boldsymbol{\epsilon}} \right) : \boldsymbol{\epsilon}[\delta\mathbf{u}] \, d\Omega \\ &- \int_{\Gamma_N^u} \mathbf{t}_p^u \cdot \delta\mathbf{u} \, d\Gamma = 0 \quad \forall \, \delta\mathbf{u} \in \mathbb{U}^0, \end{aligned} \tag{2.22a}$$

$$\begin{aligned} E'(\mathbf{u}, \varphi; \hat{\varphi}) = &\int_\Omega \left(g'(\varphi) \Psi^+(\boldsymbol{\epsilon}[\mathbf{u}]) + \frac{G_c}{c_w l} w'(\varphi) \right) (\hat{\varphi} - \varphi) \, d\Omega \\ &+ \int_\Omega \frac{G_c l}{c_w} \boldsymbol{\nabla}\varphi \cdot \boldsymbol{\nabla}(\hat{\varphi} - \varphi) \, d\Omega \geqslant 0 \quad \forall \, \hat{\varphi} \in \mathbb{P}, \end{aligned} \tag{2.22b}$$

using pertinent time-dependent Dirichlet boundary conditions $\mathbf{u}^p$ *on* Γ_D^u *and* φ^p *on* Γ_D^φ*, and Neumann boundary condition* $\mathbf{t}_p^u$ *on* Γ_N^u*. The trial and test spaces are defined as*

$$\mathbb{U} = \{\mathbf{u} \in [H^1(\Omega)]^{\dim} | \mathbf{u} = \mathbf{u}^p \text{ on } \Gamma_D^u\}, \tag{2.23a}$$

$$\mathbb{P} = \{\varphi \in [H^1(\Omega)] | \varphi \geqslant {}^n\varphi | \varphi = \varphi^p \text{ on } \Gamma_D^\varphi\}, \tag{2.23b}$$

$$\mathbb{U}^0 = \{\mathbf{u} \in [H^1(\Omega)]^{\dim} | \mathbf{u} = \mathbf{0} \text{ on } \Gamma_D^u\}. \tag{2.23c}$$

In (2.23b), the left superscript n *refers to the previous time-step.* ■

The fracture irreversibility constraint $\dot{\varphi} \geqslant 0$ manifests in the form of variational inequality phase-field evolution equation (2.22b) with a restricted space (2.23b). The variational inequality, as such, is not challenging to implement in a computational framework, if the inequality can be enforced pointwise. However, for the phase-field fracture model, pointwise enforcement of the inequality is not possible due to the gradient terms manifesting a

7 A function u for which $\int_\Omega (u)^2 + (\boldsymbol{\nabla} u)^2 < \infty$, belongs to Sobolev space of degree one, denoted by H^1. For more on function spaces, the reader is referred to [31].

higher regularity requirement $H^1(\Omega)$ on the phase-field variable and its test function. Hence, the definition in (2.23b) is not viable from a mathematical point of view and needs regularization.

2.2.2 *Computational challenges in phase-field fracture models*

Despite the popularity and the ease of implementation for modelling complex fracture topologies, the phase-field fracture model has its set of computational challenges. Broadly, these challenges are categorized into, minimizing of a non-convex energy functional (2.19) simultaneously w.r.t. the displacement and phase-field variables, fracture irreversibility and associated variational inequality (2.22b), and the requirement for extremely fine meshes in the diffused fracture region of the continuum (see Figure 2.2b). The addressment of these challenges in phase-field fracture literature is presented in the next sub-sections.

2.2.2.1 *Non-convex energy functional*

The non-convex nature of the phase-field fracture energy functional (2.19) stems from the term accounting for material degradation due to fracture, i.e., $g(\varphi)\Psi^+(\boldsymbol{\epsilon}[\mathbf{u}])$. The fracture driving energy $\Psi^+(\boldsymbol{\epsilon}[\mathbf{u}])$ is quadratic, and the degradation function $g(\varphi)$ is quadratic or higher order w.r.t to its argument. This non-convex nature manifests in the form of poor convergence behaviour of the fully coupled Newton-Raphson method, possibly due an indefinite Hessian during numerical simulations.

In the past decade, several efforts were undertaken to improve the convergence behaviour of the monolithic Newton-Raphson method, adopting techniques mostly borrowed from optimization theory. For instance, Gerasimov and De Lorenzis [75] incorporated possible negative curvature directions in line-search method. The line-search parameter range is set to $[-1, 1]$ using 10 or 20 intervals, where the functional and their derivatives were computed. Thereafter, a $\mathbb{C}^1$ continuous functional is constructed, and a line-search parameter corresponding to its minimum value is chosen as an admissible step in the iterative process. The negative curvature direction technique has been worked upon as early as the 1970s by Fletcher and Freeman [76] and Mukai and Polak [77]. However, in the context of phase-field fracture models, its robustness and efficiency is not yet established.

In another set of methods, modifications to the Hessian were proposed to obtain a convergent monolithic solution technique. For instance, Wick [78] identified the matrix block arising from the derivative of the momentum balance equation (2.27a) w.r.t the phase-field variable as the problematic component of the Hessian matrix. Based on this observation and drawing inspiration from fluid mechanics literature [79–81], in [78], Wick proposed a separation of well-posed and problematic Hessian terms. The problematic term is then scaled with heuristically computed scalar. A main drawback of this method, mentioned by Wick is the lack of rigorous convergence results. Adopting an alternative approach, Lampron, Therriault, and Lévesque

proposed monolithic solution technique in [82], based on the eigenvalue decomposition of the Hessian, and adding scaled diagonal matrices to ensure its positive definiteness. Although the method yields desirable results in the context of convergence behaviour, eigenvalue computations are expensive and as such, the method is not scalable. Finally, Wu, Huang, and Nguyen introduced the quasi-Newton BFGS[8] method as a promising solution technique for the phase-field fracture model in [83]. Aided with an existing implementation in the commercial finite element software, Abaqus, the BFGS method soared in popularity for phase-field fracture modelling. However, most studies involving the BFGS method are confined to a weak iteration terminating tolerance ($\approx 5 \cdot 10^{-3}$). This points to the lack of a rigorous convergence study of the BFGS method in the context of phase-field fracture models.

Furthermore, in an completely different approach, researchers explored convexification techniques. Heister, Wheeler, and Wick [34] proposed an extrapolation technique for the phase-field variable to be used in the momentum balance equation (2.27a). Consequently, the problematic Hessian component is circumvented, and the monolithic Newton-Raphson method is established as a convergent solution technique. However, due to the lack of temporal regularity in the phase-field variable evolution, the extrapolation technique itself is questionable as stated by the authors themselves. More recently, in [84], an outer fixed-point iterative process was proposed to correct the error introduced due to extrapolation. However, extensive studies are required to establish the convergence behaviour of the outer fixed-point iteration on the extrapolation. In yet another convexification technique, the alternate minimization[9] technique was proposed by Bourdin [22] based on the convex nature of the displacement and phase-field sub-problems. In this method, the displacement and the phase-field variational equations are solved in an alternate fashion until the $\mathbb{L}_2$ norm of the change in the phase-field reaches a certain tolerance. Although, the convex sub-problems lend robustness, the alternate iterative sequence makes the method expensive, typically requiring thousands of iterations to converge for brittle fracture benchmark problems [85].

In the aforementioned methods in this section, researchers have adopted a incremental iterative approach. Within this approach, the loading of a continuum specimen is carried out using predetermined force/displacement increments. In a deviation from this approach, the arc-length method, pioneered by Wempner [86], Riks [87, 88] and Crisfield [89], considers the load increment as an unknown. A path-following/arc-length constraint equation is added to the original system of equations to maintain static determinacy. Based on the design of the constraint equation, spherical [86, 88, 89], cylindrical [89] and elliptical [90] arc-length methods emerged as different variants. The variants were initially conceived to solve structural engineer-

8 BFGS is an acronym for its developers Charles George Broyden, Roger Fletcher, Donald Goldfarb and David Shanno.

9 also referred to as the staggered solution technique in phase-field fracture literature

ing problems exhibiting complex deformations beyond limit points[10]. Later, in [91], Verhoosel, Remmers, and Gutiérrez proposed a dissipation based arc-length constraint encompassing a larger class of material and geometric nonlinear response. In the context of phase-field fracture models, the arc-length method with a dissipation-based constraint was used by Vignollet et al. [92], and May, Vignollet, and De Borst [93]. However, both studies were limited to a single benchmark problem, and data supporting robustness and convergence behaviour were absent. In a later study, Singh et al. [94] combined the dissipation-based arc-length solver with the alternate minimization solver.

2.2.2.2 *Fracture irreversibility*

The fracture irreversibility constraint $\dot{\phi} \geqslant 0$ in the phase-field fracture model stems from the model assumption of preventing any healing of fractures. In that sense, it is similar to Continuum Damage Mechanics (CDM) [95–97], where the damage variable evolution is irreversible. However, in the case of CDM, the damage variable is local[11], hence, a local set of Karush-Kuhn-Tucker (KKT) conditions [98, 99] is used to enforce damage irreversibility. For the phase-field fracture model, the phase-field variable is a global field with a regularity requirement pertaining to the existence of its derivative. Therefore, the KKT conditions apply in a global sense, yielding a variational inequality phase-field evolution equation with restrictive test and trial spaces (see Variational Problem 2).

The implementation of a variational inequality equation in a computational framework is a challenging task. Several researchers have proposed different methods to circumvent this. For instance, Miehe, Hofacker, and Welschinger in [37] proposed a '*history variable*' method, where the local KKT conditions are enforced on the fracture driving energy $\Psi^{+}(\boldsymbol{\epsilon}[\mathbf{u}])$, as a means to satisfy fracture irreversibility. The method stems from ignoring the gradient term in the phase-field evolution equation (2.22b) and treating $\Psi^{+}(\boldsymbol{\epsilon}[\mathbf{u}])$ as the fracture driving source term. A history variable $\mathcal{H}$ stores the maximum value of this fracture driving energy $\Psi^{+}(\boldsymbol{\epsilon}[\mathbf{u}])$. Thereafter, $\Psi^{+}(\boldsymbol{\epsilon}[\mathbf{u}])$ in (2.22b) is replaced by $\mathcal{H}$. Mathematically, $\mathcal{H}$ is defined as

$$\mathcal{H} = \max\{{}^{n}\mathcal{H}, \Psi^{+}(\boldsymbol{\epsilon}[\mathbf{u}])\} \tag{2.24}$$

where, the left superscipt n refers to the previous time-step. On replacing $\Psi^{+}(\boldsymbol{\epsilon}[\mathbf{u}])$ in (2.22b) with $\mathcal{H}$, the Variational Problem 2 attains the modified form:

10 Limit points are coordinates in the load-displacement space, where load increments or displacement increments switch signs.

11 exists pointwise in the domain without any regularity requirements

Variational Problem 3. *Find* $(\mathbf{u}, \varphi) \in \mathbb{U} \times \mathbb{P}$ *such that*

$$E'(\mathbf{u}, \varphi; \delta\mathbf{u}) = \int_\Omega \left(g(\varphi) \frac{\partial \Psi^+(\boldsymbol{\epsilon}[\mathbf{u}])}{\partial \boldsymbol{\epsilon}} + \frac{\partial \Psi^-(\boldsymbol{\epsilon}[\mathbf{u}])}{\partial \boldsymbol{\epsilon}} \right) : \boldsymbol{\epsilon}[\delta\mathbf{u}] \, d\Omega \tag{2.25a}$$
$$- \int_{\Gamma_N^u} \mathbf{t}_p^u \cdot \delta\mathbf{u} \, d\Gamma = 0 \quad \forall \, \delta\mathbf{u} \in \mathbb{U}^0,$$

$$E'(\mathbf{u}, \varphi; \delta\varphi) = \int_\Omega \left(g'(\varphi)\mathcal{H} + \frac{G_c}{c_w l} w'(\varphi) \right) \delta\varphi \, d\Omega \tag{2.25b}$$
$$+ \int_\Omega \frac{G_c l}{c_w} \boldsymbol{\nabla}\varphi \cdot \boldsymbol{\nabla}\delta\varphi \, d\Omega = 0 \quad \forall \, \delta\varphi \in \mathbb{P}^0,$$

using pertinent time-dependent Dirichlet boundary conditions $\mathbf{u}^p$ *on* Γ_D^u *and* φ^p *on* Γ_D^φ*, and Neumann boundary condition* $\mathbf{t}_p^u$ *on* Γ_N^u*. The trial and test spaces are defined as*

$$\mathbb{U} = \{\mathbf{u} \in [H^1(\Omega)]^{\dim} | \mathbf{u} = \mathbf{u}^p \text{ on } \Gamma_D^u\}, \tag{2.26a}$$
$$\mathbb{P} = \{\varphi \in [H^1(\Omega)] | \varphi = \varphi^p \text{ on } \Gamma_D^\varphi\}, \tag{2.26b}$$
$$\mathbb{U}^0 = \{\mathbf{u} \in [H^1(\Omega)]^{\dim} | \mathbf{u} = \mathbf{0} \text{ on } \Gamma_D^u\}, \tag{2.26c}$$
$$\mathbb{P}^0 = \{\varphi \in [H^1(\Omega)] | \varphi = 0 \text{ on } \Gamma_D^\varphi\}. \tag{2.26d}$$

The history variable $\mathcal{H}$ *in (2.25b) is defined in (2.24).* ■

The history variable approach results in a variational equality phase-field evolution equation (2.25b) with relaxed trial (2.26b) and test (2.26d) spaces for the phase-field variable and its test function. However, the variational consistency is lost, since the energy functional (2.19) cannot be recovered from the variational equations.

The penalization method was proposed by Gerasimov and De Lorenzis [32] as a variationally consistent way of enforcing the fracture irreversibility constraint. The variational problem with the penalization method is formulated as:

Variational Problem 4. *Find* $(\mathbf{u}, \varphi) \in \mathbb{U} \times \mathbb{P}$ *such that*

$$E'(\mathbf{u}, \varphi; \delta\mathbf{u}) = \int_\Omega \left(g(\varphi) \frac{\partial \Psi^+(\boldsymbol{\epsilon}[\mathbf{u}])}{\partial \boldsymbol{\epsilon}} + \frac{\partial \Psi^-(\boldsymbol{\epsilon}[\mathbf{u}])}{\partial \boldsymbol{\epsilon}} \right) : \boldsymbol{\epsilon}[\delta\mathbf{u}] \, d\Omega \tag{2.27a}$$
$$- \int_{\Gamma_N^u} \mathbf{t}_p^u \cdot \delta\mathbf{u} \, d\Gamma = 0 \quad \forall \, \delta\mathbf{u} \in \mathbb{U}^0,$$

Variational Problem 4 (continued)

$$\begin{aligned} E'(\mathbf{u}, \varphi; \delta\varphi) = &\int_\Omega \left(g'(\varphi)\Psi^+(\boldsymbol{\epsilon}[\mathbf{u}]) + \frac{G_c}{c_w l} w'(\varphi) \right) \delta\varphi \, d\Omega \\ &+ \int_\Omega \frac{G_c l}{c_w} \boldsymbol{\nabla}\varphi \cdot \boldsymbol{\nabla}\delta\varphi \, d\Omega \\ &+ \eta \int_\Omega \langle {}^{n}\varphi - \varphi \rangle_+ \, \delta\varphi \, d\Omega = 0 \quad \forall \, \delta\varphi \in \mathbb{P}^0, \end{aligned} \tag{2.27b}$$

using pertinent time-dependent Dirichlet boundary conditions $\mathbf{u}^p$ *on* Γ_D^u *and* φ^p *on* Γ_D^φ*, and Neumann boundary condition* $\mathbf{t}_p^u$ *on* Γ_N^u*. The superscript* n *in the above equation indicates the previous (pseudo) time-step. the The trial and test spaces are defined as*

$$\mathbb{U} = \{\mathbf{u} \in [H^1(\Omega)]^{\dim} | \mathbf{u} = \mathbf{u}^p \text{ on } \Gamma_D^u\}, \tag{2.28a}$$

$$\mathbb{P} = \{\varphi \in [H^1(\Omega)] | \varphi = \varphi^p \text{ on } \Gamma_D^\varphi\}, \tag{2.28b}$$

$$\mathbb{U}^0 = \{\mathbf{u} \in [H^1(\Omega)]^{\dim} | \mathbf{u} = \mathbf{0} \text{ on } \Gamma_D^u\}, \tag{2.28c}$$

$$\mathbb{P}^0 = \{\varphi \in [H^1(\Omega)] | \varphi = 0 \text{ on } \Gamma_D^\varphi\}. \tag{2.28d}$$

■

Similar to the history-variable approach in Variational Problem 3, the penalization approach in Variational Problem 4 also relaxes the function space for the phase-field and its test function (cf. (2.28b), (2.28d) with (2.26b), (2.26d)). Theoretically, the fracture irreversibility $\dot{\varphi} \geqslant 0$ is enforced in an exact fashion only when the penalty parameter $\eta \longrightarrow \infty$. However, Gerasimov and De Lorenzis in [32] introduced the notion of a user-prescribed tolerance $\texttt{TOL}_{ir}$ on the fracture irreversibility constraint. Based on the choice of $\texttt{TOL}_{ir}$, a lower bound for the penalty parameter was proposed as

$$\eta(\texttt{TOL}_{ir}) = \begin{cases} \dfrac{G_c}{l} \dfrac{27}{64\,\texttt{TOL}_{ir}^2} & \text{AT1 model} \\ \dfrac{G_c}{l} \left(\dfrac{1}{\texttt{TOL}_{ir}^2} - 1 \right) & \text{AT2 model} \end{cases} \tag{2.29}$$

For a strict user-prescribed tolerance $\texttt{TOL}_{ir}$ on the fracture irreversibility constraint, the penalty parameter may attain values that results in an ill-conditioned system of equations, affecting numerical accuracy of the linear solvers.

Yet another approach for implementing fracture irreversibility was proposed by Heister, Wheeler, and Wick [34]. Therein, the authors adapted Hintermüller, Ito, and Kunisch's primal-dual active set method [33] for the phase-field fracture model. It is argued that the approach circumvents possible ill-conditioning of the system of equations, observed with the penalization method. The primal-dual active set method incorporates the fracture irreversibility constraint $\dot{\varphi} \geqslant 0$ using a Lagrange multiplier. The resulting

system of equations is then treated using a primal-dual active set strategy [33]. An active set $\mathcal{A}_k$ in the k^{th} Newton-Raphson iteration is defined as

$$\mathcal{A}_k = \{i | (\mathbf{B}^{-1})_{ii} (\mathbf{r}_k^{\varphi})_i + c(\tilde{\varphi}_k + \Delta\tilde{\varphi}_k - {}^n\tilde{\varphi})_i < 0\}, \tag{2.30}$$

where, i represents a Degree Of Freedom (DOF) index in the discrete system of equations, pertaining to the phase-field. Furthermore, $\mathbf{B}$ is a fictitious lumped mass matrix constructed using unit density, $\mathbf{r}_k^{\varphi}$ is the phase-field equation residual, c is a scalar constant, and $\tilde{\varphi}$ and $\Delta\tilde{\varphi}$ represents the phase-field solution vector and its increment, respectively. The left superscript n refers to the previous converged step.

In every Newton-Raphson iteration, the active set DOFs are eliminated from the system of equations. Convergence is achieved when the norm of the residual is below a certain tolerance limit and the active set does not change. Although, this primal-dual active set method circumvents the need for tuning/penalty parameters, the explicit tracking of the active/inactive sets could be expensive according to De Lorenzis and Gerasimov [28].

2.2.2.3 *Extremely fine mesh*

The phase-field fracture model requires extremely fine meshes to resolve the smeared crack region (see Figure 2.2b). This requirement may be fulfilled upon adopting a uniformly refined mesh, or pre-refining a mesh in certain sub-domains if the crack path is known *a priori*. However, the use of uniformly refined meshes increases the computational cost, warranting the need for parallel computing resources [22]. Alternatively, one may adopt mesh refinement strategies based on certain indicators. For instance, Heister, Wheeler, and Wick [34] proposed the use of a threshold phase-field value to refine certain elements in the mesh. This strategy was also adopted by [38, 100]. Furthermore, Jansari et al. [101] used recovery-based error estimates, while Wick [102] opted for posteriori error estimates based on the dual-weighted residual method as element refinement indicators. Other mesh adaptivity strategies in the phase-field fracture literature include the finite cell method [103] and the dual mesh approach [100].

In this thesis, the finite element meshes pertaining to the benchmark problems are pre-refined since the crack path is known *a priori*. Only in Chapter 6, uniformly refined meshes are used to simulate soil desiccation cracking as no information is available on the crack path.

2.3 PORO-MECHANICS

Poro-mechanics is the study of fluid-filled porous materials whose mechanical behaviour is influenced by the pore fluid [104]. Typical example of such materials include rocks and soil, biological tissues, foams, gel, and ceramics. Early theoretical developments in poro-mechanics were carried out in the context of rocks and soil by Maurice A. Biot, during 1935-1962 (see

[105–109]). Biot's theory of poro-mechanics [109] assumes a linear elastic behaviour of the solid and fluid phases, and a laminar flow of the fluid through the interconnected pores within the solid matrix. Due to the linearity assumption, Biot's theory of poro-mechanics is also referred to as the theory of poro-elasticity.

In the subsequent part of this section, the set of governing equations pertinent to poro-elasticity is derived. These equations are re-visited later in this thesis for developing hydraulic fracturing and soil desiccation cracking models in Chapters 5 and 6, respectively.

2.3.1 *The energy functional*

The energy functional for a generic continuum (2.1) is extended towards porous medium, adapting the seminal work of Biot [109]. The extended energy functional is posited as a function of the strain $\boldsymbol{\epsilon}[\mathbf{u}]$ and the increment of the fluid content ζ. The fluid content increment depends on the fluid pressure in the pore space p and the volumetric strain of solid skeleton $\epsilon_{vol}[\mathbf{u}] = \boldsymbol{\nabla} \cdot \mathbf{u}$, and is expressed as

$$\zeta = \frac{p}{M} + \alpha \boldsymbol{\nabla} \cdot \mathbf{u}. \tag{2.31}$$

Here, the coefficients M and α represent the Biot modulus and the Biot coefficient, respectively. The energy functional is then expressed as [38, 42],

$$E^*(\mathbf{u}, \zeta) = \int_\Omega \Psi(\boldsymbol{\epsilon}[\mathbf{u}])\, d\Omega + \int_\Omega \frac{p^2(\boldsymbol{\epsilon}[\mathbf{u}], \zeta)}{2M}\, d\Omega. \tag{2.32}$$

Thereafter, a Legendre transformation is carried out to replace the argument ζ with the fluid pressure p. This results in an alternative energy functional,

$$E(\mathbf{u}, p) = \int_\Omega \Psi(\boldsymbol{\epsilon}[\mathbf{u}])\, d\Omega - \int_\Omega \alpha\, p\, \boldsymbol{\nabla} \cdot \mathbf{u}\, d\Omega - \int_\Omega \frac{p^2}{2M}\, d\Omega. \tag{2.33}$$

The first variation of the energy functional (2.33) w.r.t the displacement $\mathbf{u}$ yields the momentum balance variational equation,

$$E'(\mathbf{u}, p; \delta\mathbf{u}) = \int_\Omega \boldsymbol{\sigma}(\boldsymbol{\epsilon}[\mathbf{u}]) : \boldsymbol{\epsilon}[\delta\mathbf{u}]\, d\Omega - \int_\Omega \alpha\, p\, \boldsymbol{\nabla} \cdot \delta\mathbf{u}\, d\Omega = 0. \tag{2.34}$$

The momentum balance variational equation (2.34) is applicable when the pore space is fully saturated with one type of fluid. For a porous medium, where the pore space is filled with more than one immiscible fluids (for instance, water and gas[12]), the fluid pressure p is additively decomposed as

$$p = \chi_w\, p_w + \chi_g\, p_g, \tag{2.35}$$

12 Model assumption considering water and gas as immiscible.

where, the subscripts w and g indicate water and gas phases, and χ is an experimentally determined Bishop parameter accounting for the different contact area of the fluids with the solid grains [110]. The decomposition (2.35) follows from the Representative Volume Element (RVE) based averaging theory [111]. Furthermore, in the case of microstructurally isotropic constituents, the Bishop parameter χ may be replaced by the degree of saturation S. This results in,

$$p = S_w\, p_w + S_g\, p_g. \tag{2.36}$$

At this point, it is important to note that the fluid pressures (p_w and p_g) utilized in the momentum balance variational equation (2.34) are obtained from their respective mass conservation equations.

2.3.2 *Mass conservation*

The conservation of mass states that the rate of increase in mass in any domain Ω is equal to the difference between the rate of mass entering and leaving the domain. In the context of porous medium, the mass conservation equation applies to all of its constituents, i.e., the solid matrix and the fluid phases, water and gas.

Conservation of solid mass

Let us consider a porous RVE medium occupying the domain Ω. The mass of its solid constituent m_s is expressed as

$$m_s = \int_\Omega (1-n)\, \rho_s \, d\Omega \tag{2.37}$$

where, $(1-n)$ accounts for the solid constituent volume fraction, using the porosity n, and ρ_s is the intrinsically averaged density of the solid. The conservation of the solid mass m_s is mathematically expressed as

$$\frac{D m_s}{D t} = 0. \tag{2.38}$$

Adopting the material time derivative in an Eulerian reference frame, the solid mass conservation equation (2.38) is reformulated as

$$\int_\Omega \left(\frac{\partial (1-n)\rho_s}{\partial t} + \Big[(1-n)\, \rho_s\, \dot{\mathbf{u}}_s \Big] \cdot \boldsymbol{\nabla} \right) d\Omega = 0. \tag{2.39}$$

Here, $\dot{\mathbf{u}}_s$ represents the solid skeleton velocity. Thereafter, assuming (2.39) to hold pointwise in the domain Ω in conjunction with negligible spatial variation of ρ_s and n,

$$\frac{\partial(1-n)\rho_s}{\partial t} + (1-n)\,\rho_s\,\boldsymbol{\nabla}\cdot\dot{\mathbf{u}}_s = 0. \tag{2.40}$$

The time derivative of the solid pressure density ρ_s, adopted from Verruijt [112] is stated as

$$\frac{\partial \rho_s}{\partial t} = \frac{\rho_s C_s}{1-n}\left[(\alpha-n)\frac{\partial p}{\partial t} - \frac{1}{C}\frac{\partial \epsilon_{vol}}{\partial t}\right]. \tag{2.41}$$

Note that the fluid pressure p in the above equation comprises of both the water and gas phases, expressed earlier via (2.36). Furthermore, C_s and C represent the solid grain compressibility and the compressibility of the porous medium, respectively. The use of differentiation chain rule in (2.40) in conjunction with (2.41) results in an expression for the time derivative of the porosity as

$$\frac{\partial n}{\partial t} = (\alpha-n)\,C_s\,\frac{\partial p}{\partial t} + \left(1-\frac{C_s}{C}\right)\dot{\epsilon}_{vol} - n\,\boldsymbol{\nabla}\cdot\dot{\mathbf{u}}_s. \tag{2.42}$$

Upon defining the Biot coefficient α as

$$\alpha = 1 - \frac{C_s}{C}, \tag{2.43}$$

the time derivative of the porosity, (2.42) is further simplified to,

$$\frac{\partial n}{\partial t} = (\alpha-n)\,C_s\,\frac{\partial p}{\partial t} + \alpha\dot{\epsilon}_{vol} - n\,\boldsymbol{\nabla}\cdot\dot{\mathbf{u}}_s. \tag{2.44}$$

Conservation of fluid mass

The conservation of mass of a fluid phase $\pi = w, g$ is carried out in similar fashion as the conservation of solid mass. To that end, the mass of the fluid phase π is defined as

$$m_\pi = \int_\Omega n S_\pi \rho_\pi d\Omega. \tag{2.45}$$

Here, the volume fraction of π is accounted for with nS_π, and ρ_π is its intrinsic averaged density. The conservation of the fluid mass requires

$$\frac{Dm_\pi}{Dt} = 0. \tag{2.46}$$

Similar to the derivation of the solid mass conservation, adopting the material time derivative in conjunction with negligible spatial variation of n, ρ_π and S_π results in

$$\frac{\partial(nS_\pi\rho_\pi)}{\partial t} + nS_\pi\rho_\pi \boldsymbol{\nabla}\cdot\dot{\mathbf{u}}_\pi = 0, \tag{2.47}$$

and using the chain rule of differentiation yields

$$S_\pi\rho_\pi\frac{\partial n}{\partial t} + n\rho_\pi\frac{\partial S_\pi}{\partial t} + nS_\pi\frac{\partial \rho_\pi}{\partial t} + nS_\pi\rho_\pi\boldsymbol{\nabla}\cdot\dot{\mathbf{u}}_\pi = 0. \tag{2.48}$$

In the above equation, $\frac{\partial n}{\partial t}$ is substituted from (2.42). The time derivative of the fluid pressure density ρ_π is obtained from the constitutive relationship,

$$\rho_\pi(p_\pi) := \rho_{\pi,0}\exp(p_\pi + p_{\pi,s} + p_{\pi,0}). \tag{2.49}$$

Here, $\rho_{\pi,0}$ and $p_{\pi,0}$ represent the reference fluid density and the fluid pressure, respectively, and $p_{\pi,s}$ is the initial hydrostatic fluid pressure. Incorporating (2.42) and (2.49) in (2.48) results in

$$\begin{aligned}&(\alpha-n)C_sS_\pi\rho_\pi\frac{\partial p}{\partial t} + n\rho_\pi\frac{\partial S_\pi}{\partial t} + n\rho_\pi S_\pi C_\pi\frac{\partial p_\pi}{\partial t}\\ &+ \alpha\rho_\pi S_\pi\frac{\partial \epsilon_{vol}}{\partial t} + \boldsymbol{\nabla}\cdot[nS_\pi\rho_\pi(\dot{u}_\pi - \dot{u}_s)] = 0.\end{aligned} \tag{2.50}$$

In the above expression, the fluid flow in the interconnected pore space is assumed to be laminar. As such, the Darcy's law,

$$nS_\pi\rho_\pi(\dot{u}_\pi - \dot{u}_s) = -k_{r\pi}\frac{k_i\mathbf{I}}{\mu_\pi}(\boldsymbol{\nabla}p_\pi - \rho_\pi\mathbf{g}), \tag{2.51}$$

is adopted. Here, $k_{r\pi}$ and k_i represent the relative permeability and the intrinsic permeability of the fluid phase π, respectively, and μ_π is the dynamic viscosity of the phase π. Furthermore, the pressure decomposition (2.36) is utilized, resulting in a mass conservation equation for the water phase ($\pi = w$),

$$\begin{aligned}&\left[(\alpha-n)C_sS_w^2 + nS_wC_w\right]\frac{\partial p_w}{\partial t} + (\alpha-n)C_sS_wS_g\frac{\partial p_g}{\partial t}\\ &+ \left[(\alpha-n)C_sS_w(p_w-p_g) + n\right]\frac{\partial S_w}{\partial t} + \alpha S_w\frac{\partial \epsilon_{vol}}{\partial t}\\ &+ \boldsymbol{\nabla}\cdot\left[-k_{rw}\frac{k_i\mathbf{I}}{\mu_w}(\boldsymbol{\nabla}p_w - \rho_w\mathbf{g})\right] = 0,\end{aligned} \tag{2.52}$$

and for the gas phase ($\pi = g$),

$$\begin{aligned}&\left[(\alpha-n)C_sS_g^2+nS_gC_g\right]\frac{\partial p_g}{\partial t}+(\alpha-n)C_sS_wS_g\frac{\partial p_w}{\partial t}\\&+\left[(\alpha-n)C_sS_g(p_g-p_w)+n\right]\frac{\partial S_g}{\partial t}+\alpha S_g\frac{\partial \epsilon_{vol}}{\partial t}\\&+\boldsymbol{\nabla}\cdot\left[-k_{rg}\frac{k_i\mathbf{I}}{\mu_g}(\boldsymbol{\nabla}p_g-\rho_g\mathbf{g})\right]=0.\end{aligned}\tag{2.53}$$

In the above equations (2.52,2.53), the water and gas saturation (S_w and S_g) are obtained using fluid retention models. In the context of geomechanics, the term Soil Water Retention Curve (SWRC) is prevalent. Typical examples of SWRCs include van Genuchten [113], Corey-Brooks [114], and Gardner [115] curves.

Remark 4. *Instead of modelling the porous medium as a three-phase partially saturated model, a two-phase partially saturated model may be assumed, setting the gas pressure $p_g = 0$. This eliminates the gas transport equation (2.53), and simplifies the water transport equation (2.52) to*

$$\begin{aligned}&\left[(\alpha-n)C_sS_w^2+nS_wC_w\right]\frac{\partial p_w}{\partial t}+\left[(\alpha-n)C_sS_wp_w+n\right]\frac{\partial S_w}{\partial t}\\&+\alpha S_w\frac{\partial \epsilon_{vol}}{\partial t}+\boldsymbol{\nabla}\cdot\left[-k_{rw}\frac{k_i\mathbf{I}}{\mu_w}(\boldsymbol{\nabla}p_w-\rho_w\mathbf{g})\right]=0.\end{aligned}\tag{2.54}$$

For a fully saturated two-phase porous medium, the water transport equation (2.54) is further simplified to,

$$\left[(\alpha-n)C_s+nC_w\right]\frac{\partial p_w}{\partial t}+\alpha\frac{\partial \epsilon_{vol}}{\partial t}+\boldsymbol{\nabla}\cdot\left[-\frac{k_i\mathbf{I}}{\mu_w}(\boldsymbol{\nabla}p_w-\rho_w\mathbf{g})\right]=0.\tag{2.55}$$

These equations are used for modelling soil desiccation cracking and hydraulic fracture in the latter part of this thesis.

2.4 MULTI-SCALE MODELLING OF MATERIALS

Multi-scale modelling of materials is a concept concerning the derivation of equations, parameters, and simulation algorithms, which describes the material behaviour at a given length-scale, based on the physical phenomena at a finer scale [116]. Central to this concept, is the better understanding

of the fine scale physics and topological features (e.g., spatial distribution of the material constituents, voids, defects), compared to that of the coarse scale. The fine scale material constituents may be atoms, molecules, or mesoscale entities like phases, grains. Multi-scale modelling of materials circumvents the drawback of the phenomenological constitutive material modelling approach. The constitutive material models are based on limited experimental data, and does not account for the underlying fine scale physics.

Multi-scale modelling of materials today has evolved from its early influence from the Cauchy-Born rule [117]. Different variants exists, evolving from the developments in statistical mechanics, homogenization theory and linear algebra. Broadly, the multi-scale modelling techniques maybe classified into two categories, resolved scale methods[13] and upscaling/hierarchical methods [116]. Resolved scale methods employ coarse and fine scale physics in different parts of the computational domain. At the interface between the scales, information exchange is carried out. This process is also referred to as a 'hand-shake'. Examples of the resolved scale methods include the Quasi-Continuum method [118], the multi-scale finite element method [119–122], the global-local method [123], and domain decomposition method [124].

In this thesis, the focus is towards upscaling/hierarchical multi-scale modelling methods. The upscaling methods rely on fine scale physics on an idealized domain, and communicates the average material response to the coarse scale. The idealized fine scale domain is often referred to as the microstructure, Representative Volume Element (RVE) [125], or Statistical Volume Element (SVE) [126]. Furthermore, the fine scale and coarse equations may be derived using asymptotic methods [127], variationally consistent homogenization [128] technique, or even postulated directly. Thereafter, the link between the fine scale and coarse scale is established using the Hill-Mandel macro-homogeneity conditions [129–131]. In this thesis, the variationally consistent homogenization technique is adopted to derive the fine scale and coarse scale equations.

2.4.1 *Variationally Consistent Homogenization*

The Variationally Consistent Homogenization (VCH) technique was proposed by Larsson, Runesson, and Su [128], as a method to obtain fine and coarse scale variational equations from the former. Therefore, it may be viewed as an alternative to the asymptotic methods. The VCH technique assumes the existence of fully resolved fine scale physics equations in the variational form. Thereafter, the coarse scale equations are derived using suitable averaging methods, resulting in a bottom-up approach. The essential ingredients of the VCH technique are (A) the separation of scales via the Variational Multi-Scale (VMS) method [119, 121], (B) the computational ho-

13 Resolved scale methods are also referred to as concurrent or information passing methods in multi-scale modelling literature.

mogenization or the averaging approach, (C) prolongation of solution fields using Taylor series expansion, and (D) establishing the macro-homogeneity conditions [129–131]. They are addressed in detail in the remaining part of this section. Note that the terms coarse scale and fine scale are used interchangeably with macro scale and sub scale (denoted with superscripts M and S, respectively) throughout the thesis.

(A) Variational Multi-Scale (VMS) method

The VCH technique adopts the Variational Multi-Scale (VMS) method [119, 121] as the point of departure from a fully resolved fine scale problem. The VMS method admits an additive decomposition of the solution fields and corresponding test functions into a smooth coarse scale and a fluctuating fine scale component. To put the VMS method into context, let us consider the generic continuum mechanics Variational Problem 1. For clarity, the variational equation (2.3) is re-stated,

$$\int_{\Omega} \boldsymbol{\sigma}(\mathbf{u}) : \boldsymbol{\epsilon}(\delta\mathbf{u})\, d\Omega = 0 \quad \forall\, \delta\mathbf{u} \in \mathbb{U}^0, \tag{2.56}$$

excluding external forces (e.g., traction and body forces) for simplicity. Next, the solution field $\mathbf{u}$ and the corresponding test function $\delta\mathbf{u}$ are additively decomposed as

$$\mathbf{u} = \mathbf{u}^M + \mathbf{u}^S \quad \text{and} \quad \delta\mathbf{u} = \delta\mathbf{u}^M + \delta\mathbf{u}^S. \tag{2.57}$$

Here, the superscript M and S represent the coarse (macro) scale and fine (sub) scale, respectively. Substituting (2.57) in the variational equation (2.56) resulting in two decoupled equations

$$\int_{\Omega} \boldsymbol{\sigma}[\mathbf{u}^M + \mathbf{u}^S] : \boldsymbol{\epsilon}[\delta\mathbf{u}^M]\, d\Omega = 0, \tag{2.58a}$$

$$\int_{\Omega} \boldsymbol{\sigma}[\mathbf{u}^M + \mathbf{u}^S] : \boldsymbol{\epsilon}[\delta\mathbf{u}^S]\, d\Omega = 0, \tag{2.58b}$$

pertaining to the coarse and fine scales, respectively.

Depending on the chosen test function $\delta\mathbf{u}^S$, the fine scale problem governed by the variational equation (2.58b) may exist on the entire computational domain Ω or a sub-domain. The sub-domain may comprise of a single element or set of elements. Correspondingly, this results in a coupled volume multi-scale model [132] or the domain decomposition methods [133–137]. However, these approaches are suitable only for problems with a moderate difference in length scales of coarse and fine scale physics. In contrast, the VCH technique assumes a separation of scales between coarse and fine scale physics, adopting the computational homogenization method.

(B) Homogenization of integrals

The computational homogenization method [138–141] assumes an idealized fine scale domain containing sufficient statistical information. The idealized fine scale domain is referred to as the microstructure, RVE [125] or SVE [126]. In this thesis, the term RVE is used interchangeably with fine scale domain. The RVE/fine scale domain is independent of the coarse scale discretization.

Assuming the separation of scales, the fine scale test function $\delta\mathbf{u}^S$ lives only on the integration points of the coarse scale domain. Thereafter, any integrand on the coarse scale domain is stated as an average over the fine scale domain, say $\Omega_\square$. To put it into a mathematical perspective, let us consider an integral expression over the coarse scale domain,

$$\int_\Omega f(\mathbf{x})\, d\Omega, \tag{2.59}$$

for an arbitrary fluctuating integrand function $f(\mathbf{x})$. With the assumption that an RVE exist for all $\mathbf{x} \in \Omega$, the integrand $f(\mathbf{x})$ is redefined as

$$f(\mathbf{x}) \longrightarrow f(\bar{\mathbf{x}}) \approx \bar{f}(\bar{\mathbf{x}}) = \langle f \rangle_\square(\bar{\mathbf{x}}) := \frac{1}{|\Omega_\square|} \int_{\Omega_{\square(\bar{\mathbf{x}})}} f\, d\Omega, \tag{2.60}$$

where, $\Omega_\square$ centered at $\bar{\mathbf{x}}$. It is important to note that integrals over the coarse domain, such as (2.59), are evaluated using numerical integration. Therefore, a finite number of RVEs/fine scale domains are required, each associated with a coarse scale integration point. Adapting the definition (2.60) to the integrands in the coarse and fine scale variational equations (2.58a) and (2.58b) results in

$$\int_\Omega \langle \boldsymbol{\sigma}[\mathbf{u}^M + \mathbf{u}^S] : \boldsymbol{\epsilon}[\delta\mathbf{u}^M] \rangle_\square \, d\Omega = 0, \tag{2.61a}$$

$$\int_\Omega \langle \boldsymbol{\sigma}[\mathbf{u}^M + \mathbf{u}^S] : \boldsymbol{\epsilon}[\delta\mathbf{u}^S] \rangle_\square \, d\Omega = 0. \tag{2.61b}$$

Here, the shorthand notation, $\langle f \rangle_\square = \bar{f}$ is used. It is observed that the coarse scale variational equation (2.61a) exists over the entire computational domain. Its fine scale counterpart may be expressed as a set of independent problems of the form

$$\langle \boldsymbol{\sigma}[\mathbf{u}^M + \mathbf{u}^S] : \boldsymbol{\epsilon}[\delta\mathbf{u}^S] \rangle_\square = 0, \tag{2.62}$$

because the fine scale test function $\delta\mathbf{u}^S$ lives locally at each coarse scale integration point. In this context, the term 'locally' implies no regularity requirements on $\delta\mathbf{u}^S$.

(C) Prolongation

The prolongation operation transfers information from the coarse scale onto the fine scale in the VCH technique. To that end, a smooth solution field $\bar{\mathbf{u}}(\bar{\mathbf{x}}) \; \forall \, \bar{\mathbf{x}} \in \Omega$ is assumed to exist, as shown in Figure 2.3 (left). Its contribution to the coarse scale solution field $\mathbf{u}^{\mathrm{M}}$ is established using a Taylor series expansion about $\bar{\mathbf{x}}$,

$$\mathbf{u}^{\mathrm{M}}(\bar{\mathbf{u}}, \bar{\mathbf{x}}, \mathbf{x}) = \bar{\mathbf{u}} + \underbrace{\bar{\mathbf{u}} \otimes \boldsymbol{\nabla}\big|_{\bar{\mathbf{x}}}}_{\boldsymbol{\epsilon}[\bar{\mathbf{u}}]} \cdot [\mathbf{x} - \bar{\mathbf{x}}] + \mathrm{H.O.T}, \tag{2.63}$$

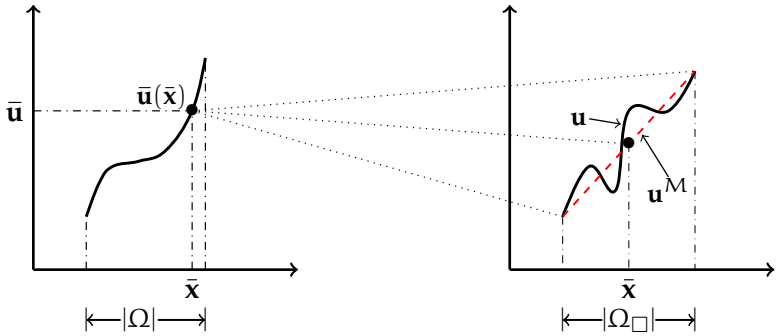

Figure 2.3: Figures showing the smooth solution field $\bar{\mathbf{u}}$ on the macro-scale domain Ω (left), and the rapidly oscillating solution field $\mathbf{u}$ on the RVE domain $\Omega_{\square}$ (right). The linear macro-scale contribution $\mathbf{u}^{\mathrm{M}}$ from $\bar{\mathbf{u}}$ is denoted by the dashed red line in the right sub-figure.

where, the Higher Order Terms (H.O.T) are ignored. This assumption is also referred to as the first-order homogenization method. Furthermore, the solution field on the fine scale, $\mathbf{u} = \mathbf{u}^{\mathrm{M}} + \mathbf{u}^{\mathrm{S}}$ is restated using (2.63) as

$$\mathbf{u}(\bar{\mathbf{u}}, \bar{\mathbf{x}}, \mathbf{x}) = \underbrace{\bar{\mathbf{u}} + \bar{\mathbf{u}} \otimes \boldsymbol{\nabla}\big|_{\bar{\mathbf{x}}} \cdot [\mathbf{x} - \bar{\mathbf{x}}]}_{\mathbf{u}^{\mathrm{M}}} + \mathbf{u}^{\mathrm{S}}. \tag{2.64}$$

Note that the coarse scale solution field contribution $\mathbf{u}^{\mathrm{M}}$ is linear, as shown by the red dashed line in Figure 2.3 (right). By definition, the average of the any fluctuating field, such as $\mathbf{u}^{\mathrm{S}}$ or $\delta\mathbf{u}$ is zero. Consequently,

$$\bar{\mathbf{u}}(\bar{\mathbf{x}}) = \langle \mathbf{u}^{\mathrm{M}}(\bar{\mathbf{u}}, \bar{\mathbf{x}}, \mathbf{x}) \rangle_{\square}, \quad \text{and} \quad \boldsymbol{\epsilon}[\bar{\mathbf{u}}(\bar{\mathbf{x}})] = \langle \boldsymbol{\epsilon}[\mathbf{u}^{\mathrm{M}}(\bar{\mathbf{u}}, \bar{\mathbf{x}}, \mathbf{x})] \rangle_{\square}. \tag{2.65}$$

Adopting a similar strategy for the test function $\delta\mathbf{u}$, one arrives at

$$\overline{\delta\mathbf{u}}(\bar{\mathbf{x}}) = \langle \delta\mathbf{u}^{\mathrm{M}}(\bar{\mathbf{u}}, \bar{\mathbf{x}}, \mathbf{x}) \rangle_{\square}, \quad \text{and} \quad \boldsymbol{\epsilon}[\overline{\delta\mathbf{u}}(\bar{\mathbf{x}})] = \langle \boldsymbol{\epsilon}[\delta\mathbf{u}^{\mathrm{M}}(\overline{\delta\mathbf{u}}, \bar{\mathbf{x}}, \mathbf{x})] \rangle_{\square} \tag{2.66}$$

On substituting (2.65) and (2.66) in the coarse scale variational equation (2.61a), one obtains

$$\int_{\Omega} \bar{\boldsymbol{\sigma}} : \boldsymbol{\epsilon}[\delta\bar{\mathbf{u}}] \, d\Omega = 0, \tag{2.67}$$

where, the homogenized stress is given by

$$\bar{\boldsymbol{\sigma}} = \langle \boldsymbol{\sigma} \rangle_{\square}. \tag{2.68}$$

Following the computation of $\bar{\mathbf{u}}$ using (2.67), its coarse scale contribution $\mathbf{u}^{M}$ is computed using (2.65). Thereafter, the coarse scale contribution drives the fine scale problem, evident from (2.61b). However, constraints must be enforced on the fine scale problem to ensure its solvability. These constraints are defined based on the (Hill-Mandel) macro-homogeneity condition [129–131].

(D) Macro-homogeneity condition

The (Hill-Mandel) macro-homogeneity condition [129–131] establishes the equivalence of virtual work between the coarse and fine scales. This requires a strain identity,

$$\boldsymbol{\epsilon}[\bar{\mathbf{u}}] = \langle \boldsymbol{\epsilon}[\mathbf{u}] \rangle_{\square}, \tag{2.69}$$

to hold. This is achieved through Dirichlet, Neumann, and Strongly Periodic boundary conditions on the RVE problem (commonly adopted in the computational homogenization literature). Recalling the stress identity (2.68) in conjunction with the aforementioned boundary conditions, the virtual work identity or the macro-homogeneity condition,

$$\bar{\boldsymbol{\sigma}} : \boldsymbol{\epsilon}[\bar{\mathbf{u}}] = \langle \boldsymbol{\sigma} : \boldsymbol{\epsilon}[\mathbf{u}] \rangle_{\square}, \tag{2.70}$$

is fulfilled. The above expression is the classical form of the macro-homogeneity condition, popular in the computational homogenization literature [142]. For a generalized form of the macro-homogeneity condition, the reader is referred to [128].

Part II

NUMERICAL METHODS FOR PHASE-FIELD FRACTURE

Development of novel numerical methods to address the computational challenges in the phase-field fracture model (Research Objectives 1 and 2).

3

MONOLITHIC SOLUTION TECHNIQUES

This chapter deals with the development of monolithic solution techniques for the phase-field fracture model. Conventional monolithic solution techniques, like the Newton-Raphson method exhibits a poor convergence behaviour. Due to an indefinite Hessian at the onset of fracture localization, the iterative process diverges, resulting in a break-down of the method. This is revealed through a numerical experiment carried out in Section 3.1.
Section 3.2 introduces a convexification technique proposed by Heister, Wheeler, and Wick for the phase-field fracture model. Its limitations w.r.t step size dependence and variational consistency is discussed, and modifications are proposed. Thereafter, in Section 3.3, Hessian modification techniques are presented. Finally, in Section 3.4, an arc-length method is proposed, adopting constraints on the incremental fracture energy. The performance of the aforementioned monolithic solution techniques is evaluated through numerical experiments on benchmark fracture problems in Section 3.5.

3.1 MINIMIZING A NON-CONVEX FUNCTIONAL

The phase-field modelling of fracture is a minimization problem, involving a non-convex energy functional (2.19). The non-convex nature of the functional stems from the degraded strain energy density, $g(\varphi)\Psi^+(\boldsymbol{\epsilon}[\mathbf{u}])$. Here, the degradation function $g(\varphi)$ is quadratic or higher order w.r.t. the phase-field φ, and the fracture driving strain energy $\Psi^+(\boldsymbol{\epsilon}[\mathbf{u}])$ is quadratic w.r.t. the strain $\boldsymbol{\epsilon}[\mathbf{u}]$. Consequently, for the Newton-Raphson method, the Hessian[1] may be indefinite. In the case of minimization problems, an indefinite Hessian does not guarantee a descent direction for the search directions[2] generated [143]. As a result, the Newton-Raphson method exhibits a poor convergence behaviour. For the phase-field modelling of fracture, several researchers [34, 75, 78] have reported the break down of the Newton-Raphson method at the onset of fracture localization.

3.1.1 *Finite element discretized equations*

An investigation into the Newton-Raphson method break down requires the finite element discretized equations for the phase-field fracture model. To that end, the Variational Problem 3 from Chapter 2 is considered as the starting point. Next, the corresponding finite element discretized equations are derived following the procedure explained in Section 2.1. The derivation is skipped here for brevity, instead the phase-field fracture Discrete Problem

1 referred to as the stiffness matrix in the computational mechanics literature
2 referred to as solution updates in the computational mechanics literature

2 is presented. Note that the terms *stiffness matrix* and *residual* are used for the Hessian and the Jacobian of the energy functional respectively.

Discrete Problem 2. *Compute the solution update* $\mathbf{s}_{k+1} = \{\Delta\tilde{\mathbf{u}}\,;\,\Delta\tilde{\varphi}\}$ *for the current iteration* $k+1$ *using*

$$\underbrace{\begin{bmatrix}\mathbf{K}^{uu} & \mathbf{K}^{u\varphi}\\ \mathbf{K}^{\varphi u} & \mathbf{K}^{\varphi\varphi}\end{bmatrix}_k}_{\text{Stiffness matrix, } \mathbf{K}_k} \underbrace{\begin{Bmatrix}\Delta\tilde{\mathbf{u}}\\ \Delta\tilde{\varphi}\end{Bmatrix}_{k+1}}_{\mathbf{s}_{k+1}} = \underbrace{\begin{Bmatrix}\mathbf{f}^{ext,u}\\ \mathbf{f}^{ext,\varphi}\end{Bmatrix}_i - \begin{Bmatrix}\mathbf{f}^{int,u}\\ \mathbf{f}^{int,\varphi}\end{Bmatrix}_k}_{\text{Residual, } \mathbf{r}_k}, \tag{3.1a}$$

and update the solution as

$$\begin{Bmatrix}\tilde{\mathbf{u}}\\ \tilde{\varphi}\end{Bmatrix}_{k+1} = \begin{Bmatrix}\tilde{\mathbf{u}}\\ \tilde{\varphi}\end{Bmatrix}_k + \alpha \begin{Bmatrix}\Delta\tilde{\mathbf{u}}\\ \Delta\tilde{\varphi}\end{Bmatrix}_{k+1}, \tag{3.1b}$$

until the norm of the residual is sufficiently small. Here, α *is the step-length. Furthermore, the stiffness matrix components are given by,*

$$\begin{aligned}
\mathbf{K}^{uu} &= \mathcal{A}\int_{\Omega_{el}} [\mathbf{B}^{u}]^{T} \Big(\underbrace{g(\varphi)\frac{\partial \boldsymbol{\sigma}^{+}}{\partial \boldsymbol{\epsilon}} + \frac{\partial \boldsymbol{\sigma}^{-}}{\partial \boldsymbol{\epsilon}}}_{\mathbf{D}} \Big) [\mathbf{B}^{u}]\, d\Omega \\
\mathbf{K}^{u\varphi} &= \mathcal{A}\int_{\Omega_{el}} [\mathbf{B}^{u}]^{T} \Big(g'(\varphi)\boldsymbol{\sigma}^{+} \Big) [\mathbf{N}^{\varphi}]\, d\Omega, \\
\mathbf{K}^{\varphi u} &= \mathcal{A}\int_{\Omega_{el}} [\mathbf{N}^{\varphi}]^{T} \Big(\frac{\partial \mathcal{H}}{\partial \boldsymbol{\epsilon}} \Big) [\mathbf{B}^{u}]\, d\Omega, \\
\mathbf{K}^{\varphi\varphi} &= \mathcal{A}\int_{\Omega_{el}} [\mathbf{B}^{\varphi}]^{T} \Big(\frac{G_c l}{c_w} \Big) [\mathbf{B}^{\varphi}] \\
&\quad + [\mathbf{N}^{\varphi}]^{T} \Big(\frac{G_c}{c_w l} w''(\varphi) + g''(\varphi)\mathcal{H} \Big) [\mathbf{N}^{\varphi}]\, d\Omega
\end{aligned} \tag{3.1c}$$

and the internal force vector components are computed as

$$\begin{aligned}
\mathbf{f}^{int,u} &= \mathcal{A}\int_{\Omega_{el}} [\mathbf{B}^{u}]^{T} \left(g(\varphi)\boldsymbol{\sigma}^{+} + \boldsymbol{\sigma}^{-} \right) d\Omega, \\
\mathbf{f}^{int,\varphi} &= \mathcal{A}\int_{\Omega_{el}} [\mathbf{B}^{\varphi}]^{T} \left(\frac{G_c l}{c_w} \boldsymbol{\nabla}\varphi \right) \\
&\quad + [\mathbf{N}^{\varphi}]^{T} \left(\frac{G_c}{c_w l} w'(\varphi) + g'(\varphi)\mathcal{H} \right) d\Omega.
\end{aligned} \tag{3.1d}$$

Note that $\mathcal{A}$ *is an assembly operator that maps element contributions to their global counterparts. Furthermore, the external force vectors* $\mathbf{f}^{ext,u}$ *and* $\mathbf{f}^{ext,\varphi}$ *are considered equal to zero. The material stiffness matrix* $\mathbf{D}$ *depends on the chosen strain energy density split (see Table 2.4). The history variable* $\mathcal{H}$ *is defined in (2.24).* ■

3.1.2 *Tapered bar tension test*

A simple numerical experiment is devised to investigate the performance of the Newton-Raphson method for the phase-field fracture model. The experiment consists of a tapered bar loaded in tension, as shown in Figure 3.1. A quasi-static loading is applied at the right edge in the form of prescribed displacement increment $\Delta\hat{u}_x = 1e-2$ [mm] for the first 25 steps, following which it is changed to $1e-4$ [mm]. The left edge remains fixed. The length of the bar is 10 [mm], and left and right edges are 1.5 [mm] and 4 [mm], respectively. The bar is discretized using three-noded triangular elements with a single integration point. Additional modelling parameters are presented in Table 3.1.

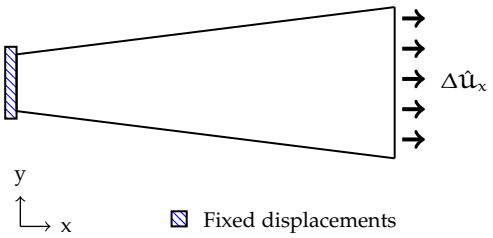

Figure 3.1: Tapered bar under tension

Parameters	**Value** [Units]
Model	Plane Strain, AT2
Energy split	None
λ	0.0 [MPa]
μ	50.0 [MPa]
G_c	1.0 [N/mm]
l	0.25 [mm]

Table 3.1: Model parameters

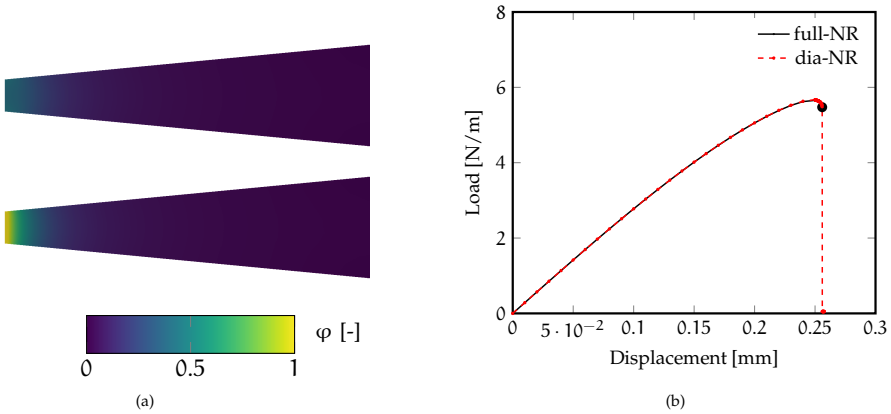

Figure 3.2: Figure (a) presents the phase-field distribution in the tapered bar, when the Newton-Raphson (full-NR) method breaks down (top) and the failure mode obtained with the diagonal only variant of the Newton-Raphson (dia-NR) method (bottom). Figure (b) presents the respective load-displacement curves. The black dot represents the last converged step for the full-NR.

Figure 3.2a (top) presents the phase-field distribution corresponding to the last converged step, obtained with the Newton-Raphson method (full-NR). Therein, the maximum value of the phase-field ≈ 0.4. From the load-displacement curve (in black), presented in Figure 3.2b, it is evident that the full-NR did not converge for the entire loading path. The black dot represents the last converged step. An eigenvalue decomposition of the Hessians (stiffness matrices) generated in the non-converged step reveals dominant negative eigenvalues in terms of magnitude. This conclusively proves the Hessian being indefinite when the phase-field reaches ≈ 0.4.

During the iterative process, the indefinite Hessian generates a sequence of solution updates not of descent direction, which results in divergence of the full-NR method.

3.1.3 *Circumventing indefinite Hessian*

In order to circumvent the undesirable effects of the indefinite Hessian(s), Nocedal and Wright [143] have proposed the use of modified Hessian(s), which are positive definite. A positive definite Hessian guarantees a descent direction for a minimization problem. When used in conjunction with Wolfe line-search conditions [144], the resulting solution technique is proven to be convergent. The proof of convergence is obtained using the Zoutendijk theorem on feasible directions [145] (see Sections 3.1 and 3.2 in [143] for a detailed derivation). Adopting the proposition of Nocedal and Wright, a variant of the Newton-Raphson method (dia-NR) is adopted, wherein the off-diagonal Hessian (stiffness matrix) blocks $\mathbf{K}^{u\varphi}$ and $\mathbf{K}^{\varphi u}$ are explicitly set to zero when computing the search direction. The dia-NR method converges for the entire loading path, evident for the load-displacement curve (in red) in Figure 3.2b. Furthermore, the phase-field also attains a value 1, signifying the detachment of the bar from its constrained left edge.

The numerical experiment on the tapered bar reveals the undesirable consequence of minimizing the phase-field fracture problem with an indefinite Hessian. Circumventing an indefinite Hessian is possible in two different ways, (i) devise a convex variant of the nonconvex phase-field fracture Discrete Problem 2, or (ii) modify the indefinite Hessian into a positive (semi) definite one.

3.2 CONVEXIFICATION VIA EXTRAPOLATION AND CORRECTION

The reformulation of a non-convex problem into a convex variant is not a menial task. It requires careful considerations of the changes introduced. One such reformulation, popular in the phase-field fracture modelling literature has been proposed by Heister, Wheeler, and Wick in [34]. Therein, the authors advocated the Hessian block $\mathbf{K}^{u\varphi}$ to be the root of all convergence problems. In order to circumvent the need for this block, the phase-field used in the momentum balance equation ($3.1d_1$) is replaced by an extrapolated phase-field, say $\hat{\varphi}$. The extrapolated phase-field is computed from the previous two converged steps of the simulation, and is expressed as

$$\hat{\varphi} = {}^{n-1}\varphi + \frac{\Delta t + {}^{n}\Delta t}{{}^{n}\Delta t}({}^{n}\varphi - {}^{n-1}\varphi). \tag{3.2}$$

Here, n and $n-1$ represent the two previous converged steps. It is important to note that the regularity of the phase-field in time is not established. As such, the extrapolation of the phase-field has no mathematically sound basis. It is only a heuristic assumption.

Incorporating the extrapolated phase-field (3.2) in the momentum balance equation (3.1d$_1$) modifies the non-convex Discrete Problem 2 into its convex variant, Discrete Problem 3. Here, the problematic Hessian block $\mathbf{K}^{u\varphi}$ (see Equation (3.3a)) is circumvented in the system of equations.

Discrete Problem 3. *Compute the solution update* $\mathbf{s}_{k+1} = \{\Delta\tilde{\mathbf{u}}\,;\,\Delta\tilde{\varphi}\}$ *for the current iteration* $k+1$ *using*

$$\underbrace{\begin{bmatrix}\mathbf{K}^{uu} & \mathbf{0}\\ \mathbf{K}^{\varphi u} & \mathbf{K}^{\varphi\varphi}\end{bmatrix}_k}_{\text{Stiffness matrix, } \mathbf{K}_k}\underbrace{\begin{Bmatrix}\Delta\tilde{\mathbf{u}}\\ \Delta\tilde{\varphi}\end{Bmatrix}_{k+1}}_{\mathbf{s}_{k+1}} = \underbrace{\begin{Bmatrix}\mathbf{f}^{ext,u}\\ \mathbf{f}^{ext,\varphi}\end{Bmatrix}_i - \begin{Bmatrix}\mathbf{f}^{int,u}\\ \mathbf{f}^{int,\varphi}\end{Bmatrix}_k}_{\text{Residual, } \mathbf{r}_k}, \tag{3.3a}$$

and update the solution fields,

$$\begin{Bmatrix}\tilde{\mathbf{u}}\\ \tilde{\varphi}\end{Bmatrix}_{k+1} = \begin{Bmatrix}\tilde{\mathbf{u}}\\ \tilde{\varphi}\end{Bmatrix}_k + \alpha\begin{Bmatrix}\Delta\tilde{\mathbf{u}}\\ \Delta\tilde{\varphi}\end{Bmatrix}_{k+1}, \tag{3.3b}$$

until the norm of the residual is sufficiently small. Here, α *is the step-length. Furthermore, the stiffness matrix components are given by,*

$$\begin{aligned}
\mathbf{K}^{uu} &= \mathcal{A}\int_{\Omega_{el}} [\mathbf{B}^{u}]^{T}\Big(\underbrace{g(\hat{\varphi})\frac{\partial\boldsymbol{\sigma}^{+}}{\partial\boldsymbol{\epsilon}} + \frac{\partial\boldsymbol{\sigma}^{-}}{\partial\boldsymbol{\epsilon}}}_{\mathbf{D}}\Big)[\mathbf{B}^{u}]\,d\Omega,\\
\mathbf{K}^{\varphi u} &= \mathcal{A}\int_{\Omega_{el}} [\mathbf{N}^{\varphi}]^{T}\left(\frac{\partial\mathcal{H}}{\partial\boldsymbol{\epsilon}}\right)[\mathbf{B}^{u}]\,d\Omega,\\
\mathbf{K}^{\varphi\varphi} &= \mathcal{A}\int_{\Omega_{el}} [\mathbf{B}^{\varphi}]^{T}\left(\frac{G_c l}{c_w}\right)[\mathbf{B}^{\varphi}]\\
&\quad + [\mathbf{N}^{\varphi}]^{T}\left(\frac{G_c}{c_w l}w''(\varphi) + g''(\varphi)\mathcal{H}\right)[\mathbf{N}^{\varphi}]\,d\Omega,
\end{aligned} \tag{3.3c}$$

and the internal force vector components are computed as

$$\begin{aligned}
\mathbf{f}^{int,u} &= \mathcal{A}\int_{\Omega_{el}} [\mathbf{B}^{u}]^{T}\left(g(\hat{\varphi})\boldsymbol{\sigma}^{+} + \boldsymbol{\sigma}^{-}\right)d\Omega,\\
\mathbf{f}^{int,\varphi} &= \mathcal{A}\int_{\Omega_{el}} [\mathbf{B}^{\varphi}]^{T}\left(\frac{G_c l}{c_w}\boldsymbol{\nabla}\varphi\right)\\
&\quad + [\mathbf{N}^{\varphi}]^{T}\left(\frac{G_c}{c_w l}w'(\varphi) + g'(\varphi)\mathcal{H}\right)d\Omega.
\end{aligned} \tag{3.3d}$$

Note that $\mathcal{A}$ *is an assembly operator that maps element contributions to their global counterparts. Furthermore, the external force vectors* $\mathbf{f}^{int,u}$ *and* $\mathbf{f}^{int,\varphi}$ *are considered equal to zero. The material stiffness matrix* $\mathbf{D}$ *depends on the chosen strain energy density split (see Table 2.4). The history variable* $\mathcal{H}$ *is defined in (2.24).* ■

Following the formulation of the phase-field extrapolation-based Discrete Problem 3, the numerical experiment on the tapered bar is revisited. The experiment has been introduced in the previous section, the geometry and the model parameters are presented in Figure 3.1 and Table 3.1 respectively. Although, the Newton-Raphson method (full-NR) is used for the simulation, due to the extrapolation (3.2), it is referred to as the extrapolation-based Newton-Raphson method (ext-NR). Furthermore, the extrapolation on the phase-field (3.2) explicitly depends on the step size. As such, an investigation into the step size sensitivity is carried out. To that end, in the post-peak regime of the load-displacement curve, the step size is varied as $1e-4$ [mm], $5e-4$ [mm] and $1e-3$ [mm], in three separate simulations.

Figure 3.3a presents the load-displacement curves obtained using the extrapolation-based Newton-Raphson method (ext-NR) with varying step sizes. It is observed that as the step size is increased from $1e-4$ [mm] to $1e-3$ [mm], the displacement at which the tapered bar loses integrity is higher. For higher step sizes the difference between the extrapolated phase-field and the actual phase-field is higher. In particular, the extrapolated phase-field lags behind the actual phase-field. In conjunction with the problem constructed where the extrapolated phase-field affects the material strength and stiffness parameters, this results in a delay in loss of integrity. Thus, the choice of the step size provides an *artificial ductility* not exhibited by the material in reality. Another critical drawback of the extrapolation-based formulation in [34] is the lack of variational consistency. The momentum balance equation ($3.1d_1$) is not consistent with the energy functional (2.19).

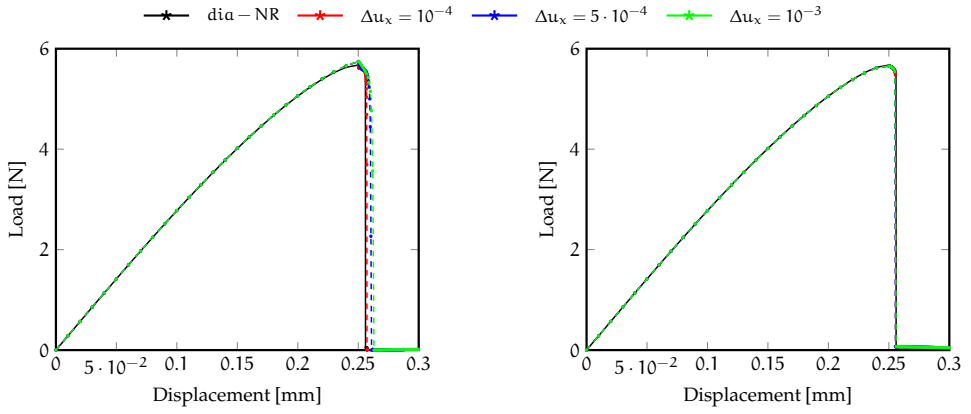

(a) ext-NR

(b) extC-NR

Figure 3.3: Figure (a) and (b) presents the load-displacement curves corresponding to the extrapolation-based Newton-Raphson method, ext-NR (see Discrete Problem 2) and extrapolation-correction Newton-Raphson method, extC-NR (see Discrete Problem 3). In both figures the red, blue and green curves correspond to the choice of step-size ($\Delta \mathbf{u}_x = 10^{-4}$, $5 \cdot 10^{-4}$, 10^{-3} [mm]). The black curve is the reference solution obtained using the diagonal only variant of the Newton-Raphson (dia-NR) method (red curve in Figure 3.2b).

Proposed modification

Variational consistency of the momentum balance equation ($3.3d_1$) can only be achieved when the extrapolated phase-field $\hat{\varphi}$ converges towards the actual phase-field φ. To that end, a modified version of the extrapolation-based Discrete Problem 3 is proposed in this thesis. The modification, however, is incremental, in the sense that an additional function defined as the difference between the extrapolated phase-field and the actual phase-field is minimized on top of the Discrete Problem 3. The additional function is given by

$$f(\hat{\varphi}) = \hat{\varphi} - \varphi. \tag{3.4}$$

Incorporating the modification, the Discrete Problem 3 assumes the form:

Discrete Problem 4. *Compute the solution* $(\mathbf{u}, \varphi)$ *for a loading step as:*

- *Set outer iteration count to zero* ($k = 0$).
- *Compute the extrapolated phase-field* $\hat{\varphi}_k$ *using* (3.2).
- *Solve Discrete Problem 3 for* $(\mathbf{u}, \varphi)$.
- *While* $\|\hat{\varphi}_k - \varphi\| > \mathtt{tolC}$,
  - *Set* $\hat{\varphi}_k = \varphi$.
  - *Solve Discrete Problem 3 for* $(\mathbf{u}, \varphi)$.
  - *Increment outer iteration count* ($k = k + 1$).

Here, tolC *is a user-defined tolerance, chosen as* 10^{-4}.

On revisiting the tapered bar experiment with the extrapolation-fixed point correction Discrete Problem 4, the load-displacement curves in Figure 3.3b are obtained. Although, the Newton-Raphson method (full-NR) is used to solve the nonlinear problem, due to the extrapolation and fixed point correction on the phase-field, it is referred to as the extC-NR variant. Furthermore, the load-displacement response corresponding to varying step sizes ($1e-4$ [mm], $5e-4$ [mm] and $1e-3$ [mm]) is similar to that obtained with the diagonal variant of the Newton-Raphson method. This points towards the success in eliminating the step size dependent artificial ductility observed with the extrapolation-based Discrete Problem 3.

3.3 HESSIAN MODIFICATION TECHNIQUES

Hessian modification techniques offer an alternative to convexification of a non-convex minimization problem. The numerical experiment on the

tapered bar in Section 3.1 clarifies the role of the indefinite Hessian in the break-down of the Newton-Raphson method. In this context, Nocedal and Wright [143] have proposed the use of modified Hessian(s), which are positive definite. A positive definite Hessian matrix always guarantees a descent direction, as such, better convergence behaviour may be expected [143].

Several techniques exist for modification of an indefinite Hessian into a positive definite one. In the context of the phase-field fracture model, three techniques are popular, (i) the BFGS[3] method [83, 85], (ii) scaling of the problematic Hessian block $\mathbf{K}^{\mathbf{u}\varphi}$ [78], and (iii) the addition of multiples of identity matrix to make a Hessian positive definite [82].

3.3.1 *BFGS method*

The BFGS method [146–149] replaces the true Hessian ($\mathbf{K}$ in Discrete Problem 2) with an approximate Hessian, say $\tilde{\mathbf{K}}$. The approximate Hessian $\tilde{\mathbf{K}}$ at $k+1$ iteration is computed as

$$\tilde{\mathbf{K}} = \tilde{\mathbf{K}}_k - \frac{(\tilde{\mathbf{K}}_k\,\mathbf{s}_k)\,(\tilde{\mathbf{K}}_k\,\mathbf{s}_k)^T}{\mathbf{s}_k^T\,\tilde{\mathbf{K}}_k\,\mathbf{s}_k} + \frac{\mathbf{y}_k\,\mathbf{y}_k^T}{\mathbf{y}_k^T\,\mathbf{s}_k}. \tag{3.5}$$

Here, $\mathbf{s}_k$ is the solution update obtained in the k^{th} iteration, and $\mathbf{y}_k$ is expressed as

$$\mathbf{y}_k = \mathbf{r}_{k+1} - \mathbf{r}_k, \tag{3.6}$$

where $\mathbf{r}$ is the residual (see Equation (3.1a) in Discrete Problem 2). The BFGS method updated Hessian (3.5) is positive definite if the previous iteration Hessian $\tilde{\mathbf{K}}_k$ is positive definite and $\mathbf{s}_k^T\,\mathbf{y}_k > 0$. To that end, in the first iteration of every step, $\mathbf{K}^{\mathbf{u}\varphi}$ and $\mathbf{K}^{\varphi\mathbf{u}}$ are explicitly set to zero.

3.3.2 *Scaling the problematic Hessian block*

In cases when the properties of the Hessian matrix block structure is known, the Hessian $\mathbf{K}$ maybe additively decomposed into a well-posed part $\mathbf{K}_w$ and a problematic part $\mathbf{K}_p$. This allows the scaling of the problematic part of the Hessian in order to achieve favourable properties for the Newton-Raphson method convergence. Such techniques are popular in the fluid mechanics literature [79–81]. In the context of the phase-field fracture model, Wick [78] proposed the Hessian decomposition

$$\tilde{\mathbf{K}} = \underbrace{\begin{bmatrix} \mathbf{K}^{\mathbf{uu}} & \mathbf{0} \\ \mathbf{K}^{\varphi\mathbf{u}} & \mathbf{K}^{\varphi\varphi} \end{bmatrix}}_{\text{Well-posed, } \mathbf{K}_w} + \omega \underbrace{\begin{bmatrix} \mathbf{0} & \mathbf{K}^{\mathbf{u}\varphi} \\ \mathbf{0} & \mathbf{0} \end{bmatrix}}_{\text{Problematic, } \mathbf{K}_p}, \tag{3.7}$$

3 acronym for the contributors Broyden, Fletcher, Goldfarb, Shanno

where a heuristically computed scalar ω scales the problematic Hessian block $\mathbf{K}_p$. Explicitly setting $\omega = 1$ results in the conventional Newton-Raphson (full-NR) method, which does not converge when the phase-field $\varphi \approx 0.4$. On the other hand, setting $\omega = 0$ eliminates the problematic $\mathbf{K}^{u\varphi}$ Hessian block, resulting in a convergent method. However, with the latter choice, some Hessian information is lost. In particular, when $\varphi < 0.4$, the Hessian is still positive definite and eliminating the block $\mathbf{K}^{u\varphi}$ may result in slow convergence behaviour.

Proposed modification

A modification to Wick's Hessian scaling method [78] is proposed. Instead of working with the Hessian for the entire finite element mesh, one can modify the integration point Hessian contributions. Similar to (3.7), a decomposition for an integration point Hessian $\mathbf{K}_{ip}$ is expressed as

$$\mathbf{K}_{ip} = \underbrace{\begin{bmatrix} \mathbf{K}^{uu} & \mathbf{0} \\ \mathbf{K}^{\varphi u} & \mathbf{K}^{\varphi\varphi} \end{bmatrix}_{ip}}_{\text{Well-posed, } \mathbf{K}_w} + \omega \underbrace{\begin{bmatrix} \mathbf{0} & \mathbf{K}^{u\varphi} \\ \mathbf{0} & \mathbf{0} \end{bmatrix}_{ip}}_{\text{Problematic, } \mathbf{K}_p}. \tag{3.8}$$

When the phase-field $\varphi \leqslant 0.4$, the convergent full-NR method is adopted by setting $\omega = 1$. However, when the phase-field grows beyond 0.4, in the corresponding integration points, the Hessian block $\mathbf{K}^{u\varphi}$ is eliminated using $\omega = 0$. Therefore, unlike Wick's Hessian scaling method, the information pertaining to the Hessian block $\mathbf{K}^{u\varphi}$ is removed only for fracturing elements with $\varphi > 0.4$.

3.3.3 *Adding multiples of identity matrix*

An indefinite Hessian matrix $\mathbf{K}$ may also be modified into a positive definite one, upon adding multiples of the identity matrix [143]. Mathematically, this operation may be stated as

$$\tilde{\mathbf{K}} = \mathbf{K} + \omega\mathbf{I}, \tag{3.9}$$

where, ω is a scaling parameter. However, computing ω is not trivial. One requires an initial guess, and repetitive iterative efforts either through Eigenvalue or Cholesky decomposition to ensure that $\tilde{\mathbf{K}}$ is positive definite. This is due to the fact that the eigenvalues of $\tilde{\mathbf{K}}$ cannot be related to the eigenvalues of $\mathbf{K}$ and $\omega\mathbf{I}$, since they do not have the same eigenvectors.

In the context of phase-field fracture models, Lampron, Therriault, and Lévesque [82] adopted this technique. Starting with an initial guess, ω is updated based on eigenvalue decomposition on the global Hessian, performed by the Pardiso solver. However, eigenvalue decomposition[4] is

4 using the Jacobi iterative method

expensive and scales $\mathcal{O}(n^3)$, n being the size of the Hessian matrix. As such, this method is not used in this thesis.

3.3.4 *Integration point Hessian eigenvalue modification*

Integration point Hessians are much smaller in size, compared to the Hessian for the entire finite element mesh. As such, its eigenvalue decomposition is also cheaper. Using this fact, a novel Hessian modification technique is proposed in this section. Starting with an integration point Hessian matrix $\mathbf{K}_{ip}$, its eigenvalue decomposition is carried out. Thereafter, the negative eigenvalues are replaced with its absolute values $abs(\cdot)$. This results in a modified integration point Hessian matrix, computed as

$$\mathbf{K}_{ip} = \mathbf{P}\, abs(\mathbf{\Lambda})\, \mathbf{P}^T, \tag{3.10}$$

where, $\mathbf{P}$ and $\mathbf{\Lambda}$ are matrices containing the eigenvectors and eigenvalues (in a diagonal representation), respectively.

From the numerical experiment on the tapered bar problem, it is evident that an integration point Hessian $\mathbf{K}_{ip}$ is positive definite until the phase-field reaches a value ≈ 0.4. Therefore, the modification (3.10) can be carried out only for those integration points where the phase-field has exceeded 0.4. With this approach, the number of eigenvalue decomposition required is limited to integration points where the fracture localizes.

3.3.5 *Revisiting the tapered bar tension test*

Figure 3.4 presents the load-displacement curves obtained using the Hessian modification techniques in Section 3.3. The step-size is set to 10^{-4} [mm] and the iteration terminating tolerance is 10^{-4}. In the figure, the black curve is the reference solution obtained using the dia-NR variant of the Newton-Raphson method (red curve in Figure 3.2b). The similarity of the curves in Figure 3.4 demonstrates the efficacy of the Hessian modification techniques (BFGS, scaling of the problematic Hessian block, Hessian eigenvalue modification) in the context of the phase-field fracture model.

3.4 ARC-LENGTH METHOD WITH FRACTURE ENERGY CONSTRAINT

The arc-length method emerged from the pioneering efforts of Wempner [86], Riks [87, 88] and Crisfield [89] as a solution technique intended to navigate through complex equilibrium paths with limit points[5]. It deviates from the conventional construct of the incremental iterative approach, where the (Dirichlet or Neumann) loading increments are prescribed by the user either explicitly or through some adaptive time-stepping scheme. The arc-length method considers the loading parametrized by a scalar variable ζ as

5 limit points are coordinates in the load-displacement space where the load/displacement increments change sign

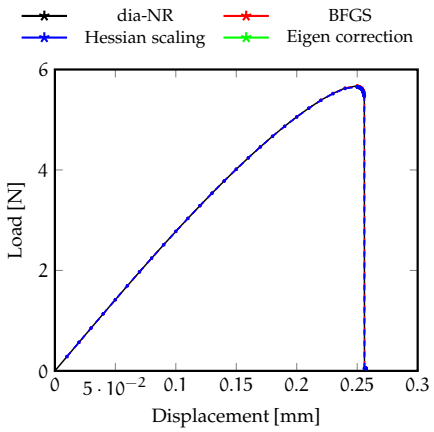

Figure 3.4: Figure presents the load-displacement curves obtained for the tapered bar tension test using the diagonal only variant of the Newton-Raphson (dia-NR) method, the BFGS method, scaling of the problematic Hessian block (Hessian scaling), and the Hessian eigenvalue correction method (Eigen correction).

an additional unknown. Thereafter, the equilibrium equation assumes the form

$$\mathbf{f}_{int} - \zeta\, \hat{\mathbf{f}}_{ext} = \mathbf{0}, \tag{3.11}$$

for a Neumann-type loading with $\hat{\mathbf{f}}_{ext}$ representing the normalized external force vector. In the case of Dirichlet-type loading, the equilibrium equation is given by

$$\mathbf{f}_{int} + \zeta\, \mathbf{K}\, \hat{\mathbf{a}}_p = \mathbf{0}, \tag{3.12}$$

with $\hat{\mathbf{a}}_p$ representing the normalized Dirichlet boundary values, and $\mathbf{K}$ the Hessian matrix. Nevertheless, due to extra unknown ζ, an additional equation is required to retain the determinate nature of the system of equations. This additional equation is often referred to as the arc-length constraint or path-following equation.

3.4.1 *Arc-length constraint equation*

Several arc-length constraint equations have been proposed since the inception of the arc-length method in [86]. A generic constraint equation for geometrically nonlinear problem may be formulated as

$$g_{arc}(\Delta\mathbf{u}, \Delta\zeta, \Delta s) := \Delta\mathbf{u}^T\, \Delta\mathbf{u} + \psi\, \Delta\zeta\, \hat{\mathbf{f}}_{ext}^T\, \hat{\mathbf{f}}_{ext} - \Delta s = 0, \tag{3.13}$$

where, Δs represents the arc-length, and ψ is a user-defined scalar. Choosing $\psi = 0$ yields the cylindrical arc-length constraint equation, while $\psi = 1$ and $\psi > 1$ result in the spherical and elliptic variants, respectively. For a comprehensive review of these variants, the reader is referred to [150, 151].

Furthermore, in the context of the phase-field fracture model, the constraint equation (3.13) does not perform well. The reason lies in the localization of the deformation into narrow bands, which renders controlling the solution through a global constraint inadequate [59]. For such cases, the energy release rate based arc-length constraint equation is proposed by Verhoosel, Remmers, and Gutiérrez in [91]. Therein, the constraint equation is stated as

$$g_{arc}(\Delta\mathbf{u}, \Delta\zeta, \Delta s) := \frac{1}{2}[\hat{\mathbf{f}}_{ext}]^T \left(\zeta_n \, \Delta\mathbf{u} - \Delta\zeta \, \mathbf{u}_n\right) - \Delta s = 0, \tag{3.14}$$

where, the subscript n corresponds to the last converged step. The energy release rate-based arc-length constraint equation has been adopted for the phase-field fracture models in [92, 93], albeit only for a limited set of brittle fracture problems.

3.4.2 *Fracture energy-based constraint*

In this thesis, a generic fracture energy-based constraint equation is proposed for the phase-field fracture model, encompassing both brittle and quasi-brittle fracture. To that end, the fracture surface energy is extracted from the phase-field fracture model energy functional (2.19). The fracture surface energy, Ψ_{frac} is expressed as

$$\Psi_{frac}(\varphi) = \int_\Omega \frac{G_c}{c_w l} \left(w(\varphi) + l^2 |\boldsymbol{\nabla}\varphi|^2\right) \, d\Omega. \tag{3.15}$$

For an explanation of the different terms and coefficients in the above equation, the reader is referred to Section 2.2.1 in Chapter 2. The incremental form of the fracture surface energy is expressed as

$$\Delta\Psi_{frac}(\varphi, \Delta\varphi) = \int_\Omega \frac{G_c}{c_w l} \left(w'(\varphi)\Delta\varphi + 2l^2 \boldsymbol{\nabla}\varphi \cdot \boldsymbol{\nabla}\Delta\varphi\right) \, d\Omega, \tag{3.16}$$

which allows one to construct an arc-length constraint equation, limiting the increment in the fracture surface energy $\Delta\Psi_{frac}$ to the arc-length Δs. Mathematically, the constraint equation is expressed as

$$g_{arc}(\varphi, \Delta\varphi) := \Delta\Psi_{frac}(\varphi, \Delta\varphi) - \Delta s = 0. \tag{3.17}$$

Equipped with the arc-length constraint equation (3.17), the phase-field Discrete Problem 2 assumes the form:

Discrete Problem 5. *Compute the solution update* $\mathbf{s}_{k+1} = \{\Delta\tilde{\mathbf{u}}\,;\,\Delta\tilde{\varphi}\,;\,\Delta\tilde{\zeta}\}$ *for the current iteration* $k+1$ *using*

$$\underbrace{\begin{bmatrix} \mathbf{K}^{uu} & \mathbf{K}^{u\varphi} & \mathbf{K}^{u\zeta} \\ \mathbf{K}^{\varphi u} & \mathbf{K}^{\varphi\varphi} & \mathbf{K}^{\varphi\zeta} \\ \mathbf{K}^{\zeta u} & \mathbf{K}^{\zeta\varphi} & \mathbf{K}^{\zeta\zeta} \end{bmatrix}_k}_{\text{Stiffness matrix, } \mathbf{K}_k} \underbrace{\begin{Bmatrix} \Delta\tilde{\mathbf{u}} \\ \Delta\tilde{\varphi} \\ \Delta\tilde{\zeta} \end{Bmatrix}_{k+1}}_{\mathbf{s}_{k+1}} = \underbrace{\begin{Bmatrix} \mathbf{f}^{ext,u} \\ \mathbf{o} \\ \mathbf{o} \end{Bmatrix}_i - \begin{Bmatrix} \mathbf{f}^{int,u} \\ \mathbf{f}^{int,\varphi} \\ \mathbf{g}_{arc} \end{Bmatrix}_k}_{\text{Residual, } \mathbf{r}_k}, \tag{3.18a}$$

and update the solution as

$$\begin{Bmatrix} \tilde{\mathbf{u}} \\ \tilde{\varphi} \\ \tilde{\zeta} \end{Bmatrix}_{k+1} = \begin{Bmatrix} \tilde{\mathbf{u}} \\ \tilde{\varphi} \\ \tilde{\zeta} \end{Bmatrix}_k + \begin{Bmatrix} \Delta\tilde{\mathbf{u}} \\ \Delta\tilde{\varphi} \\ \Delta\tilde{\zeta} \end{Bmatrix}_{k+1}, \tag{3.18b}$$

until the norm of the residual is sufficiently small. Furthermore, the stiffness matrix components are given by

$$\begin{aligned}
\mathbf{K}^{uu} &= \mathcal{A}\int_{\Omega_{el}} [\mathbf{B}^{u}]^{T} \Bigg(\underbrace{g(\varphi)\frac{\partial \boldsymbol{\sigma}^{+}}{\partial \boldsymbol{\epsilon}} + \frac{\partial \boldsymbol{\sigma}^{-}}{\partial \boldsymbol{\epsilon}}}_{\mathbf{D}} \Bigg) [\mathbf{B}^{u}]\, d\Omega, \\
\mathbf{K}^{u\varphi} &= \mathcal{A}\int_{\Omega_{el}} [\mathbf{B}^{u}]^{T} \left(g'(\varphi)\boldsymbol{\sigma}^{+} \right) [\mathbf{N}^{\varphi}]\, d\Omega, \\
\mathbf{K}^{u\zeta} &= -\hat{\mathbf{f}}_{ext}, \\
\mathbf{K}^{\varphi u} &= \mathcal{A}\int_{\Omega_{el}} [\mathbf{N}^{\varphi}]^{T} \left(\frac{\partial \mathcal{H}}{\partial \boldsymbol{\epsilon}} \right) [\mathbf{B}^{u}]\, d\Omega, \\
\mathbf{K}^{\varphi\varphi} &= \mathcal{A}\int_{\Omega_{el}} [\mathbf{B}^{\varphi}]^{T} \left(\frac{G_c l}{c_w} \right) [\mathbf{B}^{\varphi}] \\
&\quad + [\mathbf{N}^{\varphi}]^{T} \left(\frac{G_c}{c_w l} w''(\varphi) + g''(\varphi)\mathcal{H} \right) [\mathbf{N}^{\varphi}]\, d\Omega, \\
\mathbf{K}^{\varphi\zeta} &= \mathbf{K}^{u\zeta} = \mathbf{K}^{\zeta\zeta} = \mathbf{o}, \\
\mathbf{K}^{\zeta\varphi} &= \mathcal{A}\int_{\Omega_{el}} \Bigg([\mathbf{N}^{\varphi}]^{T} \frac{G_c}{c_w l} (w''(\varphi)\,\Delta\varphi + w'(\varphi)) \\
&\quad + [\mathbf{B}^{\varphi}]^{T} \frac{G_c l}{c_w} (\boldsymbol{\nabla}\Delta\varphi + \boldsymbol{\nabla}\varphi) \Bigg) d\Omega,
\end{aligned} \tag{3.18c}$$

and the internal force vector components are computed as

Discrete Problem 5 (continued)

$$
\begin{aligned}
\mathbf{f}^{\mathrm{int},\mathbf{u}} &= \mathcal{A}\int_{\Omega_{el}} [\mathbf{B}^{\mathbf{u}}]^{\mathsf{T}} \left(g(\varphi)\boldsymbol{\sigma}^{+} + \boldsymbol{\sigma}^{-}\right) \mathrm{d}\Omega, \\
\mathbf{f}^{\mathrm{int},\varphi} &= \mathcal{A}\int_{\Omega_{el}} [\mathbf{B}^{\varphi}]^{\mathsf{T}} \left(\frac{G_c l}{c_w}\boldsymbol{\nabla}\varphi\right) \\
&\quad + [\mathbf{N}^{\varphi}]^{\mathsf{T}} \left(\frac{G_c}{c_w l} w'(\varphi) + g'(\varphi)\mathcal{H}\right) \mathrm{d}\Omega, \\
g_{\mathrm{arc}} &= \mathcal{A}\int_{\Omega_{el}} \left(\frac{G_c}{c_w l}(w'(\varphi)\Delta\varphi + 2l^2\boldsymbol{\nabla}\varphi\cdot\boldsymbol{\nabla}\Delta\varphi\right) \mathrm{d}\Omega - \Delta s.
\end{aligned}
\tag{3.18d}
$$

Note that $\mathcal{A}$ is an assembly operator that maps element contributions to their global counterparts. Furthermore, the external force vector $\mathbf{f}^{\mathrm{ext},\mathbf{u}} = \zeta_k\,\hat{\mathbf{f}}_{\mathrm{ext}}$. The material stiffness matrix $\mathbf{D}$ depends on the chosen strain energy density split (see Table 2.4). The history variable $\mathcal{H}$ is defined in (2.24). ■

It is important to note that the Hessian matrix $\mathbf{K}$ in the phase-field fracture Discrete Problem 5 is sparse, since the matrix blocks $\mathbf{K}^{\varphi\zeta}$, $\mathbf{K}^{\mathbf{u}\zeta}$ and $\mathbf{K}^{\zeta\zeta}$ are equal to zero. This could lead to a poorly conditioned system of equations or a nearly singular Hessian matrix [152]. Setting $\mathbf{K}^{\zeta\zeta} = \kappa$, where $\kappa > 0$ circumvents these issues, however, at the cost of slowing down the convergence rate.

Another way of tackling the sparsity of the Hessian matrix $\mathbf{K}$ in the phase-field fracture Discrete Problem 5 is through reformulation of the arc-length constraint equation (3.17). To that end, the variational equation pertaining to phase-field evolution (see Equation (2.25b) from Variational Problem 3 in Chapter 2) is re-stated,

$$
\begin{aligned}
E'(\mathbf{u},\varphi;\delta\varphi) = &\int_{\Omega}\left(g'(\varphi)\mathcal{H} + \frac{G_c}{c_w l}w'(\varphi)\right)\delta\varphi\,\mathrm{d}\Omega \\
&+ \int_{\Omega}\frac{G_c l}{c_w}\boldsymbol{\nabla}\varphi\cdot\boldsymbol{\nabla}\delta\varphi\,\mathrm{d}\Omega = 0.
\end{aligned}
\tag{3.19}
$$

Thereafter, assuming the phase-field test function $\delta\varphi = \Delta\varphi$, the following expression is obtained,

$$
\Delta\Psi_{\mathrm{frac}} = -\int_{\Omega} g'(\varphi)\mathcal{H}\Delta\varphi\,\mathrm{d}\Omega, \tag{3.20}
$$

using the relation for $\Delta\Psi_{\mathrm{frac}}$ defined in (3.16). This allows the formulation of an alternative arc-length constraint equation, given by

$$
g_{\mathrm{arc}}(\varphi,\mathbf{u}) := \int_{\Omega} g'(\varphi)\,\mathcal{H}\,\Delta\varphi\,\mathrm{d}\Omega + \Delta s = 0. \tag{3.21}
$$

Using the constraint equation (3.21), an alternative phase-field Discrete Problem is formulated as follows:

Discrete Problem 6. *Compute the solution update* $\mathbf{s}_{k+1} = \{\Delta\tilde{\mathbf{u}}\,;\,\Delta\tilde{\varphi}\,;\,\Delta\tilde{\zeta}\}$ *for the current iteration* $k+1$ *using*

$$\underbrace{\begin{bmatrix} \mathbf{K}^{uu} & \mathbf{K}^{u\varphi} & \mathbf{K}^{u\zeta} \\ \mathbf{K}^{\varphi u} & \mathbf{K}^{\varphi\varphi} & \mathbf{K}^{\varphi\zeta} \\ \mathbf{K}^{\zeta u} & \mathbf{K}^{\zeta\varphi} & \mathbf{K}^{\zeta\zeta} \end{bmatrix}_k}_{\text{Stiffness matrix, } \mathbf{K}_k} \underbrace{\begin{Bmatrix} \Delta\tilde{\mathbf{u}} \\ \Delta\tilde{\varphi} \\ \Delta\tilde{\zeta} \end{Bmatrix}_{k+1}}_{\mathbf{s}_{k+1}} = \underbrace{\begin{Bmatrix} \mathbf{f}^{ext,u} \\ \mathbf{o} \\ \mathbf{o} \end{Bmatrix}_i - \begin{Bmatrix} \mathbf{f}^{int,u} \\ \mathbf{f}^{int,\varphi} \\ \mathbf{g}_{arc} \end{Bmatrix}_k}_{\text{Residual, } \mathbf{r}_k}, \tag{3.22a}$$

and update the solution as

$$\begin{Bmatrix} \tilde{\mathbf{u}} \\ \tilde{\varphi} \\ \tilde{\zeta} \end{Bmatrix}_{k+1} = \begin{Bmatrix} \tilde{\mathbf{u}} \\ \tilde{\varphi} \\ \tilde{\zeta} \end{Bmatrix}_k + \begin{Bmatrix} \Delta\tilde{\mathbf{u}} \\ \Delta\tilde{\varphi} \\ \Delta\tilde{\zeta} \end{Bmatrix}_{k+1}, \tag{3.22b}$$

until the norm of the residual is sufficiently small. Furthermore, the stiffness matrix components are given by

$$\begin{aligned}
\mathbf{K}^{uu} &= \mathcal{A}\int_{\Omega_{el}} [\mathbf{B}^{u}]^{T}\left(\underbrace{g(\varphi)\frac{\partial\boldsymbol{\sigma}^{+}}{\partial\boldsymbol{\epsilon}} + \frac{\partial\boldsymbol{\sigma}^{-}}{\partial\boldsymbol{\epsilon}}}_{\mathbf{D}}\right)[\mathbf{B}^{u}]\,d\Omega, \\
\mathbf{K}^{u\varphi} &= \mathcal{A}\int_{\Omega_{el}} [\mathbf{B}^{u}]^{T}\left(g'(\varphi)\boldsymbol{\sigma}^{+}\right)[\mathbf{N}^{\varphi}]\,d\Omega, \\
\mathbf{K}^{u\zeta} &= -\hat{\mathbf{f}}_{ext}, \\
\mathbf{K}^{\varphi u} &= \mathcal{A}\int_{\Omega_{el}} [\mathbf{N}^{\varphi}]^{T}\left(\frac{\partial\mathcal{H}}{\partial\boldsymbol{\epsilon}}\right)[\mathbf{B}^{u}]\,d\Omega, \\
\mathbf{K}^{\varphi\varphi} &= \mathcal{A}\int_{\Omega_{el}} [\mathbf{B}^{\varphi}]^{T}\left(\frac{G_c l}{c_w}\right)[\mathbf{B}^{\varphi}] \\
&\quad + [\mathbf{N}^{\varphi}]^{T}\left(\frac{G_c}{c_w l}w''(\varphi) + g''(\varphi)\mathcal{H}\right)[\mathbf{N}^{\varphi}]\,d\Omega, \\
\mathbf{K}^{\varphi\zeta} &= \mathbf{K}^{\zeta\zeta} = \mathbf{o}, \\
\mathbf{K}^{\zeta u} &= \mathcal{A}\int_{\Omega_{el}} [\mathbf{B}^{u}]^{T} g'(\varphi)\Delta\varphi\,\boldsymbol{\sigma}^{+}\,d\Omega, \\
\mathbf{K}^{\zeta\varphi} &= \mathcal{A}\int_{\Omega_{el}} \left([\mathbf{N}^{\varphi}]^{T}\left(g''(\varphi)\,\Delta\varphi + g'(\varphi)\right)\mathcal{H}\,d\Omega.
\end{aligned} \tag{3.22c}$$

and the internal force vector components are computed as

Discrete Problem 6 (continued)

$$
\begin{aligned}
\mathbf{f}^{\mathrm{int},\mathbf{u}} &= \mathcal{A}\int_{\Omega_{el}} [\mathbf{B}^{\mathbf{u}}]^{\mathsf{T}} \left(g(\varphi)\boldsymbol{\sigma}^{+} + \boldsymbol{\sigma}^{-}\right) \mathrm{d}\Omega, \\
\mathbf{f}^{\mathrm{int},\varphi} &= \mathcal{A}\int_{\Omega_{el}} [\mathbf{B}^{\varphi}]^{\mathsf{T}} \left(\frac{G_c l}{c_w}\boldsymbol{\nabla}\varphi\right) \\
&\quad + [\mathbf{N}^{\varphi}]^{\mathsf{T}} \left(\frac{G_c}{c_w l} w'(\varphi) + g'(\varphi)\mathcal{H}\right) \mathrm{d}\Omega, \\
g_{arc} &= \mathcal{A}\int_{\Omega_{el}} \left(g'(\varphi)\Delta\varphi\,\mathcal{H}\right) \mathrm{d}\Omega + \Delta s,
\end{aligned}
\tag{3.22d}
$$

Note that $\mathcal{A}$ is an assembly operator that maps element contributions to their global counterparts. Furthermore, the external force vector $\mathbf{f}^{\mathrm{ext},\mathbf{u}} = \zeta_k \hat{\mathbf{f}}_{\mathrm{ext}}$. The material stiffness matrix $\mathbf{D}$ depends on the chosen strain energy density split (see Table 2.4). The history variable $\mathcal{H}$ is defined in (2.24). ■

Compared to Discrete Problem 5, the Discrete Problem 6 results in comparatively less sparse Hessian matrix $\mathbf{K}$ due to the non-zero block $\mathbf{K}^{\zeta\mathbf{u}}$. As such, better conditioning properties is expected.

3.4.3 *Implementation caveats*

This section deals with the implementation caveats pertaining to the arc-length method.

Singular Hessian

The Hessian $\mathbf{K}$ pertaining to the arc-length method (see Discrete Problems 5 and 6) would be singular if adequate constraints are not enforced, and also when the solution increment $\{\Delta\tilde{\mathbf{u}}\,;\,\Delta\tilde{\varphi}\,;\,\Delta\tilde{\zeta}\}$ is zero. In this thesis, adequate constraints are always enforced on all problems. Therefore, the focus on the second source of a singular Hessian, the zero solution increment.

A zero solution increment is encountered in two scenarios, (i) at the start of an analysis from an undeformed state, and (ii) at the first iteration of every step. The first scenario is circumvented upon starting an analysis with the incremental iterative approach instead of the arc-length method (i.e., Discrete Problem 2 instead of Discrete Problem 5 or 6). As long as the incremental iterative approach is used, the zero solution increment poses no threat of singularity to the Hessian. Once the switch is made to the arc-length either when a limit point is encountered or through a user-defined criterion, the Hessian at the first iteration of every step is singular due to a zero solution increment. At the first iteration, the previous step (converged) solution is set to the current solution, as such the solution increment is zero. In order to circumvent this issue, the true solution increment is replaced by an increment computed as the difference between the two previous step

converged solution. This results in a non-zero solution increment, and then the Hessian is not singular anymore.

Switching between incremental iterative approach and the arc-length method

In the previous discussion on singular Hessian, it is established that an analysis starts with the incremental iterative approach, i.e., Discrete Problem 2. The switch to the arc-length method is made when the conventional Newton-Raphson method (full-NR) fails to converge. However, user-defined switch criterion may also be set up. One such switch criterion is proposed, based on a fracture energy threshold $\Psi_{frac,th}$. The fracture energy threshold may be computed using the expression

$$\Psi_{frac,th} = \frac{G_c}{c_w l}\, w(0.4)\, V_{elem}, \tag{3.23}$$

where, $w(0.4)$ indicates the locally dissipated fracture energy function evaluated using phase-field $\varphi = 0.4$, and V_{elem} is the volume of the smallest element in the finite element mesh.

Furthermore, a switch from the arc-length method can also be made when the load increment $\Delta\zeta$ is positive. A positive load increment is usually indicative of a well-posed Hessian, possibly positive definite. Therefore, the conventional Newton-Raphson method (full-NR) is expected to converged.

Adaptive modification of the arc-length

Another key aspect pertaining to the arc-length method is the initial value of the arc-length Δs (see Discrete Problems 5 and 6) and adaptive modifications thereof. When the switch is made from an incremental iterative approach to the arc-length method, in this thesis, Δs is set as the fracture energy dissipated in the previous step, $\Psi_{frac,n}$. Although, this initial value of Δs may be conservatively small, it allows a smooth transition from the incremental iterative approach to the arc-length method.

Furthermore, during the course of the analysis with the arc-length method, the arc-length Δs is modified based on the number of iterations required for convergence (`iiter`) and its user-defined optimum value (`optIter`). The arc-length for a new step, say $n+1$ is computed at the end of the previous step n as

$$\Delta s_{n+1} = \begin{cases} \Delta s_n, * 1.2 & \text{if iiter} < \text{optIter} \\ \Delta s_n * 0.5^{0.25(\text{iiter}-\text{optIter})} & \text{otherwise.} \end{cases} \tag{3.24}$$

3.4.4 *Revisiting the tapered bar tension test*

Figure 3.5 presents the load-displacement curves obtained using the dia-NR method (reference solution from Figure 3.2b) and the arc-length method.

Both methods predict the same peak load. Post peak, the arc-length method follows a different equilibrium path tracing a snap-back behaviour.

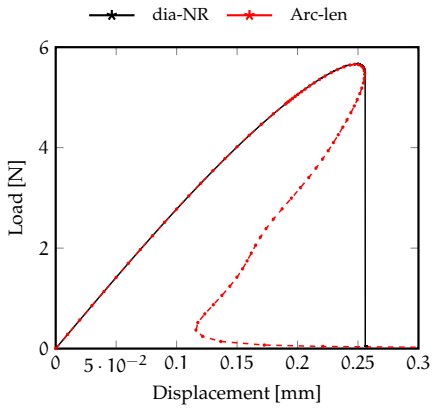

Figure 3.5: Figure presents the load-displacement curves obtained for the tapered bar tension test using the diagonal only variant of the Newton-Raphson (dia-NR) method and the arc-length (Arc-len) method.

3.5 NUMERICAL EXPERIMENTS

In this section, numerical experiments are carried out on benchmark brittle and quasi-brittle fracture problems using the monolithic solution techniques, developed in this chapter. The set of problems comprises of the single edge notched specimen under tension, and under shear [37], the Winkler L-panel experiment [153], and the concrete beam three point bending experiment carried out by Rots [154]. The objective is two-fold. First, the efficacy of the monolithic solution techniques is investigated in Section 3.5.1. Thereafter, based on numerical experiments on the single edge notched specimen under tension, the computational efficiency of the solution techniques is assessed in Section 3.5.2.

3.5.1 *Benchmark problems*

The benchmark problems comprising of the single edge notched specimen under tension, and under shear [37], the Winkler L-panel experiment [153], and the concrete beam three point bending experiment carried out by Rots [154] are presented in this section. For each problem, the geometry, loading conditions as well as the additional model parameters are presented in the respective sub-sections. All geometries are discretized using three-noded triangular elements, and a single integration point is adopted for numerical integration. In all cases, the phase-field distribution at the final step of the analysis, and pertinent load-displacement curves obtained from the different monolithic solution techniques are reported.

3.5.1.1 *Single Edge Notched specimen under Tension (SENT)*

The single edge notched specimen introduced by Miehe, Hofacker, and Welschinger [37] has been studied extensively under tensile and shear loading in the phase-field fracture literature. The geometry consists of a unit square (in mm) embedded with a horizontal notch, midway along height and equal to half of the edge length as shown in Figure 3.6. The notch is modelled explicitly in the finite element mesh. A quasi-static loading is applied at the top boundary in the form of prescribed displacement in the vertical (y) direction. The increment for the first 52 steps is $\Delta u = 1e-4$ [mm], following which it is changed to $5e-6$ [mm]. The smaller increments are adopted to capture the post peak-load brittle fracture response. However, for the arc-length method, the increments are obtained as part of the solution, since the dissipation is prescribed at every step instead. Furthermore, the bottom boundary of the SENT specimen remains fixed. Additional model parameters required for the simulation are presented in Table 3.2.

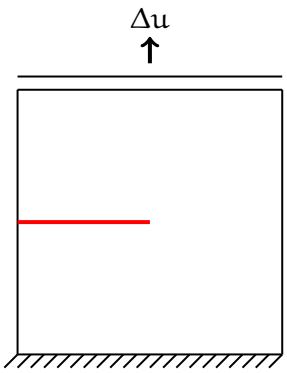

Figure 3.6: SENT specimen

Parameters	**Value** [Units]
Fracture Model	AT2
Energy Split	No Split
E_0	210.0 [GPa]
ν	0.3 [-]
G_c	2.7 [N/mm]
l	1.5e-2 [mm]
`optIter`	10 [-]

Table 3.2: Model parameters

Figure 3.7a presents the phase-field fracture distribution at the final step of the analysis. The fracture occurs as a mode I phenomenon, wherein the initial crack introduced in the mesh extends with no change in the direction. The load-displacement curves obtained using the different monolithic solution techniques are presented in Figure 3.7b. The arc-length method is able to predict snap-back responses beyond the peak load, since it allows the relaxation of the top boundary displacement as long as the specimen dissipates energy. The latter is ensured using the fracture energy-based arc-length constraint (3.21). On the contrary, in the incremental iterative solution techniques (BFGS, dia-NR, and Hessian scaling), the displacement increments are fixed. As such, snap-back responses are not achieved. Furthermore, among these solution techniques, the Hessian scaling method predicts comparatively brittle response with a straight drop in the load, while the BFGS and the dia-NR methods exhibits some artificial ductility. This behaviour is attributed to the iteration terminating tolerance. A tolerance 10^{-4} is not sufficient enough for these methods. On decreasing the tolerance to 10^{-6}, a similar response (not presented in the Figure 3.7b) as the Hessian scaling method may be obtained, as shown later in Section 3.5.2.

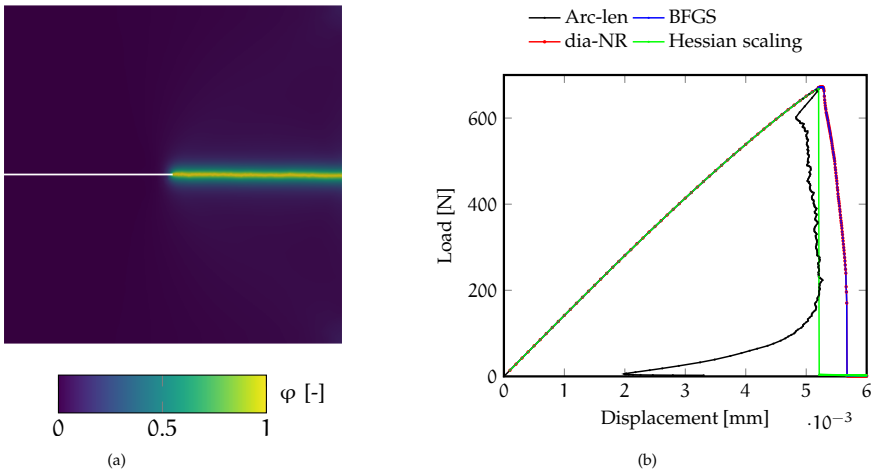

(a) (b)

Figure 3.7: Figure (a) presents the phase-field distribution in the single edge notched specimen under tension at the final step of the analysis. Figure (b) presents the respective load-displacement curves obtained using the monolithic solution techniques, arc-length (Arc-len) method, BFGS method, diagonal only variant of the Newton-Raphson (dia-NR) method, and Hessian scaling method.

3.5.1.2 *Single Edge Notched specimen under Shear (SENS)*

The single edge notched specimen in the previous section is loaded horizontally along the top edge as shown in Figure 3.8 for a shear test. The relevant model parameters are presented in Table 3.3, where a spectral decomposition based energy split [37] is adopted to capture the tension-compression asymmetric response. A quasi-static loading is applied to the top boundary in the form of prescribed displacement increment $\Delta u = 1e-4$ [mm] for the first 85 steps, following which it is changed to $1e-5$ [mm]. Furthermore, the bottom boundary remains fixed, and roller supports are implemented in left and right edges restricting the vertical displacement. Similar to the SENT numerical experiment, for the arc-length method, the displacement increments are obtained as part of the solution, since the dissipation is prescribed at every step instead.

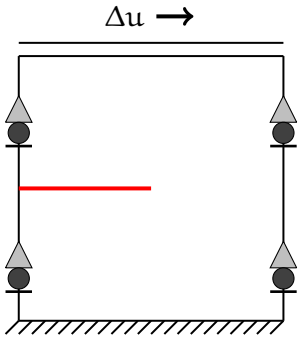

Figure 3.8: SENS specimen

Parameters	**Value** [Units]
Fracture Model	AT2
Energy Split	Spectral [37]
E_0	210.0 [GPa]
ν	0.3 [-]
G_c	2.7 [N/mm]
l	1.5e-2 [mm]
`optIter`	10 [-]

Table 3.3: Model parameters

Figure 3.9a presents the phase-field fracture distribution at the final step of the analysis. The fracture occurs as a combined mode I and II phenomenon.

The initial crack introduced in the mesh extends in a curvilinear fashion until it reaches the bottom edge, whereupon it propagates horizontally. The load-displacement curves obtained using the different monolithic solution techniques are presented in Figure 3.9b. Similar to the numerical experiments on the SENT specimen, here too, the arc-length method predicts snap-back behaviour beyond the peak load. Again, one can attribute this to arc-length method construct, where relaxation of the displacement is allowed and fracture energy-based arc-length constraint (3.21) is prescribed. The Hessian scaling method traces a similar response to that observed with the arc-length method, apart from the snap-back responses. The BFGS method and the dia-NR method, however, predicts a comparatively ductile response compared to the arc-length method and the Hessian scaling method. Similar to the SENT numerical experiment, one can argue the insufficiency of the iteration terminating tolerance 10^{-4}. Setting the tolerance to 10^{-6} eliminates this artificial ductile behaviour.

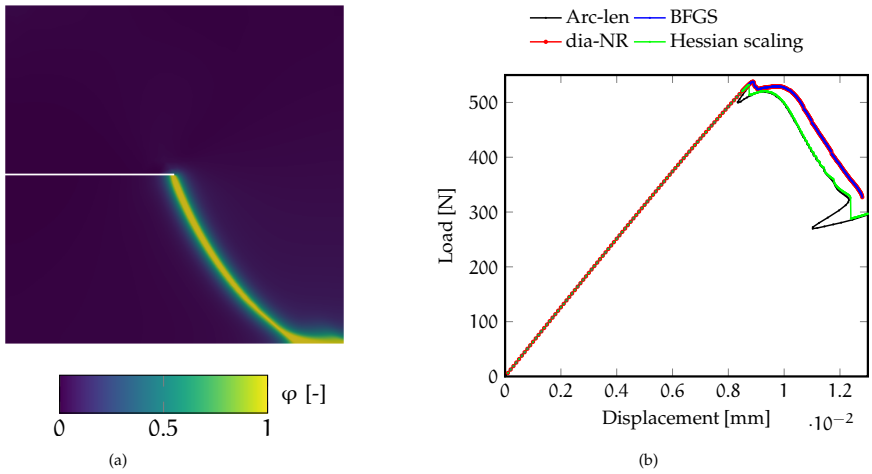

Figure 3.9: Figure (a) presents the phase-field distribution in the single edge notched specimen under shear at the final step of the analysis. Figure (b) presents the respective load-displacement curves obtained using the monolithic solution techniques, arc-length (Arc-len) method, BFGS method, diagonal only variant of the Newton-Raphson (dia-NR) method, and Hessian scaling method.

3.5.1.3 *Winkler L-panel*

Experiments on a concrete L-shaped panel was conducted by Winkler [153] in 2001, and the range of load-displacement curves as well as the observed fracture pattern was reported. Since then, in several works [2, 155] on fracture modelling, the experiment was adopted as a benchmark case. Figure 3.10 shows the geometry as well as the loading conditions for the L-panel numerical experiment. The longer edges of the panel are 500 [mm] and the smaller edges are 250 [mm]. The relevant model parameters are presented in Table 3.4. The loading is applied on the edge marked in blue, 30 [mm] in length, and is in the form of displacement increment

$\Delta u = 1e-3$ [mm]. The bottom edge remains fixed. Furthermore, for the arc-length method, one may note that dissipation is prescribed instead of displacement increments.

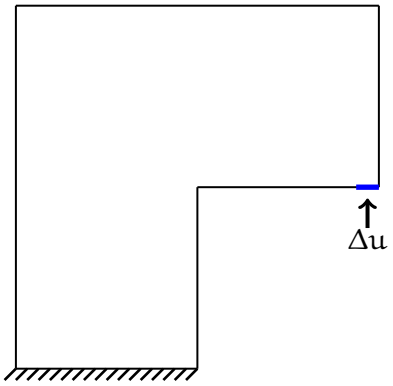

Figure 3.10: Winkler L-panel

Parameters	**Value** [Units]
Fracture Model	Quasi-Brittle
Energy Split	Spectral [37]
Softening	Cornellisen et. al. [70]
E_0	2.0e4 [MPa]
ν	0.18 [-]
f_t	2.5 [MPa]
G_c	0.130 [N/mm]
l	10 [mm]
`optIter`	10 [-]

Table 3.4: Models parameters

Figure 3.11a presents the phase-field fracture distribution at the final step of the analysis. It is in agreement with the experimentally observed fracture pattern by Winkler [153]. The load-displacement curves obtained using the different monolithic solution techniques are presented in Figure 3.11b. All curves are similar and lie in the shaded region of experimentally observed load-displacement curves.

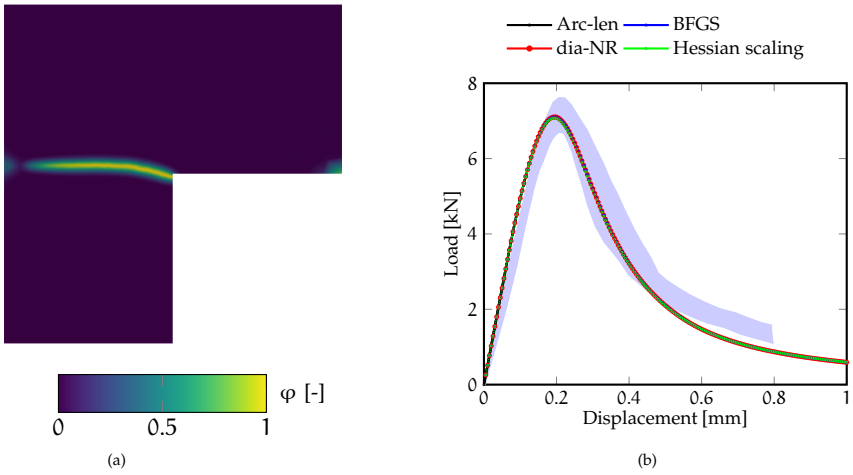

Figure 3.11: Figure (a) presents the phase-field distribution in the L-panel specimen under shear at the final step of the analysis. Figure (b) presents the respective load-displacement curves obtained using the monolithic solution techniques, arc-length (Arc-len) method, BFGS method, diagonal only variant of the Newton-Raphson (dia-NR) method, and Hessian scaling method. The experimental range from Winkler [153] is represented by the shaded region.

3.5.1.4 *Concrete beam three-point bending*

A three-point bending experiment was conducted by Rots [154] on a notched concrete beam. The beam has dimensions 450×100 [mm^2], with a notch

5×50 [mm^2]. A schematic of the beam along with the loading conditions is presented in Figure 3.12. The relevant model parameters are presented in Table 3.5. The loading is applied on a node on the top edge marked in the form of displacement increment $\Delta u = 1e-3$ [mm]. The bottom left corner is fixed, while a roller support is added on the bottom right edge. Furthermore, for the arc-length method, one may note that dissipation is prescribed instead of displacement increments.

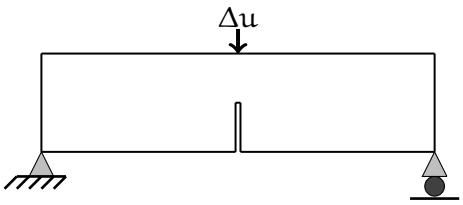

Figure 3.12: Three point bending

Parameters	Value
Fracture Model	Quasi-Brittle
Energy Split	Spectral [37]
Softening	Cornellisen et. al. [70]
E_0	2e4 [MPa]
ν	0.2 [-]
f_t	2.4 [MPa]
G_c	0.113 [N/mm]
l	2.5 [mm]
`optIter`	10 [-]

Table 3.5: Model parameters

Figure 3.13a presents the phase-field fracture distribution at the final step of the analysis. It is in agreement with the experimentally observed fracture pattern by Rots [154]. The load-displacement curves obtained using the different monolithic solution techniques are presented in Figure 3.13b. The arc-length method estimates a higher peak-load compared to the incremental iterative methods (BFGS, dia-NR and Hessian scaling). However, the peak loads are within the experimentally observed range (shaded region). The post-peak response differs from the experimental range due to the calibration of the Cornellisen et. al. softening law [70] carried out in [2] for the phase-field fracture model. Re-calibration for better a experimental fit is possible, however, it is not carried out in this thesis.

3.5.2 *Computational efficiency*

This section presents a study on the computational efficiency of the monolithic solution techniques, discussed earlier in this chapter. The total and average iterations required to achieve convergence as well as the CPU time are considered as efficiency measures. The numerical experiments are limited to the single edge notched specimen under tension (SENT), which is discretized using 13204 3-noded triangular elements, resulting 6616 nodes and 19785 unconstrained degrees of freedom. Furthermore, the iteration terminating tolerances are varied as 10^{-4}, 10^{-6} and 10^{-8}. The simulations are carried out on the HPC27 cluster at the Delft University of Technology, The Netherlands. Four cores are utilized on Intel(R) Xeon(R) CPU E5-1620 v4 processors for multi-threaded assembly of the stiffness matrix and the force vectors. The linear problem in every iteration is solved using the

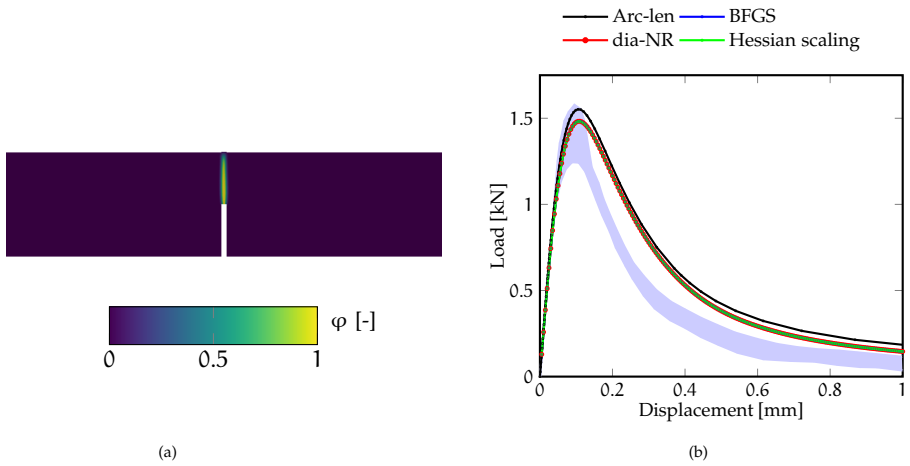

Figure 3.13: Figure (a) presents the phase-field distribution in the three-point bending specimen at the final step of the analysis. Figure (b) presents the respective load-displacement curves obtained using the monolithic solution techniques, arc-length (Arc-len) method, BFGS method, diagonal only variant of the Newton-Raphson (dia-NR) method, and Hessian scaling method. The experimental range from Rots [154] is represented by the shaded region.

shared memory Pardiso solver from Intel's oneAPI Math Kernel Library [64].

Solution technique	tol	Steps	Total Iters.	Avg. Iters.	CPU time [s]
Arc-length	10^{-4}	265	1668	6.29	1357.0
	10^{-6}	265	1763	6.65	1719.0
	10^{-8}	312	2554	8.18	1637.0
dia-NR	10^{-4}	251	5938	23.66	6638.0
	10^{-6}	251	13283	52.92	11580.0
	10^{-8}	251	30958	123.34	23630.0
BFGS	10^{-4}	251	5938	23.66	6701.0
	10^{-6}	251	13284	52.92	11740.0
	10^{-8}	251	30958	123.34	24720.0
Hessian scaling	10^{-4}	251	3473	13.84	2450.0
	10^{-6}	251	6042	24.07	4233.0
	10^{-8}	251	12993	51.77	8784.0

Table 3.6: Table presents the total numbers of steps and iterations, average iterations and CPU time (in seconds) for the SENT numerical experiment with different monolithic solution techniques and varying iteration terminating tolerances. For the arc-length method, the total iterations also include those from steps that failed to converge.

Table 3.6 presents the efficiency measures adopted for the different monolithic solution techniques. The arc-length method outperforms all other methods in terms of (total and average) iterations required for convergence,

and consequently the CPU time. It is important to note that the arc-length method has been implemented using the Sherman-Morisson formula [156], thus requiring two linear solves for each iteration. Further reduction in the CPU time may be achieved upon using a linear solver with multiple right-hand sides.

Among the incremental iterative methods (dia-NR, BFGS and Hessian scaling), the Hessian scaling method outperforms the rest. The reason being it retains more information of the true Hessian (global tangent stiffness matrix) compared to the dia-NR and BFGS methods. The problematic Hessian block $\mathbf{K}^{\mathbf{u}\varphi}$ is removed only for integration points with phase-field above 0.4. This leads to a better convergence behaviour, thereby reducing the CPU time. The dia-NR method and the BFGS method are both secant-based solution techniques, demonstrating similar performance.

Beside the efficiency measures for the different monolithic solution techniques, the convergence of the load-displacement curves w.r.t. the iteration terminating tolerance is also an important aspect. It is particularly worth investigating given the difference in the load-displacement curves observed with the BFGS method and dia-NR method compared to the Hessian scaling method for the same tolerance 10^{-4} (see Figure 3.7b in Section 3.5.1.1).

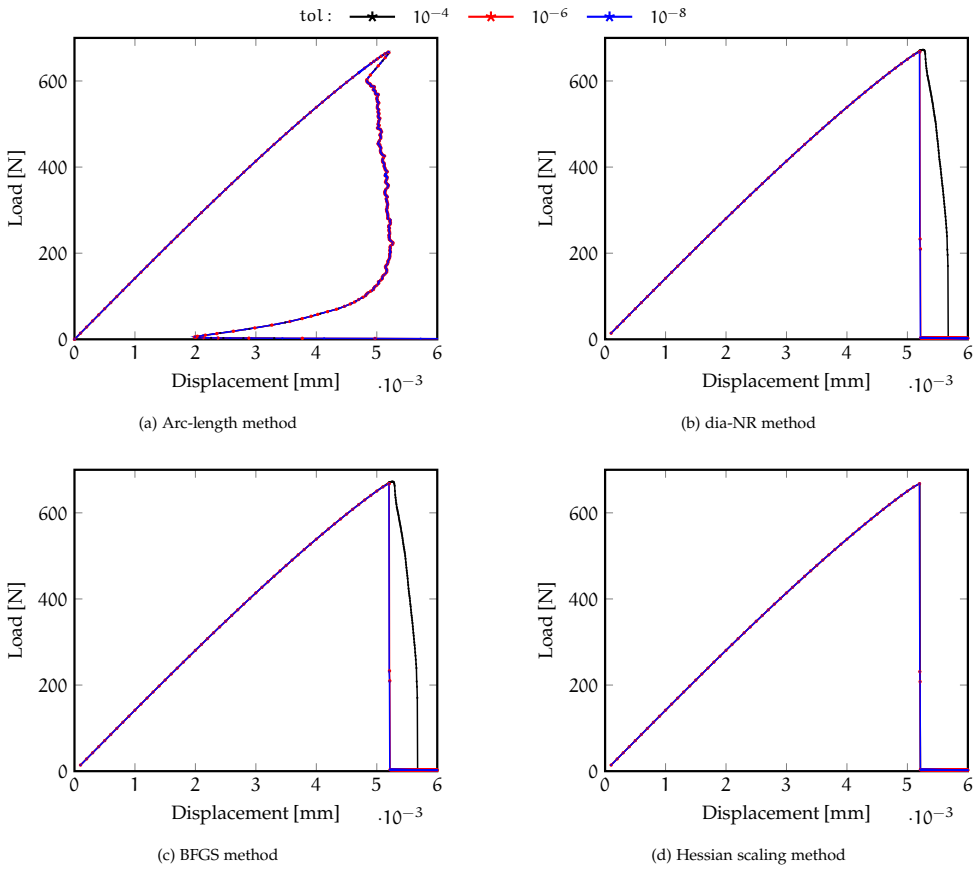

(a) Arc-length method

(b) dia-NR method

(c) BFGS method

(d) Hessian scaling method

Figure 3.14: Figure (a,b,c,d) presents the set of load-displacement curves obtained using the arc-length method, diagonal only variant of the Newton-Raphson (dia-NR) method, BFGS method and the Hessian scaling method, respectively. In each figures, the individual curves correspond to the choice of iteration terminating tolerance, varied as 10^{-4}, 10^{-6} and 10^{-8}.

Figure 3.14 presents the set of load-displacement curves obtained using the arc-length method, diagonal variant of the Newton-Raphson method (dia-NR), BFGS method, and the Hessian scaling method. For the arc-length method and the Hessian scaling method, the load-displacement curves are similar, irrespective of the chosen tolerances, thereby indicating a convergence. However, in the case of the BFGS method and dia-NR method, a tolerance of 10^{-4} yields a different post-peak response in the load-displacement curve, exhibiting an artificial ductility. On choosing stricter tolerances 10^{-6} and 10^{-8}, a convergence of the load-displacement curve is obtained.

4

VARIATIONALLY CONSISTENT FRACTURE IRREVERSIBILITY

This chapter deals with the computational methods for enforcing the fracture irreversibility constraint in phase-field fracture models. The fracture irreversibility constraint manifests in the form of variational inequality with restrictive test and trial spaces. Section 4.1 presents the pertinent equations and the implementation caveats.

A novel micromorphic phase-field fracture model is proposed in Section 4.2 for pointwise treatment of fracture irreversibility in a variationally consistent fashion. Thereafter, the arc-length method presented in the previous chapter is extended to the micromorphic phase-field fracture model. This is followed by a set of numerical experiments and pertinent discussion in Section 4.4.

4.1 VARIATIONAL INEQUALITY AND IMPLEMENTATION CAVEATS

The phase-field fracture model entails a variational inequality formulation. The inequality formulation stems from the minimization of its energy functional (2.19) in conjunction with the fracture irreversibility constraint $\dot{\varphi} \geqslant 0$. Here and throughout this thesis, φ is the phase-field variable representing fracture. The variational equations following the minimization along with pertinent trial and test spaces results in the Variational Problem 5. Herein, the phase-field evolution equation (4.1b) is observed to be a variational inequality, with a restrictive trial and test space (4.2b).

Variational Problem 5. *Find* $(\mathbf{u}, \varphi) \in \mathbb{U} \times \mathbb{P}$ *such that*

$$\begin{aligned} E'(\mathbf{u}, \varphi; \delta\mathbf{u}) = &\int_\Omega \left(g(\varphi) \frac{\partial \Psi^+(\boldsymbol{\epsilon}[\mathbf{u}])}{\partial \boldsymbol{\epsilon}} + \frac{\partial \Psi^-(\boldsymbol{\epsilon}[\mathbf{u}])}{\partial \boldsymbol{\epsilon}} \right) : \boldsymbol{\epsilon}[\delta\mathbf{u}] \, d\Omega \\ &- \int_{\Gamma^u_N} \mathbf{t}^u_p \cdot \delta\mathbf{u} \, d\Gamma = 0 \quad \forall \, \delta\mathbf{u} \in \mathbb{U}^0, \end{aligned} \tag{4.1a}$$

$$\begin{aligned} E'(\mathbf{u}, \varphi; \hat{\varphi}) = &\int_\Omega \left(g'(\varphi) \Psi^+(\boldsymbol{\epsilon}[\mathbf{u}]) + \frac{G_c}{c_w l} w'(\varphi) \right) (\hat{\varphi} - \varphi) \, d\Omega \\ &+ \int_\Omega \frac{G_c l}{c_w} \boldsymbol{\nabla}\varphi \cdot \boldsymbol{\nabla}(\hat{\varphi} - \varphi) \, d\Omega \geqslant 0 \quad \forall \, \hat{\varphi} \in \mathbb{P}, \end{aligned} \tag{4.1b}$$

using pertinent time-dependent Dirichlet boundary conditions $\mathbf{u}^p$ *on* Γ^u_D *and* φ^p *on* Γ^φ_D*, and Neumann boundary condition* $\mathbf{t}^u_p$ *on* Γ^u_N*. The trial and test spaces are defined as*

$$\mathbb{U} = \{\mathbf{u} \in [H^1(\Omega)]^{\dim} | \mathbf{u} = \mathbf{u}^p \text{ on } \Gamma^u_D\}, \tag{4.2a}$$

Variational Problem 5 (continued)

$$\mathbb{P} = \{\varphi \in [H^1(\Omega)] | \varphi \geqslant {}^{n}\varphi | \varphi = \varphi^{p} \text{ on } \Gamma_D^{\varphi}\}, \tag{4.2b}$$

$$\mathbb{U}^0 = \{\mathbf{u} \in [H^1(\Omega)]^{\dim} | \mathbf{u} = \mathbf{0} \text{ on } \Gamma_D^{u}\}. \tag{4.2c}$$

In (4.2b), the left superscript n refers to the previous time-step. ■

Transforming the inequality-based continuous Variational Problem 5 into a discrete problem using the finite element method is a challenging task. Traditionally, the finite element method is suited to equality-based equations, and offers no support in enforcing a solution to remain in a feasible region defined by inequality constraints. Therefore, the approach towards solving inequality-based variational problems is to combine the finite element method with constrained optimization techniques. Some of these techniques adopted for the phase-field fracture model include penalty method [32], augmented Lagrangian method [157], interior point method [35], and primal-dual active set method [34]. Under certain assumptions, discussed in the respective articles, these techniques offer equivalent equality-based formulations for the inequality-based continuous Variational Problem 5. In an alternative approach, some heuristic methods are also proposed for enforcing fracture irreversibility. They include the history variable approach [37] and the 'Crack-Set' method [21, 22, 158]. In this thesis, the penalty method and the history variable approach are discussed, owing to their popularity in the phase-field fracture modelling community.

Penalty method

The penalty method is proposed by Gerasimov and De Lorenzis in [32] as an equivalent equality-based reformulation of the Variational Problem 5. To that end, the energy functional (2.19) and the fracture irreversibility constraint $\dot{\varphi} \geqslant 0$ are expressed as

$$\begin{aligned} E(\mathbf{u}, \varphi) = &\int_\Omega g(\varphi)\, \Psi^{+}(\boldsymbol{\epsilon}[\mathbf{u}])\, d\Omega + \int_\Omega \Psi^{-}(\boldsymbol{\epsilon}[\mathbf{u}])\, d\Omega - \int_{\Gamma_N^{u}} \mathbf{t}_p^{u} \cdot \mathbf{u}\, d\Gamma \\ &+ \int_\Omega \frac{G_c}{c_w} \left(\frac{w(\varphi)}{l} + l|\boldsymbol{\nabla}\varphi|^2 \right) d\Omega + \int_\Omega \frac{\eta}{2} \langle {}^{n}\varphi - \varphi \rangle_+^2\, d\Omega, \end{aligned} \tag{4.3}$$

where, ${}^{n}\varphi$ represents the phase-field from the previous converged step. Theoretically, when $\eta \longrightarrow \infty$, the fracture irreversibility constraint $\dot{\varphi} \geqslant 0$ is satisfied. The corresponding Variational Problem is stated as follows:

Variational Problem 6. *Find* $(\mathbf{u}, \varphi) \in \mathbb{U} \times \mathbb{P}$ *such that*

$$\mathrm{E}'(\mathbf{u}, \varphi; \delta\mathbf{u}) = \int_\Omega \left(g(\varphi) \frac{\partial \Psi^+(\boldsymbol{\epsilon}[\mathbf{u}])}{\partial \boldsymbol{\epsilon}} + \frac{\partial \Psi^-(\boldsymbol{\epsilon}[\mathbf{u}])}{\partial \boldsymbol{\epsilon}} \right) : \boldsymbol{\epsilon}[\delta\mathbf{u}] \, \mathrm{d}\Omega \tag{4.4a}$$

$$- \int_{\Gamma^u_N} \mathbf{t}^u_p \cdot \delta\mathbf{u} \, \mathrm{d}\Gamma = 0 \quad \forall \, \delta\mathbf{u} \in \mathbb{U}^0,$$

$$\mathrm{E}'(\mathbf{u}, \varphi; \delta\varphi) = \int_\Omega \left(g'(\varphi) \Psi^+(\boldsymbol{\epsilon}[\mathbf{u}]) + \frac{G_c}{c_w \, l} w'(\varphi) \right) \delta\varphi \, \mathrm{d}\Omega \tag{4.4b}$$

$$+ \int_\Omega \frac{G_c \, l}{c_w} \boldsymbol{\nabla}\varphi \cdot \boldsymbol{\nabla}\delta\varphi \, \mathrm{d}\Omega$$

$$- \int_\Omega \eta \, \langle {}^n\varphi - \varphi \rangle_+ \, \delta\varphi \, \mathrm{d}\Omega = 0 \quad \forall \, \delta\varphi \in \mathbb{P}^0,$$

using pertinent time-dependent Dirichlet boundary conditions $\mathbf{u}^p$ *on* Γ^u_D *and* φ^p *on* Γ^φ_D*, and Neumann boundary condition* $\mathbf{t}^u_p$ *on* Γ^u_N*. The trial and test spaces are defined as*

$$\mathbb{U} = \{\mathbf{u} \in [H^1(\Omega)]^{\dim} | \mathbf{u} = \mathbf{u}^p \text{ on } \Gamma^u_D\}, \tag{4.5a}$$

$$\mathbb{P} = \{\varphi \in [H^1(\Omega)] | \varphi = \varphi^p \text{ on } \Gamma^\varphi_D\}, \tag{4.5b}$$

$$\mathbb{U}^0 = \{\mathbf{u} \in [H^1(\Omega)]^{\dim} | \mathbf{u} = \mathbf{0} \text{ on } \Gamma^u_D\}, \tag{4.5c}$$

$$\mathbb{P}^0 = \{\varphi \in [H^1(\Omega)] | \varphi = 0 \text{ on } \Gamma^\varphi_D\}. \tag{4.5d}$$

■

The equality-based Variational Problem 6 is equivalent to the inequality-based Variational Problem 5 only when $\eta \longrightarrow \infty$. However, Gerasimov and De Lorenzis introduced the notion of a user-prescribed tolerance $\mathtt{TOL}_{ir}$ on the fracture irreversibility constraint. Based on the choice of $\mathtt{TOL}_{ir}$, a lower bound for the penalty parameter was proposed as

$$\eta(\mathtt{TOL}_{ir}) = \begin{cases} \dfrac{G_c}{l} \dfrac{27}{64 \, \mathtt{TOL}^2_{ir}} & \text{AT1 model,} \\ \dfrac{G_c}{l} \left(\dfrac{1}{\mathtt{TOL}^2_{ir}} - 1 \right) & \text{AT2 model.} \end{cases} \tag{4.6}$$

From the above expression, it is clear that the penalty parameter scales inversely w.r.t the square of the fracture irreversibility constraint tolerance. Such an expression does have an influence on the ill-conditioning of the system of equation. For instance, when $\mathtt{TOL}_{ir} = 1e-4$, the penalty parameter η assumes value $\approx 10^8 \, G_c/l$. A further issue, albeit minor pertains to the lack of a penalty parameter expression for quasi-brittle fracture models.

History variable approach

The history variable approach is a heuristic method to enforce fracture irreversibility. It is proposed by Miehe, Hofacker, and Welschinger [37], where the fracture driving energy Ψ^+ is postulated as the source term, driving the evolution of the phase-field. Thereafter, fracture irreversibility is enforced through an irreversibility constraint on Ψ^+. To that end, Miehe, Hofacker, and Welschinger introduced an integration point variable, referred to as the 'history variable', defined as

$$\mathcal{H} = \max\left\{{}^{n}\mathcal{H}, \Psi^+(\boldsymbol{\epsilon}[\mathbf{u}])\right\}, \tag{4.7}$$

where n refers to the previous time-step. Finally, Ψ^+ in the phase-field evolution equation (4.1b) is replaced with $\mathcal{H}$. This transforms the phase-field evolution equation to an equality with relaxed trial and test spaces, as shown in Variational Problem 7.

Variational Problem 7. *Find* $(\mathbf{u}, \varphi) \in \mathbb{U} \times \mathbb{P}$ *such that*

$$E'(\mathbf{u}, \varphi; \delta\mathbf{u}) = \int_\Omega \left(g(\varphi) \frac{\partial \Psi^+(\boldsymbol{\epsilon}[\mathbf{u}])}{\partial \boldsymbol{\epsilon}} + \frac{\partial \Psi^-(\boldsymbol{\epsilon}[\mathbf{u}])}{\partial \boldsymbol{\epsilon}} \right) : \boldsymbol{\epsilon}[\delta\mathbf{u}] \, d\Omega \tag{4.8a}$$

$$- \int_{\Gamma^u_N} \mathbf{t}^u_p \cdot \delta\mathbf{u} \, d\Gamma = 0 \quad \forall \, \delta\mathbf{u} \in \mathbb{U}^0,$$

$$E'(\mathbf{u}, \varphi; \delta\varphi) = \int_\Omega \left(g'(\varphi)\mathcal{H} + \frac{G_c}{c_w l} w'(\varphi) \right) \delta\varphi \, d\Omega \tag{4.8b}$$

$$+ \int_\Omega \frac{G_c l}{c_w} \boldsymbol{\nabla}\varphi \cdot \boldsymbol{\nabla}\delta\varphi \, d\Omega = 0 \quad \forall \, \delta\varphi \in \mathbb{P}^0,$$

using pertinent time-dependent Dirichlet boundary conditions $\mathbf{u}^p$ *on* Γ^u_D *and* φ^p *on* Γ^φ_D*, and Neumann boundary condition* $\mathbf{t}^u_p$ *on* Γ^u_N*. The trial and test spaces are defined as*

$$\mathbb{U} = \{\mathbf{u} \in [H^1(\Omega)]^{\dim} | \mathbf{u} = \mathbf{u}^p \text{ on } \Gamma^u_D\}, \tag{4.9a}$$

$$\mathbb{P} = \{\varphi \in [H^1(\Omega)] | \varphi = \varphi^p \text{ on } \Gamma^\varphi_D\}, \tag{4.9b}$$

$$\mathbb{U}^0 = \{\mathbf{u} \in [H^1(\Omega)]^{\dim} | \mathbf{u} = \mathbf{0} \text{ on } \Gamma^u_D\}, \tag{4.9c}$$

$$\mathbb{P}^0 = \{\varphi \in [H^1(\Omega)] | \varphi = 0 \text{ on } \Gamma^\varphi_D\}. \tag{4.9d}$$

The history variable $\mathcal{H}$ *is defined in (4.7).* ■

The history variable approach, however, results in the loss of variational consistency. In particular, the energy functional (2.19) is not recovered from the variational equations (4.8a) and (4.8b). Furthermore, De Lorenzis and Gerasimov reported an over-estimation of the fracture surface energy with the history-variable approach (see Figures 7 and 9 in [28]). The

over-estimated fracture surface energy manifests in an increased fracture bandwidth (see Figures 8 and 10 in [28]).

4.2 A MICROMORPHIC PHASE-FIELD FRACTURE MODEL

In this section, a micromorphic phase-field fracture model is developed as an alternative implementation of the variational inequality (4.1b). To that end, the phase-field fracture energy functional (2.19) is extended in the spirit of micromorphic approach proposed by Forest in [159]. Thereafter, minimizing the energy functional reveals the local nature of the phase-field evolution equation, allowing a pointwise treatment of the fracture irreversibility constraint with system-level precision.

4.2.1 *The energy functional*

The energy functional for the micromorphic phase-field fracture model is expressed as

$$\begin{aligned} E(\mathbf{u},\varphi,d) = \int_\Omega g(\varphi)\,\Psi^+(\boldsymbol{\epsilon}[\mathbf{u}])\,d\Omega + \int_\Omega \Psi^-(\boldsymbol{\epsilon}[\mathbf{u}])\,d\Omega - \int_{\Gamma_N^u} \mathbf{t}_p^u \cdot \mathbf{u}\,d\Gamma \\ + \underbrace{\int_\Omega \frac{G_c}{c_w}\left(\frac{w(\varphi)}{l} + l|\nabla d|^2\right) d\Omega}_{\text{fracture surface energy}} + \underbrace{\int_\Omega \frac{\eta}{2}(\varphi - d)^2\,d\Omega}_{\text{interaction energy}}, \end{aligned} \tag{4.10}$$

resulting in a three-field problem with the displacement $\mathbf{u}$, phase-field φ, and a *newly introduced* micromorphic variable d. Compared to the original phase-field fracture model energy functional (2.19), the micromorphic variant (4.10) introduces two changes. First, the gradient of the phase-field $\nabla\varphi$ in the fracture surface energy is replaced by a gradient of the micromorphic variable ∇d. Thus, the regularity requirements on the phase-field w.r.t. the existence of its derivatives is circumvented. In other words, the phase-field becomes a local quantity. The second change in the micromorphic variant is the additional interaction term, penalizing the difference between the phase-field and the micromorphic variable. Thus, when $\eta \longrightarrow \infty$, $\varphi = d$ and the original phase-field fracture model energy functional (2.19) is recovered.

4.2.2 *Variational equations*

The set of variational equations for the micromorphic phase-field fracture model is obtained upon minimizing the energy functional (4.10) w.r.t its solution fields, the vector-valued displacement $\mathbf{u}$, and the scalar-valued phase-field φ and micromorphic variable d. With appropriately defined

test and trial Sobolev[1] spaces H^1 and the fracture irreversibility constraint $\dot{\varphi} \geqslant 0$, the complete variational problem assumes the following form:

Variational Problem 8. *Find* $(\mathbf{u}, \varphi, d) \in \mathbb{U} \times \mathbb{P} \times \mathbb{D}$ *such that*

$$E'(\mathbf{u}, \varphi, d; \delta\mathbf{u}) = \int_\Omega \left(g(\varphi) \frac{\partial \Psi^+(\boldsymbol{\epsilon}[\mathbf{u}])}{\partial \boldsymbol{\epsilon}} + \frac{\partial \Psi^-(\boldsymbol{\epsilon}[\mathbf{u}])}{\partial \boldsymbol{\epsilon}} \right) : \boldsymbol{\epsilon}[\delta\mathbf{u}] \, d\Omega - \int_{\Gamma^u_N} \mathbf{t}^u_p \cdot \delta\mathbf{u} \, d\Gamma = 0 \quad \forall \, \delta\mathbf{u} \in \mathbb{U}^0, \tag{4.11a}$$

$$E'(\mathbf{u}, \varphi, d; \hat{\varphi}) = \int_\Omega \left(g'(\varphi) \Psi^+(\boldsymbol{\epsilon}[\mathbf{u}]) + \frac{G_c}{c_w \, l} w'(\varphi) \right) (\hat{\varphi} - \varphi) \, d\Omega + \int_\Omega \eta(\varphi - d)(\hat{\varphi} - \varphi) \, d\Omega \geqslant 0 \quad \forall \, \hat{\varphi} \in \mathbb{P}, \tag{4.11b}$$

$$E'(\mathbf{u}, \varphi, d; \delta d) = \int_\Omega \frac{2 G_c \, l}{c_w} \boldsymbol{\nabla} d \cdot \boldsymbol{\nabla} \delta d \, d\Omega - \int_\Omega \eta(\varphi - d) \delta d \, d\Omega = 0 \quad \forall \, \delta d \in \mathbb{D}^0, \tag{4.11c}$$

using pertinent time-dependent Dirichlet boundary conditions $\mathbf{u}^p$ *on* Γ^u_D *and* d^p *on* Γ^d_D*, and Neumann boundary condition* $\mathbf{t}^u_p$ *on* Γ^u_N*. The trial and test spaces are defined as*

$$\mathbb{U} = \{\mathbf{u} \in [H^1(\Omega)]^{\dim} | \mathbf{u} = \mathbf{u}^p \text{ on } \Gamma^u_D\}, \tag{4.12a}$$

$$\mathbb{P} = \{\varphi \in [H^1(\Omega)] | \varphi \geqslant {}^n\varphi | \varphi = \varphi^p \text{ on } \Gamma^\varphi_D\}, \tag{4.12b}$$

$$\mathbb{D} = \{d \in [H^1(\Omega)] | d = d^p \text{ on } \Gamma^d_D\}, \tag{4.12c}$$

$$\mathbb{U}^0 = \{\mathbf{u} \in [H^1(\Omega)]^{\dim} | \mathbf{u} = \mathbf{0} \text{ on } \Gamma^u_D\}, \tag{4.12d}$$

$$\mathbb{D}^0 = \{d \in [H^1(\Omega)] | d = 0 \text{ on } \Gamma^d_D\}. \tag{4.12e}$$

In (4.12b), the left superscript n *refers to the previous time-step.* ■

The phase-field evolution equation (4.11b) corresponding to the micromorphic phase-field fracture model remains a variational inequality. However, the regularity requirement on the phase-field is reduced due to the absence of its derivatives. Therefore, (4.11b) may be assumed to hold pointwise in the computational domain Ω, without the loss of generality. In other words, it is possible to compute the phase-field φ at the integration points as the root(s) of the equation,

$$g'(\varphi)\Psi^+(\boldsymbol{\epsilon}[\mathbf{u}]) + \frac{G_c}{c_w \, l} w'(\varphi) + \eta(\varphi - d) = 0. \tag{4.13}$$

Thereafter, the fracture irreversibility constraint as well as the upper bound are enforced as ${}^n\varphi < \varphi < 1$ with system-level precision. The ability to com-

1 A function u for which $\int_\Omega (u)^2 + (\boldsymbol{\nabla} u)^2 < \infty$, belongs to Sobolev space of degree one, denoted by H^1. For more on function spaces, the reader is referred to [31].

pute the phase-field at integration points reduces the three-field Variational Problem 8 into an equivalent two-field Variational Problem 9.

Variational Problem 9. *With phase-field φ computed using (4.13), find $(\mathbf{u}, d) \in \mathbb{U} \times \mathbb{D}$ such that*

$$E'(\mathbf{u}, d; \delta\mathbf{u}) = \int_\Omega \left(g(\varphi) \frac{\partial \Psi^+(\boldsymbol{\epsilon}[\mathbf{u}])}{\partial \boldsymbol{\epsilon}} + \frac{\partial \Psi^-(\boldsymbol{\epsilon}[\mathbf{u}])}{\partial \boldsymbol{\epsilon}} \right) : \boldsymbol{\epsilon}[\delta\mathbf{u}] \, d\Omega - \int_{\Gamma_N^u} \mathbf{t}_p^u \cdot \delta\mathbf{u} \, d\Gamma = 0 \quad \forall \, \delta\mathbf{u} \in \mathbb{U}^0, \tag{4.14a}$$

$$E'(\mathbf{u}, d; \delta d) = \int_\Omega \frac{2 G_c l}{c_w} \boldsymbol{\nabla} d \cdot \boldsymbol{\nabla} \delta d \, d\Omega - \int_\Omega \eta(\varphi - d) \delta d \, d\Omega = 0 \quad \forall \, \delta d \in \mathbb{D}^0, \tag{4.14b}$$

using pertinent time-dependent Dirichlet boundary conditions $\mathbf{u}^p$ on Γ_D^u and d^p on Γ_D^d, and Neumann boundary condition $\mathbf{t}_p^u$ on Γ_N^u. The trial and test spaces are defined as

$$\mathbb{U} = \{\mathbf{u} \in [H^1(\Omega)]^{\dim} | \mathbf{u} = \mathbf{u}^p \text{ on } \Gamma_D^u\}, \tag{4.15a}$$

$$\mathbb{D} = \{d \in [H^1(\Omega)] | d = d^p \text{ on } \Gamma_D^d\}, \tag{4.15b}$$

$$\mathbb{U}^0 = \{\mathbf{u} \in [H^1(\Omega)]^{\dim} | \mathbf{u} = \mathbf{0} \text{ on } \Gamma_D^u\}, \tag{4.15c}$$

$$\mathbb{D}^0 = \{d \in [H^1(\Omega)] | d = 0 \text{ on } \Gamma_D^d\}. \tag{4.15d}$$

■

Furthermore, the integration point phase-field evolution equation (4.13) may be linear or nonlinear. It depends on the chosen degradation function $g(\varphi)$ and the locally dissipated fracture energy function $w(\varphi)$ (see Tables 2.1 and 2.3 in Chapter 2 for possible options). In the case of brittle AT1 and AT2 models, closed form expressions for the phase-field are obtained as

$$\varphi(\boldsymbol{\epsilon}[\mathbf{u}], d) = \begin{cases} \min\left(\max\left(\dfrac{2\Psi^+ + \eta d}{2\Psi^+ + \eta + \frac{G_c}{l}}, {}^n\varphi \right), 1 \right) & \text{AT1 model,} \\ \min\left(\max\left(\dfrac{2\Psi^+ + \eta d}{2\Psi^+ + \eta + \frac{G_c}{l}}, {}^n\varphi \right), 1 \right) & \text{AT2 model.} \end{cases} \tag{4.16}$$

This is a consequence of linear/quadratic functions $g(\varphi)$ and $w(\varphi)$. However, for quasi-brittle fracture models, $g(\varphi)$ is a rational fraction. Therefore, the phase-field evolution equation (4.13) becomes nonlinear, and is solved using the Newton-Raphson method.

4.3 MONOLITHIC SOLUTION TECHNIQUES

The Variational Problem 9 is non-convex, which results in a poor convergence of the Newton-Raphson method (full-NR). Similar to the phase-field fracture model, the non-convex nature is attributed to the degraded strain energy density $g(\varphi)\Psi^+$. In order to investigate the performance of the Newton-Raphson method, the Variational Problem 9 is discretized using the Finite Element Method (FEM), following the procedure explained in Section 2.1. The derivation is skipped here for brevity, instead the micromorphic phase-field fracture Discrete Problem 7 is presented.

Discrete Problem 7. *With phase-field φ evaluated using (4.13), compute the solution update $\mathbf{s}_{k+1} = \{\Delta\tilde{\mathbf{u}}\,;\,\Delta\tilde{\mathbf{d}}\}$ for the current iteration $k+1$ using*

$$\underbrace{\begin{bmatrix}\mathbf{K}^{uu} & \mathbf{K}^{ud}\\ \mathbf{K}^{du} & \mathbf{K}^{dd}\end{bmatrix}_k}_{\text{Stiffness matrix, } \mathbf{K}_k} \underbrace{\begin{Bmatrix}\Delta\tilde{\mathbf{u}}\\ \Delta\tilde{\mathbf{d}}\end{Bmatrix}_{k+1}}_{\mathbf{s}_{k+1}} = \underbrace{\begin{Bmatrix}\mathbf{f}^{ext,u}\\ \mathbf{f}^{ext,d}\end{Bmatrix}_i - \begin{Bmatrix}\mathbf{f}^{int,u}\\ \mathbf{f}^{int,d}\end{Bmatrix}_k}_{\text{Residual, } \mathbf{r}_k}, \tag{4.17a}$$

and update the solution as

$$\begin{Bmatrix}\tilde{\mathbf{u}}\\ \tilde{\mathbf{d}}\end{Bmatrix}_{k+1} = \begin{Bmatrix}\tilde{\mathbf{u}}\\ \tilde{\mathbf{d}}\end{Bmatrix}_k + \begin{Bmatrix}\Delta\tilde{\mathbf{u}}\\ \Delta\tilde{\mathbf{d}}\end{Bmatrix}_{k+1}, \tag{4.17b}$$

until the norm of the residual is sufficiently small. The stiffness matrix components are given by,

$$\begin{aligned}
\mathbf{K}^{uu} &= \mathcal{A}\int_{\Omega_{el}} [\mathbf{B}^u]^T \left(\underbrace{g(\varphi)\frac{\partial \boldsymbol{\sigma}^+}{\partial \boldsymbol{\epsilon}} + \frac{\partial \boldsymbol{\sigma}^-}{\partial \boldsymbol{\epsilon}}}_{\mathbf{D}} - g'(\varphi)\boldsymbol{\sigma}^+(\boldsymbol{\epsilon}[\mathbf{u}])\frac{\partial \varphi}{\partial \boldsymbol{\epsilon}} \right) [\mathbf{B}^u]\, d\Omega,\\
\mathbf{K}^{ud} &= \mathcal{A}\int_{\Omega_{el}} [\mathbf{B}^u]^T \left(g'(\varphi)\boldsymbol{\sigma}^+ \frac{\partial \varphi}{\partial d} \right) [\mathbf{N}^d]\, d\Omega,\\
\mathbf{K}^{du} &= \mathcal{A}\int_{\Omega_{el}} [\mathbf{N}^d]^T \left(-\eta \frac{\partial \varphi}{\partial d} \right) [\mathbf{B}^u]\, d\Omega,\\
\mathbf{K}^{dd} &= \mathcal{A}\int_{\Omega_{el}} \left([\mathbf{B}^d]^T \left(\frac{G_c l}{c_w} \right) [\mathbf{B}^d] \right.\\
&\quad \left. + [\mathbf{N}^d]^T \left(\frac{G_c}{c_w l} w''(\varphi) + \eta - \eta \frac{\partial \varphi}{\partial d} \right) [\mathbf{N}^d] \right) d\Omega,
\end{aligned} \tag{4.17c}$$

and the internal force vector components are computed as

Discrete Problem 7 (continued)

$$\mathbf{f}^{\mathrm{int},\mathbf{u}} = \mathcal{A}\int_{\Omega_{\mathrm{el}}} [\mathbf{B}^{\mathbf{u}}]^{\mathsf{T}} \left(g(\varphi)\boldsymbol{\sigma}^{+} + \boldsymbol{\sigma}^{-}\right) \mathrm{d}\Omega,$$
$$\mathbf{f}^{\mathrm{int},\mathrm{d}} = \mathcal{A}\int_{\Omega_{\mathrm{el}}} \left(\left[\mathbf{B}^{\mathrm{d}}\right]^{\mathsf{T}} \left(\frac{G_c l}{c_w}\boldsymbol{\nabla}\varphi\right) + \left[\mathbf{N}^{\mathrm{d}}\right]^{\mathsf{T}} \eta(\varphi - \mathrm{d}) \right) \mathrm{d}\Omega. \tag{4.17d}$$

Note that $\mathcal{A}$ is an assembly operator that maps element contributions to their global counterparts. Furthermore, the external force vectors $\mathbf{f}^{\mathrm{ext},\mathbf{u}}$ and $\mathbf{f}^{\mathrm{ext},\mathrm{d}}$ are considered equal to zero. The material stiffness matrix $\mathbf{D}$ depends on the chosen strain energy density split (see Table 2.4). ■

Revisiting the tapered bar tension test

In this section, the tapered bar tension test introduced in Section 3.1.2 of Chapter 3 is revisited in the context of the micromorphic phase-field fracture model. For the geometry and other model parameters, the reader is referred therein.

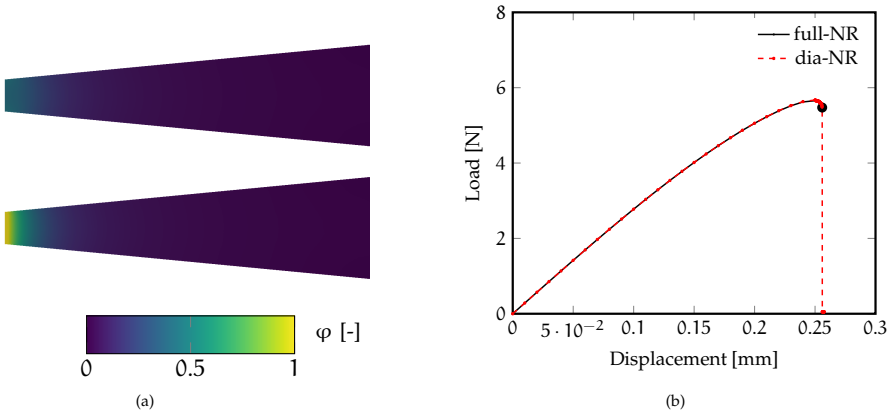

Figure 4.1: Figure (a) presents the phase-field distribution in the tapered bar, when the Newton-Raphson (full-NR) method breaks down (top) and the failure mode obtained with the diagonal only variant of the Newton-Raphson (dia-NR) method (bottom). Figure (b) presents the respective load-displacement curves. The black dot represents the last converged step for the full-NR.

Figure 4.1a (top) presents the phase-field distribution corresponding to the last converged step, obtained with the Newton-Raphson method (full-NR). Therein, the maximum value of the phase-field is ≈ 0.4. From the load-displacement curve (in black), presented in Figure 4.1b, it is evident that the full-NR does not converge for the entire loading path. The black dot represents the last converged step. Similar to the phase-field fracture model, an eigenvalue decomposition of the Hessians (stiffness matrices) generated in the non-converged step reveals dominant negative eigenvalues in terms of magnitude. This proves the Hessian being indefinite when the phase-field reaches ≈ 0.4. During the iterative process, the indefinite Hessian generates a sequence of solution updates not of descent direction, which

results in divergence of the full-NR method. However, on setting the off-diagonal Hessian (stiffness matrix) blocks $\mathbf{K}^{\mathbf{u}\,d}$ and $\mathbf{K}^{d\mathbf{u}}$ explicitly to zero, convergence is achieved for the entire loading path (see red curve in Figure 4.1b). The convergent behaviour is attributed to the positive definiteness of the Hessian. For a relevant discussion, the reader is referred to Section 3.1.3.

The monolithic solution techniques developed for the phase-field fracture model in Chapter 3 may be extended to the micromorphic variant in a straight-forward fashion. However, among these techniques, the arc-length method is adopted in this chapter, motivated by its superior performance.

4.3.1 *Arc-length method with fracture energy constraint*

The arc-length method with fracture energy constraint has been introduced in Section 3.4, albeit in the context of the phase-field fracture model. Its extension to the micromorphic phase-field fracture model only requires redefining the fracture energy.

4.3.1.1 *Fracture energy-based constraint*

The fracture energy-based arc-length constraint equation is re-stated from (3.17),

$$g_{arc} := \Delta\Psi_{frac} - \Delta s = 0, \tag{4.18}$$

where, $\Delta\Psi_{frac}$ and Δs represent the incremental fracture energy and the arc-length, respectively. Note that function arguments are excluded, since the fracture energy requires redefinition in the context of the micromorphic phase-field fracture model.

The incremental fracture energy for the phase-field fracture model (3.20) is expressed as

$$\Delta\Psi_{frac} = -\int_\Omega g'(\varphi)\mathcal{H}\Delta\varphi \, d\Omega, \tag{4.19}$$

where, $\mathcal{H}$ is the history variable associated with the Variational Problem 3. However, for the micromorphic phase-field fracture model, there is no notion of history variable. Therefore, the history variable $\mathcal{H}$ is replaced with the fracture driving energy $\Psi^+(\boldsymbol{\epsilon}[\mathbf{u}])$. With this change, and assuming $\varphi \approx d$, the incremental fracture energy is given by

$$\Delta\Psi_{frac}(\boldsymbol{\epsilon}[\mathbf{u}], d, {}^n d) = -\int_\Omega g'(d)\Psi^+(\boldsymbol{\epsilon}[\mathbf{u}])\Delta d \, d\Omega. \tag{4.20}$$

The assumption $\varphi \approx d$ holds for a sufficiently high interaction parameter η. Finally, the fracture energy based arc-length constraint is stated as

$$g_{arc} := -\int_\Omega g'(d)\Psi^+(\boldsymbol{\epsilon}[\mathbf{u}])\Delta d \, d\Omega - \Delta s = 0. \tag{4.21}$$

Augmented with the arc-length constraint equation (4.21), the micromorphic phase-field fracture Discrete Problem 7 attains the following form:

Discrete Problem 8. *Compute the solution update* $\mathbf{s}_{k+1} = \{\Delta\tilde{\mathbf{u}}\,;\,\Delta\tilde{\varphi}\,;\,\Delta\tilde{\zeta}\}$ *for the current iteration* $k+1$ *using*

$$\underbrace{\begin{bmatrix} \mathbf{K}^{uu} & \mathbf{K}^{ud} & \mathbf{K}^{u\zeta} \\ \mathbf{K}^{du} & \mathbf{K}^{dd} & \mathbf{K}^{d\zeta} \\ \mathbf{K}^{\zeta u} & \mathbf{K}^{\zeta d} & \mathbf{K}^{\zeta\zeta} \end{bmatrix}_k}_{\text{Stiffness matrix, } \mathbf{K}_k} \underbrace{\begin{Bmatrix} \Delta\tilde{\mathbf{u}} \\ \Delta\tilde{d} \\ \Delta\tilde{\zeta} \end{Bmatrix}_{k+1}}_{\mathbf{s}_{k+1}} = \underbrace{\begin{Bmatrix} \mathbf{f}^{ext,u} \\ \mathbf{o} \\ \mathbf{o} \end{Bmatrix}_i - \begin{Bmatrix} \mathbf{f}^{int,u} \\ \mathbf{f}^{int,d} \\ \mathbf{g}_{arc} \end{Bmatrix}_k}_{\text{Residual, } \mathbf{r}_k}, \tag{4.22a}$$

and update the solution as

$$\begin{Bmatrix} \tilde{\mathbf{u}} \\ \tilde{d} \\ \tilde{\zeta} \end{Bmatrix}_{k+1} = \begin{Bmatrix} \tilde{\mathbf{u}} \\ \tilde{d} \\ \tilde{\zeta} \end{Bmatrix}_k + \begin{Bmatrix} \Delta\tilde{\mathbf{u}} \\ \Delta\tilde{d} \\ \Delta\tilde{\zeta} \end{Bmatrix}_{k+1}, \tag{4.22b}$$

until the norm of the residual is sufficiently small. Furthermore, the stiffness matrix components are given by,

$$\begin{aligned}
\mathbf{K}^{uu} &= \mathcal{A} \int_{\Omega_{el}} [\mathbf{B}^u]^T \left(\underbrace{g(\varphi)\frac{\partial \boldsymbol{\sigma}^+}{\partial \boldsymbol{\epsilon}} + \frac{\partial \boldsymbol{\sigma}^-}{\partial \boldsymbol{\epsilon}}}_{\mathbf{D}} - g'(\varphi)\boldsymbol{\sigma}^+(\boldsymbol{\epsilon}[\mathbf{u}])\frac{\partial \varphi}{\partial \boldsymbol{\epsilon}} \right) [\mathbf{B}^u] \, d\Omega, \\
\mathbf{K}^{ud} &= \mathcal{A} \int_{\Omega_{el}} [\mathbf{B}^u]^T \left(g'(\varphi)\boldsymbol{\sigma}^+ \frac{\partial \varphi}{\partial d} \right) [\mathbf{N}^d] \, d\Omega, \\
\mathbf{K}^{u\zeta} &= -\hat{\mathbf{f}}_{ext}, \\
\mathbf{K}^{du} &= \mathcal{A} \int_{\Omega_{el}} [\mathbf{N}^d]^T \left(-\eta \frac{\partial \varphi}{\partial d} \right) [\mathbf{B}^u] \, d\Omega, \\
\mathbf{K}^{dd} &= \mathcal{A} \int_{\Omega_{el}} \left([\mathbf{B}^d]^T \left(\frac{G_c l}{c_w} \right) [\mathbf{B}^d] \right. \\
&\quad \left. + [\mathbf{N}^d]^T \left(\frac{G_c}{c_w l} w''(\varphi) + \eta - \eta \frac{\partial \varphi}{\partial d} \right) [\mathbf{N}^d] \right) d\Omega, \\
\mathbf{K}^{d\zeta} &= \mathbf{K}^{\zeta\zeta} = \mathbf{o}, \\
\mathbf{K}^{\zeta u} &= \mathcal{A} \int_{\Omega_{el}} [\mathbf{B}^u]^T \, g'(\varphi)\Delta\varphi \, \boldsymbol{\sigma}^+ \, d\Omega, \\
\mathbf{K}^{\zeta d} &= \mathcal{A} \int_{\Omega_{el}} [\mathbf{N}^\varphi]^T \left(g''(d)\,\Delta d + g'(d) \right) \Psi^+ \, d\Omega,
\end{aligned} \tag{4.22c}$$

and the internal force vector components are computed as

Discrete Problem 8 (continued)

$$\mathbf{f}^{\mathrm{int},\mathbf{u}} = \mathcal{A}\int_{\Omega_{\mathrm{el}}} [\mathbf{B}^{\mathbf{u}}]^{\mathsf{T}} \left(g(\varphi)\boldsymbol{\sigma}^{+} + \boldsymbol{\sigma}^{-}\right) \mathrm{d}\Omega,$$

$$\mathbf{f}^{\mathrm{int},\mathrm{d}} = \mathcal{A}\int_{\Omega_{\mathrm{el}}} \left(\left[\mathbf{B}^{\mathrm{d}}\right]^{\mathsf{T}} \left(\frac{G_c l}{c_w}\boldsymbol{\nabla}\varphi\right) + \left[\mathbf{N}^{\mathrm{d}}\right]^{\mathsf{T}} \eta(\varphi - \mathrm{d}) \right) \mathrm{d}\Omega, \quad (4.22\mathrm{d})$$

$$g_{\mathrm{arc}} = \mathcal{A}\int_{\Omega_{\mathrm{el}}} \left(g'(\mathrm{d})\Delta\mathrm{d}\,\Psi^{+}\right) \mathrm{d}\Omega + \Delta s.$$

Note that $\mathcal{A}$ is an assembly operator that maps element contributions to their global counterparts. Furthermore, the external force vector $\mathbf{f}^{\mathrm{ext},\mathbf{u}} = \zeta_k\,\hat{\mathbf{f}}_{\mathrm{ext}}$. The material stiffness matrix $\mathbf{D}$ depends on the chosen strain energy density split (see Table 2.4). ■

4.3.2 *Implementation caveats*

The use of arc-length method for the micromorphic phase-field fracture model entails similar implementation caveats compared to the phase-field fracture model. These are, possible singular Hessian, switching between the incremental iterative approach and the arc-length method, and adaptive modification of the arc-length Δs. They have been addressed in Section 3.4.3.

An additional caveat solely related to the micromorphic phase-field fracture model is the assumption $\varphi \approx \mathrm{d}$ in the arc-length constraint (4.21). For a sufficiently high interaction parameter η, the assumption holds and the incremental fracture energy is correctly computed. In other cases, the incremental fracture energy is underestimated. In the absence of an analytical expression for η, a set of numerical experiments are conducted in the next section to establish its lower bound.

4.4 NUMERICAL EXPERIMENTS

In this section, numerical experiments are carried out on benchmark brittle and quasi-brittle fracture problems using the micromorphic phase-field fracture model (see Discrete Problem 8). The problems are introduced in Section 3.5. For information on the geometry and other model parameters, the reader is referred to therein. The set of benchmark problems comprise of the Single Edge Notched specimen under tension, and under shear [37], concrete three point bending experiment [154], and the Winkler L-panel experiment [153]. The objective of the numerical experiments is three-fold. First, the influence of the interaction parameter η on the phase-field regularization and consequently the load-displacement curve are investigated. Thereafter, a comparison of the micromorphic phase-field fracture model is carried out with the history variable-based phase-field formulation (see

Discrete Problem 6). Finally, the efficacy of the micromorphic model is demonstrated.

All problems are solved using the arc-length method with fracture energy-based constraint (see Discrete Problem 8). The iterative procedure is terminated when an error measure defined as ratio of the norm of the residual in the current iteration to that of the first iteration is less than 10^{-4}. Furthermore, the linear problem in every iteration is solved using the shared memory Pardiso solver from Intel's oneAPI Math Kernel Library [64].

4.4.1 *Influence of interaction parameter*

The influence of the interaction parameter η (see Discrete Problem 8) on the fracture topology is investigated through a parametric study. To that end, the interaction parameter η is parametrized as

$$\eta = \beta \frac{G_c}{l}, \tag{4.23}$$

where, $\beta = 50, 500, 1000$ is a user-defined scalar. Thereafter, using the different β values, numerical experiments are carried out on the Single Edge Notched specimen under Tension (SENT). The SENT specimen is chosen due to the straight fracture profile, which makes it easier to obtain a symmetric phase-field profile any cross-section perpendicular to the fracture.

Figure 4.2a presents the load-displacement curves for the SENT numerical experiment using $\beta = 50, 500, 1000$. While $\beta = 500$ and 1000 yield similar curves, the response from $\beta = 50$ is different. The different response with $\beta = 50$ is attributed to insufficient regularization, $\varphi \not\approx d$. Figures 4.2b, 4.2c and 4.2d establish this reasoning. In these figures, the phase-field φ and the micromorphic variable d across a vertical cross-section at an offset 0.25 [mm] from the initial notch are plotted for $\beta = 50, 500, 1000$, respectively. For $\beta = 50$, the maximum value of the micromorphic value is ≈ 0.85, hence, phase-field values beyond 0.85 are not regularized. However, for $\beta = 500, 1000$, the regularization is sufficient i.e., $\varphi \approx d$. Therefore, the corresponding load-displacement curves are similar. In the subsequent part of this chapter, all numerical experiments are carried out using $\beta = 500$.

4.4.2 *Comparison with history variable approach*

Following De Lorenzis and Gerasimov's study [28] reporting an overestimation of the fracture energy with the history variable approach, a comparison is made with the micromorphic phase-field fracture model. Similar to the previous section, the SENT specimen is chosen for the numerical experiments. Furthermore, for both approaches, micromorphic and history variables, the iteration terminating tolerance is set to 10^{-4}, and the linear problem in every iteration is solved using the shared memory Pardiso solver from Intel's oneAPI Math Kernel Library [64].

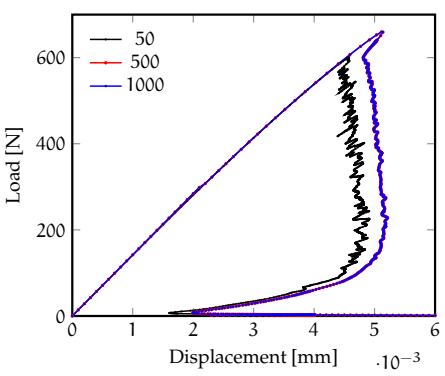

(a) Load-displacement curves

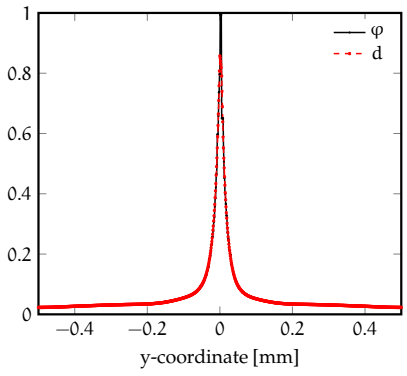

(b) Fracture profile, $\beta = 50$

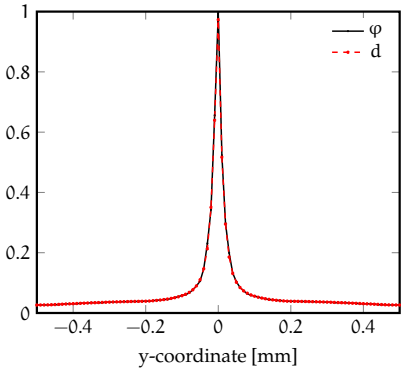

(c) Fracture profile, $\beta = 500$

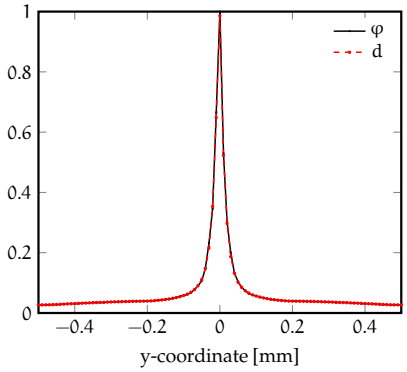

(d) Fracture profile, $\beta = 1000$

Figure 4.2: Figure (a) presents the load-displacement curves obtained using $\beta = 50, 500, 1000$. Figures (b,c,d) presents the fracture profile (phase-field φ and micromorphic variable d) across a vertical cross-section at an offset 0.25 [mm] from the initial notch. The profiles correspond to the last step in the analysis.

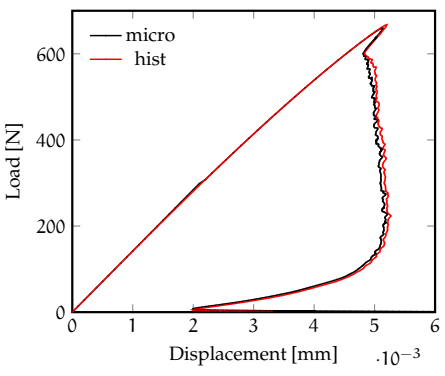

(a) Load-displacement curves

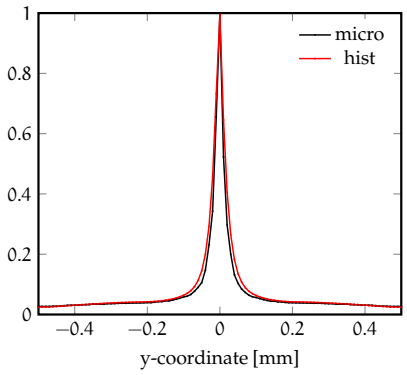

(b) Fracture profile

Figure 4.3: Figure (a) presents the load-displacement curves obtained using the micromorphic phase-field fracture model (micro) and the history variable based phase-field fracture model (hist). Figures (b) presents the fracture profile (phase-field φ and micromorphic variable d) across a vertical cross-section at an offset 0.25 [mm] from the initial notch. The profiles correspond to the last step in the analysis.

Figure 4.3a presents the load-displacement curves obtained using the micromorphic phase-field fracture model (micro) and the history variable based phase-field fracture model (hist). The history variable approach estimates a higher peak, and the post-peak branch descends at a further

displacement, compared to the micromorphic model. This points to a higher energy expended with the history variable, an observation also reported by De Lorenzis and Gerasimov [28] (see Figure 9 in [28]). Furthermore, one may also notice the widening of the phase-field localization band with the history variable in Figure 4.3b. Similar observations are also reported by De Lorenzis and Gerasimov [28], albeit for the single edge notched specimen under shear (see Figures 8 and 10 in [28]). The micromorphic phase-field fracture model predicts a narrow phase-field fracture bandwidth, compared to the history variable approach.

4.4.3 *Efficacy*

The efficacy of the micromorphic phase-field fracture model is demonstrated in this section. To that end, numerical experiments are carried out on the remaining benchmark problems from Section 3.5.1. They comprise of single edge notched specimen under under shear [37], the Winkler L-panel experiment [153], and the concrete three point bending experiment carried out by Rots [154]. For details on the geometry, loading conditions, and model parameters, the reader is referred to Section 3.5.1.

All numerical experiments are conducted using the arc-length method (see Discrete Problem 8). The iteration terminating tolerance is set to 10^{-4}, and the linear problem in every iteration is solved using the shared memory Pardiso solver from Intel's oneAPI Math Kernel Library [64].

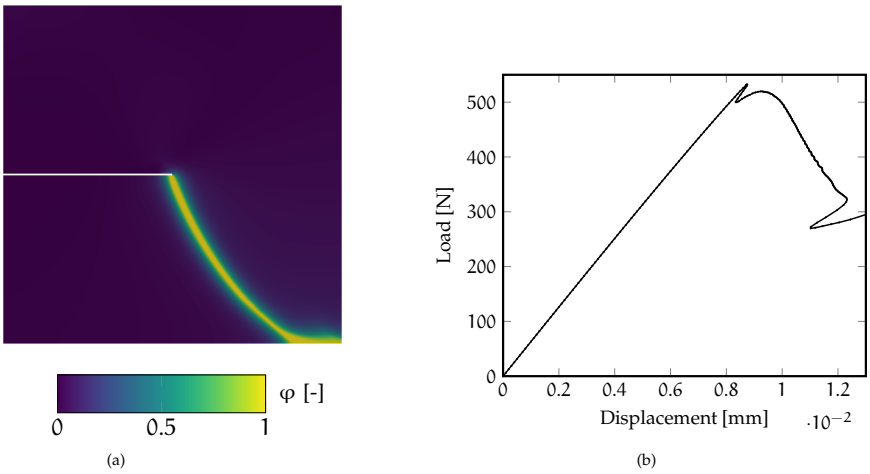

Figure 4.4: Figure (a) presents the phase-field distribution in the single edge notched specimen under shear at the final step of the analysis. Figure (b) presents the respective load-displacement curves obtained using the arc-length method.

Figure 4.4a presents the phase-field distribution at the final step of the analysis for the SENS specimen. The corresponding load-displacement curve is presented in Figure 4.4b. These results are obtained using $\beta = 500$ and are similar to that obtained for the conventional phase-field fracture model in Figures 3.9a and 3.9b.

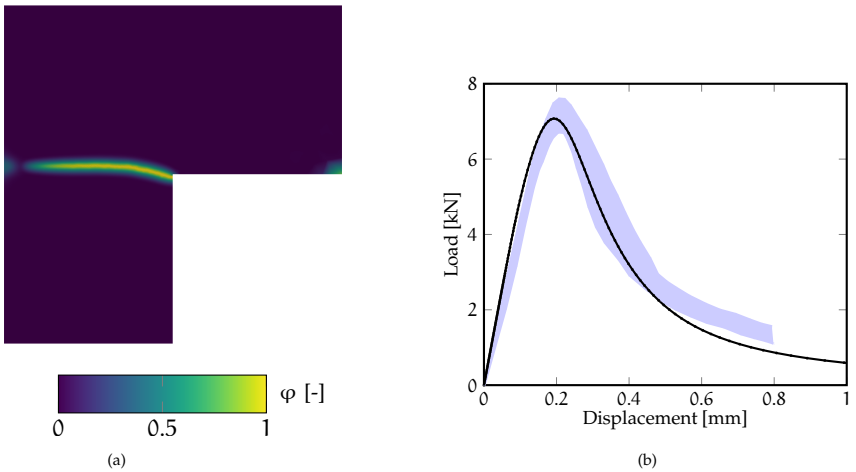

(a) (b)

Figure 4.5: Figure (a) presents the phase-field distribution in the L-panel specimen under shear at the final step of the analysis. Figure (b) presents the respective load-displacement curve obtained using the arc-length method. The experimental range from Winkler [153] is represented by the shaded region.

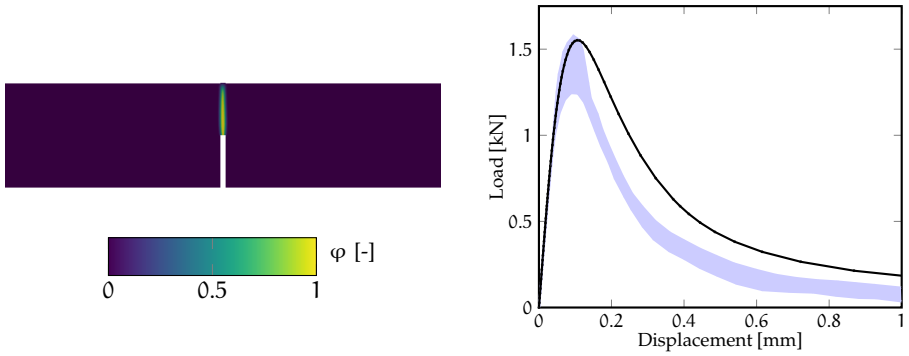

(a) (b)

Figure 4.6: Figure (a) presents the phase-field distribution in the three-point bending specimen at the final step of the analysis. Figure (b) presents the respective load-displacement curves obtained using the arc-length method. The experimental range from Rots [154] is represented by the shaded region.

Figure 4.5a presents the phase-field distribution at the final step of the analysis for Winkler L-panel specimen. The corresponding load-displacement curve is presented in Figure 4.5b. These results are obtained using $\beta = 500$, and are in agreement with the experimentally observed fracture pattern and the load-displacement curves (shaded region). One may also notice a similar agreement for the three-point bending experiments, whose phase-field distribution is presented in Figure 4.6a and load-displacement curve in Figure 4.6b.

Part III

COMPUTATIONAL MODELLING OF FRACTURES IN POROUS MEDIA

Development of numerical frameworks to model fractures in porous media (Research Objective 3).

5

HYDRAULIC FRACTURING

This chapter presents a phase-field fracture model for hydraulic fracturing and a novel time-increment based arc-length solution technique. The reader is first introduced to the state-of-the-art and current limitations in hydraulic fracture models in Section 5.1. This is followed by the phase-field hydraulic fracture model and the arc-length method in Sections 5.2 and 5.3, respectively. Finally, Section 5.4 concludes this chapter concludes with a set of numerical experiments and pertinent discussion.

5.1 STATE OF THE ART AND LIMITATIONS

Hydraulic fracturing (or fracking) is a process where a fluid (consisting of water, proppant and other chemical additives) is injected into wellbore(s) to extract petroleum and natural gas from underground shale reservoirs. Modelling the fracking process using the conventional finite element method on a fixed mesh is not possible. As such, Secchi, Simoni, and A. Schrefler introduced re-meshing techniques for modelling fracking in [160, 161]. Later, the eXtended Finite Element Method (XFEM) [15, 16] was adopted as it augments the space of shape functions with special enrichment functions capable of reproducing discontinuous and singular elastic fields associated with a fracture. The enrichment functions are dynamically incorporated into the model as the fracture propagates. The early developments of XFEM modelling of hydraulic fracturing was carried out by Gordeliy and Peirce [162–164]. Later studies involved the extension towards a three-dimensional framework [165], anisotropic modelling of the shale reservoir [166], interaction of new fractures with existing natural fractures [167], and investigations into the fracture/pore mass exchange [168] to cite a few. In an alternative approach, the Cohesive Zone Model (CZM) [12–14] was adopted in [169–171] to model hydraulic fracturing. Nevertheless, these discrete fracture modelling techniques (XFEM and CZM) require fracture tracking algorithm, re-meshing, and dynamic insertion of enriched shape functions/cohesive elements. For complex fracture topologies (branching, kinking and merging of fractures), the aforementioned requirements may be prohibitively tedious.

The phase-field fracture model [20–22] circumvents the tedious requirements of the discrete fracture models. As such, it has been adopted for a wide range of fracture problems, including hydraulic fracturing. The pioneering works in phase-field hydraulic fracture model was carried out by Mikelic, Wheeler, Wick, and Wollner [36, 38, 39, 172]. Thereafter, several variants [40, 41, 49, 173–178] have been proposed, largely differing in the degradation of the poroelastic energy, and delineation of the bulk reservoir and the fractured domains.

In the context of the degradation of the poroelastic energy (see Equation (2.33)), there is a lack of consensus w.r.t. the degradation of the fluid pressure term, $\frac{p^2}{2M}$. Zhou, Zhuang, and Rabczuk [176], and Heider and Sun [49] proposed that the phase-field based degradation be applied only on the solid skeleton. However, with this approach, the stress continuity across the fracture is not guaranteed for Biot coefficient not equal to one.

In addition to a suitable poroelastic energy definition, a proper representation of the fluid flow within the fracturing domain is necessary for obtaining the correct fluid pressure [173]. The fluid pressure plays a key role in driving solid skeleton deformation and the development (initiation and propagation) of the fracture(s) in a porous medium. In a porous medium, such as rock or soil, the fluid flow is laminar, both in the bulk reservoir and in the fractures. However, the flow type is different. In the bulk reservoir, the fluid permeates through the interconnected pores, and is represented by the Darcy's law. However, in a fracture, the fluid flow is idealized as a laminar flow between fixed parallel plates, adhering to a Poiseuille law. Therefore, it is important to delineate the bulk reservoir and the fractures in a computational domain. In discrete fracture models (e.g., XFEM [15, 16, 179], CZM [14]), the delineation is present in the model by construct. However, in phase-field fracture models, the fracture is represented by a localized band of finite width. Therefore, the delineation of the fracture from the bulk reservoir is rather heuristic, and is based on a threshold phase-field value [49, 176]. The phase-field based delineation of bulk reservoir and fracture domains has reached a common consensus. As such, it is adopted in this thesis.

Despite the aforementioned developments in phase-field hydraulic fracture models, a robust and computationally efficient solution strategy does not exist yet. Most phase-field hydraulic fracture simulations are either carried out using the alternate minimization method [21, 22] or the extrapolation-based Newton-Raphson method [34]. Although, both methods are robust due their convexification assumptions, they exhibit severe time step-size dependency. Moreover, the alternate minimization method is known to require thousands of iterations to converge during a fracture propagation step. This motivates the development of an alternative, robust and computationally efficient solution technique in the form of a novel arc-length method. The method is presented in Section 5.3, however, prior to that, the phase-field hydraulic fracture model is presented in Section 5.2.

5.2 PHASE-FIELD HYDRAULIC FRACTURING MODEL

The phase-field hydraulic fracture model consists of an energy functional (accounting for deformation of the skeleton and fracture at fixed pressure/water content) and a governing equation pertaining to the conservation of mass. The model is developed within a small strain framework. The relevant foundational concepts in phase-field fracture modelling and poromechanics are presented earlier in Section 2.2.1 and 2.3, respectively.

5.2.1 *The energy functional*

The poroelastic phase-field fracture energy functional is a combination of the linear elastic phase-field fracture energy functional (2.19) and the poroelastic energy functional (2.33). Assuming the presence of only one type of fluid, i.e., water in the pore space ($p = p_w$), the energy functional is stated as

$$\begin{aligned} E(\mathbf{u}, p_w, \varphi) = &\int_\Omega g(\varphi)\, \Psi^+(\boldsymbol{\epsilon}[\mathbf{u}])\, d\Omega + \int_\Omega \Psi^-(\boldsymbol{\epsilon}[\mathbf{u}])\, d\Omega \\ &- \int_\Omega \alpha\, p_w\, \boldsymbol{\nabla}\cdot\mathbf{u}\, d\Omega - \int_\Omega \frac{p_w^2}{2M}\, d\Omega - \int_{\Gamma_N^u} \mathbf{t}_p^u \cdot \mathbf{u}\, d\Gamma \\ &- \int_\Omega \mathbf{b}\cdot\mathbf{u}\, d\Omega + \int_\Omega \frac{G_c}{c_w}\left(\frac{w(\varphi)}{l} + l|\boldsymbol{\nabla}\varphi|^2\right) d\Omega. \end{aligned} \tag{5.1}$$

In the above energy functional, the strength and stiffness solid skeleton is reduced with a phase-field based degradation function $g(\varphi)$. The energetic term associated with the water pressure is assumed unaffected by the fracture, as such no degradation function is attached [49, 176]. You and Yoshioka [42] reported that such a construct guarantees stress continuity across a fracture only in case the Biot coefficient $\alpha = 1$. Therefore, in this chapter, all numerical experiments are conducted with $\alpha = 1$. Furthermore, the body force $\mathbf{b}$ (such as gravity) and external mechanical traction $\mathbf{t}_p^u$ are neglected, following the practice in hydraulic fracture modelling [36, 38, 39, 172]. With these modifications, the energy functional (5.1) attains the form

$$\begin{aligned} E(\mathbf{u}, p_w, \varphi) = &\int_\Omega g(\varphi)\, \Psi^+(\boldsymbol{\epsilon}[\mathbf{u}])\, d\Omega + \int_\Omega \Psi^-(\boldsymbol{\epsilon}[\mathbf{u}])\, d\Omega \\ &- \int_\Omega \alpha\, p_w\, \boldsymbol{\nabla}\cdot\mathbf{u}\, d\Omega - \int_\Omega \frac{p_w^2}{2M}\, d\Omega \\ &+ \int_\Omega \frac{G_c}{c_w}\left(\frac{w(\varphi)}{l} + l|\boldsymbol{\nabla}\varphi|^2\right) d\Omega. \end{aligned} \tag{5.2}$$

It is important to note that the water pressure p_w is obtained from the conservation of mass equation. As such, the first variation of the energy functional is carried out only w.r.t., the displacement $\mathbf{u}$ and the phase-field φ.

Remark 5. *The body force $\mathbf{b}$ (such as gravity) and external mechanical traction $\mathbf{t}_p^u$ may be retained in the energy functional (5.2) if generality is desired. However, for the benchmark problems addressed in this thesis, they are not required.*

5.2.2 *Conservation of mass*

The conservation of mass applies to the solid skeleton mass and the fluid (fluid and gas) mass. From the mathematical developments in Section 2.3.2, the conservation of solid skeleton mass in conjunction with that fluid mass yields the water transport equation (2.52), re-stated below,

$$\begin{aligned}&\left[(\alpha-n)C_s S_w^2 + nS_w C_w\right]\frac{\partial p_w}{\partial t} + (\alpha-n)C_s S_w S_g \frac{\partial p_g}{\partial t}\\ &+\left[(\alpha-n)C_s S_w(p_w-p_g)+n\right]\frac{\partial S_w}{\partial t} + \alpha S_w \frac{\partial \epsilon_{vol}}{\partial t}\\ &-\boldsymbol{\nabla}\cdot\left[k_{rw}\frac{k_i \mathbf{I}}{\mu_w}(\boldsymbol{\nabla} p_w - \rho_w \mathbf{g})\right] = 0.\end{aligned} \tag{5.3}$$

For a detailed derivation of the above equation, the reader is referred to the Section 2.3.2. It is observed that the water transport equation (5.3) presents a general case of partially saturated porous medium. However, in the case of hydraulic fracture, the pore space is assumed to be always fully saturated with water. This results in $S_w = k_{rw} = 1$ and $\frac{\partial S_w}{\partial t} = 0$. This eliminates the gas phase, i.e., $p_g = 0$ and $\frac{\partial p_g}{\partial t} = 0$. Furthermore, the effect of gravity in the Darcy's law is ignored. With these assumptions, the water transport equation (5.3) assumes the form

$$\underbrace{\left[(\alpha-n)C_s + nC_w\right]}_{\frac{1}{M}}\frac{\partial p_w}{\partial t} + \alpha\frac{\partial \epsilon_{vol}}{\partial t} - \boldsymbol{\nabla}\cdot\left[\underbrace{\frac{k_i \mathbf{I}}{\mu_w}}_{\mathbf{K}_{eff}}\boldsymbol{\nabla} p_w\right] = 0. \tag{5.4}$$

In the absence of fracture dependent coefficients, the above equation is suitable only for poroelasticity. In order to extend towards hydraulic fracture, fracture dependent coefficients are introduced in the subsequent part of this section. To that end, the bulk and fractured regions of any specimen are determined using a threshold phase-field, $\varphi = 0.8$. Poroelastic (constant) coefficients are used for the bulk region, i.e., $\varphi < 0.8$. In the fracturing region, i.e., $\varphi \geqslant 0.8$, the fracture dependent coefficients are introduced using an interpolation function. The interpolation function $h(\varphi, \epsilon_{vol}[\mathbf{u}])$ is defined as

$$h(\varphi, \epsilon_{vol}[\mathbf{u}]) = 25\,\mathscr{H}(\epsilon_{vol}[\mathbf{u}])\,\langle \varphi - 0.8\rangle_+^2, \tag{5.5}$$

where, the heaviside function $\mathscr{H}(\epsilon_{vol}[\mathbf{u}])$ is used as an indicator for open cracks. The interpolation function assumes a value zero at $\varphi = 0.8$ and reaches 1 for $\varphi = 1$. This allows defining any coefficient, say X, as

$$X = X_b + h(\varphi, \epsilon_{vol}[\mathbf{u}])\left(X_f - X_b\right), \tag{5.6}$$

where subscripts b and f indicate bulk and fracture, respectively.

Biot coefficient

The Biot coefficient α accounts for the interaction of the solid skeleton and the water pore pressure. In this chapter, α is set to 1, a choice made by Mikelić, Wheeler, and Wick [38] in their numerical experiments. However, it is important to note that Biot coefficient is formally expressed as

$$\alpha = 1 - C_s/C, \tag{5.7}$$

for linear isotropic material, with C_s and C as compressibility of the solid grains and porous medium, respectively [180].

Porosity

The porosity n in the water transport equation (5.4) refers to the initial porosity of the porous medium [112]. You and Yoshioka [42] proposed increasing the initial porosity n to 1 for a fully developed fracture $\varphi = 1$. However, one may argue that the changes in the porosity is already incorporated in the water transport equation (5.4) through the relation (2.42) (see Section 2.3.2. Based on this reasoning, the initial porosity is not tampered with in any of the numerical experiments.

Biot modulus

The Biot modulus of a linear elastic isotropic porous material is expressed as

$$\frac{1}{M} = (\alpha - n)C_s + nC_f. \tag{5.8}$$

Following the choice of constant Biot coefficient α and initial porosity n, the Biot modulus also remains constant for all numerical experiments in this chapter.

Permeability

The permeability matrix $\mathbf{K}_{eff}$ in the water transport equation (5.4) is constant, thereby ignoring possible enhancement due to fracturing of a porous medium. In order to introduce a permeability matrix that transitions from a intact material state to a fractured state, bulk permeability $\mathbf{K}_b$ and fracture permeability $\mathbf{K}_f$ are introduced.

The bulk isotropic permeability of an intact porous medium is stated as

$$\mathbf{K}_b = \frac{\kappa_i}{\mu_w}\mathbf{I}, \tag{5.9}$$

where, κ_i and μ_w represent the intrinsic permeability of the porous medium and the dynamic viscosity of water, respectively. Witherspoon et al. [181] proposed the isotropic fracture permeability $\mathbf{K}_f$ expression,

$$\mathbf{K}_f = \frac{w_f^2}{12}\mathbf{I}, \tag{5.10}$$

with fracture aperture w_f. For discrete fracture models like XFEM and CZM, the fracture aperture is obtained as a solution of the system of equations. However, for phase-field fracture model, the fracture is represented in a diffused (smeared) sense. As such, the fracture aperture is computed as a post-processing step from the solution fields (displacement $\mathbf{u}$ and phase-field φ). Miehe, Mauthe, and Teichtmeister [182] presented an approximation of the fracture aperture as

$$w_f := \langle h_{el}(1 + \mathbf{n}_\varphi \cdot \boldsymbol{\epsilon}[\mathbf{u}] \cdot \mathbf{n}_\varphi)\rangle_+, \quad \text{with} \quad \mathbf{n}_\varphi \approx \frac{\boldsymbol{\nabla}\varphi}{|\boldsymbol{\nabla}\varphi|} \tag{5.11}$$

and the characteristic element size h_{el}. However, Chukwudozie, Bourdin, and Yoshioka [183] reported two issues with the normal direction to the fracture $\mathbf{n}_\varphi$ computed using the gradient of the phase-field $\boldsymbol{\nabla}\varphi$. The gradient of the phase-field $\boldsymbol{\nabla}\varphi$ deviates from the normal direction at the tip of the fracture. Also, $\boldsymbol{\nabla}\varphi$ is not defined at fully developed fractures, i.e., $\varphi = 1$. Therefore, an alternative expression for $\mathbf{n}_\varphi$ is stated as

$$\mathbf{n}_\varphi \approx \frac{\mathbf{P}_{max}}{|\mathbf{P}_{max}|} \tag{5.12}$$

where, $\mathbf{P}_{max}$ is the eigenvector corresponding to the maximum eigenvalue of the strain tensor. Having obtained expressions for the bulk permeability $\mathbf{K}_b$ and the fracture permeability $\mathbf{K}_f$, the effective permeability $\mathbf{K}_{eff}$ is defined using the phase-field based interpolation function $h(\varphi, \epsilon_{vol})$ as

$$\mathbf{K}_{eff}(\varphi, \epsilon_{vol}[\mathbf{u}]) = \mathbf{K}_b + h(\varphi, \epsilon_{vol}[\mathbf{u}])\Big(\mathbf{K}_f - \mathbf{K}_b\Big). \tag{5.13}$$

Remark 6. *The computation of anisotropic fracture permeability may be carried out as*

$$\mathbf{K}_f = \frac{w_h^2}{12}\Big(\mathbf{I} - \mathbf{n}_\varphi \otimes \mathbf{n}_\varphi\Big). \tag{5.14}$$

However, in this chapter, the fracture permeability is assumed to be isotropic.

Darcy to Poiseuille flow transition in water transport equation

Incorporating fracture dependent permeability (5.13) in the water transport equation (5.4), one obtains

$$\underbrace{\Big[\big(\alpha - n\big)C_s + nC_w\Big]}_{\frac{1}{M}} \frac{\partial p_w}{\partial t} + \alpha \frac{\partial \epsilon_{vol}}{\partial t} - \boldsymbol{\nabla} \cdot \Big[\mathbf{K}_{eff}(\varphi, \epsilon_{vol})\boldsymbol{\nabla} p_w\Big] = 0. \tag{5.15}$$

The above equation allows a transition from a Darcy flow in the bulk intact material to a Poiseuille type flow in the diffused fracture region. Through simple mathematical derivation, one can deduce the recovery of the poroelastic water transport equation (5.4) upon closing of fracture ($\epsilon_{vol} < 0$).

5.2.3 *Variational equations*

The set of variational equations for the phase-field hydraulic fracture model is obtained through a two-fold process. First, the momentum balance and the phase-field evolution equations are obtained upon minimizing the energy functional (5.2) w.r.t., the vector-valued displacement $\mathbf{u}$ and the scalar-valued phase-field φ. Thereafter, the water transport variational equation is obtained through Backward Euler substitution of the time derivatives and a subsequent integration with a test function δp_w over the domain Ω. With appropriate test and trial spaces, and the fracture irreversibility constraint $\dot{\varphi} > 0$, the Variational Problem 10 is obtained. For brevity, the function arguments $(\varphi, \epsilon_{vol})$ in $\mathbf{K}_{eff}$ are dropped. Furthermore, the Cauchy stress $\boldsymbol{\sigma}^{\pm}[\mathbf{u}] = \frac{\partial \Psi^{\pm}[\mathbf{u}]}{\partial \boldsymbol{\epsilon}}$ is introduced.

The Variational Problem 10 entails a saddle point problem, requiring a careful choice of trial and test functions for the displacement and the water pressure to guarantee a unique solution continuously depending on the input data. The sufficient condition ensuring this uniqueness is established in the computational mechanics literature as the Ladyzhenskaya–Babuška–Brezzi (LBB) condition. In order to fulfill the LBB condition, quadratic trial and test functions are chosen for the displacement field, while the pressure field remains linear. In the discrete sense, such a choice is referred to as the Taylor and Hood element [184] following their contribution.

Variational Problem 10. *Find* $(\mathbf{u}, \varphi, p_w) \in \mathbb{U} \times \mathbb{P} \times \mathbb{Q}$ *such that*

$$E'(\mathbf{u}, p_w, \varphi; \delta\mathbf{u}) = \int_\Omega \Big(g(\varphi)\boldsymbol{\sigma}^+[\mathbf{u}] + \boldsymbol{\sigma}^-[\mathbf{u}] \Big) : \boldsymbol{\epsilon}[\delta\mathbf{u}] \, d\Omega - \int_\Omega \alpha \, p_w \mathbf{I} : \boldsymbol{\epsilon}[\delta\mathbf{u}] \, d\Omega = 0 \quad \forall \, \delta\mathbf{u} \in \mathbb{U}^0, \tag{5.16a}$$

$$E'(\mathbf{u}, p_w, \varphi; \hat{\varphi}) = \int_\Omega \left(g'(\varphi)\Psi^+(\boldsymbol{\epsilon}[\mathbf{u}]) + \frac{G_c}{c_w l} w'(\varphi) \right) (\hat{\varphi} - \varphi) \, d\Omega + \int_\Omega \frac{G_c l}{c_w} \boldsymbol{\nabla}\varphi \cdot \boldsymbol{\nabla}(\hat{\varphi} - \varphi) \, d\Omega \geqslant 0 \quad \forall \, \hat{\varphi} \in \mathbb{P}, \tag{5.16b}$$

$$\int_\Omega \left(\frac{1}{M} \frac{p_w - {}^n p_w}{\Delta t} + \alpha \frac{\epsilon_{vol} - {}^n \epsilon_{vol}}{\Delta t} \right) \delta p_w \, d\Omega + \int_\Omega \boldsymbol{\nabla}\delta p_w \, \mathbf{K}_{eff} \, \boldsymbol{\nabla} p_w \, d\Omega = \int_{\Gamma_N^{p_w}} q \, \delta p_w \, d\Gamma \quad \forall \, \delta p_w \in \mathbb{Q}, \tag{5.16c}$$

using pertinent time-dependent Dirichlet boundary conditions $\mathbf{u}^p$ *on* Γ_D^u, φ^p *on* Γ_D^φ *and* p_w^p *on* $\Gamma_D^{p_w}$, *and Neumann boundary condition* q *on* $\Gamma_N^{p_w}$. *The trial and test spaces are defined as*

$$\mathbb{U} = \{\mathbf{u} \in [H^2(\Omega)]^{\dim} | \mathbf{u} = \mathbf{u}^p \text{ on } \Gamma_D^u\}, \tag{5.17a}$$

$$\mathbb{P} = \{\varphi \in [H^2(\Omega)] | \varphi \geqslant {}^n\varphi | \varphi = \varphi^p \text{ on } \Gamma_D^\varphi\}, \tag{5.17b}$$

$$\mathbb{Q} = \{p_w \in H^1(\Omega) | p_w = p_w^p \text{ on } \Gamma_D^{p_w}\}, \tag{5.17c}$$

$$\mathbb{U}^0 = \{\mathbf{u} \in [H^2(\Omega)]^{\dim} | \mathbf{u} = \mathbf{0} \text{ on } \Gamma_D^u\}, \tag{5.17d}$$

$$\mathbb{Q}^0 = \{p_w \in H^1(\Omega) | p_w = 0 \text{ on } \Gamma_D^{p_w}\}. \tag{5.17e}$$

In (5.17b), the left superscript n *refers to the previous time-step.* ■

The fracture irreversibility constraint $\dot{\varphi} \geqslant 0$ manifests in the form of variational inequality phase-field evolution equation (5.16b) with a restricted trial/test space (5.17c) in the Variational Problem 10. However, the Finite Element Method (FEM) does not offer support in implementing such restrictive trial/test spaces. Therefore, the variational inequality is transformed in an equivalent equality using the history variable approach, proposed by Miehe, Hofacker, and Welschinger [37]. This results in an equality-based phase-field hydraulic fracture Variational Problem 11.

Variational Problem 11. *Find* $(\mathbf{u}, \varphi, p_w) \in \mathbb{U} \times \mathbb{P} \times \mathbb{Q}$ *such that*

$$E'(\mathbf{u}, p_w, \varphi; \delta\mathbf{u}) = \int_\Omega \Big(g(\varphi)\boldsymbol{\sigma}^+[\mathbf{u}] + \boldsymbol{\sigma}^-[\mathbf{u}]\Big) : \boldsymbol{\epsilon}[\delta\mathbf{u}]\, d\Omega - \int_\Omega \alpha\, p_w\, \mathbf{I} : \boldsymbol{\epsilon}[\delta\mathbf{u}]\, d\Omega = 0 \quad \forall\, \delta\mathbf{u} \in \mathbb{U}^0, \tag{5.18a}$$

$$E'(\mathbf{u}, p_w, \varphi; \delta\varphi) = \int_\Omega \left(g'(\varphi)\mathcal{H} + \frac{G_c}{c_w\, l} w'(\varphi)\right)\delta\varphi\, d\Omega + \int_\Omega \frac{G_c\, l}{c_w} \boldsymbol{\nabla}\varphi \cdot \boldsymbol{\nabla}\delta\varphi\, d\Omega = 0 \quad \forall\, \delta\varphi \in \mathbb{P}^0, \tag{5.18b}$$

$$\int_\Omega \Big(\frac{1}{M}\frac{p_w - {}^{n}p_w}{\Delta t} + \alpha \frac{\epsilon_{vol} - {}^{n}\epsilon_{vol}}{\Delta t}\Big)\delta p_w\, d\Omega + \int_\Omega \boldsymbol{\nabla}\delta p_w\, \mathbf{K}_{eff}\, \boldsymbol{\nabla} p_w\, d\Omega = \int_{\Gamma_N^{p_w}} q\, \delta p_w\, d\Gamma \quad \forall\, \delta p_w \in \mathbb{Q}, \tag{5.18c}$$

using pertinent time-dependent Dirichlet boundary conditions $\mathbf{u}^p$ *on* Γ_D^u *and* φ^p *on* Γ_D^φ*, and Neumann boundary condition* $\mathbf{t}_p^u$ *on* Γ_N^u*. The superscript* n *in the above equation indicates the previous (pseudo) time-step. the The trial and test spaces are defined as*

$$\mathbb{U} = \{\mathbf{u} \in [H^2(\Omega)]^{\dim} | \mathbf{u} = \mathbf{u}^p \text{ on } \Gamma_D^u\}, \tag{5.19a}$$
$$\mathbb{P} = \{\varphi \in [H^2(\Omega)] | \varphi = \varphi^p \text{ on } \Gamma_D^\varphi\}, \tag{5.19b}$$
$$\mathbb{Q} = \{p_w \in H^1(\Omega) | p_w = p_w^p \text{ on } \Gamma_D^{p_w}\}, \tag{5.19c}$$
$$\mathbb{U}^0 = \{\mathbf{u} \in [H^2(\Omega)]^{\dim} | \mathbf{u} = \mathbf{0} \text{ on } \Gamma_D^u\}, \tag{5.19d}$$
$$\mathbb{P}^0 = \{\varphi \in [H^2(\Omega)] | \varphi = 0 \text{ on } \Gamma_D^\varphi\}, \tag{5.19e}$$
$$\mathbb{Q}^0 = \{p_w \in H^1(\Omega) | p_w = 0 \text{ on } \Gamma_D^{p_w}\}. \tag{5.19f}$$

In (5.18b), the left superscript n *refers to the previous time-step. The history variable* $\mathcal{H}$ *in (5.18b) is defined in (2.24).* ■

The equality-based phase-field hydraulic fracture Variational Problem 11 with the history variable is pursued despite its variational inconsistency. The focus in this chapter is on solving the non-convex problem, instead of the variational inconsistency. It is established in Chapter 3 that the Newton-Raphson method performs poorly for the phase-field fracture model. Among the different techniques presented in Chapter 3, the arc-length method offers the best performance in terms of iterations required to achieve convergence. Therefore, in this chapter, a novel extension of the arc-length method for the phase-field hydraulic fracture model is pursued.

5.3 ARC-LENGTH METHOD

The arc-length method presented in Chapter 3 scales a unit external force with a scalar load factor. The load factor is an additional unknown in the system of equations[1], corresponding to a path-following/arc-length constraint equation (see Section 3.4.1). Such a construct is suitable for mechanically driven problems presented in Section 3.5, where the external load varies in the load-displacement space. However, hydraulic fracturing problems are typically driven by a constant external force (water flux, q in Variational Problem 11). As such, scaling operations are not required and the notion of a scalar load factor is rendered unusable. This motivates the need for an alternative design of the arc-length method, suitable for problems with constant external force.

A constant external force arc-length method is developed in this section. To that end, the notion of load factor is discarded. Instead, the time step-size Δt is considered as the additional unknown augmenting the solution space (displacement, water pressure and phase-field). Thereafter, a fracture energy-based arc-length constraint equation (see Section 3.4.1) is introduced to maintain the determinacy of the system of equations. The resulting problem statement is: find displacement, water pressure, phase-field and the time-step size for a constant flux and prescribed fracture energy. Following the approach in Section 3.4.2, the fracture energy constraint equation for the hydraulic fracturing problem is expressed as

$$g_{arc}(\mathbf{u}, \varphi) := \int_{\Omega} g'(\varphi)\, \Psi^{+}(\boldsymbol{\epsilon}[\mathbf{u}])\, \Delta\varphi \, d\Omega + \Delta s = 0, \tag{5.20}$$

with the arc-length Δs.

5.3.1 *Finite element discretized equations*

The finite element discretized equations for the phase-field hydraulic fracturing model are derived using the procedure explained in Section 2.1. To that end, the Variational Problem 11 in conjunction with the arc-length constraint 5.20 is identified as the point of departure from a continuous problem to a discrete one. The detailed derivation is skipped for brevity, instead the the phase-field hydraulic fracture Discrete Problem 9 is presented. Note that the terms *stiffness matrix* and *residual* are used for the Hessian and the Jacobian of the energy functional, respectively.

1 Finite element discretized equations in the context of this thesis.

Discrete Problem 9. *Compute the solution update vector* $\mathbf{s}_{k+1} = \{\Delta\tilde{\mathbf{u}}\,;\Delta\tilde{p}_w\,;\Delta\tilde{\varphi}\,;\Delta\tilde{t}\}$ *for the current iteration* $k+1$ *using*

$$\underbrace{\begin{bmatrix} \mathbf{K}^{uu} & \mathbf{K}^{up_w} & \mathbf{K}^{u\varphi} & \mathbf{K}^{u\Delta t} \\ \mathbf{K}^{p_w u} & \mathbf{K}^{p_w p_w} & \mathbf{K}^{p_w\varphi} & \mathbf{K}^{p_w\Delta t} \\ \mathbf{K}^{\varphi u} & \mathbf{K}^{\varphi p_w} & \mathbf{K}^{\varphi\varphi} & \mathbf{K}^{\varphi\Delta t} \\ \mathbf{K}^{\Delta t u} & \mathbf{K}^{\Delta t p_w} & \mathbf{K}^{\Delta t\varphi} & \mathbf{K}^{\Delta t\Delta t} \end{bmatrix}}_{\text{Stiffness matrix, } \mathbf{K}_k} \underbrace{\begin{Bmatrix} \Delta\tilde{\mathbf{u}} \\ \Delta\tilde{p}_w \\ \Delta\tilde{\varphi} \\ \Delta\tilde{t} \end{Bmatrix}}_{\mathbf{s}_{k+1}} = \underbrace{\begin{Bmatrix} \mathbf{0} \\ \mathbf{f}^{ext,p_w} \\ \mathbf{0} \\ 0 \end{Bmatrix} - \begin{Bmatrix} \mathbf{f}^{int,u} \\ \mathbf{f}^{int,p_w} \\ \mathbf{f}^{int,\varphi} \\ g_{arc} \end{Bmatrix}}_{\text{Residual, } \mathbf{r}_k}, \tag{5.21a}$$

and update the solution,

$$\begin{Bmatrix} \tilde{\mathbf{u}} \\ \tilde{p}_w \\ \tilde{\varphi} \\ \Delta t \end{Bmatrix}_{k+1} = \begin{Bmatrix} \tilde{\mathbf{u}} \\ \tilde{p}_w \\ \tilde{\varphi} \\ \Delta t \end{Bmatrix}_{k} + \begin{Bmatrix} \Delta\tilde{\mathbf{u}} \\ \Delta\tilde{p}_w \\ \Delta\tilde{\varphi} \\ \Delta\tilde{t} \end{Bmatrix}_{k+1}, \tag{5.21b}$$

until the norm of the residual is sufficiently small. The stiffness matrix components are given by,

$$\begin{aligned}
\mathbf{K}^{uu} &= \mathcal{A}\int_{\Omega_{el}} [\mathbf{B}^{u}]^{T}\left(\underbrace{g(\varphi)\frac{\partial\boldsymbol{\sigma}^{+}}{\partial\boldsymbol{\epsilon}} + \frac{\partial\boldsymbol{\sigma}^{-}}{\partial\boldsymbol{\epsilon}}}_{\mathbf{D}}\right)[\mathbf{B}^{u}]\,d\Omega, \\
\mathbf{K}^{u\varphi} &= \mathcal{A}\int_{\Omega_{el}} [\mathbf{B}^{u}]^{T}\left(g'(\varphi)\boldsymbol{\sigma}^{+}\right)[\mathbf{N}^{\varphi}]\,d\Omega, \\
\mathbf{K}^{up_w} &= \mathcal{A}\int_{\Omega_{el}} [\mathbf{B}^{u}]^{T}\left(-\alpha\mathbf{I}_{v}\right)[\mathbf{N}^{p_w}]\,d\Omega, \\
\mathbf{K}^{u\Delta t} &= \mathbf{0}, \\
\mathbf{K}^{p_w u} &= -\frac{1}{\Delta t}[\mathbf{K}^{up_w}]^{T}, \\
\mathbf{K}^{p_w p_w} &= \mathcal{A}\int_{\Omega_{el}} [\mathbf{B}^{p_w}]^{T}\,\mathbf{K}_{eff}\,[\mathbf{B}^{p_w}] \\
&\quad + [\mathbf{N}^{p_w}]^{T}\,\frac{1}{M}\,[\mathbf{N}^{p_w}]\,d\Omega, \\
\mathbf{K}^{p_w\varphi} &= \mathcal{A}\int_{\Omega_{el}} [\mathbf{B}^{p_w}]^{T}\,\frac{\partial\mathbf{K}_{eff}}{\partial\varphi}\,[\mathbf{N}^{\varphi}] \\
&\quad + [\mathbf{N}^{p_w}]^{T}\,\frac{\partial(1/M)}{\partial\varphi}\left(\frac{p_w - {}^{n}p_w}{\Delta t}\right)[\mathbf{N}^{\varphi}] \\
&\quad + [\mathbf{N}^{p_w}]^{T}\,\frac{\partial\alpha}{\partial\varphi}\left(\frac{\epsilon_{vol} - {}^{n}\epsilon_{vol}}{\Delta t}\right)[\mathbf{N}^{\varphi}]\,d\Omega, \\
\mathbf{K}^{p_w\Delta t} &= -\mathcal{A}\int_{\Omega_{el}} [\mathbf{N}^{p_w}]^{T}\,\frac{1}{M}\left(\frac{p_w - {}^{n}p_w}{\Delta t^{2}}\right)
\end{aligned} \tag{5.21c}$$

Discrete Problem 9 (continued)

$$
\begin{aligned}
&- [\mathbf{N}^{p_w}]^T \, \alpha \Big(\frac{\epsilon_{vol} - {}^n\epsilon_{vol}}{\Delta t^2} \Big) \, d\Omega, \\
\mathbf{K}^{\varphi \mathbf{u}} &= [\mathbf{K}^{\mathbf{u}\varphi}]^T \quad \textit{if} \;\; \dot{\mathcal{H}} > 0, \;\; \textit{else} \;\; \mathbf{0}, \\
\mathbf{K}^{\varphi p_w} &= \mathbf{0}, \\
\mathbf{K}^{\varphi\varphi} &= \mathcal{A} \int_{\Omega_{el}} [\mathbf{B}^{\varphi}]^T \left(\frac{G_c \, l}{c_w} \right) [\mathbf{B}^{\varphi}] \\
&\quad + [\mathbf{N}^{\varphi}]^T \left(\frac{G_c}{c_w l} w''(\varphi) + g''(\varphi) \frac{\partial \mathcal{H}}{\partial \boldsymbol{\epsilon}} \right) [\mathbf{N}^{\varphi}] \, d\Omega, \\
\mathbf{K}^{\varphi \Delta t} &= \mathbf{0}, \\
\mathbf{K}^{\Delta t \mathbf{u}} &= \mathcal{A} \int_{\Omega_{el}} g'(\varphi) \Delta\varphi \, \boldsymbol{\sigma}^+ \, [\mathbf{B}^{\mathbf{u}}] \, d\Omega, \\
\mathbf{K}^{\Delta t \varphi} &= \mathcal{A} \int_{\Omega_{el}} [\mathbf{N}^{\varphi}] \Big(g''(\varphi) \, \Delta\varphi + g'(\varphi) \Big) \Psi^+ \, d\Omega, \\
\mathbf{K}^{\Delta t p_w} &= \mathbf{K}^{\Delta t \Delta t} = 0,
\end{aligned}
$$

and the internal force vector components are computed as

$$
\begin{aligned}
\mathbf{f}^{ext,p_w} &= \mathcal{A} \int_{\Gamma_{N,el}} [\mathbf{N}^{p_w}]^T \, q \; d\Gamma, \\
\mathbf{f}^{int,\mathbf{u}} &= \mathcal{A} \int_{\Omega_{el}} [\mathbf{B}^{\mathbf{u}}]^T \left(g(\varphi) \boldsymbol{\sigma}^+ + \boldsymbol{\sigma}^- - \alpha \, p_w \mathbf{I}_v \right) d\Omega, \\
\mathbf{f}^{int,\varphi} &= \mathcal{A} \int_{\Omega_{el}} [\mathbf{B}^{\varphi}]^T \, \frac{G_c \, l}{c_w} \boldsymbol{\nabla} \varphi \\
&\quad + [\mathbf{N}^{\varphi}]^T \left(g'(\varphi) \mathcal{H} + \frac{G_c}{c_w \, l} w'(\varphi) \right) d\Omega, \qquad (5.21d) \\
\mathbf{f}^{int,p_w} &= \mathcal{A} \int_{\Omega_{el}} [\mathbf{B}^{p_w}]^T \left(\mathbf{K}_{eff} \boldsymbol{\nabla} p_w \right) \\
&\quad + [\mathbf{N}^{p_w}]^T \left(\frac{1}{M} \frac{p_w - {}^n p_w}{\Delta t} + \alpha \frac{\epsilon_{vol} - {}^n\epsilon_{vol}}{\Delta t} \right) d\Omega, \\
g_{arc} &= \mathcal{A} \int_{\Omega_{el}} \Big(g'(\varphi) \Delta\varphi \, \Psi^+ \Big) \, d\Omega + \Delta s.
\end{aligned}
$$

Note that $\mathcal{A}$ is an assembly operator that maps element contributions to their global counterparts. Furthermore, $\mathbf{I}_v$ is the Voigt representation of the identity matrix, the left superscript n refers to the previous time step, and $\mathscr{H}$ is the heaviside function. The material stiffness matrix $\mathbf{D}$ depends on the chosen strain energy density split (see Table 2.4). The history variable $\mathcal{H}$ is defined in (2.24). ■

5.3.2 *Implementation caveats*

The implementation caveats pertaining to a singular stiffness matrix (Hessian), switching between incremental iterative approach and the arc-length method, and adaptive modification of the arc-length Δs are presented in Section 3.4.3. The reader is referred to therein for more details.

5.4 NUMERICAL EXPERIMENTS

In this section, numerical experiments are carried out on three benchmark hydraulic fracturing problems, previously studied by Mikelić, Wheeler, and Wick [38]. For all problems, the geometric specimen is a square (2×2 [m^2]) embedded with varying number of initial fracture(s), as shown in Figure 5.1.

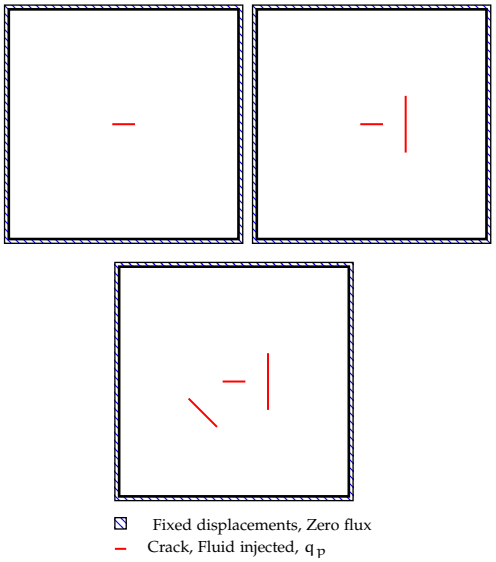

Figure 5.1: Specimen with single, double and triple initial fractures (SNF, DNF, TNF)

Parameters	**Value** [Units]
Fracture Model	AT2
Energy Split	Spectral [37]
E_0	1 [GPa]
ν	0.2 [-]
G_c	1 [N/m]
l	5e-2 [m]
α	1.0 [-]
n	0.3 [-]
$k_{i,b}$	1e-12 [m^2]
μ_f	1e-3 [Pa s]
K_s	1 [GPa]
K_f	40 [MPa]
q^p	0.01 [m/s]
`optIter`	10 [-]

Table 5.1: Model parameters

The three benchmark hydraulic fracturing problems are designed to exhibit an increasing complexity of the fracture topology. The Single Natural Fracture (SNF) specimen contains a single initial fracture, 0.4 [m] in length and is located midway along the height. On injecting water into the fracture, the fracture is expected to propagate horizontally. The Double Natural Fracture (DNF) specimen adds a vertical initial fracture of length 1 [m], at an x-offset 0.6 [m] from the centre of the specimen. A fracture merging event is expected upon injection of water in the existing fractures. Finally, the Triple Natural Fracture (TNF) adds an inclined fracture to the DNF specimen. The newly introduced fracture is a line segment from coordinates (-0.8,-0.3) to (-0.3,-0.8) assuming the axes origin placed at the centre of the specimen. The injection of water into the existing fractures would lead to two competing fracture merging events. The SNF, DNF and TNF specimens share the same model parameters, presented in Table 5.1.

The objective of the numerical experiments of the SNF, DNF and TNF hydraulic fracturing problems is two-fold. First, the problems are simulated using the arc-length method described in Section 5.3 with a fixed iteration terminating tolerance 10^{-4}. The fracture topology and pressure distribution is then reported along the observed fluid lag phenomenon. Thereafter, the efficiency of the arc-length method is investigated for the same problems using different tolerances.

Furthermore, contrary to the test and trial spaces established in the Variational Problem 11, the SNF, DNF and TNF specimens are discretized with 3-noded constant strain elements for computational efficiency. This choice is justified in Appendix A, where a comparison is carried out with results obtained using Taylor and Hood elements [184].

5.4.1 *Benchmark problems*

The numerical experiments on the SNF, DNF and TNF specimens are conducted using the arc-length method described in Section 5.3. The iterative procedure in every step is terminated when the error defined as the ratio of the norm of the residual in the current iteration to that of the first iteration is less than 10^{-4}. Furthermore, the linear problem in every iteration is solved using the shared memory Pardiso solver from Intel's oneAPI Math Kernel Library [64].

The phase-field fracture topology in the SNF specimen presented in Figure 5.2 for different times ($t = 0.01$, 0.1 and 0.2 [s]) during the analysis. The fracture topology is similar to that reported by Mikelić, Wheeler, and Wick [38]. The fracture propagation occurs as mode I phenomenon[2], a consequence of choosing the spectral decomposition [37] of the strain energy density. Although the specimen is not loaded mechanically, the constant rate of influx results in tensile stress development at the fracture tips. Beyond a certain critical stress, the initial fracture starts to propagate. This is evident from the fracture topology observed at $t = 0.1$ and 0.2 in Figures 5.2b and 5.2c.

The water pressure in the SNF specimen is presented in Figure 5.3 for the aforementioned times ($t = 0.01$, 0.1 and 0.2 [s]) during the analysis. The pressure is uniform in the bulk intact material[3]. In the fracturing region, the water pressure localizes with higher values compared to that observed in the bulk intact material. The localization of pressure is attributed to the increased in permeability in the fracturing region, computed using Witherspoon et al.'s relation (5.10) [181].

A careful look into Figure 5.3 reveals a negative water pressure development at the fracture tips. For more clarity, the water pressure along the fracture is presented in Figure 5.4. Secchi and Schrefler [161] describes this phenomenon as 'fluid lag', which arises due to a high fracture propagation velocity for a given permeability. In such a scenario, the water is not able

2 Mode I fracture is also referred to as the opening mode.

3 Bulk intact material corresponds to region with phase-field $\varphi \approx 0$.

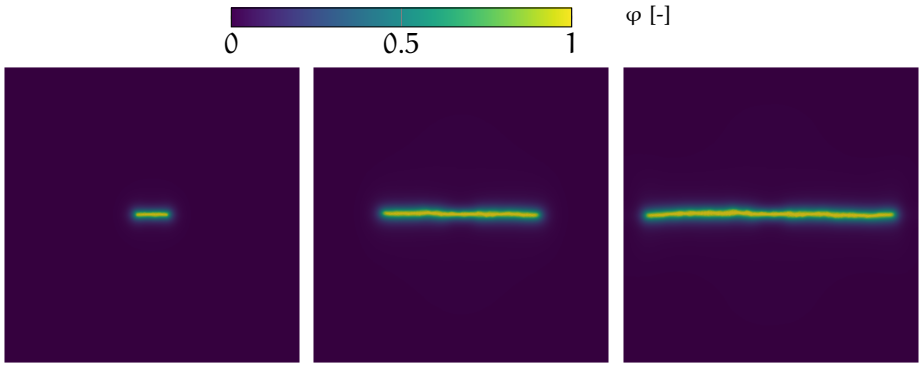

(a) t = 0.01 [s] (b) t = 0.1 [s] (c) t = 0.2 [s]

Figure 5.2: Figures (a-c) present the distribution of the phase-field variable at the different times during the analysis of the Single Natural Fracture (SNF) specimen.

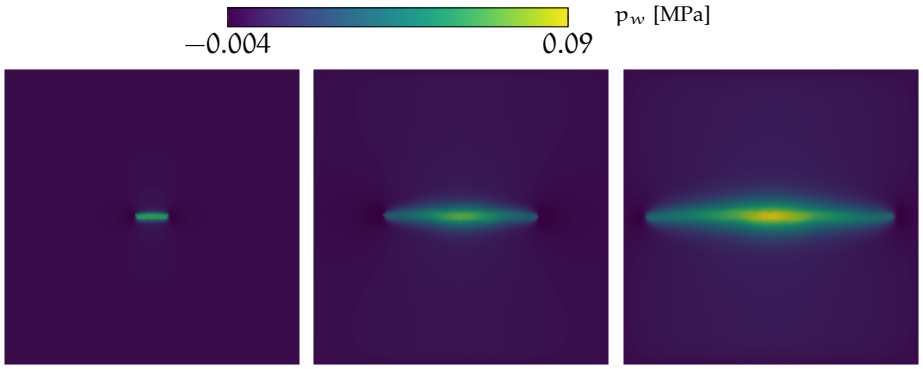

(a) t = 0.01 [s] (b) t = 0.1 [s] (c) t = 0.2 [s]

Figure 5.3: Figures (a-c) present the distribution of the water pressure at the different times during the analysis of the Single Natural Fracture (SNF) specimen.

to flow quickly enough to occupy the fracture space. Investigations into the fluid lag phenomenon is beyond the scope of this thesis. The reader is referred to Detournay and Garagash [185], instead.

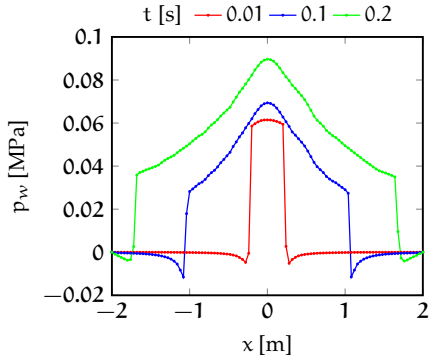

Figure 5.4: Figure presents the water pressure profile in the Single Natural Fracture (SNF) specimen along the fracture at different times (t = 0.01, 0.1 and 0.2 [s]).

Figure 5.5 presents the phase-field fracture topology observed at different times (t = 0.01, 0.026 and 0.044 [s]) during the hydraulic fracturing analysis. The fracture topology is similar to that reported by Mikelić, Wheeler, and

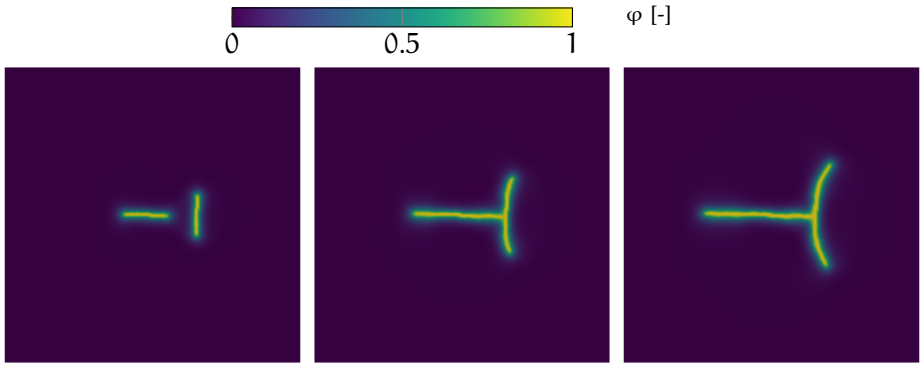

(a) t = 0.01 [s] (b) t = 0.026 [s] (c) t = 0.044 [s]

Figure 5.5: Figures (a-c) present the distribution of the phase-field variable at the different times during the analysis of the Double Natural Fracture (DNF) specimen.

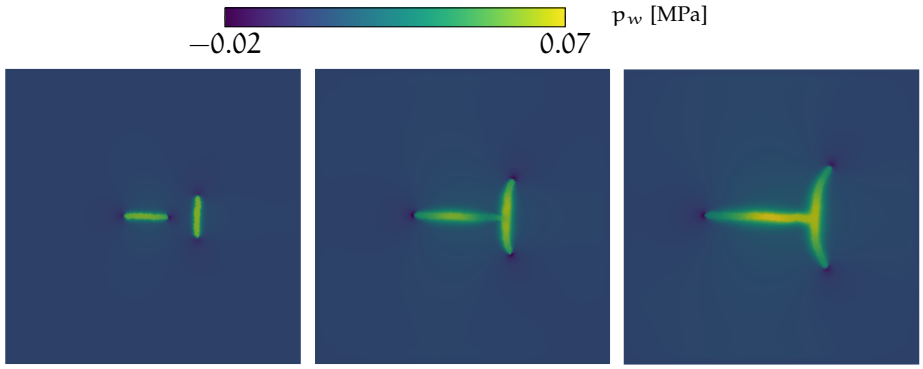

(a) t = 0.01 [s] (b) t = 0.026 [s] (c) t = 0.044 [s]

Figure 5.6: Figures (a-c) present the distribution of the water pressure at the different times during the analysis of the Double Natural Fracture (DNF) specimen.

Wick [38]. Similar to the SNF specimen, the fracture propagation occurs as mode I phenomenon, a consequence of choosing the spectral decomposition [37] of the strain energy density. However, DNF specimen exhibits a comparatively complex fracture merging behaviour. The arc-length method is able to capture this unstable fracture growth irrespective of the chosen iteration terminating tolerance. Furthermore, the water pressure distribution is presented in Figure 5.6. Similar to the SNF specimen, the fluid lag phenomenon at the fracture tips as well as the localization of water pressure are observed. Both observations are discussed in the context of the SNF specimen, hence not repeated here.

Figure 5.7 presents the phase-field fracture topology at different times ($t = 0.01$, 0.026 and 0.044 [s]) during the hydraulic fracturing analysis of the TNF specimen. Unlike the SNF and DNF specimens, two fracture merging events are observed. They are competing mechanisms from an energy minimization perspective. The first fracture merging event occurs at $t = 0.026$ seconds, when the initial horizontal fracture elongates and reaches the vertical fracture. Thereafter, the horizontal fracture follows a curvilinear path to merge with the inclined fracture at $t = 0.044$ second. Independent of the chosen iteration terminating tolerance, the same fracture topology

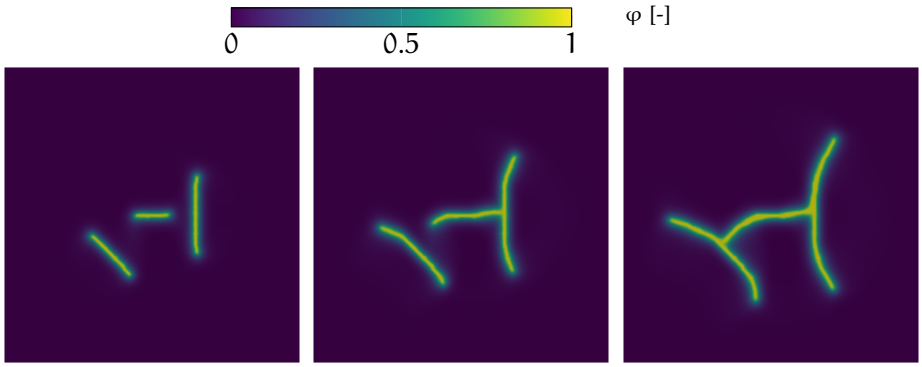

(a) t = 0.01 [s] (b) t = 0.026 [s] (c) t = 0.044 [s]

Figure 5.7: Figures (a-c) present the distribution of the phase-field variable at the different times during the analysis of the Triple Natural Fracture (TNF) specimen.

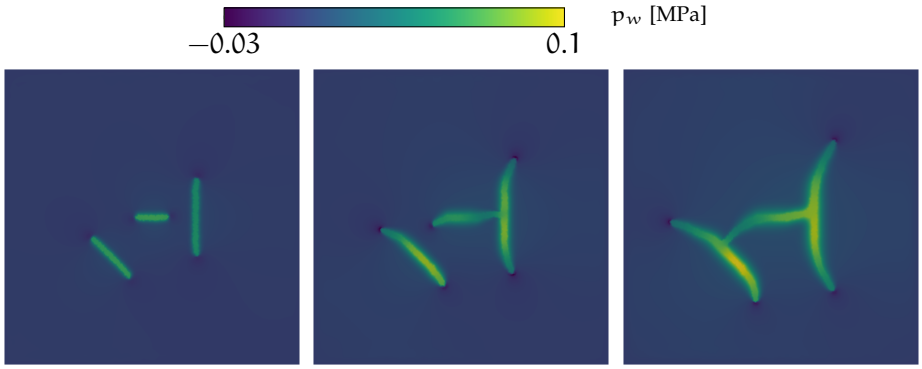

(a) t = 0.01 [s] (b) t = 0.026 [s] (c) t = 0.044 [s]

Figure 5.8: Figures (a-c) present the distribution of the water pressure at the different times during the analysis of the Triple Natural Fracture (TNF) specimen.

is predicted by the arc-length method. Furthermore, the water pressure distribution is presented in Figure 5.8. The fluid lag phenomenon and the pressure localization are observed, similar to the SNF and DNF specimens. The reason behind both observations is discussed earlier in context of the SNF specimen.

5.4.2 *Computational efficiency*

This section presents a study on the computational efficiency of the arc-length method, presented earlier in this chapter. The total and average number of iterations required to achieve convergence as well as the CPU time are considered as efficiency measures. The iteration terminating tolerances are varied as 10^{-4}, 10^{-6} and 10^{-8}. The simulations are carried out on a Dell Latitude 7490 laptop. Five cores are utilized on Intel(R) Core(TM) i7-8650U processors for multi-threaded assembly of the stiffness matrix and the force vectors. The linear problem in every iteration is solved using the shared memory Pardiso solver from Intel's oneAPI Math Kernel Library [64].

Table 5.2 presents the efficiency measures obtained for the SNF, DNF and TNF specimens. The total number of iterations as well as the average iterations are reasonable given the complexity of the problems and the non-convex nature of the phase-field fracture model. As expected, these measures and consequently the CPU time for the simulation increases with the strictness of the iteration terminating tolerances. One may also notice the increasing trend in the number of steps required to reach the same final simulated time. The reason for this behaviour is the fixed optimal number of iterations `optIter`, set to 10 and maximum number of iterations allowed to 25. With stricter tolerance, more iterations are required to achieve convergence in a step. Consequently, the arc-length estimated to the next step using (3.24) is smaller. This results in a higher number of steps required to reach the same final simulated time.

Specimen (uDOFs)	tol	Steps	Total Iters.	Avg. Iters.	CPU time [s]
SNF (28977)	10^{-4}	146	759	5.20	1925.0
	10^{-6}	128	980	7.65	3379.0
	10^{-8}	158	1408	8.91	11150.0
DNF (87028)	10^{-4}	56	342	6.11	2022.0
	10^{-6}	73	562	7.70	3074.0
	10^{-8}	151	1280	8.48	19640.0
TNF (86118)	10^{-4}	67	437	6.52	3022.0
	10^{-6}	117	857	7.32	6060.0
	10^{-8}	275	2012	7.32	35427.0

Table 5.2: Table presents the total numbers of steps and iterations, average iterations and CPU time (in seconds) for the SNF, DNF, TNF specimens simulated using the arc-length method with varying iteration terminating tolerances. uDOFs is an abbreviation for unconstrained Degrees of Freedom.

Furthermore, it is important to note that the arc-length method has been implemented using the Sherman-Morisson formula [156], thus requiring two linear solves for each iteration. Further reduction in the CPU time may be achieved upon using a linear solver accommodating multiple right-hand sides.

6

SOIL DESICCATION CRACKING

This chapter presents a phase-field fracture model for desiccation cracking in clayey soil. The reader is first introduced to the early developments, the state-of-the-art and limitations in soil desiccation modelling in Section 6.1. This is followed by the phase-field soil desiccation fracture model in Section 6.2, where a novel energy functional is developed. Finally, Section 6.3 concludes this chapter with a set of numerical experiments conducted using monolithic solution techniques from Chapter 3 and presents the relevant discussion.

6.1 STATE OF THE ART AND LIMITATIONS

Desiccation cracking of soil is an ubiquitous complex natural phenomenon observed in near-surface earth soils. The cracking is driven by the loss of soil moisture content, and subsequent inhomogeneous shrinkage. The inhomogeneous shrinkage induces tensile stresses in the soil, resulting in crack formation once the tensile strength is exceeded [186, 187]. As explained in Chapter 1, an in-depth understanding of the desiccation phenomenon is of paramount importance to several disciplines such as agricultural engineering, mining and resource engineering, geotechnical engineering, geo-environmental engineering, transport engineering, and soil science. Experimental investigations aimed at understanding the desiccation cracking phenomenon commenced as early as 1917. Kindle [188] carried out drying experiments on clay soil samples, and concluded that soil composition and tenacity '*very materially*' affects the crack spacing. Corte and Higashi [189] demonstrated the influence of sample thickness on the crack patterns and crack spacing based on indoor experiments on laboratory-made samples. Later studies established the role of several other factors, such as temperature [186], relative humidity [190], vegetation cover [191], mineral composition [192], salt content [193, 194], wetting and drying cycles [195, 196], to cite a few. The aforementioned factors and their interplay make desiccation cracking a complex multiphysics problem. However, in computational modelling of soil desiccation cracking not all factors are taken into account at once.

The computational modelling of desiccation cracking began with the Linear Elastic Fracture Mechanics (LEFM) [10, 11] based model, introduced by Lachenbruch [43]. Later, Morris, Graham, and Williams [197] adopted LEFM to propose an analytical relation for crack depth. Konrad and Ayad [198] also adopted the LEFM approach to obtain crack spacing, however, their model was unable to predict the crack spacing observed in the field experiments. The applicability of the LEFM approach was challenged by Amarasiri and Kodikara [199]. Their argument was that the LEFM assump-

tion of infinite stress at the crack tip is not realistic for soils exhibiting a limited tensile strength and display significant plastic behavior around the crack process zone. Instead of LEFM, the use of Cohesive Zone Model (CZM) was proposed. In a subsequent work, Amarasiri, Costa, and Kodikara [200] presented the CZM relevant material properties for the Werribee clay, Australia. Thereafter, the numerical modelling of desiccation cracking was carried out in [45–47] using the *'distinct element method'* [201] on a range of specimens, including both rectangular and annular shapes[1]. The distinct element method models the soil sample as an assembly of blocks separated by deformable planes. This limits the method to cases where the material and fracture topology is simple (for instance, homogeneous material exhibiting a straight crack). In an alternative approach, Pouya et al. [202] adopted the CZM within the Finite Element Method (FEM) framework for modelling desiccation cracking. However, discrete fracture modelling techniques (e.g, CZM [12–14], XFEM [15, 65, 179] or Mesh fragmentation methods [203]) require either *a priori* knowledge of the crack path or crack tracking algorithms and dynamic insertion of enriched shape functions/cohesive elements. For complex fracture topologies (branching, kinking and merging of fractures), *a priori* knowledge of crack path is not available and crack tracking algorithms may be prohibitively tedious. This has led to shift in crack modelling techniques from discrete models to smeared/diffused models [28].

The phase-field fracture model, pioneered by Francfort and Marigo [20] is a smeared crack/fracture modelling technique that has grown in popularity over the past two decades. The model circumvents the need for *a priori* knowledge of the crack path, tedious crack tracking algorithms, and *ad hoc* fracture criterion associated with the discrete models. As such, it has been widely adopted for many engineering applications, including desiccation cracking.

Cajuhi, Sanavia, and De Lorenzis [48] developed the *first*[2] phase-field fracture model for desiccation cracking of clayey soil. Using the mixture theory [111], the soil was modelled as a biphasic continua[3] undergoing an isothermal moisture loss. The pertinent system of equations followed from the extension of the LEFM phase-field fracture model (see Variational Problem 3 in Chapter 2) towards partially saturated porous media, and incorporating a water transport equation (similar to (2.52)). Hydro-mechanical coupling was incorporated in the form of gravimetric water content dependent elastic modulus and tensile strength. The corresponding phenomenological relations were adopted from Stirling [204]. The resulting model was able to predict the desiccation cracks experimentally observed by Peron et al. [205]. However, the numerical experiments demonstrated a nearly uniform suction distribution (see Figure 8 in [48]), a consequence of using constant coefficients in the water transport equation. From the perspective of the

1 Annular specimens are used for restrained ring tests.
2 To the author's knowledge
3 A biphasic soil continua comprises of solid grains and pore water.

physically observed reality, one may argue that desiccation cracks create additional surfaces which aids the loss of the soil moisture content. Consequently, the suction in the cracks is expected to be higher than the intact material. Furthermore, in the numerical experiments, Cajuhi, Sanavia, and De Lorenzis [48] adopted an explicit staggered solution technique, limiting the maximum number of staggered iterations to 10 [206]. Based on the experience of the author of this thesis and numerical experiments conducted by Kristensen and Martínez-Pañeda [85], 10 staggered iterations are not sufficient to obtain an *acceptable*[4] converged solution during the critical stages of fracture initiation and propagation.

In a later development, Heider and Sun [49] extended the fidelity of Cajuhi, Sanavia, and De Lorenzis's phase-field desiccation cracking model [48]. The soil was modelled as a triphasic continua[5] and fracture dependent permeability was integrated using an anisotropic variant of Witherspoon et al.'s cubic law [181]. Furthermore, postulating the rupture of water bridges between the soil micro-granulates during desiccation cracking, the suction was incorporated in the fracture driving energy. This reasoning is supported by Shin and Santamarina's experimental studies [207], where the authors reported fracture initiation due to rupture of the water bridges. The fracture occurred locally at tips of the flaws while the soil remained close to full saturation. Further experimental evidence of the role of suction in the fracturing process was presented by Kodikara and Costa [208]. Therein, the authors observed the fracturing phenomenon despite the soil specimen undergoing compressive stresses. Similar to Cajuhi, Sanavia, and De Lorenzis's model [48], Heider and Sun's desiccation cracking model [49] was able to qualitatively predict the cracks observed by Peron et al. [205]. However, unlike the former, the latter model demonstrates increased suction in the cracks, a consequence of adopting a fracture dependent permeability relation. Despite the improvements in fidelity, Heider and Sun's desiccation cracking model [49] lacks variational consistency. The set of variational equations was not derived from an energy functional, rather postulated as strong form equations. The loss of variational consistency follows from using a volumetric-deviatoric strain energy density decomposition (Amor, Marigo, and Maurini's decomposition in Table 2.4) in conjunction with a smooth Rankine stress-based fracture energy definition. Moreover, the numerical experiments were conducted using the staggered solution technique, adopting an iteration terminating tolerance of $2 \cdot 10^{-3}$ for the norm of the phase-field increments. In each block problem, the Newton-Raphson method was used with the maximum number of iterations set to 40. The explicit limit on the Newton-Raphson iterations and the coarse tolerance on the phase-field increments does not guarantee an acceptable converged solution. In such

4 Acceptability of a numerical solution is problem dependent. In this thesis, an acceptable solution is one when a residual or solution-based iteration terminating tolerance of 10^{-3} is met.

5 A triphasic soil continua comprises of solid grains, pore water and air.

a scenario, the numerical solution exhibits an *'artificial ductility*[6]*'* due to accumulation of errors from the previous steps in the analysis.

The early developments in phase-field desiccation cracking models [48, 49] shows the lack of consensus in the formulation of the strain energy density functional. Recently, Luo, Sanavia, and De Lorenzis [50] addressed this gap. The authors proposed two families of desiccation cracking models, based on Amor, Marigo, and Maurini's volumetric-deviatoric decomposition [72] of the effective strain and total strain[7] energy densities, respectively. Through analytical studies, the total strain variant was shown to exhibit a mixed mode (both I and II) fracturing phenomenon, while the effective strain variant is limited to mode II. Furthermore, the authors presented the inability of Miehe, Hofacker, and Welschinger's spectral decomposition approach [37] in simulating desiccation cracking. Only for the total strain based energy functional, a critical pore water pressure exists, which induces localization of the phase-field. Luo, Sanavia, and De Lorenzis's study [50] provides a rigorous assessment of the energy functional constructs for phase-field desiccation cracking model, w.r.t. fracture modes, homogeneous and bifurcated solutions.

The phase-field desiccation cracking models developed so far [48–51], consider clayey soils as a brittle material. This modelling choice is not yet supported by experimental investigations for clayey soil close to full saturation. On the contrary, Amarasiri, Costa, and Kodikara [200] presented experimental evidence of quasi-brittle behaviour of clayey soil and determined cohesive zone model properties adopting a linear softening law. Barani, Mosallanejad, and Sadrnejad [209] performed a similar study, albeit with bilinear and trilinear softening laws. In another study, Lakshmikantha, Prat, and Ledesma [210] obtained the length of the fracture process zone in clayey soils in the range 20 to 500 millimeters. As such, there is a need to develop and investigate quasi-brittle phase-field fracture models [2] in the context of desiccation cracking of clayey soil.

Another aspect, still elusive to the phase-field desiccation cracking models, is the development of robust and computationally efficient solution techniques. The studies [48–51] carried out so far, have adopted the staggered solution technique. The development and assessment of monolithic solution techniques for phase-field desiccation cracking still remains an open research question.

In this chapter, a novel unified phase-field desiccation cracking model is developed, capable of exhibiting both brittle and quasi-brittle fracturing phenomenon. To this end, Wu's unified phase-field model [2] is adopted. The fracture driving energy is assumed to contain the effective (drained) solid skeleton strain energy as well as a part of water pressure energetic term affecting the solid skeleton. This approach may be considered as a

6 Artificial ductility due to the staggered solution technique delays the fracture propagation. See Figure 4 in Kristensen and Martínez-Pañeda [85], where the delayed fracture propagation over-estimates the specimen displacement at failure.

7 Total strain is defined as, $\boldsymbol{\epsilon}_{tot} = \boldsymbol{\epsilon} - \frac{p_w}{3K}\mathbf{I}$. Here, p_w is the water pressure and K represents bulk modulus of the porous medium.

midway proposition with the effective and total strain based models as extremities. Furthermore, motivated by fidelity enhancements in [49], the intrinsic permeability is computed using Witherspoon et al.'s cubic law [181] in the fractured material zones. Finally, the numerical experiments are carried out using the monolithic solution techniques discussed earlier in this thesis (see Chapter 3). This facilitates an investigative study of the efficacy of these techniques in the context of soil desiccation cracking, a multiphysics problem.

6.2 PHASE-FIELD DESICCATION CRACKING MODEL

The phase-field desiccation cracking model consists of an energy functional (accounting for deformation of the skeleton and fracture at fixed pressure/water content) and a governing equation pertaining to the conservation of solid and water mass. The model is developed within a small strain framework. Unlike the hydraulic fracturing model developed in Chapter 5, the phase-field desiccation cracking model accounts for variable saturation. The relevant foundational concepts in phase-field fracture modelling and poro-mechanics are presented earlier in Section 2.2.1 and 2.3.

6.2.1 *The energy functional(s)*

The poroelastic phase-field fracture energy functional is a combination of the linear elastic phase-field fracture energy functional (2.19) and the poroelastic energy functional (2.33). Assuming the presence of only one type of fluid, i.e., water in the pore space with variable saturation S_w ($p := S_w\, p_w$), an energy functional is constructed as

$$\begin{aligned} E_1(\mathbf{u}, p_w, \varphi) = &\int_\Omega g(\varphi)\, \Psi^+(\boldsymbol{\epsilon}[\mathbf{u}])\, d\Omega + \int_\Omega \Psi^-(\boldsymbol{\epsilon}[\mathbf{u}])\, d\Omega \\ &- \int_\Omega \alpha\, S_w\, p_w\, \boldsymbol{\nabla}\cdot\mathbf{u}\, d\Omega - \int_\Omega \frac{(S_w\, p_w)^2}{2\,M}\, d\Omega \\ &- \int_\Omega \mathbf{b}\cdot\mathbf{u}\, d\Omega + \int_\Omega \frac{G_c}{c_w}\left(\frac{w(\varphi)}{l} + l|\boldsymbol{\nabla}\varphi|^2\right) d\Omega. \end{aligned} \tag{6.1}$$

In the above energy functional, the strength and stiffness of the solid skeleton is reduced with the phase-field degradation function $g(\varphi)$. The energy terms associated with the water pressure are assumed unaffected by the fracture, similar to the hydraulic fracturing energy functional (5.1). As such, no degradation function is attached to these terms. Furthermore, the external mechanical traction $\mathbf{t}^u_p$ is absent, since the desiccation cracking phenomenon is driven by an outflux of the water content. Furthermore, unlike the hydraulic fracturing model, the body force $\mathbf{b}$ due to the self-weight of the soil is considered in the desiccation cracking model. The force

$\mathbf{b}$ is defined as the sum of the water content and solid skeleton weights. It is expressed as

$$\mathbf{b} = \big(n S_w \rho_w + (1-n)\rho_s\big)\mathbf{g}, \tag{6.2}$$

where, n is the porosity, and ρ_w and ρ_s represent the densities of water and the solid skeleton, respectively. The acceleration due to gravity $\mathbf{g}$ is expressed as a vector with the only non-zero entry in the direction of the gravity.

Remark 7. *The governing equations in Cajuhi, Sanavia, and De Lorenzis's phase-field desiccation cracking model [48] may be obtained from the energy functional (6.1). Note that in [48], the governing equations were postulated directly in the strong form.*

Motivated by the experimental studies [207, 208] establishing the role of suction in desiccation cracking of soil close to full saturation, one may construct an alternative energy functional incorporating the positive energetic contribution of the suction in fracture initiation and propagation. To that end, when suction is encountered in conjunction with a positive volumetric strain ($\boldsymbol{\nabla}\cdot\mathbf{u} > 0$), the degradation function $g(\varphi)$ is attached to the term $\alpha\, S_w\, p_w\, \boldsymbol{\nabla}\cdot\mathbf{u}$. With this change, the energy functional E_1 (6.1) attains the form

$$\begin{aligned} E_2(\mathbf{u}, p_w, \varphi) = &\int_\Omega g(\varphi)\,\Psi^+(\boldsymbol{\epsilon}[\mathbf{u}])\,d\Omega + \int_\Omega \Psi^-(\boldsymbol{\epsilon}[\mathbf{u}])\,d\Omega \\ &- \int_\Omega h(\varphi)\,\alpha\, S_w\, p_w\, \boldsymbol{\nabla}\cdot\mathbf{u}\,d\Omega - \int_\Omega \frac{(S_w\, p_w)^2}{2M}\,d\Omega \\ &- \int_\Omega \mathbf{b}\cdot\mathbf{u}\,d\Omega + \int_\Omega \frac{G_c}{c_w}\left(\frac{w(\varphi)}{l} + l|\boldsymbol{\nabla}\varphi|^2\right)d\Omega, \end{aligned} \tag{6.3}$$

where, an additional degradation function $h(\varphi)$ is defined as

$$h(\varphi) = \begin{cases} g(\varphi), & \text{if } p_w < 0 \text{ and } \boldsymbol{\nabla}\cdot\mathbf{u} > 0 \\ 1, & \text{otherwise.} \end{cases} \tag{6.4}$$

Remark 8. *It is important to note that the energy functionals E_1 (6.1) and E_2 (6.3) would yield identical numerical results if the soil specimen remains entirely under compression.*

The phase-field desiccation cracking model energy functionals E_1 (6.1) and E_2 (6.3) are constructed in the '*effective strain*[8]' space. With this approach, the degradation function operates on the solid skeleton strain energy density. Analytical studies conducted by Luo, Sanavia, and De Lorenzis [50] show that such models exhibit solely a mode II fracturing phenomenon. Alternatively, when the energy functional is constructed in the total strain space, a mixed (both, I and II) mode fracturing phenomenon is observed [50].

A total strain space phase-field energy functional for the soil desiccation cracking phenomenon may be constructed following Heider and Sun [49] or Luo, Sanavia, and De Lorenzis [50]. In the context of partial saturated porous media, the total strain, say, $\boldsymbol{\epsilon}_{tot}$ is defined as

$$\boldsymbol{\epsilon}_{tot}[\mathbf{u}, p_w] := \boldsymbol{\epsilon}[\mathbf{u}] - \alpha\, S_w\, \frac{p_w}{3\,K}\mathbf{I}, \tag{6.5}$$

where, K is the bulk modulus of the porous medium. Incorporating (6.5) in the energy functional E_1 (6.1) together with re-arrangement of the terms yields

$$\begin{aligned} E_3(\mathbf{u}, p_w, \varphi) = &\int_\Omega g(\varphi)\, \Psi^+_{tot}(\boldsymbol{\epsilon}_{tot}[\mathbf{u}, p_w])\, d\Omega + \int_\Omega \Psi^-_{tot}(\boldsymbol{\epsilon}_{tot}[\mathbf{u}, p_w])\, d\Omega \\ &- \int_\Omega \left(\frac{\alpha^2}{K} + \frac{1}{M}\right) \frac{(S_w\, p_w)^2}{2}\, d\Omega \\ &- \int_\Omega \mathbf{b}\cdot\mathbf{u}\, d\Omega + \int_\Omega \frac{G_c}{c_w}\left(\frac{w(\varphi)}{l} + l|\boldsymbol{\nabla}\varphi|^2\right) d\Omega. \end{aligned} \tag{6.6}$$

Unlike the energy functionals E_1 (6.1) and E_2 (6.3) constructed in the effective strain space, the degradation function $g(\varphi)$ in E_3 operates on the total strain energy density instead of the solid skeleton strain energy density. Furthermore, the total strain defined in (6.5) may attain positive values due to suction ($p_w < 0$) even though the effective strain $\boldsymbol{\epsilon}[\mathbf{u}]$ is compressive. This net positive total strain contributes to a mode I fracturing phenomenon. For detailed analytical proof of the same, the reader is referred to Section 4.2 in [50]. Note that the total strain is referred to as '*effective strain*' therein.

Remark 9. *The total strain space energy functional (Equation 30) in [50] excludes the contribution* $\frac{1}{M}\frac{(S_w\, p_w)^2}{2}$. *For the system of equations solved for the displacement* $\mathbf{u}$, *water pressure* p_w, *and the phase-field* φ, *there is no consequence. However, in the context of computing the water content,*

8 Effective strain refers to the strain in the solid skeleton in a porous material.

Remark 9 (continued)

exclusion of the aforementioned term in the energy functional yields an incorrect expression.

The total strain and effective strain space approaches may be considered as extremities in the construction of an energy functional for soil desiccation cracking. With this argument, a novel energy functional is proposed, which lies in between the effective and total strain space approaches. To that end, a new strain measure, say, solid strain $\boldsymbol{\epsilon}_{sld}$ is defined as

$$\boldsymbol{\epsilon}_{sld}[\mathbf{u}, p_w] := \boldsymbol{\epsilon}[\mathbf{u}] - (\alpha - n)\, S_w \frac{p_w}{3K}\mathbf{I}. \tag{6.7}$$

The term $(\alpha - n)$ in the solid strain $\boldsymbol{\epsilon}_{sld}$ represents the fraction of the water pressure affecting the solid skeleton, where n is the porosity of the porous medium. The use of the solid strain $\boldsymbol{\epsilon}_{sld}$ implies that the total Cauchy stress is computed as

$$\boldsymbol{\sigma}(\boldsymbol{\epsilon}_{sld}[\mathbf{u}], p_w) = \boldsymbol{\sigma}_{sld}(\boldsymbol{\epsilon}_{sld}[\mathbf{u}], p_w) - n\, S_w\, p_w\, \mathbf{I}. \tag{6.8}$$

With this choice, the corresponding energy functional is constructed as,

$$\begin{aligned} E_4(\mathbf{u}, p_w, \varphi) = &\int_\Omega g(\varphi)\, \Psi^+_{sld}(\boldsymbol{\epsilon}_{sld}[\mathbf{u}, p_w])\, d\Omega + \int_\Omega \Psi^-_{sld}(\boldsymbol{\epsilon}_{sld}[\mathbf{u}, p_w])\, d\Omega \\ &- \int_\Omega n\, S_w\, p_w\, \boldsymbol{\nabla}\cdot\mathbf{u}\, d\Omega - \int_\Omega \left(\frac{(\alpha - n)^2}{K} + \frac{1}{M}\right)\frac{(S_w\, p_w)^2}{2}\, d\Omega \\ &- \int_\Omega \mathbf{b}\cdot\mathbf{u}\, d\Omega + \int_\Omega \frac{G_c}{c_w}\left(\frac{w(\varphi)}{l} + l|\boldsymbol{\nabla}\varphi|^2\right) d\Omega. \end{aligned} \tag{6.9}$$

6.2.2 *Conservation of mass*

The conservation of mass applies to the solid skeleton mass as well as the fluid (water and gas) mass. The pertinent detailed derivations are presented in Section 2.3.2. From the mathematical developments therein, the conservation of the solid skeleton mass in conjunction with that of the fluid mass yields the water transport equation (2.52), re-stated below,

$$\begin{aligned}
&\left[(\alpha-n)C_s S_w^2 + nS_w C_w\right]\frac{\partial p_w}{\partial t} + (\alpha-n)C_s S_w S_g \frac{\partial p_g}{\partial t} \\
&+ \left[(\alpha-n)C_s S_w (p_w - p_g) + n\right]\frac{\partial S_w}{\partial t} + \alpha S_w \frac{\partial \epsilon_{vol}}{\partial t} \\
&- \boldsymbol{\nabla}\cdot\left[k_{rw}\frac{k_i \mathbf{I}}{\mu_w}(\boldsymbol{\nabla} p_w - \rho_w \mathbf{g})\right] = 0.
\end{aligned} \tag{6.10}$$

A similar equation is also obtained for the gas transport (see (2.53) in Section 2.3.2). However, in the context of two-phase modelling of porous media, the gas is assumed to be at constant atmospheric pressure, i.e., $p_g = 0$ and $\frac{\partial p_g}{\partial t} = 0$. Consequently, the gas transport equation is eliminated from the system of equations. Thus, the water transport equation (6.10) attains a simplified form,

$$\begin{aligned}
&\left[(\alpha-n)C_s S_w^2 + nS_w C_w\right]\frac{\partial p_w}{\partial t} \\
&+ \left[(\alpha-n)C_s S_w p_w + n\right]\frac{\partial S_w}{\partial t} + \alpha S_w \frac{\partial \epsilon_{vol}}{\partial t} \\
&- \boldsymbol{\nabla}\cdot\left[k_{rw}\underbrace{\frac{k_i \mathbf{I}}{\mu_w}}_{\boldsymbol{\kappa}_{eff}}(\boldsymbol{\nabla} p_w - \rho_w \mathbf{g})\right] = 0.
\end{aligned} \tag{6.11}$$

Remark 10. *Unlike the hydraulic fracturing model, the water transport equation for soil desiccation cracking (6.11) incorporates the prospect of variable saturation. The saturation is a state variable depending on the suction pressure, i.e., the difference between the gas and water pressure. This enhanced model fidelity is required, given the role of suction in the development of desiccation cracks in soil [207, 208].*

The water transport equation (6.11) in its current form does not incorporate any fracture dependent coefficients. Similar to the approach adopted for hydraulic fracture modelling in Chapter 5, one may introduce fracture dependent coefficients. Thereafter, any coefficient, say χ is expressed as

$$X = X_b + h(\varphi)\Big(X_f - X_b\Big), \tag{6.12}$$

where subscripts b and f indicate bulk and fracture, respectively. The phase-field dependent interpolation function $h(\varphi)$ is defined as

$$h(\varphi) = 25\,\langle \varphi - 0.8\rangle_+^2. \tag{6.13}$$

The interpolation function assumes a value zero until $\varphi = 0.8$ and reaches 1 for $\varphi = 1$. Having defined a way to introduce fracture dependent coefficients in the water transport equation (6.11), the individual coefficients are addressed in the latter part of this section.

Biot coefficient

The Biot coefficient α accounts for the interaction of the solid skeleton and the water pore pressure. For linear isotropic materials, it is given by

$$\alpha = 1 - C_s/C, \tag{6.14}$$

where, C_s and C represent the compressibility of the solid grains and porous medium, respectively [180]. In the context of soil, the solid grains are assumed nearly incompressible. This yields $\alpha = 1$, a choice made throughout this chapter.

Porosity

The porosity n in the water transport equation (6.11) refers to the initial porosity of the porous medium [112]. For hydraulic fracturing, You and Yoshioka [42] proposed increasing the initial porosity n to 1 for a fully developed fracture $\varphi = 1$. However, one may argue that the change in the porosity is already incorporated in the water transport equation (6.11) through the relation (2.42) (see Section 2.3.2. Based on this reasoning, the initial porosity is not tampered with in this chapter.

Biot modulus

The Biot modulus of a linear elastic isotropic porous material is expressed as

$$\frac{1}{M} = (\alpha - n)C_s + nC_f. \tag{6.15}$$

For the numerical experiments on soil desiccation cracking, the Biot modulus is not required since the term $\frac{1}{M}\frac{(S_w p_w)^2}{2}$ does not enter any of the governing variational equations (presented later in Section 6.2.3).

Permeability

The permeability matrix $\mathbf{K}_{eff}$ in the water transport equation (6.11) corresponds to an intact bulk material state. In order to account for an enhancement of the permeability due to fracture, the notion of bulk and fracture permeability is introduced, adopting a dual permeability approach [211, 212]. Thereafter, the bulk permeability matrix is defined as

$$\mathbf{K}_b = \frac{\kappa_i}{\mu_w}\mathbf{I}, \tag{6.16}$$

where, κ_i and μ_w represent the intrinsic permeability of the porous medium and the dynamic viscosity of water, respectively. The fracture permeability is computed using the cubic law proposed by Witherspoon et al. [181]. For an isotropic material, the fracture permeability is expressed as

$$\mathbf{K}_f = \frac{w_f^2}{12}\mathbf{I}, \tag{6.17}$$

with fracture aperture w_f. Unlike discrete fracture models like XFEM and CZM, the fracture aperture is not readily available as a solution of the system of equations. Therefore, the fracture aperture is computed in approximated sense following Miehe, Mauthe, and Teichtmeister [182] as

$$w_f := \langle h_{el}(1 + \mathbf{n}_\varphi \cdot \boldsymbol{\epsilon}[\mathbf{u}] \cdot \mathbf{n}_\varphi)\rangle_+, \quad \text{with} \quad \mathbf{n}_\varphi \approx \frac{\mathbf{P}_{max}}{|\mathbf{P}_{max}|}, \tag{6.18}$$

where, h_{el} is the characteristic element size, and $\mathbf{P}_{max}$ is the eigenvector corresponding to the maximum eigenvalue of the strain tensor. Having obtained expressions for the bulk permeability $\mathbf{K}_b$ and the fracture permeability $\mathbf{K}_f$, the effective permeability $\mathbf{K}_{eff}$ is defined using the phase-field based interpolation function $h(\varphi)$ as

$$\mathbf{K}_{eff}(\varphi) = \mathbf{K}_b + h(\varphi)\Big(\mathbf{K}_f - \mathbf{K}_b\Big). \tag{6.19}$$

Remark 11. *Heider and Sun [49] adopted an anisotropic fracture permeability matrix, computed as*

$$\mathbf{K}_f = \frac{w_h^2}{12}\Big(\mathbf{I} - \mathbf{n}_\varphi \otimes \mathbf{n}_\varphi\Big), \tag{6.20}$$

in order to account for the preferential flow direction due to fracture. However, in this chapter, the fracture permeability is assumed isotropic. The argument for this choice is that the preferential flow direction is dictated by the localization orientation itself.

Soil-Water Retention Curve (SWRC)

The soil-water retention curve establishes the relationship between the degree of saturation S_w and the water pressure head h_w at equilibrium, i.e.,

when the water is not moving in the specimen. The water pressure head is computed as

$$h_w(p_w, p_g) = \frac{p_g - p_w}{\gamma_w\, g}, \tag{6.21}$$

where, γ_w and g represent the density of water and acceleration due to gravity, respectively. Note that, in the context of two-phase soil modelling, $p_g = 0$.

The first SWRC was proposed by Buckingham [213] as early as 1907. Since then, several other SWRCs were proposed by Gardner [115], Brooks [114] and Van Genuchten [113]. For a comparison of these SWRCs, the reader is referred to [214]. In this chapter, Van Genuchten's retention model is adopted given its popularity in the soil mechanics including desiccation cracking (see [48–51]). The Van Genuchten relations are given by

$$S_e = \frac{S_w - S_r}{S_s - S_r} = \left(1 + [\alpha_{VG}|h_w|]^{n_{VG}}\right)^{-m_{VG}}, \text{ with } m_{VG} = 1 - 1/n_{VG}, \tag{6.22}$$

where, α_{VG} is a scalar fitting parameter denoting the air entry value, and m_{VG}, n_{VG} are parameters related to the pore size distribution.

The SWRCs [113–115] proposed so far do not account for change in the degree of saturation upon fracturing of soil specimen. In the context of rock mechanics, Zhang and Fredlund [215] introduced two SWRCs, one for the rock bulk matrix and the other for the fracture rock. The degree of saturation is then computed from the two SWRCs as a weighted average of the bulk and fractured volumes. The air entry value in the fractured rock is less than that of the bulk rock. A similar model was also adopted by Abbaszadeh, Houston, and Zapata [216] in the context of the San Diego clay, USA. However, the authors also found that the cracked and intact clay SWRCs merge at low suction values, governed by the width of the crack. For this reason, in this chapter, the SWRC is considered unaffected by the fracturing phenomenon.

Following the computation of the degree of saturation S_w from the SWRC, the relative permeability k_{rw} is also determined. The simplest assumption $k_{rw} = S_w$ was adopted by Romm [217]. In later developments, comparatively sophisticated models were proposed by Fourar and Lenormand [218], Corey [219] and Mualem [220]. In this chapter, Mualem's expression for relative permeability is adopted. The relative permeability is given by

$$k_{rw} = \sqrt{S_e}\left(1 - \left[1 - (S_e)^{\frac{1}{m_{VG}}}\right]^{m_{VG}}\right)^2. \tag{6.23}$$

All parameters on the right hand side of the above equation correspond to Van Genuchten's SWRC.

Darcy to Poiseuille flow transition in water transport equation

Incorporating fracture dependent permeability (6.19) in the water transport equation (6.11), one obtains

$$\underbrace{\left[(\alpha-n)C_s S_w^2 + n S_w C_w\right]}_{C_1}\frac{\partial p_w}{\partial t} + \underbrace{\left[(\alpha-n)C_s S_w p_w + n\right]}_{C_2}\frac{\partial S_w}{\partial t} + \alpha S_w \frac{\partial \epsilon_{vol}}{\partial t} - \boldsymbol{\nabla}\cdot\left[k_{rw}\,\mathbf{K}_{eff}(\varphi)(\boldsymbol{\nabla} p_w - \rho_w \mathbf{g})\right] = 0. \tag{6.24}$$

The above equation allows a seamless transition from a Darcy flow in the intact soil material to a Poiseuille type flow in the diffused fractures, based on the dual permeability model (6.19). All other coefficients and state variables may also be expressed in a dual model approach similar to the permeability. However, the need for incorporating these changes requires either a theoretical reasoning (for instance, a micromechanical approach [221]) or experimental evidence.

6.2.3 *Variational equations*

The set of variational equations for the phase-field desiccation cracking model is obtained through a two-fold process. First, the momentum balance equation and the phase-field evolution equation are obtained upon minimizing the energy functional (E_1, E_2, E_3 or E_4) w.r.t., the vector-valued displacement $\mathbf{u}$ and the scalar-valued phase-field φ. Thereafter, the water transport variational equation is obtained through Backward Euler substitution of the time derivatives and a subsequent integration with a test function δp_w over the domain Ω. The irreversibility of the phase-field is enforced using the history-variable approach proposed by Miehe, Hofacker, and Welschinger [37]. Due to the four different energy functionals introduced in Section 6.2.1, four Variational Problems 12, 13, 14, and 15 are obtained.

Each of the aforementioned Variational Problems entails a saddle point problem, requiring a careful choice of trial and test functions for the displacement and the water pressure to guarantee a unique solution continuously depending on the input data. The sufficient condition ensuring this uniqueness is established in the computational mechanics literature as the Ladyzhenskaya–Babuška–Brezzi (LBB) condition. In order to fulfill the LBB condition, quadratic trial and test functions are chosen for the displacement field, while the pressure field remains linear. In the discrete sense, such a choice is referred to as the Taylor and Hood element [184] following their contribution. Furthermore, quadratic trial and test functions are also chosen

for the phase-field. This choice was also adopted in [48–50]. Finally, for brevity, the function argument (φ) in $\mathbf{K}_{eff}$ is dropped henceforth, and the Cauchy stress definitions

$$\boldsymbol{\sigma}^{\pm}(\boldsymbol{\epsilon}[\mathbf{u}]) = \frac{\partial \Psi^{\pm}(\boldsymbol{\epsilon}[\mathbf{u}])}{\partial \boldsymbol{\epsilon}}, \tag{6.25}$$

$$\boldsymbol{\sigma}^{\pm}_{tot}(\boldsymbol{\epsilon}[\mathbf{u}], p_w) = \frac{\partial \Psi^{\pm}_{tot}(\boldsymbol{\epsilon}[\mathbf{u}], p_w)}{\partial \boldsymbol{\epsilon}}, \tag{6.26}$$

$$\boldsymbol{\sigma}^{\pm}_{sld}(\boldsymbol{\epsilon}[\mathbf{u}], p_w) = \frac{\partial \Psi^{\pm}_{sld}(\boldsymbol{\epsilon}[\mathbf{u}], p_w)}{\partial \boldsymbol{\epsilon}}, \tag{6.27}$$

are incorporated, wherever relevant. Variational Problem 12 corresponding to the energy functional E_1 assumes the form:

Variational Problem 12. *Find* $(\mathbf{u}, \varphi, p_w) \in \mathbb{U} \times \mathbb{P} \times \mathbb{Q}$ *such that*

$$E_1'(\mathbf{u}, p_w, \varphi; \delta\mathbf{u}) = \int_\Omega \Big(g(\varphi)\boldsymbol{\sigma}^{+}(\boldsymbol{\epsilon}[\mathbf{u}]) + \boldsymbol{\sigma}^{-}(\boldsymbol{\epsilon}[\mathbf{u}]) \Big) : \boldsymbol{\epsilon}[\delta\mathbf{u}] \, d\Omega - \int_\Omega \alpha \, S_w \, p_w \, \mathbf{I} : \boldsymbol{\epsilon}[\delta\mathbf{u}] \, d\Omega = 0 \quad \forall \, \delta\mathbf{u} \in \mathbb{U}^0, \tag{6.28a}$$

$$E_1'(\mathbf{u}, p_w, \varphi; \delta\varphi) = \int_\Omega \left(g'(\varphi)\mathcal{H} + \frac{G_c}{c_w \, l} w'(\varphi) \right) \delta\varphi \, d\Omega + \int_\Omega \frac{G_c \, l}{c_w} \boldsymbol{\nabla}\varphi \cdot \boldsymbol{\nabla}\delta\varphi \, d\Omega = 0 \quad \forall \, \delta\varphi \in \mathbb{P}^0, \tag{6.28b}$$

$$\begin{aligned} &\int_\Omega \left(C_1 \frac{p_w - {}^{n}p_w}{\Delta t} + C_2 \frac{S_w - {}^{n}S_w}{\Delta t} \right) \delta p_w \, d\Omega \\ &+ \int_\Omega \alpha \, S_w \, \frac{\epsilon_{vol} - {}^{n}\epsilon_{vol}}{\Delta t} \delta p_w \, d\Omega \\ &+ \int_\Omega \boldsymbol{\nabla}\delta p_w \, k_{rw} \, \mathbf{K}_{eff} \left(\boldsymbol{\nabla} p_w - \rho_w \mathbf{g} \right) d\Omega \\ &= \int_{\Gamma_N^{p_w}} q \, \delta p_w \, d\Gamma \quad \forall \, \delta p_w \in \mathbb{Q}, \end{aligned} \tag{6.28c}$$

using pertinent time-dependent Dirichlet boundary conditions $\mathbf{u}^p$ *on* Γ_D^u, φ^p *on* Γ_D^φ, *and* p_w^p *on* $\Gamma_D^{p_w}$. *The trial and test spaces are defined as*

$$\mathbb{U} = \{\mathbf{u} \in [H^2(\Omega)]^{\dim} | \mathbf{u} = \mathbf{u}^p \text{ on } \Gamma_D^u\}, \tag{6.29a}$$

$$\mathbb{P} = \{\varphi \in [H^2(\Omega)] | \varphi = \varphi^p \text{ on } \Gamma_D^\varphi\}, \tag{6.29b}$$

$$\mathbb{Q} = \{p_w \in H^1(\Omega) | p_w = p_w^p \text{ on } \Gamma_D^{p_w}\}, \tag{6.29c}$$

$$\mathbb{U}^0 = \{\mathbf{u} \in [H^2(\Omega)]^{\dim} | \mathbf{u} = \mathbf{0} \text{ on } \Gamma_D^u\}, \tag{6.29d}$$

$$\mathbb{P}^0 = \{\varphi \in [H^2(\Omega)] | \varphi = 0 \text{ on } \Gamma_D^\varphi\}, \tag{6.29e}$$

Variational Problem 12 (continued)

$$\mathbb{Q}^0 = \{p_w \in H^1(\Omega) | p_w = 0 \text{ on } \Gamma_D^{p_w}\}. \tag{6.29f}$$

In (6.28c), the left superscript n refers to the previous time-step. The storage coefficients C_1 and C_2 are defined in (6.24). The history variable $\mathcal{H}$ is defined in (2.24). ■

The Variational Problem 13 corresponds to the energy functional E_2. The contribution of suction towards fracture driving energy is incorporated only when positive volumetric strain is encountered. This results in the modified definition of the history-variable $\mathcal{H}$ in (6.32).

Variational Problem 13. *Find $(\mathbf{u}, \varphi, p_w) \in \mathbb{U} \times \mathbb{P} \times \mathbb{Q}$ such that*

$$\begin{aligned} E_2'(\mathbf{u}, p_w, \varphi; \delta\mathbf{u}) = &\int_\Omega \Big(g(\varphi)\boldsymbol{\sigma}^+(\boldsymbol{\epsilon}[\mathbf{u}]) + \boldsymbol{\sigma}^-(\boldsymbol{\epsilon}[\mathbf{u}]) \Big) : \boldsymbol{\epsilon}[\delta\mathbf{u}] \, d\Omega \\ &- \int_\Omega h(\varphi)\, \alpha\, S_w\, p_w\, \mathbf{I} : \boldsymbol{\epsilon}[\delta\mathbf{u}] \, d\Omega = 0 \quad \forall\, \delta\mathbf{u} \in \mathbb{U}^0, \end{aligned} \tag{6.30a}$$

$$\begin{aligned} E_2'(\mathbf{u}, p_w, \varphi; \delta\varphi) = &\int_\Omega \left(g'(\varphi)\mathcal{H} + \frac{G_c}{c_w\, l} w'(\varphi) \right) \delta\varphi \, d\Omega \\ &+ \int_\Omega \frac{G_c\, l}{c_w} \boldsymbol{\nabla}\varphi \cdot \boldsymbol{\nabla}\delta\varphi \, d\Omega = 0 \quad \forall\, \delta\varphi \in \mathbb{P}^0, \end{aligned} \tag{6.30b}$$

$$\begin{aligned} &\int_\Omega \Big(C_1 \frac{p_w - {}^n p_w}{\Delta t} + C_2 \frac{S_w - {}^n S_w}{\Delta t} \Big) \delta p_w \, d\Omega \\ &+ \int_\Omega \alpha\, S_w \, \frac{\epsilon_{vol} - {}^n \epsilon_{vol}}{\Delta t} \delta p_w \, d\Omega \\ &+ \int_\Omega \boldsymbol{\nabla}\delta p_w \, k_{rw} \, \mathbf{K}_{eff} \Big(\boldsymbol{\nabla} p_w - \rho_w \mathbf{g} \Big) \, d\Omega \\ &= \int_{\Gamma_N^{p_w}} q \, \delta p_w \, d\Gamma \quad \forall\, \delta p_w \in \mathbb{Q}, \end{aligned} \tag{6.30c}$$

using pertinent time-dependent Dirichlet boundary conditions $\mathbf{u}^p$ on Γ_D^u, φ^p on Γ_D^φ, and p_w^p on $\Gamma_D^{p_w}$. The trial and test spaces are defined as

$$\mathbb{U} = \{\mathbf{u} \in [H^2(\Omega)]^{\dim} | \mathbf{u} = \mathbf{u}^p \text{ on } \Gamma_D^u\}, \tag{6.31a}$$

$$\mathbb{P} = \{\varphi \in [H^2(\Omega)] | \varphi = \varphi^p \text{ on } \Gamma_D^\varphi\}, \tag{6.31b}$$

$$\mathbb{Q} = \{p_w \in H^1(\Omega) | p_w = p_w^p \text{ on } \Gamma_D^{p_w}\}, \tag{6.31c}$$

$$\mathbb{U}^0 = \{\mathbf{u} \in [H^2(\Omega)]^{\dim} | \mathbf{u} = \mathbf{0} \text{ on } \Gamma_D^u\}, \tag{6.31d}$$

$$\mathbb{P}^0 = \{\varphi \in [H^2(\Omega)] | \varphi = 0 \text{ on } \Gamma_D^\varphi\}, \tag{6.31e}$$

Variational Problem 13 (continued)

$$\mathbb{Q}^0 = \{p_w \in H^1(\Omega) | p_w = 0 \text{ on } \Gamma_D^{p_w}\}. \tag{6.31f}$$

The interpolation function $h(\varphi)$ is defined in (6.4).In (6.30c), the left superscript n refers to the previous time-step. The storage coefficients C_1 and C_2 are defined in (6.24). The history variable $\mathcal{H}$ is defined as

$$\mathcal{H} = \begin{cases} \max\left\{{}^n\mathcal{H}, \Psi^+(\boldsymbol{\epsilon}[\mathbf{u}]) - \alpha\, S_w\, p_w\, \epsilon_{vol}\right\}, & \text{if } p_w < 0 \text{ and } \boldsymbol{\nabla}\cdot\mathbf{u} > 0 \\ \max\left\{{}^n\mathcal{H}, \Psi^+(\boldsymbol{\epsilon}[\mathbf{u}])\right\}, & \text{otherwise.} \end{cases} \tag{6.32}$$

■

The Variational Problem 14 corresponds to the novel energy functional E_3. The contribution of suction towards fracture driving energy is incorporated irrespective of the strain in the solid skeleton. To that end, the strain energy densities are constructed in the total strain space, as in (6.6). Accordingly, the history-variable $\mathcal{H}$ is defined in (6.35).

Variational Problem 14. *Find $(\mathbf{u}, \varphi, p_w) \in \mathbb{U} \times \mathbb{P} \times \mathbb{Q}$ such that*

$$\begin{aligned} E_3'(\mathbf{u}, p_w, \varphi; \delta\mathbf{u}) &= \int_\Omega \Big(g(\varphi)\boldsymbol{\sigma}_{tot}^+(\boldsymbol{\epsilon}_{tot}[\mathbf{u}, p_w]) \\ &\quad + \boldsymbol{\sigma}_{tot}^-(\boldsymbol{\epsilon}_{tot}[\mathbf{u}, p_w]) \Big) : \boldsymbol{\epsilon}[\delta\mathbf{u}]\, d\Omega \\ &= 0 \quad \forall\, \delta\mathbf{u} \in \mathbb{U}^0, \end{aligned} \tag{6.33a}$$

$$\begin{aligned} E_3'(\mathbf{u}, p_w, \varphi; \delta\varphi) &= \int_\Omega \left(g'(\varphi)\mathcal{H} + \frac{G_c}{c_w\, l} w'(\varphi) \right) \delta\varphi\, d\Omega \\ &\quad + \int_\Omega \frac{G_c\, l}{c_w} \boldsymbol{\nabla}\varphi \cdot \boldsymbol{\nabla}\delta\varphi\, d\Omega = 0 \quad \forall\, \delta\varphi \in \mathbb{P}^0, \end{aligned} \tag{6.33b}$$

$$\begin{aligned} &\int_\Omega \left(C_1 \frac{p_w - {}^n p_w}{\Delta t} + C_2 \frac{S_w - {}^n S_w}{\Delta t} \right) \delta p_w\, d\Omega \\ &+ \int_\Omega \alpha\, S_w\, \frac{\epsilon_{vol} - {}^n\epsilon_{vol}}{\Delta t} \delta p_w\, d\Omega \\ &+ \int_\Omega \boldsymbol{\nabla}\delta p_w\, k_{rw}\, \mathbf{K}_{eff} \left(\boldsymbol{\nabla} p_w - \rho_w \mathbf{g} \right) d\Omega \\ &= \int_{\Gamma_N^{p_w}} q\, \delta p_w\, d\Gamma \quad \forall\, \delta p_w \in \mathbb{Q}, \end{aligned} \tag{6.33c}$$

Variational Problem 14 (continued)

using pertinent time-dependent Dirichlet boundary conditions $\mathbf{u}^p$ *on* Γ_D^u, φ^p *on* Γ_D^φ, *and* p_w^p *on* $\Gamma_D^{p_w}$. *The trial and test spaces are defined as*

$$\mathbb{U} = \{\mathbf{u} \in [H^2(\Omega)]^{\dim} | \mathbf{u} = \mathbf{u}^p \text{ on } \Gamma_D^u\}, \tag{6.34a}$$
$$\mathbb{P} = \{\varphi \in [H^2(\Omega)]] | \varphi = \varphi^p \text{ on } \Gamma_D^\varphi\}, \tag{6.34b}$$
$$\mathbb{Q} = \{p_w \in H^1(\Omega) | p_w = p_w^p \text{ on } \Gamma_D^{p_w}\}, \tag{6.34c}$$
$$\mathbb{U}^0 = \{\mathbf{u} \in [H^2(\Omega)]^{\dim} | \mathbf{u} = \mathbf{0} \text{ on } \Gamma_D^u\}, \tag{6.34d}$$
$$\mathbb{P}^0 = \{\varphi \in [H^2(\Omega)]] | \varphi = 0 \text{ on } \Gamma_D^\varphi\}, \tag{6.34e}$$
$$\mathbb{Q}^0 = \{p_w \in H^1(\Omega) | p_w = 0 \text{ on } \Gamma_D^{p_w}\}. \tag{6.34f}$$

In (6.33c), the left superscript n *refers to the previous time-step. The storage coefficients* C_1 *and* C_2 *are defined in (6.24). The history variable* $\mathcal{H}$ *is defined as*

$$\mathcal{H} = \max\left\{{}^n\mathcal{H},\, \Psi_{tot}^+(\boldsymbol{\epsilon}_{tot}[\mathbf{u}, p_w])\right\}. \tag{6.35}$$

■

Finally, the Variational Problem 15 corresponds to the energy functional E_4. The contribution of suction towards fracture driving energy is incorporated irrespective of the strain in the solid skeleton, however, with a different magnitude compared to the Variational Problem 14. Consequently, the modified definition of the history-variable $\mathcal{H}$ in (6.38) is adopted.

Variational Problem 15. *Find* $(\mathbf{u}, \varphi, p_w) \in \mathbb{U} \times \mathbb{P} \times \mathbb{Q}$ *such that*

$$\begin{aligned} E_4'(\mathbf{u}, p_w, \varphi; \delta\mathbf{u}) = &\int_\Omega \Big(g(\varphi)\boldsymbol{\sigma}_{sld}^+(\boldsymbol{\epsilon}_{sld}[\mathbf{u}, p_w]) \\ &+ \boldsymbol{\sigma}_{sld}^-(\boldsymbol{\epsilon}_{sld}[\mathbf{u}, p_w])\Big) : \boldsymbol{\epsilon}[\delta\mathbf{u}]\, d\Omega \\ &- n\, S_w\, p_w\, \mathbf{I} : \boldsymbol{\epsilon}[\delta\mathbf{u}]\, d\Omega = 0 \quad \forall\, \delta\mathbf{u} \in \mathbb{U}^0, \end{aligned} \tag{6.36a}$$

$$\begin{aligned} E_4'(\mathbf{u}, p_w, \varphi; \delta\varphi) = &\int_\Omega \left(g'(\varphi)\mathcal{H} + \frac{G_c}{c_w\, l} w'(\varphi)\right)\delta\varphi\, d\Omega \\ &+ \int_\Omega \frac{G_c\, l}{c_w} \boldsymbol{\nabla}\varphi \cdot \boldsymbol{\nabla}\delta\varphi\, d\Omega = 0 \quad \forall\, \delta\varphi \in \mathbb{P}^0, \end{aligned} \tag{6.36b}$$

$$\begin{aligned} &\int_\Omega \left(C_1 \frac{p_w - {}^n p_w}{\Delta t} + C_2 \frac{S_w - {}^n S_w}{\Delta t}\right)\delta p_w\, d\Omega \\ &+ \int_\Omega \alpha\, S_w\, \frac{\epsilon_{vol} - {}^n\epsilon_{vol}}{\Delta t}\delta p_w\, d\Omega \end{aligned}$$

Variational Problem 15 (continued)

$$+\int_{\Omega} \boldsymbol{\nabla}\delta p_w \, k_{rw} \, \mathbf{K}_{eff} \left(\boldsymbol{\nabla} p_w - \rho_w \mathbf{g}\right) d\Omega$$
$$= \int_{\Gamma_N^{p_w}} q \, \delta p_w \, d\Gamma \quad \forall \, \delta p_w \in \mathcal{Q}, \tag{6.36c}$$

using pertinent time-dependent Dirichlet boundary conditions $\mathbf{u}^p$ *on* Γ_D^u, φ^p *on* Γ_D^φ, *and* p_w^p *on* $\Gamma_D^{p_w}$. *The trial and test spaces are defined as*

$$\mathcal{U} = \{\mathbf{u} \in [H^2(\Omega)]^{\dim} | \mathbf{u} = \mathbf{u}^p \text{ on } \Gamma_D^u\}, \tag{6.37a}$$
$$\mathcal{P} = \{\varphi \in [H^2(\Omega)] | \varphi = \varphi^p \text{ on } \Gamma_D^\varphi\}, \tag{6.37b}$$
$$\mathcal{Q} = \{p_w \in H^1(\Omega) | p_w = p_w^p \text{ on } \Gamma_D^{p_w}\}, \tag{6.37c}$$
$$\mathcal{U}^0 = \{\mathbf{u} \in [H^2(\Omega)]^{\dim} | \mathbf{u} = \mathbf{0} \text{ on } \Gamma_D^u\}, \tag{6.37d}$$
$$\mathcal{P}^0 = \{\varphi \in [H^2(\Omega)] | \varphi = 0 \text{ on } \Gamma_D^\varphi\}, \tag{6.37e}$$
$$\mathcal{Q}^0 = \{p_w \in H^1(\Omega) | p_w = 0 \text{ on } \Gamma_D^{p_w}\}. \tag{6.37f}$$

In (6.36c), the left superscript n *refers to the previous time-step. The storage coefficients* C_1 *and* C_2 *are defined in (6.24). The history variable* $\mathcal{H}$ *is defined as*

$$\mathcal{H} = \max\left\{{}^n\mathcal{H}, \Psi_{sld}^+(\boldsymbol{\epsilon}_{sld}[\mathbf{u}, p_w])\right\}. \tag{6.38}$$

■

6.2.4 *Finite element discretized equations*

The finite element discretized equations for the phase-field desiccation cracking model are derived using the procedure explained in Section 2.1. To that end, the Variational Problems 12, 13, 14, and 15 are identified as points of departure from a continuous problem to a discrete one. The detailed derivations are skipped for brevity. Instead the corresponding Discrete Problems 10, 11, 12, and 13 are presented.

Discrete Problem 10. *Compute the solution update vector* $\mathbf{s}_{k+1} = \{\Delta\tilde{\mathbf{u}}\,;\Delta\tilde{p}_w\,;\,\Delta\tilde{\varphi}\}$ *for the current iteration* $k+1$ *using*

$$\underbrace{\begin{bmatrix} \mathbf{K}^{\mathbf{u}\mathbf{u}} & \mathbf{K}^{\mathbf{u}p_w} & \mathbf{K}^{\mathbf{u}\varphi} \\ \mathbf{K}^{p_w\mathbf{u}} & \mathbf{K}^{p_wp_w} & \mathbf{K}^{p_w\varphi} \\ \mathbf{K}^{\varphi\mathbf{u}} & \mathbf{K}^{\varphi p_w} & \mathbf{K}^{\varphi\varphi} \end{bmatrix}}_{\text{Stiffness matrix, } \mathbf{K}_k} \underbrace{\begin{Bmatrix} \Delta\tilde{\mathbf{u}} \\ \Delta\tilde{p}_w \\ \Delta\tilde{\varphi} \end{Bmatrix}}_{\mathbf{s}_{k+1}} = \underbrace{\begin{Bmatrix} \mathbf{0} \\ \mathbf{f}^{ext,p_w} \\ \mathbf{0} \end{Bmatrix} - \begin{Bmatrix} \mathbf{f}^{int,\mathbf{u}} \\ \mathbf{f}^{int,p_w} \\ \mathbf{f}^{int,\varphi} \end{Bmatrix}}_{\text{Residual, } \mathbf{r}_k}, \tag{6.39a}$$

and update the solution,

$$\begin{Bmatrix} \tilde{\mathbf{u}} \\ \tilde{p}_w \\ \tilde{\varphi} \end{Bmatrix}_{k+1} = \begin{Bmatrix} \tilde{\mathbf{u}} \\ \tilde{p}_w \\ \tilde{\varphi} \end{Bmatrix}_{k} + \begin{Bmatrix} \Delta\tilde{\mathbf{u}} \\ \Delta\tilde{p}_w \\ \Delta\tilde{\varphi} \end{Bmatrix}_{k+1}, \tag{6.39b}$$

until the norm of the residual is sufficiently small. The stiffness matrix components are given by,

$$\begin{aligned}
\mathbf{K}^{\mathbf{u}\mathbf{u}} &= \mathcal{A}\int_{\Omega_{el}} [\mathbf{B}^{\mathbf{u}}]^T \Big(\underbrace{g(\varphi)\frac{\partial\boldsymbol{\sigma}^+}{\partial\boldsymbol{\epsilon}} + \frac{\partial\boldsymbol{\sigma}^-}{\partial\boldsymbol{\epsilon}}}_{\mathbf{D}} \Big) [\mathbf{B}^{\mathbf{u}}]\, d\Omega, \\
\mathbf{K}^{\mathbf{u}p_w} &= -\mathcal{A}\int_{\Omega_{el}} [\mathbf{B}^{\mathbf{u}}]^T \alpha\Big(S_w + \frac{\partial S_w}{\partial p_w}p_w\Big)\mathbf{I}_v\, [\mathbf{N}^{p_w}]\, d\Omega \\
&\quad -\mathcal{A}\int_{\Omega_{el}} [\mathbf{N}^{\mathbf{u}}]^T n\frac{\partial S_w}{\partial p_w}\rho_w\,\mathbf{g}\, [\mathbf{N}^{p_w}]\, d\Omega \\
\mathbf{K}^{\mathbf{u}\varphi} &= \mathcal{A}\int_{\Omega_{el}} [\mathbf{B}^{\mathbf{u}}]^T \Big(g'(\varphi)\boldsymbol{\sigma}^+\Big)\, [\mathbf{N}^{\varphi}]\, d\Omega, \\
\mathbf{K}^{p_w\mathbf{u}} &= \frac{1}{\Delta t}\mathcal{A}\int_{\Omega_{el}} [\mathbf{N}^{p_w}]^T \alpha\, S_w\, \mathbf{I}_v\, [\mathbf{B}^{\mathbf{u}}]\, d\Omega, \\
\mathbf{K}^{p_wp_w} &= \mathcal{A}\int_{\Omega_{el}} \Bigg([\mathbf{B}^{p_w}]^T k_{rw}\,\mathbf{K}_{eff}\, [\mathbf{B}^{p_w}] \\
&\quad + [\mathbf{B}^{p_w}]^T \frac{\partial k_{rw}}{\partial p_w}\,\mathbf{K}_{eff}\Big(\boldsymbol{\nabla}p_w - \rho_w\,\mathbf{g}\Big)\, [\mathbf{N}^{p_w}] \\
&\quad + [\mathbf{N}^{p_w}]^T \Big(C_1 + \frac{\partial C_1}{\partial p_w}(p_w - {}^n p_w) \\
&\quad + C_2\frac{\partial S_w}{\partial p_w} + \frac{\partial C_2}{\partial p_w}(S_w - {}^n S_w)\Big)\, [\mathbf{N}^{p_w}] \Bigg)\, d\Omega, \\
\mathbf{K}^{p_w\varphi} &= \mathcal{A}\int_{\Omega_{el}} [\mathbf{B}^{p_w}]^T k_{rw}\frac{\partial\mathbf{K}_{eff}}{\partial\varphi}(\boldsymbol{\nabla}p_w - \rho_w\,\mathbf{g})\, [\mathbf{N}^{\varphi}] \\
\mathbf{K}^{\varphi\mathbf{u}} &= [\mathbf{K}^{\mathbf{u}\varphi}]^T \;\; \textit{if} \;\; \dot{\mathcal{H}} > 0, \;\; \textit{else} \;\; \mathbf{0}, \\
\mathbf{K}^{\varphi p_w} &= \mathbf{0},
\end{aligned} \tag{6.39c}$$

Discrete Problem 10 (continued)

$$
\begin{aligned}
\mathbf{K}^{\varphi\varphi} &= \mathcal{A}\int_{\Omega_{el}} \Bigg([\mathbf{B}^{\varphi}]^{\mathsf{T}} \left(\frac{G_c\, l}{c_w}\right) [\mathbf{B}^{\varphi}] \\
&\quad + [\mathbf{N}^{\varphi}]^{\mathsf{T}} \left(\frac{G_c}{c_w l} w''(\varphi) + g''(\varphi)\frac{\partial \mathcal{H}}{\partial \boldsymbol{\epsilon}}\right) [\mathbf{N}^{\varphi}] \Bigg)\, d\Omega,
\end{aligned}
$$

and the internal force vector components are computed as

$$
\begin{aligned}
\mathbf{f}^{ext,p_w} &= \mathcal{A}\int_{\Gamma_{N,el}} [\mathbf{N}^{p_w}]^{\mathsf{T}}\, q\; d\Gamma, \\
\mathbf{f}^{int,\mathbf{u}} &= \mathcal{A}\int_{\Omega_{el}} [\mathbf{B}^{\mathbf{u}}]^{\mathsf{T}} \left(g(\varphi)\boldsymbol{\sigma}^{+} + \boldsymbol{\sigma}^{-} - \alpha\, S_w\, p_w \mathbf{I}_v\right) d\Omega, \\
\mathbf{f}^{int,\varphi} &= \mathcal{A}\int_{\Omega_{el}} [\mathbf{B}^{\varphi}]^{\mathsf{T}} \frac{G_c\, l}{c_w} \boldsymbol{\nabla}\varphi \\
&\quad + [\mathbf{N}^{\varphi}]^{\mathsf{T}} \left(g'(\varphi)\mathcal{H} + \frac{G_c}{c_w\, l} w'(\varphi)\right) d\Omega, \qquad (6.39d) \\
\mathbf{f}^{int,p_w} &= \mathcal{A}\int_{\Omega_{el}} \Bigg([\mathbf{B}^{p_w}]^{\mathsf{T}} \mathbf{K}_{eff} \Big(\boldsymbol{\nabla} p_w - \rho_w\, \mathbf{g}\Big) \\
&\quad + [\mathbf{N}^{p_w}]^{\mathsf{T}} \frac{1}{\Delta t} \Big(C_1 (p_w - {}^{n}p_w) + C_2 (S_w - {}^{n}S_w) \\
&\quad + \alpha\, S_w\, (\epsilon_{vol} - {}^{n}\epsilon_{vol}) \Big) \Bigg)\, d\Omega.
\end{aligned}
$$

Note that $\mathcal{A}$ is an assembly operator that maps element contributions to their global counterparts. Furthermore, $\mathbf{I}_v$ is the Voigt representation of the identity matrix, the left superscript n refers to the previous time step, and $\mathscr{H}$ is the heaviside function. The material stiffness matrix $\mathbf{D}$ depends on the chosen strain energy density split (see Table 2.4). The history variable $\mathcal{H}$ is defined in (2.24). ■

Discrete Problem 11. *Compute the solution update vector* $\mathbf{s}_{k+1} = \{\Delta\tilde{\mathbf{u}}\,;\Delta\tilde{p}_w\,;\,\Delta\tilde{\varphi}\}$ *for the current iteration* $k+1$ *using*

$$\underbrace{\begin{bmatrix} \mathbf{K}^{\mathbf{u}\mathbf{u}} & \mathbf{K}^{\mathbf{u}p_w} & \mathbf{K}^{\mathbf{u}\varphi} \\ \mathbf{K}^{p_w\mathbf{u}} & \mathbf{K}^{p_wp_w} & \mathbf{K}^{p_w\varphi} \\ \mathbf{K}^{\varphi\mathbf{u}} & \mathbf{K}^{\varphi p_w} & \mathbf{K}^{\varphi\varphi} \end{bmatrix}}_{\text{Stiffness matrix, } \mathbf{K}_k} \underbrace{\begin{Bmatrix} \Delta\tilde{\mathbf{u}} \\ \Delta\tilde{p}_w \\ \Delta\tilde{\varphi} \end{Bmatrix}}_{\mathbf{s}_{k+1}} = \underbrace{\begin{Bmatrix} \mathbf{o} \\ \mathbf{f}^{ext,p_w} \\ \mathbf{o} \end{Bmatrix} - \begin{Bmatrix} \mathbf{f}^{int,\mathbf{u}} \\ \mathbf{f}^{int,p_w} \\ \mathbf{f}^{int,\varphi} \end{Bmatrix}}_{\text{Residual, } \mathbf{r}_k}, \tag{6.40a}$$

and update the solution,

$$\begin{Bmatrix} \tilde{\mathbf{u}} \\ \tilde{p}_w \\ \tilde{\varphi} \end{Bmatrix}_{k+1} = \begin{Bmatrix} \tilde{\mathbf{u}} \\ \tilde{p}_w \\ \tilde{\varphi} \end{Bmatrix}_{k} + \begin{Bmatrix} \Delta\tilde{\mathbf{u}} \\ \Delta\tilde{p}_w \\ \Delta\tilde{\varphi} \end{Bmatrix}_{k+1}, \tag{6.40b}$$

until the norm of the residual is sufficiently small. The stiffness matrix components are given by,

$$\begin{aligned}
\mathbf{K}^{\mathbf{u}\mathbf{u}} &= \mathcal{A}\int_{\Omega_{el}} [\mathbf{B}^{\mathbf{u}}]^T \Big(\underbrace{g(\varphi)\frac{\partial\boldsymbol{\sigma}^+}{\partial\boldsymbol{\epsilon}} + \frac{\partial\boldsymbol{\sigma}^-}{\partial\boldsymbol{\epsilon}}}_{\mathbf{D}} \Big) [\mathbf{B}^{\mathbf{u}}]\, d\Omega, \\
\mathbf{K}^{\mathbf{u}p_w} &= -\mathcal{A}\int_{\Omega_{el}} [\mathbf{B}^{\mathbf{u}}]^T h(\varphi)\,\alpha \Big(S_w + \frac{\partial S_w}{\partial p_w} p_w\Big)\mathbf{I}_v\, [\mathbf{N}^{p_w}]\, d\Omega \\
&\quad -\mathcal{A}\int_{\Omega_{el}} [\mathbf{N}^{\mathbf{u}}]^T n \frac{\partial S_w}{\partial p_w}\rho_w\,\mathbf{g}\, [\mathbf{N}^{p_w}]\, d\Omega \\
\mathbf{K}^{\mathbf{u}\varphi} &= \mathcal{A}\int_{\Omega_{el}} [\mathbf{B}^{\mathbf{u}}]^T \Big(g'(\varphi)\boldsymbol{\sigma}^+ - h'(\varphi)\alpha\, S_w\, p_w\, \mathbf{I}_v \Big)\, [\mathbf{N}^{\varphi}]\, d\Omega, \\
\mathbf{K}^{p_w\mathbf{u}} &= \frac{1}{\Delta t}\mathcal{A}\int_{\Omega_{el}} [\mathbf{N}^{p_w}]^T \alpha\, S_w\, \mathbf{I}_v\, [\mathbf{B}^{\mathbf{u}}]\, d\Omega, \\
\mathbf{K}^{p_wp_w} &= \mathcal{A}\int_{\Omega_{el}} \Bigg([\mathbf{B}^{p_w}]^T k_{rw}\, \mathbf{K}_{eff}\, [\mathbf{B}^{p_w}] \\
&\quad + [\mathbf{B}^{p_w}]^T \frac{\partial k_{rw}}{\partial p_w}\, \mathbf{K}_{eff}\Big(\boldsymbol{\nabla} p_w - \rho_w\,\mathbf{g}\Big)\, [\mathbf{N}^{p_w}] \\
&\quad + [\mathbf{N}^{p_w}]^T \Big(C_1 + \frac{\partial C_1}{\partial p_w}(p_w - {}^n p_w) \\
&\quad + C_2\frac{\partial S_w}{\partial p_w} + \frac{\partial C_2}{\partial p_w}(S_w - {}^n S_w)\Big)\, [\mathbf{N}^{p_w}] \Bigg)\, d\Omega, \qquad (6.40c) \\
\mathbf{K}^{p_w\varphi} &= \mathcal{A}\int_{\Omega_{el}} [\mathbf{B}^{p_w}]^T k_{rw} \frac{\partial \mathbf{K}_{eff}}{\partial\varphi}(\boldsymbol{\nabla} p_w - \rho_w\,\mathbf{g})\, [\mathbf{N}^{\varphi}] \\
\mathbf{K}^{\varphi\mathbf{u}} &= [\mathbf{K}^{\mathbf{u}\varphi}]^T \;\; \textit{if} \;\; \dot{\mathcal{H}} > 0, \;\; \textit{else} \;\; \mathbf{o}, \\
\mathbf{K}^{\varphi p_w} &= \mathbf{o},
\end{aligned}$$

Discrete Problem 11 (continued)

$$\begin{aligned}\mathbf{K}^{\varphi\varphi} &= \mathcal{A}\int_{\Omega_{el}}\left([\mathbf{B}^{\varphi}]^{\mathsf{T}}\left(\frac{G_c\, l}{c_w}\right)[\mathbf{B}^{\varphi}]\right.\\ &\quad\left.+[\mathbf{N}^{\varphi}]^{\mathsf{T}}\left(\frac{G_c}{c_w l}w''(\varphi)+g''(\varphi)\frac{\partial\mathcal{H}}{\partial\boldsymbol{\epsilon}}\right)[\mathbf{N}^{\varphi}]\right)\mathrm{d}\Omega,\end{aligned}$$

and the internal force vector components are computed as

$$\begin{aligned}\mathbf{f}^{ext,p_w} &= \mathcal{A}\int_{\Gamma_{N,el}}[\mathbf{N}^{p_w}]^{\mathsf{T}}\,q\;\mathrm{d}\Gamma,\\ \mathbf{f}^{int,\mathbf{u}} &= \mathcal{A}\int_{\Omega_{el}}[\mathbf{B}^{\mathbf{u}}]^{\mathsf{T}}\left(g(\varphi)\boldsymbol{\sigma}^{+}+\boldsymbol{\sigma}^{-}-h(\varphi)\,\alpha\,S_w\,p_w\mathbf{I}_v\right)\mathrm{d}\Omega,\\ \mathbf{f}^{int,\varphi} &= \mathcal{A}\int_{\Omega_{el}}[\mathbf{B}^{\varphi}]^{\mathsf{T}}\frac{G_c\, l}{c_w}\boldsymbol{\nabla}\varphi\\ &\quad+[\mathbf{N}^{\varphi}]^{\mathsf{T}}\left(g'(\varphi)\mathcal{H}+\frac{G_c}{c_w l}w'(\varphi)\right)\mathrm{d}\Omega, \qquad (6.40d)\\ \mathbf{f}^{int,p_w} &= \mathcal{A}\int_{\Omega_{el}}\left([\mathbf{B}^{p_w}]^{\mathsf{T}}\mathbf{K}_{eff}\left(\boldsymbol{\nabla}p_w-\rho_w\,\mathbf{g}\right)\right.\\ &\quad+[\mathbf{N}^{p_w}]^{\mathsf{T}}\frac{1}{\Delta t}\left(C_1(p_w-{}^{n}p_w)+C_2(S_w-{}^{n}S_w)\right.\\ &\quad\left.\left.+\alpha\,S_w\,(\epsilon_{vol}-{}^{n}\epsilon_{vol})\right)\right)\mathrm{d}\Omega.\end{aligned}$$

Note that $\mathcal{A}$ is an assembly operator that maps element contributions to their global counterparts. Furthermore, $\mathbf{I}_v$ is the Voigt representation of the identity matrix, the left superscript n refers to the previous time step, and $\mathscr{H}$ is the heaviside function. The material stiffness matrix $\mathbf{D}$ depends on the chosen strain energy density split (see Table 2.4). The degradation function $h(\varphi)$ is defined in (6.4). The history variable $\mathcal{H}$ is defined as

$$\mathcal{H}=\begin{cases}\max\left\{{}^{n}\mathcal{H},\Psi^{+}(\boldsymbol{\epsilon}[\mathbf{u}])-\alpha\,S_w\,p_w\,\epsilon_{vol}\right\}, & \text{if } p_w<0 \text{ and } \boldsymbol{\nabla}\cdot\mathbf{u}>0\\ \max\left\{{}^{n}\mathcal{H},\Psi^{+}(\boldsymbol{\epsilon}[\mathbf{u}])\right\}, & \text{otherwise.}\end{cases} \qquad (6.40e)$$

■

Discrete Problem 12. *Compute the solution update vector* $\mathbf{s}_{k+1} = \{\Delta\tilde{\mathbf{u}}\,;\Delta\tilde{p}_w\,;\,\Delta\tilde{\varphi}\}$ *for the current iteration* $k+1$ *using*

$$\underbrace{\begin{bmatrix} \mathbf{K}^{\mathbf{u}\mathbf{u}} & \mathbf{K}^{\mathbf{u}p_w} & \mathbf{K}^{\mathbf{u}\varphi} \\ \mathbf{K}^{p_w\mathbf{u}} & \mathbf{K}^{p_wp_w} & \mathbf{K}^{p_w\varphi} \\ \mathbf{K}^{\varphi\mathbf{u}} & \mathbf{K}^{\varphi p_w} & \mathbf{K}^{\varphi\varphi} \end{bmatrix}}_{\text{Stiffness matrix, } \mathbf{K}_k} \underbrace{\begin{Bmatrix} \Delta\tilde{\mathbf{u}} \\ \Delta\tilde{p}_w \\ \Delta\tilde{\varphi} \end{Bmatrix}}_{\mathbf{s}_{k+1}} = \underbrace{\begin{Bmatrix} \mathbf{0} \\ \mathbf{f}^{ext,p_w} \\ \mathbf{0} \end{Bmatrix} - \begin{Bmatrix} \mathbf{f}^{int,\mathbf{u}} \\ \mathbf{f}^{int,p_w} \\ \mathbf{f}^{int,\varphi} \end{Bmatrix}}_{\text{Residual, } \mathbf{r}_k}, \tag{6.41a}$$

and update the solution,

$$\begin{Bmatrix} \tilde{\mathbf{u}} \\ \tilde{p}_w \\ \tilde{\varphi} \end{Bmatrix}_{k+1} = \begin{Bmatrix} \tilde{\mathbf{u}} \\ \tilde{p}_w \\ \tilde{\varphi} \end{Bmatrix}_{k} + \begin{Bmatrix} \Delta\tilde{\mathbf{u}} \\ \Delta\tilde{p}_w \\ \Delta\tilde{\varphi} \end{Bmatrix}_{k+1}, \tag{6.41b}$$

until the norm of the residual is sufficiently small. The stiffness matrix components are given by,

$$\begin{aligned}
\mathbf{K}^{\mathbf{u}\mathbf{u}} &= \mathcal{A}\int_{\Omega_{el}} [\mathbf{B}^{\mathbf{u}}]^T \Bigg(\underbrace{g(\varphi)\frac{\partial \boldsymbol{\sigma}^{+}_{tot}}{\partial \boldsymbol{\epsilon}} + \frac{\partial \boldsymbol{\sigma}^{-}_{tot}}{\partial \boldsymbol{\epsilon}}}_{\mathbf{D}} \Bigg) [\mathbf{B}^{\mathbf{u}}]\, d\Omega, \\
\mathbf{K}^{\mathbf{u}p_w} &= -\mathcal{A}\int_{\Omega_{el}} [\mathbf{B}^{\mathbf{u}}]^T \left(g(\varphi)\frac{\partial \boldsymbol{\sigma}^{+}_{tot}}{\partial p_w} + \frac{\partial \boldsymbol{\sigma}^{-}_{tot}}{\partial p_w} \right) [\mathbf{N}^{p_w}]\, d\Omega \\
&\quad -\mathcal{A}\int_{\Omega_{el}} [\mathbf{N}^{\mathbf{u}}]^T n \frac{\partial S_w}{\partial p_w} \rho_w \mathbf{g}\, [\mathbf{N}^{p_w}]\, d\Omega \\
\mathbf{K}^{\mathbf{u}\varphi} &= \mathcal{A}\int_{\Omega_{el}} [\mathbf{B}^{\mathbf{u}}]^T \left(g'(\varphi)\boldsymbol{\sigma}^{+}_{tot} \right) [\mathbf{N}^{\varphi}]\, d\Omega, \\
\mathbf{K}^{p_w\mathbf{u}} &= \frac{1}{\Delta t}\mathcal{A}\int_{\Omega_{el}} [\mathbf{N}^{p_w}]^T \alpha S_w \mathbf{I}_v\, [\mathbf{B}^{\mathbf{u}}]\, d\Omega, \\
\mathbf{K}^{p_wp_w} &= \mathcal{A}\int_{\Omega_{el}} \Bigg([\mathbf{B}^{p_w}]^T k_{rw}\, \mathbf{K}_{eff}\, [\mathbf{B}^{p_w}] \\
&\quad + [\mathbf{B}^{p_w}]^T \frac{\partial k_{rw}}{\partial p_w}\, \mathbf{K}_{eff} \Big(\boldsymbol{\nabla} p_w - \rho_w \mathbf{g} \Big) [\mathbf{N}^{p_w}] \\
&\quad + [\mathbf{N}^{p_w}]^T \Big(C_1 + \frac{\partial C_1}{\partial p_w}(p_w - {}^n p_w) \\
&\quad + C_2 \frac{\partial S_w}{\partial p_w} + \frac{\partial C_2}{\partial p_w}(S_w - {}^n S_w) \Big) [\mathbf{N}^{p_w}] \Bigg)\, d\Omega, \qquad (6.41c) \\
\mathbf{K}^{p_w\varphi} &= \mathcal{A}\int_{\Omega_{el}} [\mathbf{B}^{p_w}]^T k_{rw} \frac{\partial \mathbf{K}_{eff}}{\partial \varphi} (\boldsymbol{\nabla} p_w - \rho_w \mathbf{g})\, [\mathbf{N}^{\varphi}] \\
\mathbf{K}^{\varphi\mathbf{u}} &= [\mathbf{K}^{\mathbf{u}\varphi}]^T \quad \textit{if } \mathcal{H} > 0, \quad \textit{else } \mathbf{0},
\end{aligned}$$

Discrete Problem 12 (continued)

$$
\begin{aligned}
\mathbf{K}^{\varphi p_w} &= \mathcal{A}\int_{\Omega_{el}} [\mathbf{N}^{\varphi}]^{\mathsf{T}} \left(g'(\varphi)\frac{\partial \mathcal{H}}{\partial p_w}\right) [\mathbf{N}^{\varphi}]\, \mathrm{d}\Omega, \quad \textit{if } \dot{\mathcal{H}} > 0, \quad \textit{else } \mathbf{o} \\
\mathbf{K}^{\varphi\varphi} &= \mathcal{A}\int_{\Omega_{el}} \Bigg([\mathbf{B}^{\varphi}]^{\mathsf{T}} \left(\frac{G_c\, l}{c_w}\right) [\mathbf{B}^{\varphi}] \\
&\quad + [\mathbf{N}^{\varphi}]^{\mathsf{T}} \left(\frac{G_c}{c_w l} w''(\varphi) + g''(\varphi)\frac{\partial \mathcal{H}}{\partial \boldsymbol{\epsilon}}\right) [\mathbf{N}^{\varphi}] \Bigg)\, \mathrm{d}\Omega,
\end{aligned}
$$

and the internal force vector components are computed as

$$
\begin{aligned}
\mathbf{f}^{ext,p_w} &= \mathcal{A}\int_{\Gamma_{N,el}} [\mathbf{N}^{p_w}]^{\mathsf{T}}\, q\, \mathrm{d}\Gamma, \\
\mathbf{f}^{int,\mathbf{u}} &= \mathcal{A}\int_{\Omega_{el}} [\mathbf{B}^{\mathbf{u}}]^{\mathsf{T}} \left(g(\varphi)\boldsymbol{\sigma}^{+}_{tot} + \boldsymbol{\sigma}^{-}_{tot}\right) \mathrm{d}\Omega, \\
\mathbf{f}^{int,\varphi} &= \mathcal{A}\int_{\Omega_{el}} [\mathbf{B}^{\varphi}]^{\mathsf{T}} \frac{G_c\, l}{c_w}\boldsymbol{\nabla}\varphi \\
&\quad + [\mathbf{N}^{\varphi}]^{\mathsf{T}} \left(g'(\varphi)\mathcal{H} + \frac{G_c}{c_w l} w'(\varphi)\right) \mathrm{d}\Omega, \qquad (6.41d) \\
\mathbf{f}^{int,p_w} &= \mathcal{A}\int_{\Omega_{el}} \Bigg([\mathbf{B}^{p_w}]^{\mathsf{T}}\, \mathbf{K}_{eff}\Big(\boldsymbol{\nabla} p_w - \rho_w\, \mathbf{g}\Big) \\
&\quad + [\mathbf{N}^{p_w}]^{\mathsf{T}} \frac{1}{\Delta t}\Big(C_1(p_w - {}^{n}p_w) + C_2(S_w - {}^{n}S_w) \\
&\quad + \alpha\, S_w\, (\epsilon_{vol} - {}^{n}\epsilon_{vol})\Big)\Bigg)\, \mathrm{d}\Omega.
\end{aligned}
$$

Note that $\mathcal{A}$ is an assembly operator that maps element contributions to their global counterparts. Furthermore, $\mathbf{I}_v$ is the Voigt representation of the identity matrix, the left superscript n refers to the previous time step, and $\mathscr{H}$ is the heaviside function. The material stiffness matrix $\mathbf{D}$ depends on the chosen strain energy density split (see Table 2.4). The history variable $\mathcal{H}$ is defined as

$$
\mathcal{H} = \max\left\{ {}^{n}\mathcal{H},\, \Psi^{+}_{tot}(\boldsymbol{\epsilon}_{tot}[\mathbf{u}, p_w])\right\}. \qquad (6.41e)
$$

■

Discrete Problem 13. *Compute the solution update vector* $\mathbf{s}_{k+1} = \{\Delta\tilde{\mathbf{u}}\,;\Delta\tilde{p}_w\,;\Delta\tilde{\varphi}\}$ *for the current iteration* $k+1$ *using*

$$\underbrace{\begin{bmatrix}\mathbf{K}^{\mathbf{u}\mathbf{u}} & \mathbf{K}^{\mathbf{u}p_w} & \mathbf{K}^{\mathbf{u}\varphi}\\ \mathbf{K}^{p_w\mathbf{u}} & \mathbf{K}^{p_wp_w} & \mathbf{K}^{p_w\varphi}\\ \mathbf{K}^{\varphi\mathbf{u}} & \mathbf{K}^{\varphi p_w} & \mathbf{K}^{\varphi\varphi}\end{bmatrix}}_{\text{Stiffness matrix, } \mathbf{K}_k}\underbrace{\begin{Bmatrix}\Delta\tilde{\mathbf{u}}\\ \Delta\tilde{p}_w\\ \Delta\tilde{\varphi}\end{Bmatrix}}_{\mathbf{s}_{k+1}} = \underbrace{\begin{Bmatrix}\mathbf{0}\\ \mathbf{f}^{ext,p_w}\\ \mathbf{0}\end{Bmatrix} - \begin{Bmatrix}\mathbf{f}^{int,\mathbf{u}}\\ \mathbf{f}^{int,p_w}\\ \mathbf{f}^{int,\varphi}\end{Bmatrix}}_{\text{Residual, } \mathbf{r}_k}, \tag{6.42a}$$

and update the solution,

$$\begin{Bmatrix}\tilde{\mathbf{u}}\\ \tilde{p}_w\\ \tilde{\varphi}\end{Bmatrix}_{k+1} = \begin{Bmatrix}\tilde{\mathbf{u}}\\ \tilde{p}_w\\ \tilde{\varphi}\end{Bmatrix}_{k} + \begin{Bmatrix}\Delta\tilde{\mathbf{u}}\\ \Delta\tilde{p}_w\\ \Delta\tilde{\varphi}\end{Bmatrix}_{k+1}, \tag{6.42b}$$

until the norm of the residual is sufficiently small. The stiffness matrix components are given by,

$$\begin{aligned}
\mathbf{K}^{\mathbf{u}\mathbf{u}} &= \mathcal{A}\int_{\Omega_{el}} [\mathbf{B}^{\mathbf{u}}]^T \Big(\underbrace{g(\varphi)\frac{\partial\boldsymbol{\sigma}^+_{sld}}{\partial\boldsymbol{\epsilon}} + \frac{\partial\boldsymbol{\sigma}^-_{sld}}{\partial\boldsymbol{\epsilon}}}_{\mathbf{D}}\Big)\,[\mathbf{B}^{\mathbf{u}}]\;d\Omega,\\
\mathbf{K}^{\mathbf{u}p_w} &= -\mathcal{A}\int_{\Omega_{el}} [\mathbf{B}^{\mathbf{u}}]^T \Big(g(\varphi)\frac{\partial\boldsymbol{\sigma}^+_{sld}}{\partial p_w} + \frac{\partial\boldsymbol{\sigma}^-_{sld}}{\partial p_w}\Big)\,[\mathbf{N}^{p_w}]\;d\Omega\\
&\quad -\mathcal{A}\int_{\Omega_{el}} [\mathbf{B}^{\mathbf{u}}]^T\, n\Big(S_w + \frac{\partial S_w}{\partial p_w}p_w\Big)\mathbf{I}_v\,[\mathbf{N}^{p_w}]\;d\Omega\\
&\quad -\mathcal{A}\int_{\Omega_{el}} [\mathbf{N}^{\mathbf{u}}]^T\, n\frac{\partial S_w}{\partial p_w}\rho_w\,\mathbf{g}\,[\mathbf{N}^{p_w}]\;d\Omega\\
\mathbf{K}^{\mathbf{u}\varphi} &= \mathcal{A}\int_{\Omega_{el}} [\mathbf{B}^{\mathbf{u}}]^T \Big(g'(\varphi)\boldsymbol{\sigma}^+_{sld}\Big)\,[\mathbf{N}^{\varphi}]\;d\Omega,\\
\mathbf{K}^{p_w\mathbf{u}} &= \frac{1}{\Delta t}\mathcal{A}\int_{\Omega_{el}} [\mathbf{N}^{p_w}]^T\,\alpha\,S_w\,\mathbf{I}_v\,[\mathbf{B}^{\mathbf{u}}]\;d\Omega,\\
\mathbf{K}^{p_wp_w} &= \mathcal{A}\int_{\Omega_{el}} \Big([\mathbf{B}^{p_w}]^T\,k_{rw}\,\mathbf{K}_{eff}\,[\mathbf{B}^{p_w}]\\
&\quad + [\mathbf{B}^{p_w}]^T\,\frac{\partial k_{rw}}{\partial p_w}\,\mathbf{K}_{eff}\Big(\boldsymbol{\nabla}p_w - \rho_w\,\mathbf{g}\Big)\,[\mathbf{N}^{p_w}]\\
&\quad + [\mathbf{N}^{p_w}]^T\Big(C_1 + \frac{\partial C_1}{\partial p_w}(p_w - {}^np_w)\\
&\quad + C_2\frac{\partial S_w}{\partial p_w} + \frac{\partial C_2}{\partial p_w}(S_w - {}^nS_w)\Big)\,[\mathbf{N}^{p_w}]\Big)\;d\Omega,\\
\mathbf{K}^{p_w\varphi} &= \mathcal{A}\int_{\Omega_{el}} [\mathbf{B}^{p_w}]^T\,k_{rw}\frac{\partial\mathbf{K}_{eff}}{\partial\varphi}(\boldsymbol{\nabla}p_w - \rho_w\,\mathbf{g})\,[\mathbf{N}^{\varphi}]
\end{aligned} \tag{6.42c}$$

Discrete Problem 13 (continued)

$$
\begin{aligned}
\mathbf{K}^{\varphi \mathbf{u}} &= [\mathbf{K}^{\mathbf{u}\varphi}]^{\mathsf{T}} \;\; \textit{if} \;\; \dot{\mathcal{H}} > 0, \;\; \textit{else} \;\; \mathbf{0}, \\
\mathbf{K}^{\varphi p_w} &= \mathcal{A} \int_{\Omega_{el}} [\mathbf{N}^{\varphi}]^{\mathsf{T}} \left(g'(\varphi) \frac{\partial \mathcal{H}}{\partial p_w} \right) [\mathbf{N}^{\varphi}] \, d\Omega, \;\; \textit{if} \;\; \dot{\mathcal{H}} > 0, \;\; \textit{else} \;\; \mathbf{0} \\
\mathbf{K}^{\varphi\varphi} &= \mathcal{A} \int_{\Omega_{el}} \Bigg([\mathbf{B}^{\varphi}]^{\mathsf{T}} \left(\frac{G_c \, l}{c_w} \right) [\mathbf{B}^{\varphi}] \\
&\quad + [\mathbf{N}^{\varphi}]^{\mathsf{T}} \left(\frac{G_c}{c_w l} w''(\varphi) + g''(\varphi) \frac{\partial \mathcal{H}}{\partial \boldsymbol{\epsilon}} \right) [\mathbf{N}^{\varphi}] \Bigg) \, d\Omega,
\end{aligned}
$$

and the internal force vector components are computed as

$$
\begin{aligned}
\mathbf{f}^{ext,p_w} &= \mathcal{A} \int_{\Gamma_{N,el}} [\mathbf{N}^{p_w}]^{\mathsf{T}} \, q \, d\Gamma, \\
\mathbf{f}^{int,\mathbf{u}} &= \mathcal{A} \int_{\Omega_{el}} [\mathbf{B}^{\mathbf{u}}]^{\mathsf{T}} \left(g(\varphi) \boldsymbol{\sigma}^{+}_{sld} + \boldsymbol{\sigma}^{-}_{sld} - n \, S_w \, p_w \, \mathbf{I}_v \right) d\Omega, \\
\mathbf{f}^{int,\varphi} &= \mathcal{A} \int_{\Omega_{el}} [\mathbf{B}^{\varphi}]^{\mathsf{T}} \frac{G_c \, l}{c_w} \boldsymbol{\nabla} \varphi \\
&\quad + [\mathbf{N}^{\varphi}]^{\mathsf{T}} \left(g'(\varphi) \mathcal{H} + \frac{G_c}{c_w \, l} w'(\varphi) \right) d\Omega, \qquad (6.42d) \\
\mathbf{f}^{int,p_w} &= \mathcal{A} \int_{\Omega_{el}} \Bigg([\mathbf{B}^{p_w}]^{\mathsf{T}} \mathbf{K}_{eff} \Big(\boldsymbol{\nabla} p_w - \rho_w \, \mathbf{g} \Big) \\
&\quad + [\mathbf{N}^{p_w}]^{\mathsf{T}} \frac{1}{\Delta t} \Big(C_1 (p_w - {}^{n}p_w) + C_2 (S_w - {}^{n}S_w) \\
&\quad + \alpha \, S_w \, (\epsilon_{vol} - {}^{n}\epsilon_{vol}) \Big) \Bigg) \, d\Omega.
\end{aligned}
$$

Note that $\mathcal{A}$ is an assembly operator that maps element contributions to their global counterparts. Furthermore, $\mathbf{I}_v$ is the Voigt representation of the identity matrix, the left superscript n refers to the previous time step, and $\mathcal{H}$ is the heaviside function. The material stiffness matrix $\mathbf{D}$ depends on the chosen strain energy density split (see Table 2.4). The history variable $\mathcal{H}$ is defined as

$$
\mathcal{H} = \max \left\{ {}^{n}\mathcal{H}, \, \Psi^{+}_{sld}(\boldsymbol{\epsilon}_{sld}[\mathbf{u}, p_w]) \right\}. \qquad (6.42e)
$$

■

In order to guarantee a unique solution for the chosen input parameters in the numerical experiments, the Discrete Problems 10, 11, 12 and 13 are discretized using Taylor and Hood elements [184]. A Taylor and Hood triangular element comprises of 6 nodes (3 vertices and 3 midway along the element edges). The displacement and phase-field Degrees Of Freedom (DOF) exist on all nodes, while the pressure DOFs are allocated only on the 3 vertex nodes. Compared to the 3-noded triangular element (used in

Chapters 3, 4 and 5), the Taylor and Hood is computationally expensive. This is consequence of fulfilling the LBB condition, discussed earlier in Section 6.2.3.

Remark 12. *An alternative approach to fulfill the LBB condition is through stabilization techniques that allows an equal order element for all solution fields (displacement, water pressure and phase-field). Examples of stabilization techniques include the Finite Calculus formulation [222], Fluid Pressure Laplacian method [223, 224], Polynomial Pressure Projection (PPP) method [225], and assumed strain finite element formulation [226, 227]. Besides Gavagnin, Sanavia, and De Lorenzis's PPP implementation for deviatoric fractures [51], to the best of the author's knowledge, the use of stabilization techniques for damage and fracture problems is absent. Most stabilization techniques are developed within the poro-elasticity framework.*

6.3 NUMERICAL EXPERIMENTS

In this section, soil desiccation cracking numerical experiments are carried out representative specimens. The objective is three-fold. Firstly, the role of energy functional constructs in modelling of the fracturing phenomenon is investigated in Section 6.3.1. Secondly, a parametric study exploring the role of specimen thickness (Section 6.3.2), bulk intrinsic permeability (Section 6.3.3) and the fracture model (Section 6.3.4) in the fracturing process. A comparison of the observed trends is made with those obtained experimentally by Stirling, Glendinning, and Davie [228] and Peron et al. [205]. Finally, in Section 6.3.5, the computational efficiency of the monolithic solution techniques are discussed.

Two rectangular specimens are considered for the numerical experiments and are shown in Figure 6.1. The smaller specimen measuring 50 [mm] by 30 [mm] is embedded with a notch located midway on the top surface. In order to force a single crack emanating from the notch, roller supports constraint the left and right edges, while the bottom edge remains fixed. The outflux of the water content takes places on the top edge. Next, the larger specimen is a rectangular block measuring 300 [mm] in width while the thickness H is varied. The specimen is devoid of any notches. Unlike the smaller specimen, in this specimen, the displacements are constrained in both directions on the left, right and bottom edges. The outflux of water content takes place on the top edge. The geometry of the larger specimen is inspired from Peron et al.'s desiccation cracking experiments [205]. Both specimens are discretized using 6-noded Taylor and Hood elements [184] The use of LBB condition violating 3-noded constant strain elements result in orthogonal widening of fracture as shown in Appendix A.

In the context of material properties, the Lower Durham Boulder (LDB) clay is adopted due to the thorough material characterization (composition via XRD analysis, geo-technical classification, availability of mechanical

and retention model parameters [204, 228]). The LDB clay was used in the construction of the BIONICS full-scale trial embankment near Newcastle-upon-Tyne in the United Kingdom [229, 230]. Stirling, Glendinning, and Davie [228] proposed the relevant mechanical and retention model parameters for numerical modelling of desiccation cracking. The Young's modulus E_0 and the tensile strength f_t were considered gravimetric water content dependent. They are expressed as

$$E_0 = 1770 \cdot 10^6 \, e^{(-14\, wc)} \quad \text{[Pa]} \tag{6.43}$$

$$f_t = 228.85 \cdot 10^3 \, e^{(-29.7\, wc)} \, \text{[Pa]}, \tag{6.44}$$

where, the gravimetric water content wc is computed as

$$wc = \frac{n\, S_w}{(1-n)\gamma_{sp}}, \text{ with soil specific gravity, } \gamma_{sp} = 2.65. \tag{6.45}$$

Using the above relations, water content dependent Griffith fracture toughness G_c is given by

$$G_c = \begin{cases} \dfrac{6\,l}{E_0}\left(\dfrac{16\, f_t}{9}\right)^2 & \text{Brittle AT2} \\ \dfrac{l_{ch}\, f_t^2}{E_0} & \text{Cohesive zone.} \end{cases} \tag{6.46}$$

Additional model parameters adopted for the soil desiccation cracking numerical experiments are presented in Table 6.1.

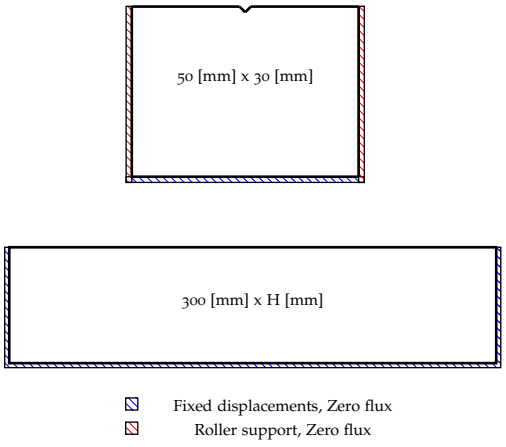

Figure 6.1: Soil desiccation cracking specimens

Parameters	**Value** [Units]
Fracture Model	Varied (AT2, CZM-Linear)
Energy Split	Vol-Dev [72]
ν	0.3 [-]
l	0.002 [m]
l_{ch}	Varied [m]
α	1.0 [-]
n	0.5 [-]
$k_{i,b}$	Varied [m^2]
μ_w	1e-3 [Pa s]
C_s	1e-10 [Pa]
C_w	4.54e-10 [Pa]
α_{VG}	0.028 [m^{-1}]
n_{VG}	1.3 [-]
Δt	5 [s]
q^p	6e-7 [m/s]

Table 6.1: Model parameters

Finally, the numerical experiments are carried out using the Hessian scaling method (see Section 3.3.2). In adapting the method for the desiccation

cracking Discrete Problems 10, 11, 12 and 13, the stiffness matrix block $\mathbf{K}^{p_w\varphi}$ is explicitly set to zero. Furthermore, the iterative procedure in every step is terminated when the error defined as the ratio of the norm of the residual in the current iteration to that of the first iteration is less than 10^{-4}. The shared memory Pardiso solver from Intel's oneAPI Math Kernel Library [64] is used to solve the linear problem in each iteration.

6.3.1 *Choice of energy functional*

The investigation into the role of energy functional constructs in soil desiccation cracking is carried out using the small specimen with a single notch (see Figure 6.1). The Discrete Problems 10, 11, 12 and 13 corresponding to the energy functionals E_1, E_2, E_3 and E_4 are solved using the model parameters presented in Table 6.1. The brittle AT2 fracture model is chosen for this study, and the intrinsic permeability κ_i is set to $1e-15$ [m^2]. Furthermore, the effective permeability $\mathbf{K}_{eff}$ (6.19) irrespective of fracture is explicitly set to the bulk permeability $\mathbf{K}_b$. This is done to highlight the development of pressure localization in the fracture for the total strain-based energy functional E_3 without introducing a fracture permeability $\mathbf{K}_f > \mathbf{K}_b$. The other energy functionals do not exhibit this pressure localization.

Figure 6.2 presents the phase-field distribution in the notched specimen at the first instance of fracture propagation corresponding to the energy functionals E_1, E_2, E_3 and E_4. It is observed that the energy functionals E_1 and E_2 yield identical phase-field distributions. The reason being the specimen remaining under compression throughout the simulation. Consequently, there is no difference between E_1 and E_2 (cf. (6.1) and (6.3)).

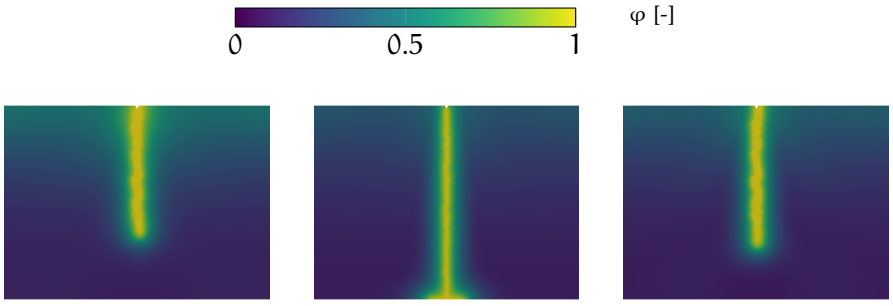

(a) E_1 and E_2, t = 1240 [s] (b) E_3, t = 1105 [s] (c) E_4, t = 1240 [s]

Figure 6.2: Figures (a-c) present the distribution of the phase-field variable pertinent to the energy functionals E_1, E_2, E_3 and E_4 during the analysis of the small notched specimen. The time stamp presented records the first instance of fracture propagation.

Figure 6.2 also presents another noticeable feature pertaining the choice of energy functionals, i.e., the length of the fracture. At the first instance of fracture propagation, E_3 results in a complete fracture of the notched specimen at 1105 seconds. This feature is attributed to the mixed (I and II) mode fracturing phenomenon. The total volumetric strain shown in Figure 6.3b contributes to the fracturing phenomenon in addition to the deviatoric

strain energy component. In energy functionals E_1 and E_2, the contribution of the volumetric strain in the fracturing process is missing, due to its compressive nature (see Figure 6.3a). However, for the energy functional E_4, the positive solid strain volumetric contribution ahead of the fracture tip (see Figure 6.3c) contributes to the fracturing process. This explains the increase in the fracture length for the E_4 case, compared to E_1 and E_2. However, compared to the total strain based energy functional E_3, the E_4 incorporates only a part of the suction in its computation of the volumetric strain (cf. (6.5) and (6.7)). This explains the shorter fracture length observed with E_4 compared to the E_3 case.

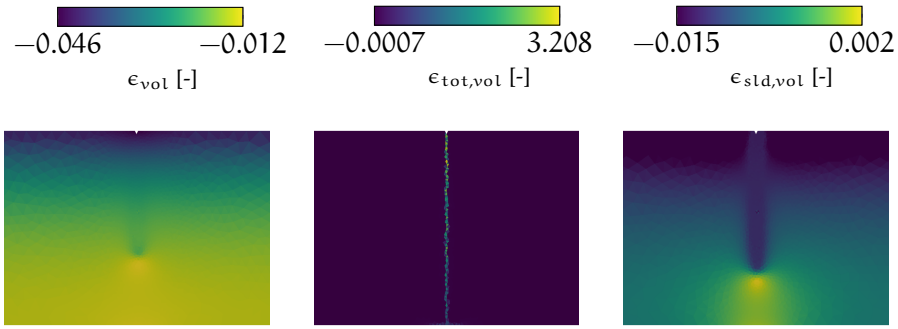

(a) E_1 and E_2, t = 1240 [s] (b) E_3, t = 1105 [s] (c) E_4, t = 1240 [s]

Figure 6.3: Figures (a-c) present the distribution of the different volumetric strain measures pertinent to the energy functionals E_1, E_2, E_3 and E_4 during the analysis of the small notched specimen.

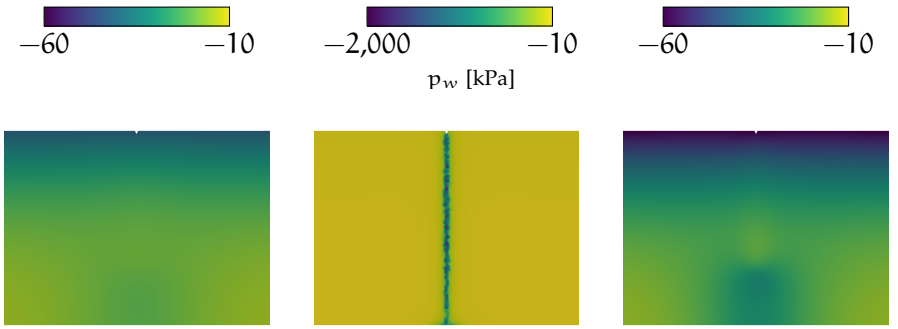

(a) E_1 and E_2, t = 1240 [s] (b) E_3, t = 1105 [s] (c) E_4, t = 1240 [s]

Figure 6.4: Figures (a-c) present the distribution of the water pressure with energy functionals E_1, E_2, E_3 and E_4 during the analysis of the small notched specimen. The effective permeability $\mathbf{K}_{eff}$ (6.19) explicitly set to the bulk permeability $\mathbf{K}_b$.

Figure 6.4 presents the water pressure distribution corresponding to the phase-field distributions in Figure 6.2. Due to the effective permeability $\mathbf{K}_{eff}$ explicitly set to the bulk permeability $\mathbf{K}_b$, the energy functionals E_1, E_2 and E_4 do not exhibit any localization of the water pressure. However, in the case of the total strain-based energy functional E_3, the water pressure localizes in the fracture. This behaviour is attributed to the drop in saturation levels from 100% to $\approx$ 70% in the fracture zone and subsequent change in

the relative permeability. For E_1, E_2 and E_4, the saturation level remains close to 99% even in the fracture. Therefore, the pressure localization is not observed. For these energy functionals, the localization of water pressure is triggered upon enhancing the effective permeability $\mathbf{K}_{eff}$ (6.19) with a fracture permeability contribution $\mathbf{K}_f > \mathbf{K}_b$.

Figure 6.5 presents the water pressure distribution for the energy functionals E_1, E_2 and E_4 upon introducing a fracture permeability based on Witherspoon et al.'s relation (6.17) [181]. Despite the saturation level remaining close to 99% even in the fracture, the fracture permeability $\mathbf{K}_f > \mathbf{K}_b$ induces a localization in the water pressure.

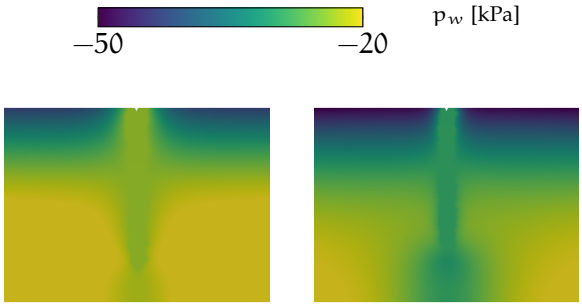

(a) E_1 and E_2, t = 1240 [s] (b) E_4, t = 1240 [s]

Figure 6.5: Figures (a-b) present the distribution of the water pressure with energy functionals E_1, E_2 and E_4 during the analysis of the small notched specimen. The effective permeability $\mathbf{K}_{eff}$ (6.19) is enhanced with a fracture permeability $\mathbf{K}_f$ (6.17).

6.3.2 *Effect of specimen thickness*

The investigation into the effect of specimen thickness in soil desiccation cracking is carried out using the long specimen devoid of notches (see Figure 6.1). The specimen thickness is varied as $H = 12.5$ [mm] and 50 [mm].

Based on the numerical studies conducted by Stirling, Glendinning, and Davie [228], material heterogeneity is incorporated by adopting a random Gaussian distribution of the porosity. A standard deviation 5% of the mean porosity is assumed. Furthermore, the numerical experiment is limited to the Discrete Problem 13 (corresponding to the novel energy functional E_4) and the brittle AT2 fracture model. The intrinsic permeability κ_i is set to $1e-15$ [m^2] and the other model parameters required for the analyses are presented in Table 6.1. Note that the fracture permeability $\mathbf{K}_f$ is computed using Witherspoon et al.'s relation (6.17) [181].

Figure 6.6 presents the phase-field distributions observed with varying thickness of the long specimen. An increase in the specimen thickness from 12.5 [mm] to 50 [mm] led to a reduction in the number of cracks reaching the bottom edge from 6 to 4 (excluding the detachment on the left and right edges). Tollenaar, van Paassen, and Jommi [231] attributed this behaviour partly to the desiccation rates, i.e., thinner specimen dries quickly. Scherer

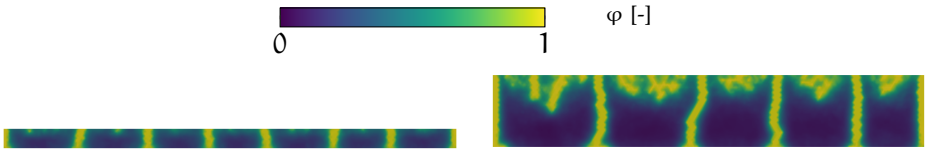

(a) H = 12.5 [mm], t = 5500 [s] (b) H = 50 [mm], t = 25000 [s]

Figure 6.6: Figures (a-b) present the phase-field distributions corresponding to varying thickness of the specimen. The bulk intrinsic permeability κ_i is set to $1e-15$ [m^2].

[232] stated that the drying fronts are irregular during the quicker drying processes, contributing to the presence of more flaws, thereby leading to the generation of more fractures. The specimen thickness dependent number of desiccation cracks were reported in the experimental studies by Peron et al. [205] and Tollenaar, van Paassen, and Jommi [231], albeit with a different set of specimen geometries.

6.3.3 *Effect of bulk intrinsic permeability*

The investigation into the effect of bulk intrinsic permeability in soil desiccation cracking is carried out using the long specimen devoid of notches (see Figure 6.1) with a fixed thickness $H = 50$ [mm]. The bulk intrinsic permeability is varied as $\kappa_i = 5e-15$ [m^2] and $1e-15$ [m^2]. Note that the fracture permeability $\mathbf{K}_f$ is computed using Witherspoon et al.'s relation (6.17) [181]. Similar to the previous section, material heterogeneity is incorporated by adopting a random Gaussian distribution of the porosity. A standard deviation 5% of the mean porosity is assumed. Furthermore, the numerical experiment is limited to the Discrete Problem 13 (corresponding to the novel energy functional E_4) and the brittle AT2 fracture model. The other model parameters required for the analyses are presented in Table 6.1.

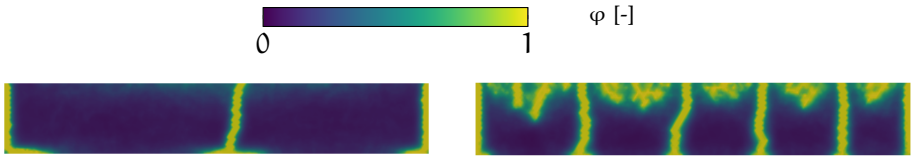

(a) $\kappa_i = 5e-15$ [m^2], t = 15000 [s] (b) $\kappa_i = 1e-15$ [m^2], t = 25000 [s]

Figure 6.7: Figures (a-b) present the phase-field distributions corresponding to varying bulk intrinsic permeability κ_i. The specimen thickness is fixed at 50 [mm].

Figure 6.7 presents the phase-field distributions observed with varying bulk intrinsic permeability for the long specimen with fixed thickness, 50 [mm]. Figure 6.7b corresponding to $\kappa_i = 1e-15$ [m^2] is the same as Figure 6.6b. On comparing with Figure 6.7a corresponding to $\kappa_i = 5e-15$ [m^2], it is clear that an increase in the bulk intrinsic permeability leads to a reduction in the number of cracks. Similar observations from numerical experiments were also reported in [48, 49]. According to Stirling, Glendinning, and Davie [228], a lower bulk intrinsic permeability reduces the ability of the water to migrate from the specimen depth to the drying surface under capillary

forces. Subsequently, it leads to the formation of the desiccated crust in an accelerated fashion through multiple cracks.

6.3.4 *Effect of fracture model type*

The investigation into the effect of fracture model (brittle or quasi-brittle) type in soil desiccation cracking is carried out using the long specimen devoid of notches (see Figure 6.1) with a fixed thickness $H = 50$ [mm]. Two fracture model types are considered in this study, brittle AT2 model and the Cohesive Zone Model with Linear softening (CZM-Linear) model. For the CZM-Linear model, Irwin's characteristic length is varied as 50 [mm], 100 [mm] and 200 [mm]. These chosen values lies in the range 20 [mm] to 500 [mm] reported by Lakshmikantha, Prat, and Ledesma [210] for clayey soils. Furthermore, the bulk intrinsic permeability κ_i is set to $1e-15$ [m^2], while the fracture permeability $\mathbf{K}_f$ is computed using Witherspoon et al.'s relation (6.17) [181]. Similar to the previous section, material heterogeneity is incorporated by adopting a random Gaussian distribution of the porosity. A standard deviation 5% of the mean porosity is assumed. The numerical experiment is limited to the Discrete Problem 13 (corresponding to the novel energy functional E_4). The additional model parameters required for the analyses are presented in Table 6.1.

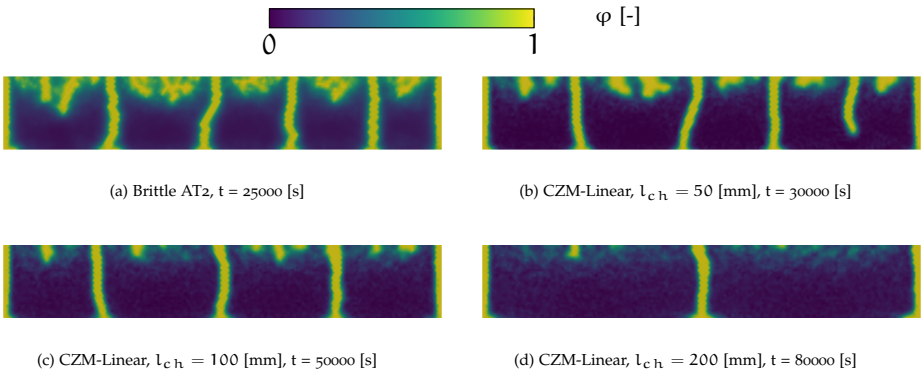

(a) Brittle AT2, t = 25000 [s]

(b) CZM-Linear, $l_{ch} = 50$ [mm], t = 30000 [s]

(c) CZM-Linear, $l_{ch} = 100$ [mm], t = 50000 [s]

(d) CZM-Linear, $l_{ch} = 200$ [mm], t = 80000 [s]

Figure 6.8: Figures (a-d) present the phase-field distributions corresponding to the different fracture models, brittle AT2 and Cohesive Zone Model with Linear softening (CZM-Linear). The specimen thickness is fixed at 50 [mm] and l_{ch} represents the fracture characteristic length.

Figure 6.8 presents the phase-field distributions observed with varying fracture model types, namely the Brittle AT2 model and the Cohesive Zone Model with Linear Softening (CZM-Linear). As observed earlier in Figures 6.7b and 6.6b, the Brittle AT2 model exhibits 4 cracks that reach the bottom of the specimen (excluding the detachment on the left and right edges). A similar observation is made with the CZM-Linear model using $l_{ch} = 50$ [mm]. The reason for this behaviour is that a vanishing l_{ch} asymptotically recovers Griffith's brittle fracture case [233]. However, as one opts for higher values of l_{ch}, not only does the number of cracks reduced but also they appear at a later time during the analyses (see Figures 6.8c and 6.8d). The

behaviour is attributed to the higher Griffith's fracture toughness G_c with increasing l_{ch} through the relation (6.46).

6.3.5 *Computational efficiency*

This section presents a study on the computational efficiency of the Hessian scaling method and the BFGS method in the context of the soil desiccation cracking model. The relevant theoretical details of these methods are presented in Section 3.3.1 and 3.3.4, respectively. The total and average number of iterations required to achieve convergence for the entire simulation and the CPU time are considered as the efficiency measures. Furthermore, the iteration terminating tolerances are varied as 10^{-4} and 10^{-6}. The simulations are carried out on the Vera cluster at the Chalmers Centre for Computational Science and Engineering. Five cores are utilized on Intel Xeon Gold 6130 processors with 15 GB RAM for multi-threaded assembly of the stiffness matrix and the force vectors. The linear problem in every iteration is solved using the shared memory Pardiso solver from Intel's oneAPI Math Kernel Library [64].

A single numerical experiment setup is chosen for the efficiency assessment of the monolithic solution techniques. The long specimen devoid of notches (see Figure 6.1) is chosen with dimensions 300 [mm] by 12.5 [mm]. The specimen is discretized using 2596 6-noded Taylor-Hood elements, yielding 15278 Degrees of Freedom (DOFs) upon incorporating the necessary Dirichlet boundary conditions. Moreover, similar to previous studies, material heterogeneity is incorporated by adopting a random Gaussian distribution of the porosity. A standard deviation 5% of the mean porosity is assumed. The numerical experiment is limited to the Discrete Problem 13 (corresponding to the novel energy functional E_4) and the brittle AT2 fracture model. The intrinsic permeability κ_i is set to $1e-15$ [m^2] and the other model parameters required for the analyses are presented in Table 6.1. Note that the fracture permeability $\mathbf{K}_f$ is computed using Witherspoon et al.'s relation (6.17) [181]. Figure 6.6a presents the phase-field distribution at 5500 seconds, which is the final time of the simulation.

Solution technique	tol	Steps (Failed)	Total Iters.	Avg. Iters.	CPU time [hour]
BFGS	10^{-4}	1108 (4)	39958	36.06	14.98
	10^{-6}	NC	-	-	-
Hessian scaling	10^{-4}	1104 (9)	46635	42.24	24.66
	10^{-6}	1116 (33)	183075	164.04	50.85

Table 6.2: Table presents the total numbers of steps and iterations, average iterations and CPU time (in hours) for the soil desiccation cracking specimen, simulated using the BFGS and Hessian scaling methods with varying iteration terminating tolerances. The failure to converge for the entire simulation is indicated with NC (Not Converged).

Table 6.2 presents the computational efficiency measures obtained for the soil desiccation cracking specimen. For the iteration terminating tolerance 10^{-4}, the BFGS method performs better than the Hessian scaling method in

terms of iterations required for convergence. The lesser number of iterations also reflects in the CPU time expended for the simulation. However, upon using a stricter tolerance 10^{-6}, the BFGS method fails to achieve convergence at the onset of fracture propagation in the specimen. On the contrary, the Hessian scaling method converges for the entire simulation, demonstrating a higher degree of robustness.

Part IV

MULTI-SCALE MODELLING OF FRACTURES

Development of multi-scale techniques for homogenization of fractured media (Research Objective 4).

7

A MULTI-SCALE FRAMEWORK FOR PHASE-FIELD FRACTURE MODEL

This chapter presents a variationally consistent multi-scale phase-field fracture model for materials exhibiting a hierarchy of length scales. The reader is first introduced to the state of the art and the limitations of the current multi-scale models in Section 7.1. Thereafter, the Variationally Consistent Homogenization (VCH) technique (see Section 2.4.1) is used to develop a hierarchical two-scale phase-field fracture model in Section 7.2. Therein, the coarse scale as well as the fine scale (RVE) variational problems are presented. Numerical experiments on RVEs are presented in Section 7.3. The chapter concludes with an academic FE^2 problem in Section 7.4, demonstrating solvability of the multi-scale equations in a coupled sense.

7.1 STATE OF THE ART AND LIMITATIONS

The phase-field fracture model has been employed for studying fracturing phenomenon on a single scale, i.e., at the coarse/engineering scale of observation. This includes brittle fracture of glass [234], ductile fracture of metals [235–237], quasi-brittle concrete fracture [238], fracture due to bending of thin films [239], hydraulic fracturing [40, 41, 49, 173–178], soil desiccation cracking [48, 49], and corrosion assisted cracking [240] to cite a few. In this thesis as well, so far, the models and the numerical experiments are confined to single scale studies (in Chapters 3 to 6). The application of the phase-field fracture model in a multi-scale context is rather sparse. There has been a few studies involving the resolved scale method (multi-scale finite element method [52–54] and global-local method [241]) and upscaling/hierarchical method [56, 57].

The resolved scale multi-scale modelling approach employs coarse and fine scale physics in different parts of the computational domain. At the interface between the scales, exchange of information is carried out. Among the different types of resolved scale methods, Patil, Mishra, and Singh [52] used the Multi-scale Finite Element Method (MsFEM) for brittle fracture problems. The authors then extended their study for modelling failure in composites [53], and for fractures in highly heterogeneous materials (matrix with voids and/or inclusions) [54]. The MsFEM [119–122] embeds a fine scale domain within a coarse scale element. The effect of the fine scale features (voids, cracks and other heterogeneities) are then transferred onto the coarse scale using multi-scale basis functions, computed numerically on-the-fly. However, the MsFEM is applicable when the coarse scale and the fine scale features are comparable in terms of the length-scale. If the fine scale features are several orders of magnitude lower than the coarse scale in

length-scale, the MsFEM fine scale problem may be prohibitively expensive. Similar restrictions also apply to another resolved scale method, the global-local method [123]. The global-local method was used in conjunction with the phase-field fracture models by Gerasimov et al. [241].

Contrary to the resolved scale method, the upscaling/hierarchical multi-scale modelling technique assumes a separation of scales between the coarse scale and the fine scale. Based on averaging (homogenization) techniques and statistical representativeness, smaller[1] fine scale domain may be used. He, Schuler, and Newell [56] adopted the Finite Element-Heterogeneous Multi-scale Method (FE-HMM) for computing the coarse scale (homogenized) elastic stiffness tensor, accounting for fine scale pore structure. However, fractures in the fine scale was not considered in the study. In another study, Fantoni et al. [57] obtained homogenized responses of fine scale microstructures with varying phase-field fracture values in an offline phase. Thereafter, the coarse scale material response was computed using a closed-form expression based on two-scale asymptotic homogenization and interpolation of the phase-field variable. Such a method, however, requires the computation of all possible fracturing scenarios in the fine scale. This could be a prohibitively challenging task. An elegant alternative upscaling/hierarchical multi-scale phase-field framework may be devised that accounts for the pertinent physics on both the coarse and the fine scale. To that end, the Variationally Consistent Homogenization (VCH) technique [128] is adopted. The VCH technique has been adopted to develop hierarchical multi-scale frameworks to study porous media [242–246], chloride diffusion in concrete [247], gradient-enhanced visco-plastic dissipative materials [248], computational homogenization of fine scale fracture modelled with the eXtended Finite Element Method (XFEM) [249, 250], reinforced concrete [251, 252], upscaling of chemo-mechanical and electro-chemical properties of battery electrolyte [253, 254], and homogenization of plates [255], to cite a few. However, the VCH technique has not yet been adopted for phase-field fracture models.

7.2 MULTI-SCALE PHASE-FIELD FRACTURE MODEL

A variationally consistent multi-scale phase-field fracture model is developed using the VCH technique. The important theoretical concepts pertinent to the VCH techniques has been addressed earlier in Section 2.4.1. The Variational Problem 3 is used as the point of departure from the single fully resolved scale analysis to a multi-scale one.

1 compared to that in the resolved scale methods

7.2.1 *Variational Multi-Scale (VMS) method*

Let us consider the variational equations (2.25a, 2.25b) for the phase-field fracture model excluding surface traction and body force,

$$\int_\Omega \left(g(\varphi) \frac{\partial \Psi^+(\boldsymbol{\epsilon}[\mathbf{u}])}{\partial \boldsymbol{\epsilon}} + \frac{\partial \Psi^-(\boldsymbol{\epsilon}[\mathbf{u}])}{\partial \boldsymbol{\epsilon}} \right) : \boldsymbol{\epsilon}[\delta \mathbf{u}] \, d\Omega = 0, \tag{7.1a}$$

$$\int_\Omega \left(g'(\varphi) \mathcal{H}(\boldsymbol{\epsilon}[\mathbf{u}^M + \mathbf{u}^S]) + \frac{G_c}{c_w \, l} w'(\varphi) \right) \delta\varphi \, d\Omega + \int_\Omega \frac{G_c \, l}{c_w} \boldsymbol{\nabla}\varphi \cdot \boldsymbol{\nabla}\delta\varphi \, d\Omega = 0. \tag{7.1b}$$

The Variational Multi-Scale (VMS) method admits an additive decomposition of the solution fields $(\mathbf{u}, \varphi)$ and the test functions $(\delta\mathbf{u}, \delta\varphi)$ as

$$\mathbf{u} = \mathbf{u}^M + \mathbf{u}^S \quad \text{and} \quad \delta\mathbf{u} = \delta\mathbf{u}^M + \delta\mathbf{u}^S, \tag{7.2a}$$

$$\varphi = \varphi^M + \varphi^S \quad \text{and} \quad \delta\varphi = \delta\varphi^M + \delta\varphi^S. \tag{7.2b}$$

Substituting (7.2a) and (7.2b) in (7.1a) and (7.1b) results in a set of coarse scale variational equations,

$$\int_\Omega \underbrace{\left(g(\varphi^M + \varphi^S) \frac{\partial \Psi^+(\boldsymbol{\epsilon}[\mathbf{u}^M + \mathbf{u}^S])}{\partial \boldsymbol{\epsilon}} + \frac{\partial \Psi^-(\boldsymbol{\epsilon}[\mathbf{u}^M + \mathbf{u}^S])}{\partial \boldsymbol{\epsilon}} \right)}_{\boldsymbol{\sigma}(\varphi^M + \varphi^S, \boldsymbol{\epsilon}[\mathbf{u}^M + \mathbf{u}^S])} : \boldsymbol{\epsilon}[\delta\mathbf{u}^M] \, d\Omega = 0, \tag{7.3a}$$

$$\begin{aligned} \int_\Omega \underbrace{\left(g'(\varphi^M + \varphi^S) \mathcal{H}(\boldsymbol{\epsilon}[\mathbf{u}^M + \mathbf{u}^S]) + \frac{G_c}{c_w \, l} w'(\varphi^M + \varphi^S) \right)}_{\Upsilon(\varphi^M + \varphi^S, \boldsymbol{\epsilon}[\mathbf{u}^M + \mathbf{u}^S])} \delta\varphi^M \, d\Omega \\ + \int_\Omega \underbrace{\frac{G_c \, l}{c_w} \boldsymbol{\nabla}(\varphi^M + \varphi^S)}_{\Phi(\varphi^M + \varphi^S)} \cdot \boldsymbol{\nabla}\delta\varphi^M \, d\Omega = 0, \end{aligned} \tag{7.3b}$$

and a set of fine scale variational equations,

$$\int_\Omega \underbrace{\left(g(\varphi^M + \varphi^S) \frac{\partial \Psi^+(\boldsymbol{\epsilon}[\mathbf{u}^M + \mathbf{u}^S])}{\partial \boldsymbol{\epsilon}} + \frac{\partial \Psi^-(\boldsymbol{\epsilon}[\mathbf{u}^M + \mathbf{u}^S])}{\partial \boldsymbol{\epsilon}} \right)}_{\boldsymbol{\sigma}(\varphi^M + \varphi^S, \boldsymbol{\epsilon}[\mathbf{u}^M + \mathbf{u}^S])} : \boldsymbol{\epsilon}[\delta\mathbf{u}^S] \, d\Omega = 0, \tag{7.4a}$$

$$\int_\Omega \underbrace{\left(g'(\varphi^M + \varphi^S)\mathcal{H}(\boldsymbol{\epsilon}[\mathbf{u}^M + \mathbf{u}^S]) + \frac{G_c}{c_w l} w'(\varphi^M + \varphi^S) \right)}_{\Upsilon(\varphi^M+\varphi^S, \boldsymbol{\epsilon}[\mathbf{u}^M+\mathbf{u}^S])} \delta\varphi^S \, d\Omega + \int_\Omega \underbrace{\frac{G_c l}{c_w} \boldsymbol{\nabla}(\varphi^M + \varphi^S)}_{\Phi(\varphi^M+\varphi^S)} \cdot \boldsymbol{\nabla}\delta\varphi^S \, d\Omega = 0. \tag{7.4b}$$

Note the shorthand expressions $\boldsymbol{\sigma}(\varphi^M + \varphi^S, \boldsymbol{\epsilon}[\mathbf{u}^M + \mathbf{u}^S])$, $\Upsilon(\varphi^M + \varphi^S, \boldsymbol{\epsilon}[\mathbf{u}^M + \mathbf{u}^S])$ and $\Phi(\varphi^M + \varphi^S)$ in the above equations. Henceforth, they would used wherever brevity is suited.

The coarse scale and fine scale variational equations operate over the entire computational domain. However, further assumptions may be made on the fine scale test functions $\delta\mathbf{u}^S$ and $\delta\varphi^S$. Depending on their existence, the fine scale variational equations may be localized to sub-domains, resulting in a resolved scale method, similar to Patil, Mishra, and Singh [52]. However, with the VCH technique, the fine scale test functions $\delta\mathbf{u}^S$ and $\delta\varphi^S$ instead localize to the coarse scale integration points.

7.2.2 *Homogenization of integrals*

Upon localizing the fine scale test functions $\delta\mathbf{u}^S$ and $\delta\varphi^S$ to coarse scale integration points, the fine scale domain becomes independent of the coarse scale discretization. This allows the use of computational homogenization technique [138–141], wherein the fine scale domain is only required to contain sufficient statistical information to capture the fine scale physics. For this reason, the fine scale domain is also referred to as microstructure, RVE [125] or SVE [126]. Henceforth, the term RVE is used interchangeably with fine scale domain. The RVE domain is represented using $\Omega_\square$.

The computational homogenization technique allows restating the integrands in the coarse scale and fine scale variational equations as averages over the RVE domain (2.60). Using the shorthand expressions, the coarse scale variational equations (7.3a, 7.3b) are restated as

$$\int_\Omega \left\langle \boldsymbol{\sigma}(\varphi^M + \varphi^S, \boldsymbol{\epsilon}[\mathbf{u}^M + \mathbf{u}^S]) : \boldsymbol{\epsilon}[\delta\mathbf{u}^M] \right\rangle_\square d\Omega = 0, \tag{7.5a}$$

$$\int_\Omega \left\langle \Upsilon(\varphi^M + \varphi^S, \boldsymbol{\epsilon}[\mathbf{u}^M + \mathbf{u}^S])\delta\varphi^M \right\rangle_\square d\Omega + \int_\Omega \left\langle \Phi(\varphi^M + \varphi^S) \cdot \boldsymbol{\nabla}\delta\varphi^M \right\rangle_\square d\Omega = 0. \tag{7.5b}$$

Similarly, the fine scale variational equations (7.4a, 7.4b) assumes the form

$$\int_\Omega \left\langle \boldsymbol{\sigma}(\varphi^M + \varphi^S, \boldsymbol{\epsilon}[\mathbf{u}^M + \mathbf{u}^S]) : \boldsymbol{\epsilon}[\delta\mathbf{u}^S] \right\rangle_\square d\Omega = 0, \tag{7.6a}$$

$$\int_\Omega \left\langle \Upsilon(\varphi^M + \varphi^S, \boldsymbol{\epsilon}[\mathbf{u}^M + \mathbf{u}^S])\delta\varphi^S \right\rangle_\square \mathrm{d}\Omega + \int_\Omega \left\langle \Phi(\varphi^M + \varphi^S) \cdot \boldsymbol{\nabla}\delta\varphi^S \right\rangle_\square \mathrm{d}\Omega = 0. \tag{7.6b}$$

The fine scale variational equations (7.6a, 7.6b) may be simplified further, since the test functions $\delta\mathbf{u}^S$ and $\delta\varphi^S$ are localized to every coarse scale integration point. Therefore, there are no regularity requirements and the fine scale variational equations (7.6a, 7.6b) may operate on individual RVE domains attached to the coarse scale integration points, independent of each other. The fine scale variational equations on individual RVE domains are stated as

$$\left\langle \boldsymbol{\sigma}(\varphi^M + \varphi^S, \boldsymbol{\epsilon}[\mathbf{u}^M + \mathbf{u}^S]) : \boldsymbol{\epsilon}[\delta\mathbf{u}^S] \right\rangle_\square = 0, \tag{7.7a}$$

$$\left\langle \Upsilon(\varphi^M + \varphi^S, \boldsymbol{\epsilon}[\mathbf{u}^M + \mathbf{u}^S])\delta\varphi^S \right\rangle_\square + \left\langle \Phi(\varphi^M + \varphi^S) \cdot \boldsymbol{\nabla}\delta\varphi^S \right\rangle_\square = 0. \tag{7.7b}$$

7.2.3 *Prolongation*

The prolongation operation in the VCH technique transfers information from the coarse scale onto the fine scale. To that end, the VCH technique assumes the presence of smooth coarse scale fields $\bar{\mathbf{u}}(\bar{\mathbf{x}})$, $\bar{\varphi}(\bar{\mathbf{x}})\,\forall\,\bar{\mathbf{x}} \in \Omega$. Their corresponding coarse scale contributions $\mathbf{u}^M$ and φ^M are obtained through a Taylor series expansion about $\bar{\mathbf{x}}$,

$$\mathbf{u}^M(\bar{\mathbf{u}}, \bar{\mathbf{x}}, \mathbf{x}) = \bar{\mathbf{u}} + \underbrace{\bar{\mathbf{u}} \otimes \boldsymbol{\nabla}\big|_{\bar{\mathbf{x}}}}_{\boldsymbol{\epsilon}[\bar{\mathbf{u}}]} \cdot [\mathbf{x} - \bar{\mathbf{x}}] + \text{H.O.T}, \tag{7.8a}$$

$$\varphi^M(\bar{\varphi}, \bar{\mathbf{x}}, \mathbf{x}) = \bar{\varphi} + \boldsymbol{\nabla}\bar{\varphi}\big|_{\bar{\mathbf{x}}} \cdot [\mathbf{x} - \bar{\mathbf{x}}] + \text{H.O.T}. \tag{7.8b}$$

where, H.O.T refers to higher order terms, which are ignored in first order homogenization technique. Similar expressions are also obtained for the corresponding test functions,

$$\delta\mathbf{u}^M(\delta\bar{\mathbf{u}}, \bar{\mathbf{x}}, \mathbf{x}) = \delta\bar{\mathbf{u}} + \underbrace{\delta\bar{\mathbf{u}} \otimes \boldsymbol{\nabla}\big|_{\bar{\mathbf{x}}}}_{\boldsymbol{\epsilon}[\delta\bar{\mathbf{u}}]} \cdot [\mathbf{x} - \bar{\mathbf{x}}] + \text{H.O.T}, \tag{7.9a}$$

$$\delta\varphi^M(\delta\bar{\varphi}, \bar{\mathbf{x}}, \mathbf{x}) = \delta\bar{\varphi} + \boldsymbol{\nabla}\delta\bar{\varphi}\big|_{\bar{\mathbf{x}}} \cdot [\mathbf{x} - \bar{\mathbf{x}}] + \text{H.O.T}, \tag{7.9b}$$

In equations (7.8a) and (7.9a), the skew symmetric part of the displacement gradient is also ignored due to rigid body invariance. Furthermore, on substituting (7.8a - 7.9b) in the coarse scale variational equations (7.5a, 7.5b), and in conjunction with appropriately defined trial and test spaces, the complete coarse scale problem is stated as:

Variational Problem 16. *Find* $(\bar{\mathbf{u}}, \bar{\varphi}) \in \overline{\mathbb{U}} \times \overline{\mathbb{P}}$ *such that*

$$\int_\Omega \bar{\boldsymbol{\sigma}} : \boldsymbol{\epsilon}[\delta\bar{\mathbf{u}}]\, d\Omega = 0 \qquad \forall\, \delta\bar{\mathbf{u}} \in \overline{\mathbb{U}}^0, \quad (7.10a)$$

$$\int_\Omega \left(\bar{\Upsilon} + \bar{\Lambda}\right) \cdot \boldsymbol{\nabla}\delta\bar{\varphi}\, d\Omega + \int_\Omega \bar{\Phi}\, \delta\bar{\varphi}\, d\Omega = 0 \qquad \forall\, \delta\bar{\varphi} \in \overline{\mathbb{P}}^0, \quad (7.10b)$$

using pertinent time-dependent Dirichlet boundary conditions $\bar{\mathbf{u}}^p$ *on* Γ_D^u *and* $\bar{\varphi}^p$ *on* Γ_D^φ. *The Neumann boundaries are assumed homogeneous (zero traction). Furthermore, the terms in the integrands are defined as*

$$\bar{\boldsymbol{\sigma}} = \left\langle \boldsymbol{\sigma}(\varphi^M + \varphi^S, \boldsymbol{\epsilon}[\mathbf{u}^M + \mathbf{u}^S]) \right\rangle_\square, \quad (7.11a)$$

$$\bar{\Upsilon} = \langle \Upsilon \rangle_\square, \quad (7.11b)$$

$$\bar{\Phi} = \langle \Phi \rangle_\square, \quad (7.11c)$$

$$\bar{\Lambda} = \langle \Phi(\mathbf{x} - \bar{\mathbf{x}}) \rangle_\square, \quad (7.11d)$$

and the trial and test spaces are defined as

$$\overline{\mathbb{U}} = \{\bar{\mathbf{u}} \in [H^1(\Omega)]^{\dim} | \bar{\mathbf{u}} = \bar{\mathbf{u}}^p \text{ on } \Gamma_D^{\bar{\mathbf{u}}}\}, \quad (7.12a)$$

$$\overline{\mathbb{P}} = \{\bar{\varphi} \in [H^1(\Omega)] | \bar{\varphi} = \bar{\varphi}^p \text{ on } \Gamma_D^{\bar{\varphi}}\}, \quad (7.12b)$$

$$\overline{\mathbb{U}}^0 = \{\bar{\mathbf{u}} \in [H^1(\Omega)]^{\dim} | \bar{\mathbf{u}} = \mathbf{0} \text{ on } \Gamma_D^{\bar{\mathbf{u}}}\}, \quad (7.12c)$$

$$\overline{\mathbb{P}}^0 = \{\bar{\varphi} \in [H^1(\Omega)] | \bar{\varphi} = 0 \text{ on } \Gamma_D^{\bar{\varphi}}\}. \quad (7.12d)$$

Remark 13. *The computational homogenization in this thesis is carried out through averaging over the RVE volume domain. However, the VCH framework offers the flexibility to use other homogenization measures, such as averaging over a surface/boundary or even volume averaging over a sub-domain of the RVE, such as the failure zone averaging technique [256].*

7.2.4 *Macro-homogeneity condition*

The (Hill-Mandel) macro-homogeneity condition [129–131] establishes the equivalence of virtual work between the coarse and fine scale. An outcome of establishing the macro-homogeneity condition is the set of boundary

conditions required to solve the fine scale variational equations. In the VCH technique, the fine scale variational equations are presented in conjunction with the macro-homogeneity conditions in canonical format [257]. For the phase-field fracture model, the fine scale canonical problem is stated as:

Variational Problem 17. *Find* $(\mathbf{u}, \varphi, \boldsymbol{\lambda}^{\mathbf{u}}, \lambda^{\varphi}, \mu^{\varphi}) \in \mathbb{U}_{\square} \times \mathbb{P}_{\square} \times \mathbb{T}_{\square} \times \mathbb{Q}_{\square} \times \mathbb{R}$ *such that*

$$\left\langle \boldsymbol{\sigma}(\varphi, \boldsymbol{\epsilon}[\mathbf{u}]) : \boldsymbol{\epsilon}[\delta \mathbf{u}^{S}] \right\rangle_{\square} - \frac{1}{|\Omega_{\square}|} \int_{\Gamma_{\square}^{+}} \boldsymbol{\lambda}^{\mathbf{u}} \cdot [\![\delta \mathbf{u}^{S}]\!]_{\square} \, d\Gamma = 0 \qquad \forall\, \delta \mathbf{u} \in \mathbb{U}_{\square}, \tag{7.13a}$$

$$\left\langle \Upsilon(\varphi, \boldsymbol{\epsilon}[\mathbf{u}]) \delta \varphi^{S} \right\rangle_{\square} + \left\langle \Phi(\varphi) \cdot \boldsymbol{\nabla} \delta \varphi^{S} \right\rangle_{\square} - \frac{1}{|\Omega_{\square}|} \int_{\Gamma_{\square}^{+}} \boldsymbol{\lambda}^{\varphi} \cdot [\![\delta \varphi^{S}]\!]_{\square} \, d\Gamma - \frac{1}{|\Omega_{\square}|} \int_{\Omega_{\square}} \mu^{\varphi} \delta \varphi^{S} \, d\Omega = 0 \qquad \forall\, \delta \varphi \in \mathbb{P}_{\square}, \tag{7.13b}$$

$$-\frac{1}{|\Omega_{\square}|} \int_{\Gamma_{\square}^{+}} \delta \boldsymbol{\lambda}^{\mathbf{u}} \cdot [\![\mathbf{u}]\!]_{\square} \, d\Gamma = -\frac{1}{|\Omega_{\square}|} \int_{\Gamma_{\square}^{+}} \delta \boldsymbol{\lambda}^{\mathbf{u}} \otimes [\![\mathbf{x}]\!]_{\square} \, d\Gamma : \bar{\boldsymbol{\epsilon}} \qquad \forall\, \delta \boldsymbol{\lambda}^{\mathbf{u}} \in \mathbb{T}_{\square}, \tag{7.13c}$$

$$-\frac{1}{|\Omega_{\square}|} \int_{\Gamma_{\square}^{+}} \delta \lambda^{\varphi} \cdot [\![\varphi]\!]_{\square} \, d\Gamma = -\frac{1}{|\Omega_{\square}|} \int_{\Gamma_{\square}^{+}} \delta \lambda^{\varphi} \otimes [\![\mathbf{x}]\!]_{\square} \, d\Gamma \cdot \boldsymbol{\nabla} \bar{\varphi} \qquad \forall\, \delta \lambda^{\varphi} \in \mathbb{Q}_{\square}, \tag{7.13d}$$

$$-\delta \mu^{\varphi} \langle \varphi \rangle_{\square} = -\delta \mu^{\varphi} \bar{\varphi} \qquad \forall\, \delta \mu^{\varphi} \in \mathbb{R}, \tag{7.13e}$$

with pertinent spaces

$$\mathbb{U}_{\square} := \left\{ \mathbf{u} \in [H^{1}(\Omega)]^{\dim} \,\middle|\, \int_{\Omega_{\square}} \mathbf{u} \, d\Omega = 0 \text{ in } \Omega_{\square} \right\}, \tag{7.14a}$$

$$\mathbb{P}_{\square} := \left\{ \varphi \in [H^{1}(\Omega)]^{1} \right\}, \tag{7.14b}$$

$$\mathbb{T}_{\square} := \left\{ \boldsymbol{\lambda}^{\mathbf{u}} \in [L_{2}(\Gamma_{\square}^{+})]^{\dim} \right\}, \tag{7.14c}$$

$$\mathbb{Q}_{\square} := \left\{ \lambda^{\varphi} \in [L_{2}(\Gamma_{\square}^{+})] \right\}. \tag{7.14d}$$

The jump operator $[\![\bullet]\!]_{\square}$ *in equations (7.13a - 7.13d) is defined as* $[\![\bullet]\!]_{\square} = \bullet^{+} - \bullet^{-}$. *Here, the superscripts* $+$ *and* $-$ *are indicative of the fine scale (RVE)*

Variational Problem 17 (continued)

boundaries with positive and negative outward normal vectors, respectively (see Figure 7.1a). ■

A key property of the fine scale (RVE) canonical Variational Problem 17 is that it satisfies the macro-homogeneity condition by construct. In order to obtain a proof of the same, let us assume $\delta\mathbf{u}^S = \mathbf{u}$, $\delta\varphi^S = \varphi$, $\delta\boldsymbol{\lambda}^{\mathbf{u}} = \boldsymbol{\lambda}^{\mathbf{u}}$, $\delta\lambda^{\varphi} = \lambda^{\varphi}$ and $\delta\mu^{\varphi} = \mu^{\varphi}$. Thereafter, these expressions are substituted in variational equations (7.13a - 7.13e), resulting in,

$$\begin{aligned}
&\Big\langle \boldsymbol{\sigma}(\varphi, \boldsymbol{\epsilon}[\mathbf{u}]) : \boldsymbol{\epsilon}[\mathbf{u}] \Big\rangle_{\square} \\
&- \frac{1}{|\Omega_{\square}|} \int_{\Gamma^+_{\square}} \boldsymbol{\lambda}^{\mathbf{u}} \cdot [\![\mathbf{u}]\!]_{\square} \, \mathrm{d}\Gamma = 0 && \forall\, \delta\mathbf{u} \in \mathbb{U}_{\square}, && (7.15a) \\
&\Big\langle \Upsilon(\varphi, \boldsymbol{\epsilon}[\mathbf{u}])\varphi \Big\rangle_{\square} + \Big\langle \Phi(\varphi) \cdot \boldsymbol{\nabla}\varphi \Big\rangle_{\square} \\
&- \frac{1}{|\Omega_{\square}|} \int_{\Gamma^+_{\square}} \boldsymbol{\lambda}^{\varphi} \cdot [\![\varphi]\!]_{\square} \, \mathrm{d}\Gamma \\
&- \frac{1}{|\Omega_{\square}|} \int_{\Omega_{\square}} \mu^{\varphi} \varphi \, \mathrm{d}\Omega = 0 && \forall\, \delta\varphi \in \mathbb{P}_{\square}, && (7.15b) \\
&- \frac{1}{|\Omega_{\square}|} \int_{\Gamma^+_{\square}} \boldsymbol{\lambda}^{\mathbf{u}} \cdot [\![\mathbf{u}]\!]_{\square} \, \mathrm{d}\Gamma \\
&\qquad = -\frac{1}{|\Omega_{\square}|} \int_{\Gamma^+_{\square}} \boldsymbol{\lambda}^{\mathbf{u}} \otimes [\![\mathbf{x}]\!]_{\square} \, \mathrm{d}\Gamma : \bar{\boldsymbol{\epsilon}} && \forall\, \boldsymbol{\lambda}^{\mathbf{u}} \in \mathbb{T}_{\square}, && (7.15c) \\
&- \frac{1}{|\Omega_{\square}|} \int_{\Gamma^+_{\square}} \boldsymbol{\lambda}^{\varphi} \cdot [\![\varphi]\!]_{\square} \, \mathrm{d}\Gamma \\
&\qquad = -\frac{1}{|\Omega_{\square}|} \int_{\Gamma^+_{\square}} \boldsymbol{\lambda}^{\varphi} \otimes [\![\mathbf{x}]\!]_{\square} \, \mathrm{d}\Gamma \cdot \boldsymbol{\nabla}\bar{\varphi} && \forall\, \boldsymbol{\lambda}^{\varphi} \in \mathbb{Q}_{\square}, && (7.15d) \\
&- \mu^{\varphi} \langle \varphi \rangle_{\square} = -\mu^{\varphi} \bar{\varphi} && \forall\, \mu^{\varphi} \in \mathbb{R}. && (7.15e)
\end{aligned}$$

Upon subtracting (7.15c) from (7.15a), and (7.15d, 7.15e) from (7.15b), one obtains

$$\begin{aligned}
&\Big\langle \boldsymbol{\sigma}(\varphi, \boldsymbol{\epsilon}[\mathbf{u}]) : \boldsymbol{\epsilon}[\mathbf{u}] \Big\rangle_{\square} \\
&= \frac{1}{|\Omega_{\square}|} \int_{\Gamma^+_{\square}} \boldsymbol{\lambda}^{\mathbf{u}} \otimes [\![\mathbf{x}]\!]_{\square} \, \mathrm{d}\Gamma : \bar{\boldsymbol{\epsilon}}, && (7.16a) \\
&\Big\langle \Upsilon(\varphi, \boldsymbol{\epsilon}[\mathbf{u}])\varphi \Big\rangle_{\square} + \Big\langle \Phi(\varphi) \cdot \boldsymbol{\nabla}\varphi \Big\rangle_{\square} \\
&= \frac{1}{|\Omega_{\square}|} \int_{\Gamma^+_{\square}} \boldsymbol{\lambda}^{\varphi} \otimes [\![\mathbf{x}]\!]_{\square} \, \mathrm{d}\Gamma \cdot \boldsymbol{\nabla}\bar{\varphi} + \mu^{\varphi} \bar{\varphi}. && (7.16b)
\end{aligned}$$

The next step is to identify the Lagrange multipliers $\boldsymbol{\lambda}^{\mathbf{u}}$, λ^{φ} and μ^{φ} in terms of the physical quantities $\boldsymbol{\sigma}$, Υ and Λ. To that end, let us assume $\delta\mathbf{u}^S = 1$ and $\delta\varphi^S = 1$. Substituting these expressions in the variational equations (7.13a) and (7.13b) yields

$$\underbrace{\Big\langle \boldsymbol{\sigma}(\varphi, \boldsymbol{\epsilon}[\mathbf{u}]) \Big\rangle_{\square}}_{\overline{\boldsymbol{\sigma}}} = \frac{1}{|\Omega_{\square}|} \int_{\Gamma^{+}_{\square}} \boldsymbol{\lambda}^{\mathbf{u}} \otimes [\![\mathbf{x}]\!]_{\square} \, \mathrm{d}\Gamma, \tag{7.17a}$$

$$\underbrace{\Big\langle \Phi(\varphi) \Big\rangle_{\square}}_{\overline{\Phi}} = \mu^{\varphi}. \tag{7.17b}$$

Similarly, substituting $\delta\varphi^{S} = [\mathbf{x} - \bar{\mathbf{x}}] \cdot \boldsymbol{\nabla}\overline{\varphi}$ in (7.13b), the interpretation of the Lagrange multiplier λ^{φ} is obtained as

$$\underbrace{\Big\langle \Upsilon(\varphi, \boldsymbol{\epsilon}[\mathbf{u}]) \Big\rangle_{\square}}_{\overline{\Upsilon}} + \underbrace{\Big\langle \Phi(\varphi) \cdot [\mathbf{x} - \bar{\mathbf{x}}] \Big\rangle_{\square}}_{\overline{\Lambda}} = \frac{1}{|\Omega_{\square}|} \int_{\Gamma^{+}_{\square}} \lambda^{\varphi} \otimes [\![\mathbf{x}]\!]_{\square} \, \mathrm{d}\Gamma. \tag{7.17c}$$

Finally, the sum of equations (7.16a, 7.16b) in conjunction with (7.17a - 7.17c) results in the macro-homogeneity condition,

$$\begin{aligned} \Big\langle \boldsymbol{\sigma}(\varphi, \boldsymbol{\epsilon}[\mathbf{u}]) \colon \boldsymbol{\epsilon}[\mathbf{u}] \Big\rangle_{\square} + \Big\langle \Upsilon(\varphi, \boldsymbol{\epsilon}[\mathbf{u}]) \varphi \Big\rangle_{\square} + \Big\langle \Phi(\varphi) \cdot \boldsymbol{\nabla}\varphi \Big\rangle_{\square} \\ = \overline{\boldsymbol{\sigma}} \colon \bar{\boldsymbol{\epsilon}} + (\overline{\Upsilon} + \overline{\Lambda}) \cdot \boldsymbol{\nabla}\overline{\varphi} + \overline{\Phi}\overline{\varphi}. \end{aligned} \tag{7.18}$$

Remark 14. *In subsequent sections, the proof of (Hill-Mandel) macro-homogeneity condition for the RVE strong periodicity, Neumann and Dirichlet problems is skipped, since these are special cases of the RVE canonical Variational Problem 17.*

7.2.5 *Fine scale (RVE) Weak/Strong Periodicity problem*

The fine scale (RVE) canonical Variational Problem 17 is presented in the weak micro-periodicity format, a concept introduced by Larsson et al. [257]. The weak micro-periodicity format allows an independent discretization of the Lagrange multipliers $(\boldsymbol{\lambda}^{\mathbf{u}}, \lambda^{\varphi})$ from those adopted for the displacement and the phase-field.

From the canonical weak periodicity format, the strongly periodic variational problem is obtained upon choosing the same discretization for the Lagrange multipliers $(\lambda^{\mathbf{u}}, \lambda^{\varphi})$ as those adopted for the displacement and the phase-field. Figure 7.1b presents such a scenario, where the black nodes correspond to the displacement and the phase-field Degrees of Freedom (DOFs), while the red nodes represent the Lagrange multiplier DOFs. However, such a discretization results in a singular problem, due to duplication of constraint equations for nodes shared between the Lagrange multiplier elements [249, 258]. It is possible to identify and eliminate the duplicate constraint equations, however, the process is tedious and error-prone. Alternatively, one could augment the test and trial spaces for the displacement

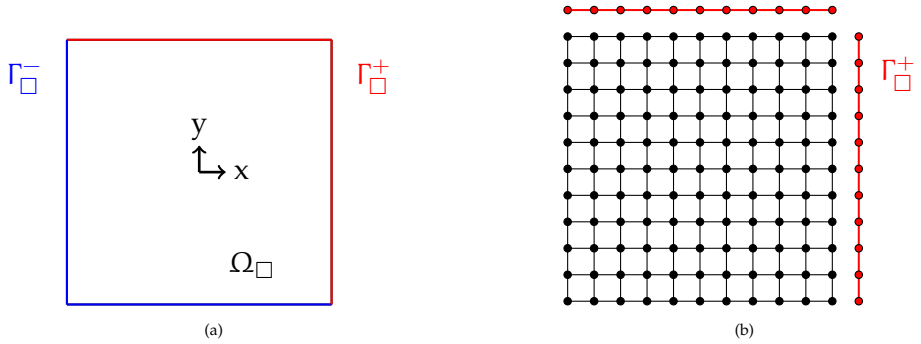

Figure 7.1: Figure (a) shows a 2D fine scale (RVE) domain with positive and negative boundaries, $\Gamma^+_\square$ and $\Gamma^-_\square$. Figure (b) presents a discretization of the 2D RVE. The black circles indicate nodes corresponding to displacement and phase-field dofs, while red circles represent nodes for the Lagrange multipliers $\lambda^{\mathbf{u}}$ and λ^{φ}.

and phase-field DOFs with periodicity constraints. This results in the Variational Problem 18, whereby the Lagrange multipliers $(\boldsymbol{\lambda}^{\mathbf{u}}, \lambda^{\varphi})$ are eliminated from the system of equations.

Variational Problem 18. *Find* $(\mathbf{u}, \varphi, \mu^{\varphi}) \in \mathbb{U}_\square \times \mathbb{P}_\square \times \mathbb{R}$ *such that*

$$\left\langle \boldsymbol{\sigma}(\varphi, \boldsymbol{\epsilon}[\mathbf{u}]) \colon \boldsymbol{\epsilon}[\delta\mathbf{u}^{S}] \right\rangle_\square = 0 \qquad \forall\, \delta\mathbf{u} \in \mathbb{U}_\square, \tag{7.19a}$$

$$\left\langle \Upsilon(\varphi, \boldsymbol{\epsilon}[\mathbf{u}])\delta\varphi^{S} \right\rangle_\square + \left\langle \Phi(\varphi) \cdot \boldsymbol{\nabla}\delta\varphi^{S} \right\rangle_\square - \frac{1}{|\Omega_\square|}\int_{\Omega_\square} \mu^{\varphi}\delta\varphi^{S}\, d\Omega = 0 \qquad \forall\, \delta\varphi \in \mathbb{P}_\square, \tag{7.19b}$$

$$-\delta\mu^{\varphi}\langle\varphi\rangle_\square = -\delta\mu^{\varphi}\,\overline{\varphi} \qquad \forall\, \delta\mu^{\varphi} \in \mathbb{R}, \tag{7.19c}$$

with pertinent spaces

$$\mathbb{U}_\square(\bar{\boldsymbol{\epsilon}}) := \left\{ \mathbf{u} \in [H^1(\Omega)]^{\dim} \;\middle|\; \int_{\Omega_\square} \mathbf{u}\, d\Omega = 0 \text{ in } \Omega_\square \;\middle|\; \mathbf{u}^+ - \mathbf{u}^- = \bar{\boldsymbol{\epsilon}} \cdot [\mathbf{x}^+ - \mathbf{x}^-] \text{ on } \Gamma^+_\square \right\}, \tag{7.20a}$$

$$\mathbb{P}_\square(\boldsymbol{\nabla}\overline{\varphi}) := \left\{ \varphi \in [H^1(\Omega)]^1 \;\middle|\; \varphi^+ - \varphi^- = \boldsymbol{\nabla}\overline{\varphi} \cdot [\mathbf{x}^+ - \mathbf{x}^-] \text{ on } \Gamma^+_\square \right\}. \tag{7.20b}$$

The jump operator $[\![\bullet]\!]_\square$ *in equations (7.13a - 7.13d) is defined as* $[\![\bullet]\!]_\square = \bullet^+ - \bullet^-$. *Here, the superscripts* $+$ *and* $-$ *are indicative of the fine scale (RVE) boundaries with positive and negative outward normal vectors, respectively (see Figure 7.1a).* ■

7.2.6 *Fine scale (RVE) Neumann problem*

The fine scale (RVE) Neumann problem is obtained from the canonical weak micro-periodicity Variational Problem 17 upon choosing the space for the Lagrange multipliers $\mathbb{T}_\square \ni \boldsymbol{\lambda}^{\mathbf{u}}$ and $\mathbb{Q}_\square \ni \lambda^\varphi$ as

$$\mathbb{T}_\square := \left\{ \boldsymbol{\lambda}^{\mathbf{u}} \in [\mathrm{L}_2(\Gamma_\square^+)]^{\dim} \,\middle|\, \boldsymbol{\lambda}^{\mathbf{u}} = \bar{\boldsymbol{\sigma}} \cdot \mathbf{n} \text{ on } \Gamma_\square,\ \bar{\boldsymbol{\sigma}} \in \mathbb{R}^{\dim\times\dim}_{\mathrm{sym}} \right\}, \tag{7.21a}$$

$$\mathbb{Q}_\square := \left\{ \lambda^\varphi \in [\mathrm{L}_2(\Gamma_\square^+)] \,\middle|\, \lambda^\varphi = (\bar{\Upsilon} + \bar{\Lambda}) \cdot \mathbf{n} \text{ on } \Gamma_\square,\ (\bar{\Upsilon} + \bar{\Lambda}) \in \mathbb{R}^{\dim} \right\}. \tag{7.21b}$$

Here, $\bar{\boldsymbol{\sigma}}$ and $(\bar{\Upsilon} + \bar{\Lambda})$ are identified as dual quantities to the coarse scale strain $\bar{\boldsymbol{\epsilon}}$ and phase-field gradient $\boldsymbol{\nabla}\bar{\varphi}$, while $\mathbf{n}$ is the normal to the fine scale (RVE) domain boundary. Using the spaces (7.21a, 7.21b) in the Variational Problem 17, the Neumann Variational Problem 19 is obtained as follows:

Variational Problem 19. *Find* $(\mathbf{u},\ \varphi,\ \bar{\boldsymbol{\sigma}},\ \bar{\Upsilon} + \bar{\Lambda},\ \mu^\varphi) \in \mathbb{U}_\square \times \mathbb{P}_\square \times \mathbb{R}^{\dim\times\dim}_{\mathrm{sym}} \times \mathbb{R}^{\dim} \times \mathbb{R}$ *such that*

$$\langle \boldsymbol{\sigma} : \boldsymbol{\epsilon}[\delta\mathbf{u}^{\mathrm{S}}] \rangle_\square - \bar{\boldsymbol{\sigma}} : \langle \boldsymbol{\epsilon}[\delta\mathbf{u}^{\mathrm{S}}] \rangle_\square = 0 \qquad \forall\, \delta\mathbf{u} \in \mathbb{U}_\square, \tag{7.22a}$$

$$\begin{aligned} &\langle \boldsymbol{\gamma} \cdot \boldsymbol{\nabla}\delta\varphi^{\mathrm{S}} \rangle_\square + \langle \Phi\delta\varphi^{\mathrm{S}} \rangle_\square \\ &- (\bar{\Upsilon} + \bar{\Lambda}) \cdot \langle \boldsymbol{\nabla}\delta\varphi \rangle_\square - \mu^\varphi \langle \delta\varphi \rangle_\square = 0 \end{aligned} \qquad \forall\, \delta\varphi \in \mathbb{P}_\square, \tag{7.22b}$$

$$-\delta\bar{\boldsymbol{\sigma}} : \langle \boldsymbol{\epsilon}[\mathbf{u}] \rangle_\square = -\delta\bar{\boldsymbol{\sigma}} : \bar{\boldsymbol{\epsilon}} \qquad \forall\, \delta\bar{\boldsymbol{\sigma}} \in \mathbb{R}^{\dim\times\dim}_{\mathrm{sym}}, \tag{7.22c}$$

$$-\delta(\bar{\Upsilon} + \bar{\Lambda}) \cdot \langle \boldsymbol{\nabla}\varphi \rangle_\square = -\delta(\bar{\Upsilon} + \bar{\Lambda}) \cdot \boldsymbol{\nabla}\bar{\varphi} \qquad \forall\, \delta(\bar{\Upsilon} + \bar{\Lambda}) \in \mathbb{R}^{\dim}, \tag{7.22d}$$

$$-\delta\mu^\varphi \langle \varphi \rangle_\square = -\delta\mu^\varphi \bar{\varphi} \qquad \forall\, \delta\mu^\varphi \in \mathbb{R}, \tag{7.22e}$$

using pertinent spaces

$$\begin{aligned} \mathbb{U}_\square := \Bigg\{ \mathbf{u} \in [\mathrm{H}^1(\Omega)]^{\dim} \,\Bigg|\, &\int_{\Omega_\square} \mathbf{u}\, \mathrm{d}\Omega = 0 \text{ in } \Omega_\square, \\ &\int_{\Gamma_\square} (\mathbf{u} \otimes \mathbf{n})^{\mathrm{skew}}\, \mathrm{d}\Gamma = 0 \text{ on } \Gamma_\square \Bigg\}, \end{aligned} \tag{7.23a}$$

$$\mathbb{P}_\square := \left\{ \varphi \in \mathrm{H}^1(\Omega) \right\}. \tag{7.23b}$$

■

7.2.7 *Fine scale (RVE) Dirichlet problem*

The fine scale (RVE) Dirichlet problem arises from setting the fine scale solution contributions $\mathbf{u}^S$ and φ^S to zero on the boundary $\Gamma_\square$. This results in the Dirichlet Variational Problem 20, defined as follows:

Variational Problem 20. *Find* $(\mathbf{u}, \varphi, \mu^\varphi) \in \mathbb{U}_\square \times \mathbb{P}_\square \times \mathbb{R}$ *with*

$$\left\langle \boldsymbol{\sigma}(\varphi, \boldsymbol{\epsilon}[\mathbf{u}]) : \boldsymbol{\epsilon}[\delta\mathbf{u}^S] \right\rangle_\square = 0 \qquad \forall\, \delta\mathbf{u} \in \mathbb{U}_\square, \tag{7.24a}$$

$$\left\langle \Upsilon(\varphi, \boldsymbol{\epsilon}[\mathbf{u}])\delta\varphi^S \right\rangle_\square + \left\langle \Phi(\varphi) \cdot \boldsymbol{\nabla}\delta\varphi^S \right\rangle_\square - \frac{1}{|\Omega_\square|}\int_{\Omega_\square} \mu^\varphi \delta\varphi^S \, \mathrm{d}\Omega = 0 \qquad \forall\, \delta\varphi \in \mathbb{P}_\square, \tag{7.24b}$$

$$-\delta\mu^\varphi \langle\varphi\rangle_\square = -\delta\mu^\varphi \bar{\varphi} \qquad \forall\, \delta\mu^\varphi \in \mathbb{R}, \tag{7.24c}$$

with pertinent spaces

$$\mathbb{U}_\square(\bar{\boldsymbol{\epsilon}}) := \left\{ \mathbf{u} \in [\mathrm{H}^1(\Omega)]^{\dim} \,\middle|\, \int_{\Omega_\square} \mathbf{u} \, \mathrm{d}\Omega = 0 \text{ in } \Omega_\square \,\middle|\, \mathbf{u}^\pm = \bar{\boldsymbol{\epsilon}} \cdot [\mathbf{x}^\pm - \bar{\mathbf{x}}] \text{ on } \Gamma_\square \right\}, \tag{7.25a}$$

$$\mathbb{P}_\square(\bar{\varphi}, \boldsymbol{\nabla}\bar{\varphi}) := \left\{ \varphi \in \mathrm{H}^1(\Omega) \,\middle|\, \varphi^\pm = \bar{\varphi} + \boldsymbol{\nabla}\bar{\varphi} \cdot [\mathbf{x}^\pm - \bar{\mathbf{x}}] \text{ on } \Gamma_\square \right\}, \tag{7.25b}$$

$$\mathbb{U}^0_\square := \left\{ \mathbf{u} \in [\mathrm{H}^1(\Omega)]^{\dim} \,\middle|\, \mathbf{u}^\pm = \mathbf{0} \text{ on } \Gamma_\square \right\}, \tag{7.25c}$$

$$\mathbb{P}^0_\square := \left\{ \varphi \in \mathrm{H}^1(\Omega) \,\middle|\, \varphi^\pm = 0 \text{ on } \Gamma_\square \right\}. \tag{7.25d}$$

■

7.2.8 *Selective homogenization*

The concept of selective homogenization is introduced to enable selective upscaling of coarse scale quantities from the fine scale physics. As an example, one could restrain the phase-field to live only on the fine scale (choosing $\delta\varphi^M = 0$). Consequently, the coarse scale phase-field evolution equation (7.10b) in Variational Problem 16 would cease to exist. The coarse scale Variational Problem would assume the form

Variational Problem 21. *Find* $\bar{\mathbf{u}} \in \overline{\mathbb{U}}$ *such that*

$$\int_\Omega \bar{\boldsymbol{\sigma}} : \boldsymbol{\epsilon}[\delta\bar{\mathbf{u}}] \, d\Omega = 0 \qquad \forall \, \delta\bar{\mathbf{u}} \in \overline{\mathbb{U}}^0, \tag{7.26a}$$

using pertinent time-dependent Dirichlet boundary condition $\bar{\mathbf{u}}^p$ *on* Γ_D^u. *The Neumann boundaries are assumed homogeneous (zero traction). Furthermore, the terms in the integrand is defined as*

$$\bar{\boldsymbol{\sigma}} = \left\langle \boldsymbol{\sigma}(\varphi^M + \varphi^S, \boldsymbol{\epsilon}[\mathbf{u}^M + \mathbf{u}^S]) \right\rangle_\square, \tag{7.27a}$$

and the trial and test spaces are defined as

$$\overline{\mathbb{U}} = \{\bar{\mathbf{u}} \in [H^1(\Omega)]^{\dim} | \bar{\mathbf{u}} = \bar{\mathbf{u}}^p \text{ on } \Gamma_D^{\bar{\mathbf{u}}}\}, \tag{7.28a}$$

$$\overline{\mathbb{U}}^0 = \{\bar{\mathbf{u}} \in [H^1(\Omega)]^{\dim} | \bar{\mathbf{u}} = \mathbf{0} \text{ on } \Gamma_D^{\bar{\mathbf{u}}}\}. \tag{7.28b}$$

■

Although the coarse scale phase-field evolution equation is eliminated, the effect of fracture on the fine scale (RVE) domain is accounted for, in the homogenized stress $\bar{\boldsymbol{\sigma}}$ (see Equation (7.27a)). Furthermore, it is important to note that the coarse scale Variational Problem 21 would exhibit mesh-dependent response, in the absence of any regularization. For more on this topic, the reader is referred to [259].

In an alternative approach, the fine scale phase-field evolution equation may be eliminated, upon choosing $\delta\varphi^S = 0$. With this choice, the coarse scale phase-field $\bar{\varphi}$ is assumed to be uniformly distributed over the fine scale (RVE) domain. Furthermore, the need for introducing computational homogenization on the coarse scale phase-field evolution is circumvented. Instead, the single scale phase-field evolution equation (2.25b) from Variational Problem 3 is adopted. With these changes, the coarse scale Variational Problem assumes the following form:

Variational Problem 22. *Find* $(\bar{\mathbf{u}}, \bar{\varphi}) \in \overline{\mathbb{U}} \times \overline{\mathbb{P}}$ *such that*

$$\int_\Omega \bar{\boldsymbol{\sigma}} : \boldsymbol{\epsilon}[\delta\bar{\mathbf{u}}] \, d\Omega = 0 \qquad \forall \, \delta\bar{\mathbf{u}} \in \overline{\mathbb{U}}^0, \tag{7.29a}$$

$$\int_\Omega \frac{G_c \, l}{c_w} \boldsymbol{\nabla}\varphi \cdot \boldsymbol{\nabla}\delta\varphi \, d\Omega + \int_\Omega \left(\frac{G_c}{c_w \, l} w'(\varphi) + g'(\varphi)\mathcal{H} \right) \delta\varphi \, d\Omega = 0 \qquad \forall \, \delta\varphi \in \overline{\mathbb{P}}^0, \tag{7.29b}$$

Variational Problem 22 (continued)

using pertinent time-dependent Dirichlet boundary conditions $\bar{\mathbf{u}}^p$ *on* Γ_D^u *and* $\bar{\varphi}^p$ *on* Γ_D^φ. *The Neumann boundaries are assumed homogeneous (zero traction). Furthermore, the homogenized stress is defined as*

$$\bar{\boldsymbol{\sigma}} = \left\langle \boldsymbol{\sigma}(\varphi, \boldsymbol{\epsilon}[\mathbf{u}^M + \mathbf{u}^S]) \right\rangle_\square, \tag{7.30a}$$

and the trial and test spaces are defined as

$$\bar{\mathbb{U}} = \{\bar{\mathbf{u}} \in [H^1(\Omega)]^{\dim} | \bar{\mathbf{u}} = \bar{\mathbf{u}}^p \text{ on } \Gamma_D^{\bar{\mathbf{u}}}\}, \tag{7.31a}$$
$$\bar{\mathbb{P}} = \{\varphi \in [H^1(\Omega)] | \varphi = \varphi^p \text{ on } \Gamma_D^{\bar{\varphi}}\}, \tag{7.31b}$$
$$\bar{\mathbb{U}}^0 = \{\bar{\mathbf{u}} \in [H^1(\Omega)]^{\dim} | \bar{\mathbf{u}} = \mathbf{0} \text{ on } \Gamma_D^{\bar{\mathbf{u}}}\}, \tag{7.31c}$$
$$\bar{\mathbb{P}}^0 = \{\varphi \in [H^1(\Omega)] | \varphi = 0 \text{ on } \Gamma_D^{\bar{\varphi}}\}. \tag{7.31d}$$

■

The upscaling/hierarchical multi-scale phase-field fracture models developed so far, by He, Schuler, and Newell [56] and Fantoni et al. [57] are close variants of the Variational Problem 22.

7.3 FINE SCALE (RVE) NUMERICAL EXPERIMENTS

In this section, the numerical experiments on the fine scale (RVE) domains are carried out. The role of RVE boundary conditions on the (homogenized) coarse scale quantities is investigated. To that end, three different RVEs are considered, with varying topological features, as shown in Figure 7.2. All RVEs are unit squares (in mm).

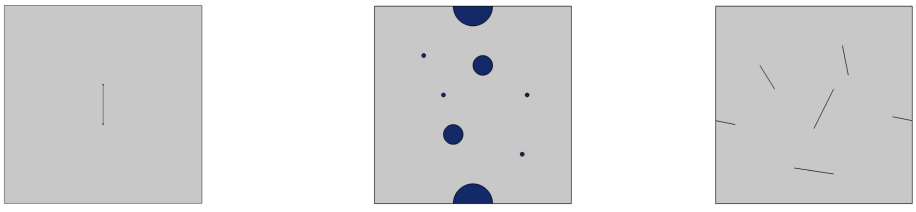

(a) RVE with single fracture (b) RVE with stiff inclusions (c) RVE with random fractures

Figure 7.2: Figure showing the different RVEs used for the numerical experiments.

Figure 7.2a shows the simplest RVE with a homogeneous material distribution and an initial fracture. The RVE is symmetric w.r.t. the initial fracture topology. The second RVE, shown in Figure 7.2b, presents a matrix with randomly placed stiff inclusions (in blue). The inclusions close to the RVE boundary are placed strategically such that they adhere to wall-periodicity. Similar RVEs may be found in engineered materials such as fibre-reinforced composites [260, 261]. Finally, Figure 7.2c presents an RVE with a homoge-

neous material distribution with randomly placed initial defects (fractures). It is important to note that the latter two RVEs do not exhibit symmetry w.r.t. to material and fracture topology, respectively.

The material properties and other relevant model assumptions for the RVEs in Figure 7.2 are presented in Table 7.1. The matrix material properties remain same for all RVEs, while the inclusion material properties apply only to the RVE in Figure 7.2b. Furthermore, the numerical experiments are carried out in the commercial software COMSOL Multiphysics, where the Variational Problems are directly modelled using the Weak Form PDE interface.

Property	Value
RVE	1 [mm] $\times$ 1 [mm], Plane strain
λ_{matrix}, $\lambda_{\text{inclusion}}$	131.154 [GPa], 13100.154 [GPa]
μ_{matrix}, $\mu_{\text{inclusion}}$	80.769 [GPa], 8000.769 [GPa]
$G_{c,\text{matrix}}$, $G_{c,\text{inclusion}}$	2700 [N/m], 270000 [N/m]
l	1.5e-2 [mm]
max. element size	$l/2$

Table 7.1: RVE geometric and material properties

7.3.1 *Influence of fine scale (RVE) boundary conditions*

The influence of the fine scale (RVE) boundary conditions is investigated using the RVEs in Figure 7.2. All RVEs are driven only by a quasi-static coarse scale strain loading in the horizontal direction ($\Delta\bar{\epsilon}_{xx} = 1e-5$). The coarse scale phase-field and its gradient are assumed to be non-existent, following the selective homogenization strategy in Variational Problem 21. The different boundary conditions, viz., Strongly Periodic (SPBC), Neumann (NBC), and Dirichlet (DBC) follow from the Variational Problems 18, 19, 20.

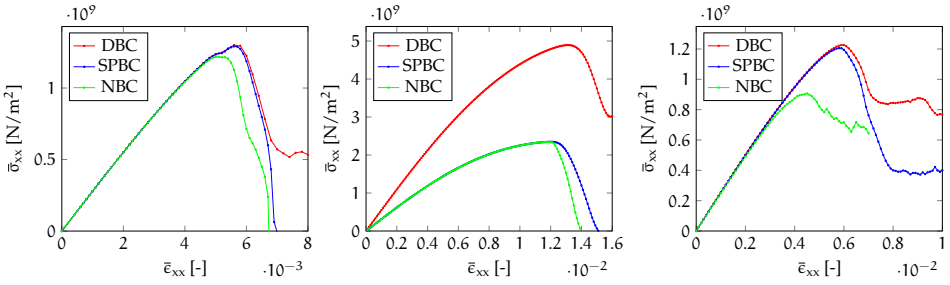

(a) RVE with single fracture (b) RVE with stiff inclusions (c) RVE with random fractures

Figure 7.3: Figure showing homogenized stress-strain (x-direction) curves for the different RVEs.

Figure 7.3 presents the (homogenized) coarse scale stress-strain response for the different RVEs with different boundary conditions (DBC, NBC, SPBC). Each sub-figure corresponds to a single RVE, where the different

curves represent the aforementioned boundary conditions. Based on these sub-figures, it is possible to conclude that the effect of the phase-field, thence dissipation is implicitly contained in the homogenized stress $\bar{\sigma}$. The phase-field evolution within an RVE manifests in the form of a softening type stress-strain response. Also, for each RVE, the SPBC homogenized stress-strain curve is bounded between that obtained using DBC and NBC. This bounded behaviour has also been reported in [257]. Moreover, it is possible to explain the individual homogenized stress-strain response for each RVE using the phase-field fracture topology.

Figure 7.4 presents the phase-field fracture topology at the final step of the analysis for the RVE with a single fracture. The topology remains the same irrespective of the boundary conditions (DBC, NBC, SPBC). Consequently, the homogenized stress-strain curves are similar, until the strain $\bar{\epsilon}_{xx} \approx 7e-3$. At this point, the curve obtained using DBC starts to deviate and demonstrates a stiffening response (evident from the horizontal plateau). This stiff response is due to the DBC construct, where the fracture is not allowed to reach the RVE boundary. Upon reaching the boundary, the fracture spreads horizontally, parallel to the RVE boundary, as shown in Figure 7.4a.

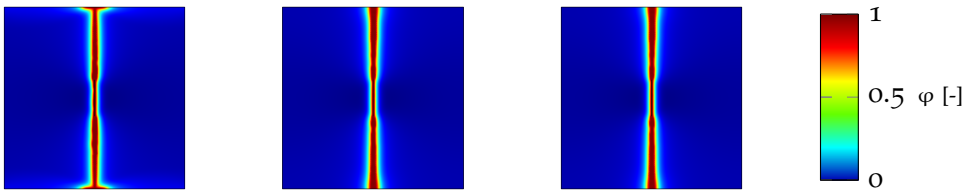

(a) DBC (b) NBC (c) SPBC

Figure 7.4: Figure showing phase-field distribution in the final time-step for the RVE with single fracture.

Figure 7.5 presents the phase-field fracture topology at the final step of the analysis for the RVE with inclusions. Unlike the RVE with a single fracture, here, the fracture topologies differ with boundary conditions. For the DBC, the fracture does not penetrate the RVE boundary, thereby manifesting in a stiff response (see red curve in Figure 7.3b). The SPBC and NBC curves are similar as both circumvent the artificial stiffening at the RVE boundary, and due to the similar amount of energy dissipated despite the difference in the fracture topologies.

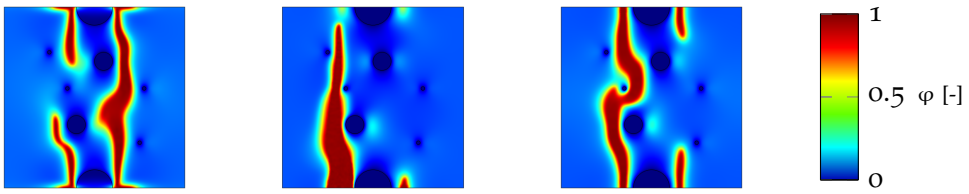

(a) DBC (b) NBC (c) SPBC

Figure 7.5: Figure showing phase-field distribution in the final time-step for the RVE with stiff inclusions.

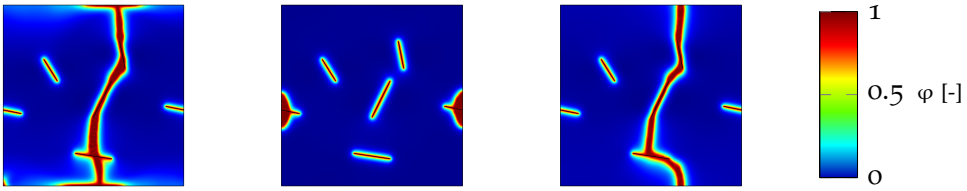

(a) DBC (b) NBC (c) SPBC

Figure 7.6: Figure showing phase-field distribution in the final time-step for the RVE with random fractures.

Figure 7.6 presents the phase-field fracture topology at the final step of the analysis for the RVE with random initial defects (fractures). The fracture topologies differ with boundary conditions. For the DBC, the fracture does not penetrate the RVE boundary, thereby manifesting in a stiff response (see red curve in Figure 7.3c). In the case of the NBC, a widening of the initial fractures on the RVE boundary is observed. Due to the enforcement of an average stress/strain over the RVE domain, the NBC results in highly localized deformation whenever the RVE boundary intersects a weaker material or a defect (fracture). The SPBC is able to circumvent the stiffening response exhibited by the DBC as well as the highly localized deformations observed with the NBC.

Motivated by the numerical experiments on the fine scale (RVE) domains, in the subsequent part of this chapter, the SPBC is used. The use of SPBC has also been proposed by Sluis et al. [262] and Terada et al. [263].

7.3.2 *Upscaling coarse scale quantities*

This section concerns the upscaling of quantities relevant on the coarse scale Variational Problem 16. These are $\bar{\boldsymbol{\sigma}}$, $\bar{\Phi}$ and $\bar{\Upsilon} + \bar{\Lambda}$, dual to the coarse scale strain $\bar{\boldsymbol{\epsilon}}$, phase-field $\bar{\varphi}$ and its gradient $\boldsymbol{\nabla}\bar{\varphi}$, respectively. Contrary to the numerical experiments conducted in the previous section, here, the RVE is driven not only by the strain $\bar{\boldsymbol{\epsilon}}$ but also by the coarse scale phase-field $\bar{\varphi}$ and its gradient $\boldsymbol{\nabla}\bar{\varphi}$. This is a consequence of choosing coarse scale Variational Problem 16 instead of the selective homogenization variant Variational Problem 21.

Adopting the coarse scale Variational Problem 16 brings new challenges for numerical experiments on an RVE. In addition to the quasi-static evolution of coarse scale strain $\bar{\boldsymbol{\epsilon}}$, one also requires the evolution of the coarse scale phase-field $\bar{\varphi}$ and its gradient $\boldsymbol{\nabla}\bar{\varphi}$. Similar to the previous section, the RVE is driven by a strain increment $\Delta\bar{\epsilon}_{xx} = 1e-5$. The coarse scale phase-field $\bar{\varphi}$ is obtained artificially[2] from the numerical experiments carried out in the previous section. Homogenizing the phase-field in the RVE with inclusions, $\bar{\varphi}$ evolution in Figure 7.7 is obtained.

2 Artificial in the sense that it is not obtained consistently from a coarse scale analysis.

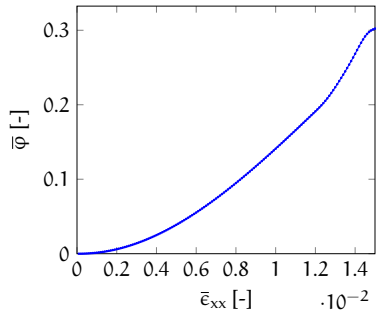

Figure 7.7: Figure showing homogenized phase-field $\overline{\varphi}$ as a function of the homogenized strain $\bar{\epsilon}_{xx}$ for the RVE with inclusion.

Finally, the coarse scale phase-field gradient is parametrized,

$$\boldsymbol{\nabla}\overline{\varphi} := \boldsymbol{\alpha}\overline{\varphi} = [\alpha_x, \alpha_y]^T \beta(\bar{\epsilon}_{xx}), \tag{7.32}$$

where α_x [mm^{-1}] and α_y [mm^{-1}] are constants, and $\beta(\bar{\epsilon}_{xx})$ is a function depending on the coarse scale strain[3]. Based on the choice of α_x and α_y, different parametrizations of the $\boldsymbol{\nabla}\overline{\varphi}$ are obtained. For instance, setting $\alpha_x = \alpha_y = 0$ or $\beta(\bar{\epsilon}_{xx}) = 0$ results in $\boldsymbol{\nabla}\overline{\varphi} = 0$. In this section, α_y is set to zero, while α_x is varied as $\{0, 0.01, 0.1, 0.5, 1\}$ [mm^{-1}].

Figure 7.8 presents the upscaled/homogenized quantities pertinent to the coarse scale. They have been defined earlier in (7.11a - 7.11d). Each curve in every sub-figure is obtained for a chosen coarse scale phase-field gradient $\boldsymbol{\nabla}\overline{\varphi}$, parametrized using (7.32). With this approach, the influence of the coarse scale phase-field gradient on the coarse scale homogenized quantities is investigated. The homogenized stress is presented as a function of the coarse scale strain in Figure 7.8a. Here, the effect of coarse scale phase-field gradient is negligible, since the curves appear to be overlapping. A similar observation is made in Figure 7.8b for the coarse scale quantity $\overline{\Phi}$, which represents the volume-average of the imbalance between the fracture driving and the resisting forces, excluding the gradient effects. For both coarse scale quantities, the objectivity w.r.t. the coarse scale phase-field gradient is due to the phase-field fracture topology, which remains same as presented in Figure 7.5c. Although, the phase-field fracture topology remains unchanged as in Figure 7.5c, the coarse scale phase-field gradient influences the RVE phase-field gradient in the vicinity of the fracture. This manifests in a coarse scale phase-field gradient dependent response of its dual quantity $\overline{\Upsilon} + \overline{\Lambda}$, as shown in Figure 7.8c. A non-zero $\overline{\Upsilon} + \overline{\Lambda}$ regularizes the coarse phase-field, as it provides an implicit length, based on the fine scale (RVE) features.

Remark 15. *The contribution of $\overline{\Upsilon}$ to the coarse scale quantity $\overline{\Upsilon} + \overline{\Lambda}$ is presented in Figure 7.8d. On comparing Figures 7.8c and 7.8d, it is safe to*

3 β can also be introduced as a time-dependent function

Remark 15 (continued)

conclude that $\overline{\Lambda}$ may provide a dominant contribution, depending on the fracture topology.

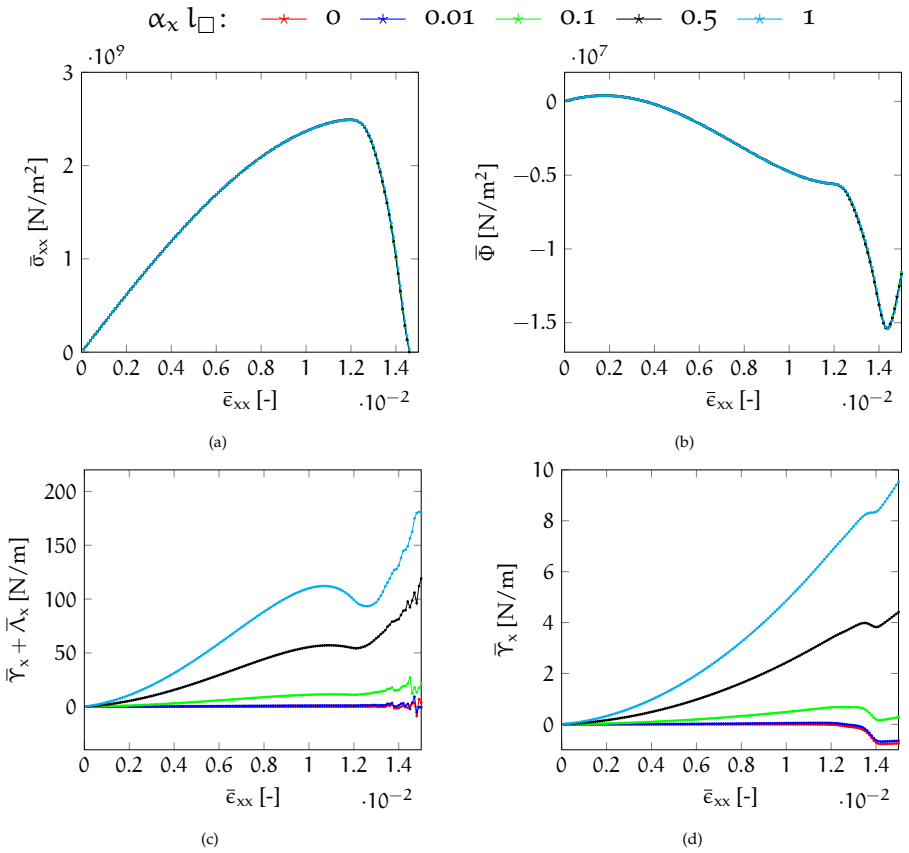

Figure 7.8: Figure showing homogenized coarse scale quantities defined in (7.11a - 7.11d).

7.4 A MULTI-SCALE NUMERICAL EXPERIMENT

In this section, a multi-scale numerical experiment is conducted, considering both, a coarse scale domain and a fine scale (RVE) domain. As a consequence, the coarse scale Variational Problem 16 or 21 and the fine scale Variational Problem 18 are solved, simultaneously. A schematic of such a process is present in Figure 7.9. Here, the coarse scale domain is a one-dimensional (1D) bar, fixed on the left edge, while a displacement $\bar{\mathbf{u}}^p$ is prescribed on the right edge. Furthermore, every coarse scale integration point is associated with a fine scale (RVE) domain $\Omega_\square$. The communication between the coarse scale and fine scale domains is represented by the set of dashed arrows in Figure 7.9.

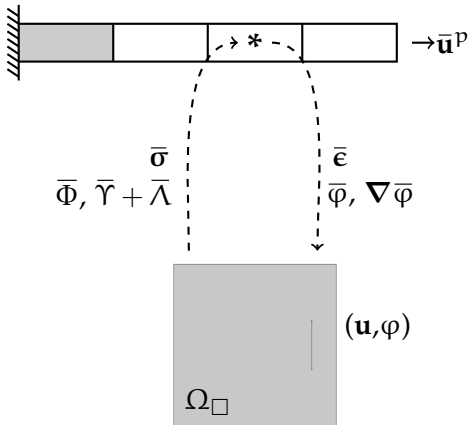

Figure 7.9: Figure showing a multi-scale problem schematic with a one-dimensional bar under uniaxial tension and its corresponding two-dimensional RVE.

7.4.1 *Multi-scale FE^2 analysis*

The multi-scale problem schematic in Figure 7.9 is popularly known as the FE^2 method. The term 'FE^2' was coined by Feyel [141, 264] and relates to the use the Finite Element Method (FEM) to solve both, the coarse scale problem and the fine scale (RVE) problem. Algorithm 1 describes the communication between the coarse scale and the fine scale in the FE^2 context. Assuming that the coarse scale problem is solved using the Newton-Raphson method, one assembles a residual vector and a stiffness matrix for every iteration within a loading step. The assembly is performed element-wise. For each element, one extracts the solution fields ($\bar{\mathbf{u}}$ and $\bar{\varphi}$ in this case), and computes the coarse scale strain $\bar{\boldsymbol{\epsilon}}$, phase-field $\bar{\varphi}$ and its gradient $\boldsymbol{\nabla}\bar{\varphi}$, which drives the RVE Variational Problem 18. The RVE problem is solved for its solution fields ($\mathbf{u}$ and φ), and then the coarse scale dual quantities $\bar{\boldsymbol{\sigma}}$, $\bar{\Phi}$ and $\bar{\Upsilon} + \bar{\Lambda}$ are computed using Equations 7.11a - 7.11d. With the dual quantities, the coarse scale integration point residual is computed. However, Newton-Raphson method being a second-order optimization technique, one also requires the stiffness matrix. For computing the stiffness matrix, the derivatives of $\bar{\boldsymbol{\sigma}}$, $\bar{\Phi}$ and $\bar{\Upsilon} + \bar{\Lambda}$ w.r.t. $\bar{\boldsymbol{\epsilon}}$, $\bar{\varphi}$ and $\boldsymbol{\nabla}\bar{\varphi}$ are obtained using the perturbation method. The perturbation factor adopted for $\bar{\boldsymbol{\epsilon}}$, $\bar{\varphi}$ and $\boldsymbol{\nabla}\bar{\varphi}$ is $1e-8$.

Remark 16. *In the absence of an open-source software capable of performing an FE^2 analysis[a], the open-source FE^2 software package* `openFE2` *(*`https://github.com/ritukeshbharali/openFE2`*) was developed. Here, the coarse scale problem is solved in MATLAB, while the fine scale (RVE) problems are solved in COMSOL Multiphysics (Version 5.5). Leveraging on the Parallel Computing Toolbox in MATLAB, multiple RVE problems may be solved in parallel. The comments in blue in Algorithm 1 presents the junctures where the coarse scale problem in MATLAB communicates with the RVE problem in COMSOL Multiphysics.*

Remark 16 (continued)

[a] At the time of performing this study in 2019.

Algorithm 1: For every coarse scale iteration in a time-step

Input: Coarse scale solution
Output: Coarse scale residual and stiffness matrix

for *each element* `ielem` *in coarse domain mesh* **do**
- Set element residual and stiffness matrix to zero
- Extract element solutions ($\bar{\mathbf{u}}_{\texttt{ielem}}$, $\overline{\varphi}_{\texttt{ielem}}$)
- **for** *each integration point* **do**
  - Compute $\bar{\epsilon}$, $\overline{\varphi}$ and $\boldsymbol{\nabla}\overline{\varphi}$
  - `/* Begin communication with RVE model in COMSOL Multiphysics */`
  - Solve RVE problem using SPBC (Variational Problem 18)
  - Compute coarse scale quantities $\bar{\sigma}$, $\overline{\Phi}$ and $\overline{\Upsilon} + \overline{\Lambda}$ (see Equations 7.11a - 7.11d)
  - Perturb $\bar{\epsilon}$, $\overline{\varphi}$ and $\boldsymbol{\nabla}\overline{\varphi}$, and solve RVE problem
  - Compute perturbed coarse scale quantities $\bar{\sigma}$, $\overline{\Phi}$ and $\overline{\Upsilon} + \overline{\Lambda}$ (see Equations 7.11a - 7.11d)
  - Compute derivatives of $\bar{\sigma}$, $\overline{\Phi}$ and $\overline{\Upsilon} + \overline{\Lambda}$ w.r.t $\bar{\epsilon}$, $\overline{\varphi}$ and $\boldsymbol{\nabla}\overline{\varphi}$ through forward difference.
  - Discard perturbed quantities and send $\bar{\sigma}$, $\overline{\Phi}$ and $\overline{\Upsilon} + \overline{\Lambda}$ and their derivatives to the coarse scale.
  - `/* Ends communication with COMSOL Multiphysics */`
  - Compute integration point residual and stiffness matrix.
- Update element residual and stiffness matrix.
- Assemble global residual and stiffness matrix with element contribution.

7.4.2 *Coarse and fine scale geometry and material properties*

The geometric and material properties of the coarse scale and fine scale (RVE) domains are defined in this section. The coarse scale domain is a 4 meter long 1D bar, as shown in Figure 7.9. It is discretized using 4 elements of equal length. The area of the 1D bar is assumed as unity for all elements except the one highlighted in grey. For the highlighted element, the cross-sectional area is reduced by 10%, in order to induce strain localization.

Each coarse scale integration point is associated with the same fine scale (RVE) domain. The RVE domain is a unit square (in mm) embedded with an initial single fracture. This RVE is chosen instead of the RVEs in Figures 7.2b and 7.2c to reduce computational expense. The fracture propagation path in the chosen RVE is simple and known *a priori*, allowing pre-refinement. This reduces the computational expense compared to RVEs exhibiting complex fracture topology, where uniform mesh is required. Furthermore, the goal

in this thesis is to address the solvability of the FE^2 problem with the multi-scale phase-field fracture models developed in this chapter. Therefore, numerical experiments with topologically complex RVEs are avoided.

7.4.3 *Fully coupled model vs Selective homogenization*

The solvability of the FE^2 problem in Figure 7.9 is investigated using two variants of the multi-scale phase-field fracture model. The first variant, termed as 'fully coupled FE^2 model' retains the momentum balance equation and the phase-field evolution equation on both the coarse scale and the fine scale. The relevant coarse scale and fine scale problems are Variational Problems 16 and 18, respectively. The second variant, addressed henceforth as the 'selective FE^2 model' discards the phase-field evolution equation on the coarse scale. For this model, the relevant coarse scale and fine scale Variational Problems are 21 and 18, respectively.

Figure 7.10 presents the load-displacement curves obtained using the fully coupled and the selective FE^2 models. A similar response is recorded until the peak load, while the post-peak behaviours are different. The difference in the post peak behaviour is attributed to the coarse scale phase-field evolution equation in the fully coupled FE^2, which provides a regularization of the coarse scale phase-field. This coarse scale regularization is absent in the selective FE^2 model.

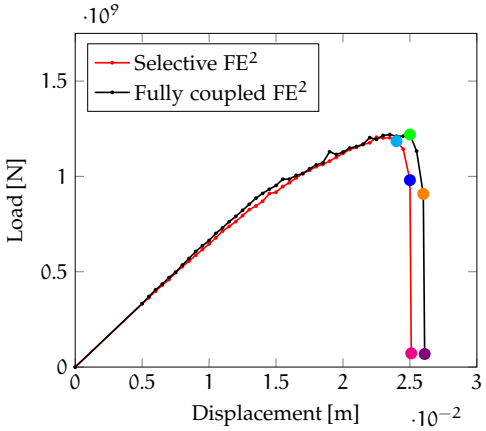

Figure 7.10: Figure showing the coarse scale load-displacement curves for the fully coupled and selective FE^2 models. The colored markers represent coordinates, where the coarse scale integration point phase-fields are presented in Figure 7.11.

The difference between the fully coupled and selective FE^2 models lies in coarse scale phase-field regularization. This aspect is emphasized through Figure 7.11, where the coarse scale phase-field is represented through color bar corresponding to coordinates marked in the load-displacement curves in Figure 7.10. For the selective FE^2 model, as the load-displacement curve traverses through the post-peak regime, the coarse scale phase-field grows only in one integration point, as shown in Figure 7.11a. This local behaviour is expected due to the omission of the coarse scale phase-field evolution equation, and has been already explained in Section 7.2.8. However, as ob-

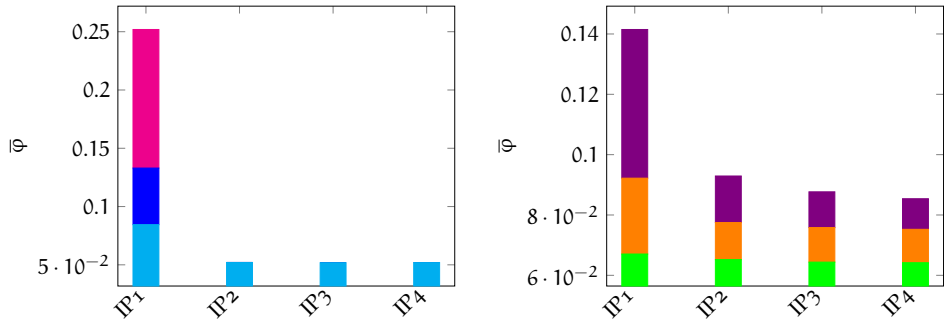

(a) Selective FE^2

(b) Fully coupled FE^2

Figure 7.11: Figure showing the phase-field at the coarse scale Integration Points (IPs). The color in the bars represent coordinates of the load-displacement curves in Figure 7.10.

served from Figure 7.11b, the fully coupled FE^2 model result in coarse scale phase-field regularized response as the load-displacement curve traverses through the post-peak regime. The evolution of the coarse scale phase-field is not limited to one integration point beyond the peak-load.

Part V

EPILOGUE

Concluding remarks of this thesis and future research directions.

8

CONCLUSION AND OUTLOOK

Numerical methods and a multi-scale modelling framework have been developed for the phase-field fracture model in this thesis. The numerical methods are focused on solving the pertinent non-convex fracture problem as well as enforcing the irreversibility of fracture(s) in a variationally consistent fashion. To that end, robust and computationally efficient monolithic solution techniques (arc-length method and Hessian scaling method) are proposed to simulate fracturing in linear elastic and poro-elastic media. A micromorphic variant of the phase-field fracture model is put-forth as a variationally consistent way of enforcing fracture irreversibility pointwise in a computational domain. The proposed monolithic techniques and the micromorphic phase-field fracture model are tested on benchmark problems, encompassing both brittle and quasi-brittle fracturing processes. Furthermore, in the view of material heterogeneity, a variationally consistent multi-scale phase-field fracture framework is developed. Fine scale (micro-structural) material features such as material constituents, voids and defects are explicitly modelled in a Representative Volume Element (RVE), and engineering/coarse scale mechanical response is derived using homogenization techniques. The novel numerical methods and multi-scale framework is a step further towards robust, computationally efficient and accurate modelling of fractures in engineering materials and structures.

NEW DEVELOPMENTS

The new developments are presented in the order of their appearance in the thesis.

1. A fixed-point iterative correction of the extrapolated phase-field is proposed for Heister, Wheeler, and Wick's extrapolation-based monolithic solution technique [34]. The original technique exhibits a step-size dependent solution, which is eliminated with the correction step. [*Chapter 3*.]

2. A Hessian scaling method has been developed, which operates on integration point Hessians. Based on a threshold value of the integration point phase-field $\varphi = 0.4$, the problematic *displacement phase-field* Hessian block is explicitly set to zero. [*Chapter 3*.]

3. Two path-following constraint equations have been proposed for use in the arc-length method. The first equation adopts the incremental fracture surface energy from the phase-field fracture energy functional. The second approach is a reformulation of the first equation in terms

of the degradation function and the fracture driving energy. [*Chapter 3, published as Bharali et al. [265].*]

4. A micromorphic phase-field fracture model has been developed for variationally consistent enforcement of fracture irreversibility constraint. The model transforms the phase-field into a local variable, thereby allowing a pointwise treatment of fracture irreversibility using a *max* operator. A micromorphic field variable is introduced to ensure regularization of the fracture. [*Chapter 4, published as Bharali, Larsson, and Jänicke [238].*]

5. The arc-length method with fracture energy-based path-following constraint is extended to the micromorphic phase-field fracture model. [*Chapter 4.*]

6. A novel constant flux arc-length method has been developed for phase-field hydraulic fracturing problems. The time-step size is considered as the unknown instead of a load parameter. A load parameter scales the external force (flux), and is not relevant for constant flux problems. [*Chapter 5.*]

7. A novel energy functional is proposed for modelling soil desiccation cracking incorporating the part of the water pressure propagating into the solid skeleton in the fracture driving energy. [*Chapter 6.*]

8. Motivated by experimental studies in the literature, the energy functional for soil desiccation cracking is developed in an unified sense encompassing both brittle and quasi-brittle fracture. [*Chapter 6.*]

9. A variationally consistent hierarchical multi-scale phase-field fracture framework has been developed for heterogeneous materials. Therein, the momentum balance equation and the phase-field evolution equation exist in both coarse (engineering) and fine scales. [*Chapter 7, published as Bharali, Larsson, and Jänicke [1, 266].*]

10. The notion of *selective homogenization* is introduced, where the phase-field is forced to live only on the fine scale. This eliminates the coarse scale phase-field evolution equation and results in the conventional multi-scale approaches found in the literature. [*Chapter 7, published as Bharali, Larsson, and Jänicke [1, 266].*]

11. Canonical fine scale (RVE) problem has been developed in a weak micro-periodicity format. The set of equations satisfies the macro-homogeneity condition *a priori*. Furthermore, it is shown that the RVE strongly periodic, Neumann and Dirichlet problems are obtained as special cases, based on appropriate choice of test and trial spaces. [*Chapter 7, published as Bharali, Larsson, and Jänicke [1, 266].*]

CONCLUSION

The new developments (numerical methods and multi-scale framework) in phase-field fracture modelling have been tested on benchmark problems as well as on manufactured academic problems. From these numerical experiments, the following conclusions are made:

1. The arc-length method with an incremental fracture energy based path following constraint outperforms other monolithic solution techniques (diagonal variant of Newton-Raphson method (dia-NR), BFGS method and Hessian scaling method) in terms of (total and average) iterations required for convergence. For an iteration terminating tolerance 10^{-4}, the CPU time reported for the arc-length method is ≈ 5 times lower than the secant based method (dia-NR and BFGS methods) and ≈ 1.8 times lower than the Hessian scaling method. For stricter tolerance 10^{-8}, the CPU time savings are factor ≈ 15 compared to the secant based methods and ≈ 5 compared to the Hessian scaling method. Based on this computational efficiency, the arc-length method is recommended as a computationally efficient monolithic solution technique for phase-field fracture models.

2. In scenarios where the displacement increments are meant to be prescribed and not computed based on path-following constraints, the Hessian scaling method is proposed as a computationally efficient monolithic solution technique. Compared to secant (dia-NR and BFGS) based methods it retains more information of the true Hessian, resulting in superior convergence and reduction in CPU time.

3. Both the arc-length method and the Hessian scaling method exhibits superior convergence w.r.t. varying iteration terminating tolerance, compared to secant based (dia-NR and BFGS) methods. For the single edge notched specimen under tension, a tolerance 10^{-4} is sufficient for the arc-length method and the Hessian scaling method. However, for secant based methods, similar solution is achieved at a stricter tolerance 10^{-6}.

4. From an ease of implementation perspective, the Hessian scaling method is easier to implement in existing finite element codes. The arc-length method requires developing and integrating a new nonlinear solver module.

5. The micromorphic phase-field fracture model is variationally consistent w.r.t enforcing phase-field fracture irreversibility. The irreversibility constraint is treated pointwise on the integration point phase-field variable with system-level precision. Unlike the history variable approach, a comparatively narrow phase-field profile is achieved. Thus, the fracture energy is not over-estimated.

6. The micromorphic phase-field model developed is unified in the sense that it can be used for both brittle and quasi-brittle fracture problems. The model offers flexibility in the choice of phase-field degradation and local dissipation function. Furthermore, the interaction parameter can be interpreted as a penalty parameter or as an additional material parameter calibrated using experimental observations.

7. The micromorphic phase-field model can use the arc-length method developed for the conventional phase-field fracture model in a straightforward fashion. No modelling changes are required. This also shows the versatility, not only of the micromorphic model but also of the arc-length method proposed earlier.

8. The constant flux arc-length method, developed for phase-field hydraulic fracturing, demonstrates computational efficiency and robustness. For iteration terminating tolerances varied as 10^{-4}, 10^{-6} and 10^{-8}, convergence in every step is achieved in less than 25 iterations. Most often, researchers adopt alternate minimization technique for hydraulic fracturing, requiring thousands of iterations to converge. For computational efficiency and robustness, the constant flux arc-length method is recommended instead.

9. In soil desiccation modelling, the novel energy functional (that incorporates the part of the water pressure propagating into the solid skeleton in the fracture driving energy) is a midway proposition between the energy functionals constructed in the effective strain and total strain spaces. Numerical experiments performed in this thesis corroborates this hypothesis.

10. Cohesive zone modelling of soil desiccation cracking within the phase-field fracture framework qualitatively recovers the brittle fracture behaviour for '*low*' values of Irwin's characteristic length. The choice of the characteristic length affects both the number of cracks and their time of propagation. The brittle AT2 model does not incorporate Irwin's characteristic length. As such, for greater flexibility in model calibration, the cohesive zone approach is recommended.

11. The Hessian scaling method is recommended for modelling soil desiccation cracking due to its robustness. Numerical experiments conducted in this thesis demonstrate its ability to converge for iteration terminating tolerances up to 10^{-6}. The BFGS method offers a greater computational efficiency for a tolerance 10^{-4}, but is not able to converge for a stricter tolerance 10^{-6}.

12. The variationally consistent hierarchical multi-scale phase-field fracture framework is recommended for mechanical problems involving heterogeneous materials. Unlike the previous multi-scale frameworks, both stationary and propagating fractures on the fine scale accounts

for the coarse/engineering scale mechanical response. On the engineering scale, the fracture length-scale is implicitly contained through the homogenized quantities.

13. The *selective homogenization* method is recommended to be used with caution as it results in a local material response on the coarse/engineering scale.

14. Finally, it is recommended to use strong periodicity fine scale (RVE) problem since it circumvents artificial stiffening on the RVE boundary as well as artificial softening when fractures intersect the RVE boundary, observed with Dirichlet and Neumann RVE problems, respectively.

FUTURE RESEARCH DIRECTIONS

The numerical methods and the multi-scale phase-field fracture framework developed in this thesis are tested on two-dimensional problems. The extension towards three-dimensional problems may be carried out in a straight-forward fashion. Unlike the discrete fracture models (CZM, XFEM), the phase-field fracture model does not require any additional *ad hoc* criterion for extension towards three-dimensional problems. However, modelling three-dimensional problems would require iterative solvers (CG, GMRES or others) and appropriate preconditioning techniques. Nevertheless, it would be interesting to test computational efficiency and robustness of the numerical methods in a three-dimensional setting.

The arc-length method in this thesis has been implemented using the Sherman-Morisson formula. This results in two linear solves within a single nonlinear iteration. Therefore, one might adopt solvers that operate on multiple right hand sides to save even more computational time. Furthermore, the constant-flux variant of the arc-length method may be adopted for other coupled mechanical-diffusion problems, such as heat transfer and corrosion. This would establish its versatility and robustness across a series of multiphysics problems.

In this thesis, the micromorphic phase-field fracture model is developed, replacing the gradient of the phase-field with a gradient on the micromorphic variable. An alternative micromorphic model may be proposed, replacing the phase-field in the entire fracture surface energy term with the micromorphic variable. Thereafter, one may look into the performance of the two variants for low values of the interaction parameter. Also, adapting the micromorphic model for multiphysics problems open a plethora of research avenues accompanied by possibly interesting challenges.

In the context of hydraulic fracture, a computationally efficient and robust monolithic solution technique is developed. A logical next step would be the transition from academic examples towards real-world data. Based on geological exploration data, the layered rock structure including the natural fractures may be modelled for realistic scenarios. For a given water flux (in-

jection), the possibility of ground water contamination through leakage may be estimated. Such a study would be linked to the United Nations Sustainability Goal 6 (clean water and sanitation) and 12 (responsible consumption and production).

A computationally efficient and robust monolithic solution technique still elusive when it comes to soil desiccation modelling. Some of the monolithic solution techniques developed in this thesis offers only a proof of solvability through numerical experiments. However, there is scope to improve the solution techniques to achieve higher rates of convergence. Furthermore, in this thesis as well as in literature pertaining to phase-field desiccation modelling, Taylor and Hood element is adopted to satisfy the LBB condition. However, the Taylor and Hood element is computationally expensive due to the additional degrees of freedom it introduces. Alternatively, one may investigate the possibility of using stabilization techniques so that lower equal order element may be used, thus reducing the computational cost. In terms of model fidelity, enhancements may be introduced to match the crack spacing, crack depth and the crack propagation in time with field observations. This would enable slope stability assessments in dykes and embankments in the view of increasing global temperatures due to climate change.

The multi-scale phase-field fracture framework was tested using a simple academic problem, comprising of a two-dimensional RVE and a one-dimensional bar on the coarse/engineering scale. Extension towards real-world problems is possible but computationally prohibitively expensive. One may require a lot of parallel computing resources. Alternatively, surrogate models using reduced order modelling techniques or machine learning may be developed to reduce the computational cost.

Part VI

APPENDIX

A

THE LADYZHENSKAYA–BABUŠKA–BREZZI (LBB) CONDITION FOR PORO-MECHANICS

This chapter investigates the effect of violating the Ladyzhenskaya–Babuška–Brezzi (LBB) condition in poro-mechanics applications (hydraulic fracturing and soil desiccation cracking problems). To that end, numerical experiments are conducted on hydraulic fracturing and desiccation cracking specimens using 3-noded triangular elements and 6-noded Taylor and Hood elements.

A.1 THE LBB CONDITION FOR STABILITY AND UNIQUENESS

The Ladyzhenskaya–Babuška–Brezzi (LBB) condition is a sufficient condition that guarantees a unique solution continuously dependent on input data for a given saddle point problem. For mathematical details pertaining to the LBB condition, the reader is referred to the book 'Mixed Finite Element Methods and Applications' by Boffi, Brezzi, Fortin, et al. [267]. Without delving into the rigorous mathematics, one may discretize a saddle point problem, for instance in poro-mechanics (irrespective of the phase-field), with a Taylor and Hood element [184] to fulfill the LBB condition. The Taylor and Hood element adopts quadratic trial and test functions for the displacement field, while the pressure field remains linear. A lower order LBB fulfilling element is the Mini element [268], which is a 3-noded triangular element embedded with a bubble function for the displacement field. However, the Mini element entails modelling complexity pertaining to the bubble function degree of freedom. As such, the Taylor and Hood element is adopted in this thesis.

The LBB condition ensures the numerical stability for a saddle point problem solution for a range of input data. For a given set of input data, one may achieve a unique solution even without the use of LBB stable elements such as the Taylor and Hood element [184] or the Mini element [268]. An element with equal order test and trial functions for the displacement and the pressure field may suffice. This aspect is investigated is the following sections.

A.2 LINEAR ELEMENT VS TAYLOR AND HOOD ELEMENT IN HYDRAULIC FRACTURING

In this section, a hydraulic fracturing numerical experiment is carried out on a Single Natural Fracture (SNF) specimen using 3-noded constant strain elements and 6-noded Taylor and Hood elements. The specimen is introduced earlier in Section 5.4.1. For details pertaining to geometry and model parameters, the reader is referred to Figure 5.1 and Table 5.1.

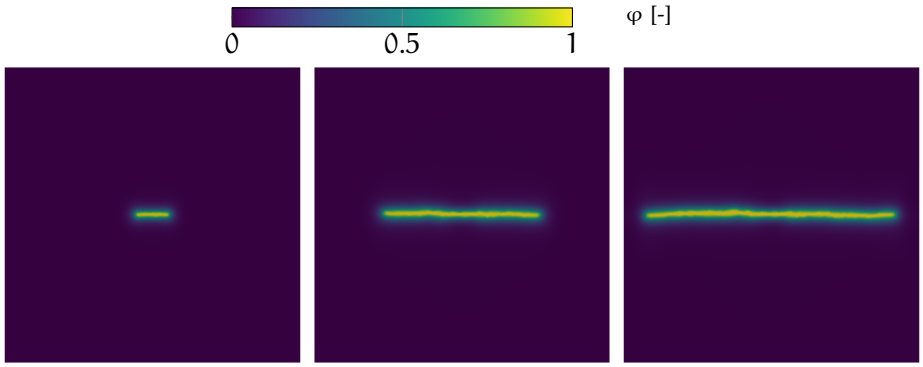

(a) t = 0.01 [s] (b) t = 0.1 [s] (c) t = 0.2 [s]

Figure A.1: Figures (a-c) present the distribution of the phase-field variable at the different times during the analysis of the Single Natural Fracture (SNF) specimen with 6-noded Taylor and Hood elements.

Figure A.1 presents the distribution of the phase-field in the SNF specimen obtained at different simulation times using 6-noded Taylor and Hood elements. On using a less computationally expensive 3-noded constant strain element, the distribution of the phase-field remains the same. The water pressure distribution obtained using 6-noded Taylor and Hood elements is presented in Figure A.2. Similar pressure distribution is also obtained with 3-noded constant strain elements (see Figure 5.3).

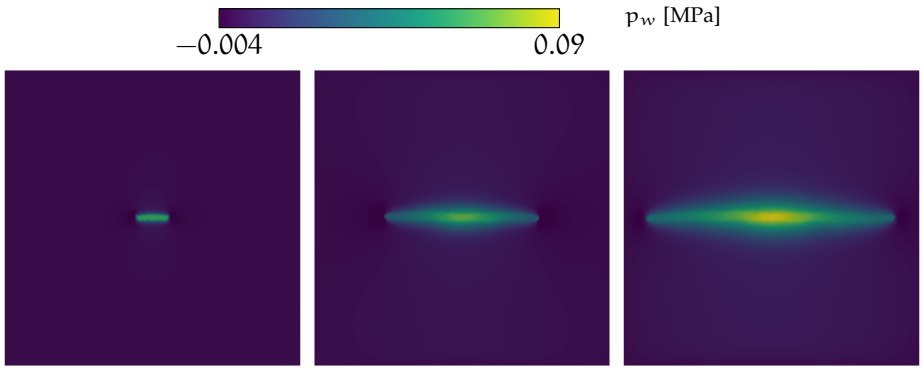

(a) t = 0.01 [s] (b) t = 0.1 [s] (c) t = 0.2 [s]

Figure A.2: Figures (a-c) present the distribution of the water pressure at the different times during the analysis of the Single Natural Fracture (SNF) specimen with 6-noded Taylor and Hood elements.

In the context of computational expense, the 6-noded Taylor and Hood element introduces additional degrees of freedom due to the higher order displacement and phase-field test and trial functions. This leads to higher computational cost compared to the 3-noded constant strain element, observed from the CPU time required for the simulation in Table A.1.

Element type (uDOFs)	tol	Steps	Total Iters.	Avg. Iters.	CPU time [s]
Constant strain (28977)	10^{-4}	146	759	5.20	1925.0
	10^{-6}	128	980	7.65	3379.0
	10^{-8}	158	1408	8.91	11150.0
Taylor and Hood (94870)	10^{-4}	163	1222	7.49	8552.0
	10^{-6}	200	1528	7.64	10887.0
	10^{-8}	244	2210	9.06	45236.0

Table A.1: Table presents the total numbers of steps and iterations, average iterations and CPU time (in seconds) for the SNF specimen simulated using the arc-length method with varying iteration terminating tolerances and element type. uDOFs is an abbreviation for unconstrained Degrees of Freedom.

A.3 LINEAR ELEMENT VS TAYLOR AND HOOD ELEMENT IN SOIL DESICCATION CRACKING

In this section, a soil desiccation cracking numerical experiment is carried out on a notched specimen using 3-noded constant strain elements and 6-noded Taylor and Hood elements. The specimen is introduced earlier in Section 5.4.1. The energy functional E_4 and its corresponding Discrete Problem 13 is adopted for this study. For details pertaining to geometry and model parameters, the reader is referred to Figure 6.1and Table 6.1.

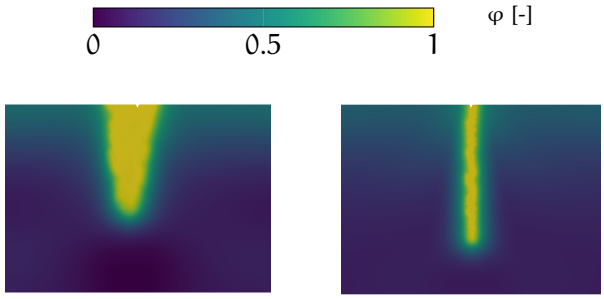

(a) Constant strain element, t = 1810 [s] (b) Taylor and Hood element, t = 1240 [s]

Figure A.3: Figures (a-b) present the distribution of the phase-field variable pertinent to the energy functional E_4. The sub-figures correspond to the 3-noded constant strain element and the 6-noded Taylor and Hood element, respectively.

Figure A.3 presents the distribution of the phase-field in the notched soil specimen obtained using the 3-noded constant strain element and the 6-noded Taylor and Hood element. For both elements, the phase-field variable interpolation order follows that of the displacement field. Unlike the LBB stable Taylor and Hood element, the constant strain element results in an orthogonal widening of the fracture. The orthogonal widening of the fracture remains on further refining the mesh with the 3-noded constant strain elements. This justifies that Taylor and Hood element outperforms the lower order 3-noded constant strain element.

BIBLIOGRAPHY

[1] Ritukesh Bharali et al. "Computational homogenisation of phase-field fracture." In: *European Journal of Mechanics - A/Solids* 88 (2021), p. 104247. ISSN: 0997-7538. DOI: 10.1016/j.euromechsol.2021.104247.

[2] Jian-Ying Wu. "A unified phase-field theory for the mechanics of damage and quasi-brittle failure." In: *Journal of the Mechanics and Physics of Solids* 103 (2017), pp. 72–99. DOI: 10.1016/j.jmps.2017.03.015.

[3] Anil K Chopra and P Chakrabarti. "The Koyna earthquake and the damage to Koyna dam." In: *Bulletin of the Seismological Society of America* 63.2 (1973), pp. 381–397. DOI: 10.1785/BSSA0630020381.

[4] Raghvendra Singh et al. "Analysis of earth dams affected by the 2001 Bhuj Earthquake." In: *Engineering geology* 80.3-4 (2005), pp. 282–291. DOI: 10.1016/j.enggeo.2005.06.002.

[5] KS Jagadish et al. "Behaviour of masonry structures during the Bhuj earthquake of January 2001." In: *Journal of Earth System Science* 112.3 (2003), pp. 431–440. DOI: 10.1007/BF02709270.

[6] Katsuichiro Goda et al. "The 2015 Gorkha Nepal earthquake: insights from earthquake damage survey." In: *Frontiers in Built Environment* 1 (2015), p. 8. DOI: 10.3389/fbuil.2015.00008.

[7] M Di Ludovico et al. "Remarks on damage and response of school buildings after the Central Italy earthquake sequence." In: *Bulletin of earthquake engineering* 17.10 (2019), pp. 5679–5700. DOI: 10.1007/s10518-018-0332-x.

[8] J.J.B. Bronswijk. "Modeling of water balance, cracking and subsidence of clay soils." In: *Journal of Hydrology* 97.3 (1988), pp. 199–212. ISSN: 0022-1694. DOI: 10.1016/0022-1694(88)90115-1.

[9] Hideo Kobayashi and Hisahiro Onoue. "Brittle fracture of liberty ships." In: *Failure Knowledge Database* 100 (1943), p. 67. URL: https://www.shippai.org/fkd/en/hfen/HB1011020.pdf.

[10] Alan Arnold Griffith and Geoffrey Ingram Taylor. "VI. The phenomena of rupture and flow in solids." In: *Philosophical Transactions of the Royal Society of London. Series A, Containing Papers of a Mathematical or Physical Character* 221.582-593 (1921), pp. 163–198. DOI: 10.1098/rsta.1921.0006.

[11] G.R. Irwin. "Analysis of Stresses and Strains near the End of a Crack Traversing a Plate." In: *Journal of Applied Mechanics-Transactions of the ASME* E24 (1957), pp. 351–369. DOI: 10.1115/1.4011547.

[12] D.S. Dugdale. "Yielding of steel sheets containing slits." In: *Journal of the Mechanics and Physics of Solids* 8.2 (1960), pp. 100–104. ISSN: 0022-5096. DOI: 10.1016/0022-5096(60)90013-2.

[13] G.I. Barenblatt. "The Mathematical Theory of Equilibrium Cracks in Brittle Fracture." In: ed. by H.L. Dryden et al. Vol. 7. Advances in Applied Mechanics. Elsevier, 1962, pp. 55–129. DOI: 10.1016/S0065-2156(08)70121-2.

[14] MGGV Elices et al. "The cohesive zone model: advantages, limitations and challenges." In: *Engineering fracture mechanics* 69.2 (2002), pp. 137–163. DOI: 10.1016/S0013-7944(01)00083-2.

[15] Natarajan Sukumar et al. "Extended finite element method for three-dimensional crack modelling." In: *International journal for numerical methods in engineering* 48.11 (2000), pp. 1549–1570. DOI: 10.1002/1097-0207(20000820)48:11<1549::AID-NME955>3.0.CO;2-A.

[16] Nicolas Moës and Ted Belytschko. "Extended finite element method for cohesive crack growth." In: *Engineering fracture mechanics* 69.7 (2002), pp. 813–833. DOI: 10.1016/S0013-7944(01)00128-X.

[17] Amir R Khoei. *Extended finite element method: theory and applications*. John Wiley & Sons, 2014. ISBN: 9781118869673. DOI: 10.1002/9781118869673.

[18] Christian Linder and Francisco Armero. "Finite elements with embedded strong discontinuities for the modeling of failure in solids." In: *International Journal for Numerical Methods in Engineering* 72.12 (2007), pp. 1391–1433. DOI: 10.1002/nme.2042.

[19] José M Sancho et al. "An embedded crack model for finite element analysis of concrete fracture." In: *Engineering fracture mechanics* 74.1-2 (2007), pp. 75–86. DOI: 10.1016/j.engfracmech.2006.01.015.

[20] G.A. Francfort and J.-J. Marigo. "Revisiting brittle fracture as an energy minimization problem." In: *Journal of the Mechanics and Physics of Solids* 46.8 (Aug. 1998), pp. 1319–1342. ISSN: 00225096. DOI: 10.1016/S0022-5096(98)00034-9.

[21] B. Bourdin et al. "Numerical experiments in revisited brittle fracture." In: *Journal of the Mechanics and Physics of Solids* 48.4 (2000), pp. 797–826. ISSN: 0022-5096. DOI: 10.1016/S0022-5096(99)00028-9.

[22] B. Bourdin. "Numerical implementation of the variational formulation for quasi-static brittle fracture." In: *Interfaces and Free Boundaries* 9 (2007), pp. 411–430. DOI: 10.4171/IFB/171.

[23] R. H. J. Peerlings et al. "Gradient enhanced damage for quasi-brittle materials." In: *International Journal for Numerical Methods in Engineering* 39.19 (1996), pp. 3391–3403. DOI: 10.1002/(SICI)1097-0207(19961015)39:19<3391::AID-NME7>3.0.CO;2-D.

[24] M.G.D. Geers et al. "Strain-based transient-gradient damage model for failure analyses." In: *Computer Methods in Applied Mechanics and Engineering* 160.1 (1998), pp. 133–153. ISSN: 0045-7825. DOI: 10.1016/S0045-7825(98)80011-X.

[25] Stewart A Silling. "Reformulation of elasticity theory for discontinuities and long-range forces." In: *Journal of the Mechanics and Physics of Solids* 48.1 (2000), pp. 175–209. DOI: 10.1016/S0022-5096(99)00029-0.

[26] Stewart A Silling and Ebrahim Askari. "A meshfree method based on the peridynamic model of solid mechanics." In: *Computers & structures* 83.17-18 (2005), pp. 1526–1535. DOI: 10.1016/j.compstruc.2004.11.026.

[27] Pablo Seleson et al. "Peridynamics as an upscaling of molecular dynamics." In: *Multiscale Modeling & Simulation* 8.1 (2009), pp. 204–227. DOI: 10.1137/09074807X.

[28] Laura De Lorenzis and Tymofiy Gerasimov. "Numerical implementation of phase-field models of brittle fracture." In: *Modeling in Engineering Using Innovative Numerical Methods for Solids and Fluids*. Springer, 2020, pp. 75–101. ISBN: 978-3-030-37518-8. DOI: 10.1007/978-3-030-37518-8_3.

[29] Thomas Wick. *Multiphysics phase-field fracture: modeling, adaptive discretizations, and solvers*. Vol. 28. Walter de Gruyter GmbH & Co KG, 2020. DOI: 10.1515/9783110497397.

[30] Olgierd Cecil Zienkiewicz et al. *The finite element method*. Vol. 3. McGraw-hill London, 1977.

[31] Susanne C Brenner et al. *The mathematical theory of finite element methods*. Vol. 3. Springer, 2008. ISBN: 978-0-387-75934-0. DOI: 10.1007/978-0-387-75934-0.

[32] Tymofiy Gerasimov and Laura De Lorenzis. "On penalization in variational phase-field models of brittle fracture." In: *Computer Methods in Applied Mechanics and Engineering* 354 (2019), pp. 990–1026. DOI: 10.1016/j.cma.2019.05.038.

[33] M. Hintermüller et al. "The Primal-Dual Active Set Strategy as a Semismooth Newton Method." In: *SIAM Journal on Optimization* 13.3 (2002), pp. 865–888. DOI: 10.1137/S1052623401383558.

[34] Timo Heister et al. "A primal-dual active set method and predictor-corrector mesh adaptivity for computing fracture propagation using a phase-field approach." In: *Computer Methods in Applied Mechanics and Engineering* (2015). ISSN: 00457825. DOI: 10.1016/j.cma.2015.03.009.

[35] J. Wambacq et al. "Interior-point methods for the phase-field approach to brittle and ductile fracture." In: *Computer Methods in Applied Mechanics and Engineering* 375 (2021), p. 113612. ISSN: 0045-7825. DOI: 10.1016/j.cma.2020.113612.

[36] M.F. Wheeler et al. "An augmented-Lagrangian method for the phase-field approach for pressurized fractures." In: *Computer Methods in Applied Mechanics and Engineering* 271 (2014), pp. 69–85. ISSN: 0045-7825. DOI: 10.1016/j.cma.2013.12.005.

[37] Christian Miehe et al. "A phase field model for rate-independent crack propagation: Robust algorithmic implementation based on operator splits." In: *Computer Methods in Applied Mechanics and Engineering* 199.45-48 (2010), pp. 2765–2778. ISSN: 00457825. DOI: 10.1016/j.cma.2010.04.011.

[38] A. Mikelić et al. "Phase-field modeling of a fluid-driven fracture in a poroelastic medium." In: *Computational Geosciences* 19.6 (Dec. 2015), pp. 1171–1195. ISSN: 1573-1499. DOI: 10.1007/s10596-015-9532-5.

[39] Andro Mikelić et al. "A Phase-Field Method for Propagating Fluid-Filled Fractures Coupled to a Surrounding Porous Medium." In: *Multiscale Modeling & Simulation* 13.1 (2015), pp. 367–398. DOI: 10.1137/140967118.

[40] Keita Yoshioka and Blaise Bourdin. "A variational hydraulic fracturing model coupled to a reservoir simulator." In: *International Journal of Rock Mechanics and Mining Sciences* 88 (2016), pp. 137–150. ISSN: 1365-1609. DOI: 10.1016/j.ijrmms.2016.07.020.

[41] Chukwudi Chukwudozie et al. "A variational phase-field model for hydraulic fracturing in porous media." In: *Computer Methods in Applied Mechanics and Engineering* 347 (2019), pp. 957–982. ISSN: 0045-7825. DOI: 10.1016/j.cma.2018.12.037.

[42] Tao You and Keita Yoshioka. "On poroelastic strain energy degradation in the variational phase-field models for hydraulic fracture." In: *Computer Methods in Applied Mechanics and Engineering* 416 (2023), p. 116305. ISSN: 0045-7825. DOI: 10.1016/j.cma.2023.116305.

[43] Arthur H. Lachenbruch. "Depth and spacing of tension cracks." In: *Journal of Geophysical Research (1896-1977)* 66.12 (1961), pp. 4273–4292. DOI: 10.1029/JZ066i012p04273.

[44] H. Peron et al. "Discrete element modelling of drying shrinkage and cracking of soils." In: *Computers and Geotechnics* 36.1 (2009), pp. 61–69. ISSN: 0266-352X. DOI: 10.1016/j.compgeo.2008.04.002.

[45] Aruna L. Amarasiri and Jayantha K. Kodikara. "Numerical Modeling of Desiccation Cracking Using the Cohesive Crack Method." In: *International Journal of Geomechanics* 13.3 (2013), pp. 213–221. DOI: 10.1061/(ASCE)GM.1943-5622.0000192.

[46] Aruna L. Amarasiri and Jayantha K. Kodikara. "Numerical modelling of a field desiccation test." In: *Géotechnique* 63.11 (2013), pp. 983–986. DOI: 10.1680/geot.12.P.010.

[47] Aruna Amarisiri et al. "Numerical modelling of desiccation cracking in a restrained ring test." In: *Canadian Geotechnical Journal* 51.1 (Nov. 2014), pp. 67–76. DOI: 10.1139/cgj-2012-0408.

[48] Tuanny Cajuhi et al. "Phase-field modeling of fracture in variably saturated porous media." In: *Computational Mechanics* 61.3 (2018), pp. 299–318. DOI: 10.1007/s00466-017-1459-3.

[49] Yousef Heider and WaiChing Sun. "A phase field framework for capillary-induced fracture in unsaturated porous media: Drying-induced vs. hydraulic cracking." In: *Computer Methods in Applied Mechanics and Engineering* 359 (2020), p. 112647. ISSN: 0045-7825. DOI: 10.1016/j.cma.2019.112647.

[50] Chenyi Luo et al. "Phase-field modeling of drying-induced cracks: Choice of coupling and study of homogeneous and localized damage." In: *Computer Methods in Applied Mechanics and Engineering* 410 (2023), p. 115962. ISSN: 0045-7825. DOI: 10.1016/j.cma.2023.115962.

[51] Claudio Gavagnin et al. "Stabilized mixed formulation for phase-field computation of deviatoric fracture in elastic and poroelastic materials." In: *Computational Mechanics* 65.6 (June 2020), pp. 1447–1465. ISSN: 1432-0924. DOI: 10.1007/s00466-020-01829-x.

[52] RU Patil et al. "An adaptive multiscale phase field method for brittle fracture." In: *Computer Methods in Applied Mechanics and Engineering* 329 (2018), pp. 254–288. DOI: 10.1016/j.cma.2017.09.021.

[53] RU Patil et al. "A new multiscale phase field method to simulate failure in composites." In: *Advances in Engineering Software* 126 (2018), pp. 9–33. DOI: 10.1016/j.advengsoft.2018.08.010.

[54] RU Patil et al. "A multiscale framework based on phase field method and XFEM to simulate fracture in highly heterogeneous materials." In: *Theoretical and Applied Fracture Mechanics* 100 (2019), pp. 390–415. DOI: 10.1016/j.tafmec.2019.02.002.

[55] Nima Noii et al. "An adaptive global–local approach for phase-field modeling of anisotropic brittle fracture." In: *Computer Methods in Applied Mechanics and Engineering* 361 (2020), p. 112744. DOI: 10.1016/j.cma.2019.112744.

[56] Bang He et al. "A numerical-homogenization based phase-field fracture modeling of linear elastic heterogeneous porous media." In: *Computational Materials Science* 176 (2020), p. 109519. DOI: 10.1016/j.commatsci.2020.109519.

[57] Francesca Fantoni et al. "A phase field approach for damage propagation in periodic microstructured materials." In: *International Journal of Fracture* 223.1 (2020), pp. 53–76. DOI: 10.1007/s10704-019-00400-x.

[58] Thomas JR Hughes. *The finite element method: linear static and dynamic finite element analysis*. Dover Publications, New York, 2012. ISBN: 978-0-486-41181-1.

[59] René De Borst et al. *Nonlinear finite element analysis of solids and structures*. John Wiley & Sons, 2012. ISBN: 9781118375938. DOI: 10.1002/9781118375938.

[60] J. H. Wegstein. "Accelerating Convergence of Iterative Processes." In: *Commun. ACM* 1.6 (June 1958), pp. 9–13. ISSN: 0001-0782. DOI: 10.1145/368861.368871.

[61] Timothy A. Davis. "Algorithm 832: UMFPACK V4.3—an Unsymmetric-Pattern Multifrontal Method." In: *ACM Trans. Math. Softw.* 30.2 (May 2004), pp. 196–199. ISSN: 0098-3500. DOI: 10.1145/992200.992206.

[62] P.R. Amestoy et al. "Multifrontal parallel distributed symmetric and unsymmetric solvers." In: *Computer Methods in Applied Mechanics and Engineering* 184.2 (2000), pp. 501–520. ISSN: 0045-7825. DOI: 10.1016/S0045-7825(99)00242-X.

[63] Olaf Schenk. "Scalable parallel sparse LU factorization methods on shared memory multiprocessors." PhD thesis. ETH Zurich, 2000. URL: https://www.research-collection.ethz.ch/bitstream/handle/20.500.11850/144477/eth-23343-02.pdf.

[64] Intel. *Intel oneAPI Math Kernel Library*. Version 2022.0.2. Sept. 27, 2023. URL: https://www.intel.com/content/www/us/en/developer/tools/oneapi/onemkl.html.

[65] J.M. Melenk and I. Babuška. "The partition of unity finite element method: Basic theory and applications." In: *Computer Methods in Applied Mechanics and Engineering* 139.1 (1996), pp. 289–314. ISSN: 0045-7825. DOI: 10.1016/S0045-7825(96)01087-0.

[66] Eric Lorentz and V Godard. "Gradient damage models: Toward full-scale computations." In: *Computer Methods in Applied Mechanics and Engineering* 200.21-22 (2011), pp. 1927–1944. DOI: 10.1016/j.cma.2010.06.025.

[67] Luigi Ambrosio and Vincenzo Maria Tortorelli. "Approximation of functional depending on jumps by elliptic functional via t-convergence." In: *Communications on Pure and Applied Mathematics* 43.8 (1990), pp. 999–1036. DOI: 10.1002/cpa.3160430805.

[68] Kim Pham et al. "Gradient damage models and their use to approximate brittle fracture." In: *International Journal of Damage Mechanics* 20.4 (2011), pp. 618–652. DOI: 10.1177/1056789510386852.

[69] Michael J Borden et al. "A phase-field formulation for fracture in ductile materials: Finite deformation balance law derivation, plastic degradation, and stress triaxiality effects." In: *Computer Methods in Applied Mechanics and Engineering* 312 (2016), pp. 130–166. DOI: 10.1016/j.cma.2016.09.005.

[70] H Cornelissen et al. "Experimental determination of crack softening characteristics of normalweight and lightweight." In: *Heron* 31.2 (1986), pp. 45–46. URL: http://resolver.tudelft.nl/uuid:08c29b39-5c60-4ab6-b9d5-643d11007f7c.

[71] Giovanni Lancioni and Gianni Royer-Carfagni. "The variational approach to fracture mechanics. A practical application to the French Panthéon in Paris." In: *Journal of elasticity* 95.1-2 (2009), pp. 1–30. DOI: 10.1007/s10659-009-9189-1.

[72] Hanen Amor et al. "Regularized formulation of the variational brittle fracture with unilateral contact: Numerical experiments." In: *Journal of the Mechanics and Physics of Solids* 57.8 (2009), pp. 1209–1229. DOI: 10.1016/j.jmps.2009.04.011.

[73] Laura De Lorenzis and Corrado Maurini. "Nucleation under multiaxial loading in variational phase-field models of brittle fracture." In: *International Journal of Fracture* (June 2021). ISSN: 1573-2673. DOI: 10.1007/s10704-021-00555-6.

[74] Tianyi Li. "Gradient-Damage Modeling of Dynamic Brittle F racture: Variational Principles and Numerical Simulations." PhD thesis. Université Paris-Saclay, Oct. 2016. URL: https://hal.science/hal-01248263/document.

[75] T. Gerasimov and L. De Lorenzis. "A line search assisted monolithic approach for phase-field computing of brittle fracture." In: *Computer Methods in Applied Mechanics and Engineering* 312 (Dec. 2016), pp. 276–303. ISSN: 00457825. DOI: 10.1016/j.cma.2015.12.017.

[76] R. Fletcher and T. L. Freeman. "A modified Newton method for minimization." In: *Journal of Optimization Theory and Applications* 23.3 (Nov. 1977), pp. 357–372. ISSN: 1573-2878. DOI: 10.1007/BF00933446.

[77] H. Mukai and E. Polak. "A second-order method for unconstrained optimization." In: *Journal of Optimization Theory and Applications* 26.4 (Dec. 1978), pp. 501–513. ISSN: 1573-2878. DOI: 10.1007/BF00933149.

[78] Thomas Wick. "Modified Newton methods for solving fully monolithic phase-field quasi-static brittle fracture propagation." In: *Computer Methods in Applied Mechanics and Engineering* 325 (2017), pp. 577–611. ISSN: 0045-7825. DOI: 10.1016/j.cma.2017.07.026.

[79] Jaroslav Hron et al. "A Computational Comparison of Two FEM Solvers for Nonlinear Incompressible Flow." In: *Challenges in Scientific Computing - CISC 2002*. Ed. by Eberhard Bänsch. Berlin, Heidelberg: Springer Berlin Heidelberg, 2003, pp. 87–109. ISBN: 978-3-642-19014-8. DOI: 10.1007/978-3-642-19014-8_5.

[80] Saptarshi Mandal et al. "Modified Newton Solver for Yield Stress Fluids." In: *Numerical Mathematics and Advanced Applications ENUMATH 2015*. Ed. by Bülent Karasözen et al. Cham: Springer International Publishing, 2016, pp. 481–490. ISBN: 978-3-319-39929-4. DOI: 10.1007/978-3-319-39929-4_46.

[81] C. Mehlmann and T. Richter. "A modified global Newton solver for viscous-plastic sea ice models." In: *Ocean Modelling* 116 (2017), pp. 96–107. ISSN: 1463-5003. DOI: 10.1016/j.ocemod.2017.06.001.

[82] Olivier Lampron et al. "An efficient and robust monolithic approach to phase-field quasi-static brittle fracture using a modified Newton method." In: *Computer Methods in Applied Mechanics and Engineering* 386 (2021), p. 114091. ISSN: 0045-7825. DOI: 10.1016/j.cma.2021.114091.

[83] Jian-Ying Wu et al. "On the BFGS monolithic algorithm for the unified phase field damage theory." In: *Computer Methods in Applied Mechanics and Engineering* 360 (2020), p. 112704. ISSN: 0045-7825. DOI: 10.1016/j.cma.2019.112704.

[84] Leon Kolditz et al. "A modified combined active-set Newton method for solving phase-field fracture into the monolithic limit." In: *Computer Methods in Applied Mechanics and Engineering* 414 (2023), p. 116170. ISSN: 0045-7825. DOI: 10.1016/j.cma.2023.116170.

[85] Philip K. Kristensen and Emilio Martínez-Pañeda. "Phase field fracture modelling using quasi-Newton methods and a new adaptive step scheme." In: *Theoretical and Applied Fracture Mechanics* 107 (2020), p. 102446. ISSN: 0167-8442. DOI: 10.1016/j.tafmec.2019.102446.

[86] Gerald A. Wempner. "Discrete approximations related to nonlinear theories of solids." In: *International Journal of Solids and Structures* 7.11 (1971), pp. 1581–1599. ISSN: 0020-7683. DOI: 10.1016/0020-7683(71)90038-2.

[87] E. Riks. "The Application of Newton's Method to the Problem of Elastic Stability." In: *Journal of Applied Mechanics* 39.4 (Dec. 1972), pp. 1060–1065. ISSN: 0021-8936. DOI: 10.1115/1.3422829.

[88] E. Riks. "An incremental approach to the solution of snapping and buckling problems." In: *International Journal of Solids and Structures* 15.7 (1979), pp. 529–551. ISSN: 0020-7683. DOI: 10.1016/0020-7683(79)90081-7.

[89] M.A. Crisfield. "A FAST INCREMENTAL/ITERATIVE SOLUTION PROCEDURE THAT HANDLES "SNAP-THROUGH"." In: *Computational Methods in Nonlinear Structural and Solid Mechanics*. Ed. by AHMED K. NOOR and HARVEY G. McCOMB. Pergamon, 1981, pp. 55–62. ISBN: 978-0-08-027299-3. DOI: 10.1016/B978-0-08-027299-3.50009-1.

[90] K. C. Park. "A family of solution algorithms for nonlinear structural analysis based on relaxation equations." In: *International Journal for Numerical Methods in Engineering* 18.9 (1982), pp. 1337–1347. DOI: 10.1002/nme.1620180906.

[91] Clemens V. Verhoosel et al. "A dissipation-based arc-length method for robust simulation of brittle and ductile failure." In: *International Journal for Numerical Methods in Engineering* 77.9 (2009), pp. 1290–1321. DOI: 10.1002/nme.2447.

[92] Julien Vignollet et al. "Phase-field models for brittle and cohesive fracture." In: *Meccanica* 49.11 (2014), pp. 2587–2601. DOI: 10.1007/s11012-013-9862-0.

[93] Stefan May et al. "A numerical assessment of phase-field models for brittle and cohesive fracture: Γ-convergence and stress oscillations." In: *European Journal of Mechanics-A/Solids* 52 (2015), pp. 72–84. DOI: 10.1016/j.euromechsol.2015.02.002.

[94] N Singh et al. "A fracture-controlled path-following technique for phase-field modeling of brittle fracture." In: *Finite Elements in Analysis and Design* 113 (2016), pp. 14–29. DOI: 10.1016/j.finel.2015.12.005.

[95] L.M. Kachanov. *The theory of creep*. Part 2. National Lending Library for Science & Technology, 1967. URL: https://books.google.se/books?id=JA03wAEACAAJ.

[96] Yu. N. Rabotnov et al. "Creep Problems in Structural Members." In: *Journal of Applied Mechanics* 37.1 (Mar. 1970), pp. 249–249. ISSN: 0021-8936. DOI: 10.1115/1.3408479.

[97] Jean Lemaitre and Jean-Louis Chaboche. *Mechanics of Solid Materials*. Cambridge University Press, 1990. DOI: 10.1017/CBO9781139167970.

[98] William Karush. "Minima of functions of several variables with inequalities as side constraints." In: *M. Sc. Dissertation. Dept. of Mathematics, Univ. of Chicago* (1939). URL: https://cir.nii.ac.jp/crid/1572824501070501888.

[99] H. W. Kuhn and A. W. Tucker. "Nonlinear programming." In: *Proceedings of the Second Berkeley Symposium on Mathematical Statistics and Probability, 1950*, 1951, pp. 481–492.

[100] Somdatta Goswami et al. "Adaptive phase field analysis with dual hierarchical meshes for brittle fracture." In: *Engineering Fracture Mechanics* 218 (2019), p. 106608. DOI: 10.1016/j.engfracmech.2019.106608.

[101] Chintan Jansari et al. "Adaptive phase field method for quasi-static brittle fracture using a recovery based error indicator and quadtree decomposition." In: *Engineering Fracture Mechanics* 220 (2019), p. 106599. DOI: 10.1016/j.engfracmech.2019.106599.

[102] Thomas Wick. "Goal functional evaluations for phase-field fracture using PU-based DWR mesh adaptivity." In: *Computational Mechanics* 57.6 (2016), pp. 1017–1035. DOI: 10.1007/s00466-016-1275-1.

[103] Sindhu Nagaraja et al. "Phase-field modeling of brittle fracture with multi-level hp-FEM and the finite cell method." In: *Computational mechanics* 63.6 (2019), pp. 1283–1300. DOI: 10.1007/s00466-018-1649-7.

[104] Olivier Coussy. *Poromechanics*. John Wiley & Sons, 2004. ISBN: 9780470092712. DOI: 10.1002/0470092718.

[105] Maurice A. Biot. "General Theory of Three-Dimensional Consolidation." In: *Journal of Applied Physics* 12.2 (Feb. 1941), pp. 155–164. ISSN: 0021-8979. DOI: 10.1063/1.1712886.

[106] M. A. Biot. "Theory of Elasticity and Consolidation for a Porous Anisotropic Solid." In: *Journal of Applied Physics* 26.2 (Feb. 1955), pp. 182–185. ISSN: 0021-8979. DOI: 10.1063/1.1721956.

[107] M. A. Biot. "General Solutions of the Equations of Elasticity and Consolidation for a Porous Material." In: *Journal of Applied Mechanics* 23.1 (Mar. 1956), pp. 91–96. ISSN: 0021-8936. DOI: 10.1115/1.4011213.

[108] M. A. Biot and D. G. Willis. "The Elastic Coefficients of the Theory of Consolidation." In: *Journal of Applied Mechanics* 24.4 (Dec. 1957), pp. 594–601. ISSN: 0021-8936. DOI: 10.1115/1.4011606.

[109] M. A. Biot. "Mechanics of Deformation and Acoustic Propagation in Porous Media." In: *Journal of Applied Physics* 33.4 (June 2004), pp. 1482–1498. ISSN: 0021-8979. DOI: 10.1063/1.1728759.

[110] A. W. Bishop. "The Principle of Effective Stress." In: *Teknisk Ukeblad* 39 (1959), pp. 859–863. URL: https://api.semanticscholar.org/CorpusID:208830828.

[111] B. A. Schrefler et al. "Mechanics of Partially Saturated Porous Media." In: *Numerical Methods and Constitutive Modelling in Geomechanics*. Ed. by C. S. Desai and G. Gioda. Vienna: Springer Vienna, 1990, pp. 169–209. ISBN: 978-3-7091-2832-9. DOI: 10.1007/978-3-7091-2832-9_2.

[112] Arnold Verruijt. "Theory and problems of poroelasticity." In: *Delft University of Technology* 71 (2013), p. 465. URL: https://geo.verruijt.net/.

[113] M Th Van Genuchten. "A closed-form equation for predicting the hydraulic conductivity of unsaturated soils." In: *Soil science society of America journal* 44.5 (1980), pp. 892–898. DOI: 10.2136/sssaj1980.03615995004400050002x.

[114] Royal Harvard Brooks. "Hydraulic properties of porous media." PhD thesis. Colorado State University, 1965. ISBN: 9781084094253.

[115] WR Gardner. "Field measurement of soil water diffusivity." In: *Soil Science Society of America Journal* 34.5 (1970), pp. 832–833. DOI: 10.2136/sssaj1970.03615995003400050045x.

[116] Jacob Fish et al. "Mesoscopic and multiscale modelling in materials." In: *Nature Materials* 20.6 (June 2021), pp. 774–786. ISSN: 1476-4660. DOI: 10.1038/s41563-020-00913-0.

[117] J.L. Ericksen. "On the Cauchy—Born Rule." In: *Mathematics and Mechanics of Solids* 13.3-4 (2008), pp. 199–220. DOI: 10.1177/1081286507086898.

[118] E.B. Tadmor et al. "Quasicontinuum analysis of defects in solids." In: *Philosophical Magazine A* 73.6 (1996), pp. 1529–1563. DOI: 10.1080/01418619608243000.

[119] Thomas J.R. Hughes. "Multiscale phenomena: Green's functions, the Dirichlet-to-Neumann formulation, subgrid scale models, bubbles and the origins of stabilized methods." In: *Computer Methods in Applied Mechanics and Engineering* 127.1 (1995), pp. 387–401. ISSN: 0045-7825. DOI: 10.1016/0045-7825(95)00844-9.

[120] Thomas Y. Hou and Xiao-Hui Wu. "A Multiscale Finite Element Method for Elliptic Problems in Composite Materials and Porous Media." In: *Journal of Computational Physics* 134.1 (1997), pp. 169–189. ISSN: 0021-9991. DOI: 10.1006/jcph.1997.5682.

[121] Thomas J.R. Hughes et al. "The variational multiscale method—a paradigm for computational mechanics." In: *Computer Methods in Applied Mechanics and Engineering* 166.1 (1998). Advances in Stabilized Methods in Computational Mechanics, pp. 3–24. ISSN: 0045-7825. DOI: 10.1016/S0045-7825(98)00079-6.

[122] Weinan E et al. "Heterogeneous multiscale method: A general methodology for multiscale modeling." In: *Phys. Rev. B* 67 (9 Mar. 2003), p. 092101. DOI: 10.1103/PhysRevB.67.092101.

[123] C. D. Mote Jr. "Global-local finite element." In: *International Journal for Numerical Methods in Engineering* 3.4 (1971), pp. 565–574. DOI: 10.1002/nme.1620030410.

[124] H.A. Schwarz. "Ueber einige Abbildungsaufgaben." In: *Journal für die reine und angewandte Mathematik* 1869.70 (1869), pp. 105–120. DOI: doi:10.1515/crll.1869.70.105.

[125] IM Gitman et al. "Representative volume: Existence and size determination." In: *Engineering fracture mechanics* 74.16 (2007), pp. 2518–2534. DOI: 10.1016/j.engfracmech.2006.12.021.

[126] Martin Ostoja-Starzewski. "Material spatial randomness: From statistical to representative volume element." In: *Probabilistic engineering mechanics* 21.2 (2006), pp. 112–132. DOI: 10.1016/j.probengmech.2005.07.007.

[127] Nikolai Sergeevich Bakhvalov and Grigory Panasenko. *Homogenisation: averaging processes in periodic media: mathematical problems in the mechanics of composite materials*. Vol. 36. Springer Science & Business Media, 2012. ISBN: 978-94-009-2247-1. DOI: 10.1007/978-94-009-2247-1.

[128] Fredrik Larsson et al. "Variationally consistent computational homogenization of transient heat flow." In: *International Journal for Numerical Methods in Engineering* 81.13 (2010), pp. 1659–1686. DOI: 10.1002/nme.2747.

[129] Rodney Hill. "Elastic properties of reinforced solids: some theoretical principles." In: *Journal of the Mechanics and Physics of Solids* 11.5 (1963), pp. 357–372. DOI: 10.1016/0022-5096(63)90036-X.

[130] R Hill. "On macroscopic effects of heterogeneity in elastoplastic media at finite strain." In: *Mathematical proceedings of the Cambridge philosophical society*. Vol. 95. 3. Cambridge University Press. 1984, pp. 481–494. DOI: 10.1017/S0305004100061818.

[131] Sia Nemat-Nasser. "Averaging theorems in finite deformation plasticity." In: *Mechanics of Materials* 31.8 (1999), pp. 493–523. DOI: 10.1016/S0167-6636(98)00073-8.

[132] I.M. Gitman et al. "Coupled-volume multi-scale modelling of quasi-brittle material." In: *European Journal of Mechanics - A/Solids* 27.3 (2008), pp. 302–327. ISSN: 0997-7538. DOI: 10.1016/j.euromechsol.2007.10.004.

[133] P-A Guidault and Ted Belytschko. "On the L2 and the H1 couplings for an overlapping domain decomposition method using Lagrange multipliers." In: *International journal for numerical methods in engineering* 70.3 (2007), pp. 322–350. DOI: 10.1002/nme.1882.

[134] Andrea Hund and Ekkehard Ramm. "Locality constraints within multiscale model for non-linear material behaviour." In: *International journal for numerical methods in engineering* 70.13 (2007), pp. 1613–1632. DOI: 10.1002/nme.1953.

[135] Stefan Eckardt and Carsten Könke. "Adaptive damage simulation of concrete using heterogeneous multiscale models." In: *Journal of Algorithms & Computational Technology* 2.2 (2008), pp. 275–298. DOI: 10.1260/174830108784646661.

[136] Thomas Hettich et al. "Modeling of failure in composites by X-FEM and level sets within a multiscale framework." In: *Computer Methods in Applied Mechanics and Engineering* 197.5 (2008), pp. 414–424. DOI: 10.1016/j.cma.2007.07.017.

[137] J Mergheim. "A variational multiscale method to model crack propagation at finite strains." In: *International journal for numerical methods in engineering* 80.3 (2009), pp. 269–289. DOI: 10.1002/nme.2602.

[138] PM Suquet. "Local and global aspects in the mathematical theory of plasticity." In: *Plasticity today* (1985), pp. 279–309. URL: https://cir.nii.ac.jp/crid/1571980074668663424.

[139] JoséMiranda Guedes and Noboru Kikuchi. "Preprocessing and post-processing for materials based on the homogenization method with adaptive finite element methods." In: *Computer methods in applied mechanics and engineering* 83.2 (1990), pp. 143–198. DOI: 10.1016/0045-7825(90)90148-F.

[140] Kenjiro Terada and Noboru Kikuchi. "Nonlinear homogenization method for practical applications." In: *American Society of Mechanical Engineers, Applied Mechanics Division, AMD* 212 (1995), pp. 1–16. URL: https://www.scopus.com/inward/record.uri?eid=2-s2.0-0029423823&partnerID=40&md5=ddae8ba93fd9111cf0e07361f247f62f.

[141] Frédéric Feyel and Jean-Louis Chaboche. "FE2 multiscale approach for modelling the elastoviscoplastic behaviour of long fibre SiC/Ti composite materials." In: *Computer methods in applied mechanics and engineering* 183.3-4 (2000), pp. 309–330. DOI: 10.1016/S0045-7825(99)00224-8.

[142] Tarek I Zohdi and Peter Wriggers. *An introduction to computational micromechanics*. Springer Science & Business Media, 2008. ISBN: 978-3-540-32360-0. DOI: 10.1007/978-3-540-32360-0.

[143] Jorge Nocedal and Stephen J Wright. *Numerical optimization*. Springer, 1999. ISBN: 978-0-387-30303-1. DOI: 10.1007/978-0-387-40065-5.

[144] Philip Wolfe. "Convergence Conditions for Ascent Methods." In: *SIAM Review* 11.2 (1969), pp. 226–235. DOI: 10.1137/1011036.

[145] Guus Zoutendijk. *Methods of feasible directions*. Vol. 150. Elsevier Amsterdam, 1960. URL: https://ir.cwi.nl/pub/32064/32064D.pdf.

[146] C. G. BROYDEN. "The Convergence of a Class of Double-rank Minimization Algorithms 1. General Considerations." In: *IMA Journal of Applied Mathematics* 6.1 (Mar. 1970), pp. 76–90. ISSN: 0272-4960. DOI: 10.1093/imamat/6.1.76.

[147] R. Fletcher. "A new approach to variable metric algorithms." In: *The Computer Journal* 13.3 (Jan. 1970), pp. 317–322. ISSN: 0010-4620. DOI: 10.1093/comjnl/13.3.317.

[148] Donald Goldfarb. "A Family of Variable-Metric Methods Derived by Variational Means." In: *Mathematics of Computation* 24.109 (1970), pp. 23–26. ISSN: 00255718, 10886842. DOI: 10.2307/2004873.

[149] D. F. Shanno. "Conditioning of Quasi-Newton Methods for Function Minimization." In: *Mathematics of Computation* 24.111 (1970), pp. 647–656. ISSN: 00255718, 10886842. DOI: 10.2307/2004840.

[150] M. G. D. Geers. "Enhanced solution control for physically and geometrically non-linear problems. Part I—the subplane control approach." In: *International Journal for Numerical Methods in Engineering* 46.2 (1999), pp. 177–204. DOI: 10.1002/(SICI)1097-0207(19990920)46:2<177::AID-NME668>3.0.CO;2-L.

[151] M. G. D. Geers. "Enhanced solution control for physically and geometrically non-linear problems. Part II—comparative performance analysis." In: *International Journal for Numerical Methods in Engineering* 46.2 (1999), pp. 205–230. DOI: 10.1002/(SICI)1097-0207(19990920)46:2<205::AID-NME669>3.0.CO;2-S.

[152] Tim Hageman and René de Borst. "A time-based arc-length like method to remove step size effects during fracture propagation." In: *International Journal for Numerical Methods in Engineering* 123.1 (2022), pp. 180–196. DOI: 10.1002/nme.6852.

[153] Bernhard Josef Winkler. *Traglastuntersuchungen von unbewehrten und bewehrten Betonstrukturen auf der Grundlage eines objektiven Werkstoffgesetzes für Beton*. Innsbruck University Press, 2001. ISBN: 9783901249532.

[154] Jan Rots. "Computational modeling of concrete fracture." PhD thesis. Building 23, Stevinweg 1, 2628 CN, Delft, The Netherlands: Technische Universiteit Delft, 1988. URL: http://resolver.tudelft.nl/uuid:06985d0d-1230-4a08-924a-2553a171f08f.

[155] Jörg F Unger et al. "Modelling of cohesive crack growth in concrete structures with the extended finite element method." In: *Computer methods in applied mechanics and engineering* 196.41-44 (2007), pp. 4087–4100. DOI: 10.1016/j.cma.2007.03.023.

[156] Jack Sherman and Winifred J. Morrison. "Adjustment of an Inverse Matrix Corresponding to a Change in One Element of a Given Matrix." In: *The Annals of Mathematical Statistics* 21.1 (1950), pp. 124–127. DOI: 10.1214/aoms/1177729893.

[157] Thomas Wick. "An Error-Oriented Newton/Inexact Augmented Lagrangian Approach for Fully Monolithic Phase-Field Fracture Propagation." In: *SIAM Journal on Scientific Computing* 39.4 (2017), B589–B617. ISSN: 1064-8275. DOI: 10.1137/16m1063873.

[158] Siobhan Burke et al. "An adaptive finite element approximation of a variational model of brittle fracture." In: *SIAM Journal on Numerical Analysis* 48.3 (2010), pp. 980–1012. DOI: 10.1137/080741033.

[159] Samuel Forest. "Micromorphic approach for gradient elasticity, viscoplasticity, and damage." In: *Journal of Engineering Mechanics* 135.3 (2009), pp. 117–131. DOI: 10.1061/(ASCE)0733-9399(2009)135:3(117).

[160] Stefano Secchi et al. "Mesh adaptation and transfer schemes for discrete fracture propagation in porous materials." In: *International Journal for Numerical and Analytical Methods in Geomechanics* 31.2 (2007), pp. 331–345. DOI: 10.1002/nag.581.

[161] S. Secchi and B. A. Schrefler. "A method for 3-D hydraulic fracturing simulation." In: *International Journal of Fracture* 178.1 (Nov. 2012), pp. 245–258. ISSN: 1573-2673. DOI: 10.1007/s10704-012-9742-y.

[162] Elizaveta Gordeliy and Anthony Peirce. "Coupling schemes for modeling hydraulic fracture propagation using the XFEM." In: *Computer Methods in Applied Mechanics and Engineering* 253 (2013), pp. 305–322. DOI: 10.1016/j.cma.2012.08.017.

[163] Elizaveta Gordeliy and Anthony Peirce. "Implicit level set schemes for modeling hydraulic fractures using the XFEM." In: *Computer Methods in Applied Mechanics and Engineering* 266 (2013), pp. 125–143. DOI: 10.1016/j.cma.2013.07.016.

[164] Elizaveta Gordeliy and Anthony Peirce. "Enrichment strategies and convergence properties of the XFEM for hydraulic fracture problems." In: *Computer Methods in Applied Mechanics and Engineering* 283 (2015), pp. 474–502. ISSN: 0045-7825. DOI: 10.1016/j.cma.2014.09.004.

[165] P. Gupta and C. A. Duarte. "Coupled hydromechanical-fracture simulations of nonplanar three-dimensional hydraulic fracture propagation." In: *International Journal for Numerical and Analytical Methods in Geomechanics* 42.1 (2018), pp. 143–180. DOI: 10.1002/nag.2719.

[166] Mao Sheng et al. "XFEM modeling of multistage hydraulic fracturing in anisotropic shale formations." In: *Journal of Petroleum Science and Engineering* 162 (2018), pp. 801–812. ISSN: 0920-4105. DOI: 10.1016/j.petrol.2017.11.007.

[167] A.R. Khoei et al. "An enriched–FEM technique for numerical simulation of interacting discontinuities in naturally fractured porous media." In: *Computer Methods in Applied Mechanics and Engineering* 331 (2018), pp. 197–231. ISSN: 0045-7825. DOI: 10.1016/j.cma.2017.11.016.

[168] A. Jafari et al. "Fully coupled XFEM formulation for hydraulic fracturing simulation based on a generalized fluid leak-off model." In: *Computer Methods in Applied Mechanics and Engineering* 373 (2021), p. 113447. ISSN: 0045-7825. DOI: 10.1016/j.cma.2020.113447.

[169] Julien Réthoré et al. "A two-scale approach for fluid flow in fractured porous media." In: *International Journal for Numerical Methods in Engineering* 71.7 (2007), pp. 780–800. DOI: 10.1002/nme.1962.

[170] Julien Réthoré et al. "A two-scale model for fluid flow in an unsaturated porous medium with cohesive cracks." In: *Computational Mechanics* 42.2 (July 2008), pp. 227–238. ISSN: 1432-0924. DOI: 10.1007/s00466-007-0178-6.

[171] T. Mohammadnejad and A.R. Khoei. "An extended finite element method for hydraulic fracture propagation in deformable porous media with the cohesive crack model." In: *Finite Elements in Analysis and Design* 73 (2013), pp. 77–95. ISSN: 0168-874X. DOI: 10.1016/j.finel.2013.05.005.

[172] Andro Mikelić et al. "A quasi-static phase-field approach to pressurized fractures." In: *Nonlinearity* 28.5 (Apr. 2015), p. 1371. DOI: 10.1088/0951-7715/28/5/1371.

[173] Zachary A. Wilson and Chad M. Landis. "Phase-field modeling of hydraulic fracture." In: *Journal of the Mechanics and Physics of Solids* 96 (2016), pp. 264–290. ISSN: 0022-5096. DOI: 10.1016/j.jmps.2016.07.019.

[174] Sanghyun Lee et al. "Iterative coupling of flow, geomechanics and adaptive phase-field fracture including level-set crack width approaches." In: *Journal of Computational and Applied Mathematics* 314 (2017), pp. 40–60. DOI: 10.1016/j.cam.2016.10.022.

[175] David Santillán et al. "Phase field model of fluid-driven fracture in elastic media: Immersed-fracture formulation and validation with analytical solutions." In: *Journal of Geophysical Research: Solid Earth* 122.4 (2017), pp. 2565–2589. DOI: 10.1002/2016JB013572.

[176] Shuwei Zhou et al. "Phase-field modeling of fluid-driven dynamic cracking in porous media." In: *Computer Methods in Applied Mechanics and Engineering* 350 (2019), pp. 169–198. ISSN: 0045-7825. DOI: 10.1016/j.cma.2019.03.001.

[177] Andre Costa et al. "A multi-resolution approach to hydraulic fracture simulation." In: *International Journal of Fracture* 237.1 (Sept. 2022), pp. 165–188. ISSN: 1573-2673. DOI: 10.1007/s10704-022-00662-y.

[178] Wolfgang Ehlers and Chenyi Luo. "A phase-field approach embedded in the Theory of Porous Media for the description of dynamic hydraulic fracturing." In: *Computer Methods in Applied Mechanics and Engineering* 315 (2017), pp. 348–368. ISSN: 0045-7825. DOI: 10.1016/j.cma.2016.10.045.

[179] Nicolas Moës et al. "A finite element method for crack growth without remeshing." In: *International Journal for Numerical Methods in Engineering* 46.1 (1999), pp. 131–150. DOI: 10.1002/(SICI)1097-0207(19990910)46:1<131::AID-NME726>3.0.CO;2-J.

[180] Olgierd C Zienkiewicz et al. *Computational geomechanics*. Vol. 613. John Wiley & Sons, 1999. ISBN: 0-471-98285-7.

[181] P. A. Witherspoon et al. "Validity of Cubic Law for fluid flow in a deformable rock fracture." In: *Water Resources Research* 16.6 (1980), pp. 1016–1024. DOI: 10.1029/WR016i006p01016.

[182] Christian Miehe et al. "Minimization principles for the coupled problem of Darcy–Biot-type fluid transport in porous media linked to phase field modeling of fracture." In: *Journal of the Mechanics and Physics of Solids* 82 (2015), pp. 186–217. ISSN: 0022-5096. DOI: 10.1016/j.jmps.2015.04.006.

[183] Chukwudi Chukwudozie et al. "A variational phase-field model for hydraulic fracturing in porous media." In: *Computer Methods in Applied Mechanics and Engineering* 347 (2019), pp. 957–982. DOI: 10.1016/j.cma.2018.12.037.

[184] C. Taylor and P. Hood. "A numerical solution of the Navier-Stokes equations using the finite element technique." In: *Computers & Fluids* 1.1 (1973), pp. 73–100. ISSN: 0045-7930. DOI: 10.1016/0045-7930(73)90027-3.

[185] E. Detournay and D. I. Garagash. "The near-tip region of a fluid-driven fracture propagating in a permeable elastic solid." In: *Journal of Fluid Mechanics* 494 (2003), pp. 1–32. DOI: 10.1017/S0022112003005275.

[186] Chaosheng Tang et al. "Influencing factors of geometrical structure of surface shrinkage cracks in clayey soils." In: *Engineering Geology* 101.3 (2008), pp. 204–217. ISSN: 0013-7952. DOI: 10.1016/j.enggeo.2008.05.005.

[187] S. COSTA et al. "Salient factors controlling desiccation cracking of clay in laboratory experiments." In: *Géotechnique* 63.1 (2013), pp. 18–29. DOI: 10.1680/geot.9.P.105.

[188] E. M. Kindle. "Some Factors Affecting the Development of Mud-Cracks." In: *The Journal of Geology* 25.2 (1917), pp. 135–144. ISSN: 00221376, 15375269. URL: http://www.jstor.org/stable/30060962.

[189] Arturo Corte and Akira Higashi. *Experimental research on desiccation cracks in soil*. Tech. rep. 1964. URL: https://usace.contentdm.oclc.org/digital/collection/p266001coll1/id/6153/.

[190] Hao Zeng et al. "Desiccation cracking of soil subjected to different environmental relative humidity conditions." In: *Engineering Geology* 297 (2022), p. 106536. ISSN: 0013-7952. DOI: 10.1016/j.enggeo.2022.106536.

[191] J.H. Li et al. "Cracking and vertical preferential flow through landfill clay liners." In: *Engineering Geology* 206 (2016), pp. 33–41. ISSN: 0013-7952. DOI: 10.1016/j.enggeo.2016.03.006.

[192] Zhipeng Huo et al. "Factors influencing the development of diagenetic shrinkage macro-fractures in shale." In: *Journal of Petroleum Science and Engineering* 183 (2019), p. 106365. ISSN: 0920-4105. DOI: 10.1016/j.petrol.2019.106365.

[193] Y.F. Deng et al. "Effect of pore water chemistry on the hydro-mechanical behaviour of Lianyungang soft marine clay." In: *Applied Clay Science* 95 (2014), pp. 167–175. ISSN: 0169-1317. DOI: 10.1016/j.clay.2014.04.007.

[194] Tongwei Zhang et al. "Porewater salinity effect on flocculation and desiccation cracking behaviour of kaolin and bentonite considering working condition." In: *Engineering Geology* 251 (2019), pp. 11–23. ISSN: 0013-7952. DOI: 10.1016/j.enggeo.2019.02.007.

[195] Chao-Sheng Tang et al. "Desiccation and cracking behaviour of clay layer from slurry state under wetting–drying cycles." In: *Geoderma* 166.1 (2011), pp. 111–118. ISSN: 0016-7061. DOI: 10.1016/j.geoderma.2011.07.018.

[196] Ben-Gang Tian et al. "Effects of compaction state on desiccation cracking behaviour of a clayey soil subjected to wetting-drying cycles." In: *Engineering Geology* 302 (2022), p. 106650. ISSN: 0013-7952. DOI: 10.1016/j.enggeo.2022.106650.

[197] Peter H. Morris et al. "Cracking in drying soils." In: *Canadian Geotechnical Journal* 29.2 (1992), pp. 263–277. DOI: 10.1139/t92-030.

[198] J -M Konrad and R Ayad. "A idealized framework for the analysis of cohesive soils undergoing desiccation." In: *Canadian Geotechnical Journal* 34.4 (1997), pp. 477–488. DOI: 10.1139/t97-015.

[199] Aruna Amarasiri and Jayantha Kodikara. "Use of Material Interfaces in DEM to Simulate Soil Fracture Propagation in Mode I Cracking." In: *International Journal of Geomechanics* 11.4 (2011), pp. 314–322. DOI: 10.1061/(ASCE)GM.1943-5622.0000090.

[200] Aruna L. Amarasiri et al. "Determination of cohesive properties for mode I fracture from compacted clay beams." In: *Canadian Geotechnical Journal* 48.8 (2011), pp. 1163–1173. DOI: 10.1139/t11-031.

[201] P. A. Cundall and O. D. L. Strack. "A discrete numerical model for granular assemblies." In: *Géotechnique* 29.1 (1979), pp. 47–65. DOI: 10.1680/geot.1979.29.1.47. URL: 10.1680/geot.1979.29.1.47.

[202] Amade Pouya et al. "Modeling soil desiccation cracking by analytical and numerical approaches." In: *International Journal for Numerical and Analytical Methods in Geomechanics* 43.3 (2019), pp. 738–763. DOI: 10.1002/nag.2887.

[203] Marcelo Sánchez et al. "Modeling 3-D desiccation soil crack networks using a mesh fragmentation technique." In: *Computers and Geotechnics* 62 (2014), pp. 27–39. ISSN: 0266-352X. DOI: 10.1016/j.compgeo.2014.06.009.

[204] Ross Alexander Stirling. "Multiphase modelling of desiccation cracking in compacted soil." PhD thesis. Newcastle University, 2014. URL: http://hdl.handle.net/10443/2492.

[205] Hervé Peron et al. "Desiccation cracking of soils." In: *European Journal of Environmental and Civil Engineering* 13.7-8 (2009), pp. 869–888. DOI: 10.1080/19648189.2009.9693159.

[206] Tuanny Cajuhi. "Fracture in porous media: phase-field modeling, simulation and experimental validation." PhD thesis. Technische Universität Braunschweig, 2019. URL: https://leopard.tu-braunschweig.de/servlets/MCRFileNodeServlet/dbbs_derivate_00045168/Diss_Cajuhi_Tuanny.pdf.

[207] H. Shin and J.C. Santamarina. "Desiccation cracks in saturated fine-grained soils: particle-level phenomena and effective-stress analysis." In: *Géotechnique* 61.11 (2011), pp. 961–972. DOI: 10.1680/geot.8.P.012.

[208] Jayantha Kodikara and Susanga Costa. "Desiccation Cracking in Clayey Soils: Mechanisms and Modelling." In: *Multiphysical Testing of Soils and Shales*. Ed. by Lyesse Laloui and Alessio Ferrari. Berlin, Heidelberg: Springer Berlin Heidelberg, 2013, pp. 21–32. ISBN: 978-3-642-32492-5. DOI: 10.1007/978-3-642-32492-5_2.

[209] Omid Reza Barani et al. "Fracture Analysis of Cohesive Soils Using Bilinear and Trilinear Cohesive Laws." In: *International Journal of Geomechanics* 16.4 (2016), p. 04015088. DOI: 10.1061/(ASCE)GM.1943-5622.0000630.

[210] MR Lakshmikantha et al. "Relation between tensile strength and fracture toughness for soils and rocks." In: *Proceedings of the 3rd International Workshop of Young Doctors in Geomechanics, Champs-sur-Marne, France*. 2008, pp. 19–21.

[211] H. H. Gerke and M. T. van Genuchten. "A dual-porosity model for simulating the preferential movement of water and solutes in structured porous media." In: *Water Resources Research* 29.2 (1993), pp. 305–319. DOI: 10.1029/92WR02339.

[212] T. Vogel et al. "Modeling flow and transport in a two-dimensional dual-permeability system with spatially variable hydraulic properties." In: *Journal of Hydrology* 238.1 (2000), pp. 78–89. ISSN: 0022-1694. DOI: 10.1016/S0022-1694(00)00327-9.

[213] Edgar Buckingham. "Studies on the movement of soil moisture." In: *Bureau of Soils, Bulletin* 38 (1907).

[214] Tao Pan et al. "Comparison of three models fitting the soil water retention curves in a degraded alpine meadow region." In: *Scientific Reports* 9.1 (Dec. 2019), p. 18407. ISSN: 2045-2322. DOI: 10.1038/s41598-019-54449-8.

[215] Limin Zhang and DG Fredlund. "Characteristics of water retention curves for unsaturated fractured rocks." In: *Proceedings of the 2nd Asian Conference on Unsaturated Soils, Osaka, Japan*. 2003, pp. 15–17. URL: https://hdl.handle.net/1783.1/11134.

[216] M. M. Abbaszadeh et al. "Influence of Soil Cracking on the Soil-Water Characteristic Curve of Clay Soil." In: *Soils and Rocks* (2015). URL: https://www.soilsandrocks.com/sr-381049.

[217] Evgenii Solomonovich Romm. *Fluid flow in fractured rocks*. Phillips Petroleum Company, 1972.

[218] *A Viscous Coupling Model for Relative Permeabilities in Fractures*. Vol. All Days. SPE Annual Technical Conference and Exhibition. Sept. 1998, SPE-49006–MS. DOI: 10.2118/49006-MS.

[219] Arthur T Corey. "The interrelation between gas and oil relative permeabilities." In: *Producers monthly* (1954), pp. 38–41. URL: https://cir.nii.ac.jp/crid/1570009749409873792.

[220] Yechezkel Mualem. "A new model for predicting the hydraulic conductivity of unsaturated porous media." In: *Water Resources Research* 12.3 (1976), pp. 513–522. DOI: 10.1029/WR012i003p00513.

[221] Sia Nemat-Nasser and Muneo Hori. *Micromechanics: overall properties of heterogeneous materials*. Elsevier, 2013. ISBN: 0444898816.

[222] Eugenio Oñate et al. "Finite calculus formulation for incompressible solids using linear triangles and tetrahedra." In: *International Journal for Numerical Methods in Engineering* 59.11 (2004), pp. 1473–1500. DOI: 10.1002/nme.922.

[223] "Stabilized mixed finite element formulations for materially nonlinear partially saturated two-phase media." In: *Computer Methods in Applied Mechanics and Engineering* 195.13 (2006), pp. 1517–1546. ISSN: 0045-7825. DOI: 10.1016/j.cma.2005.05.044.

[224] G. Aguilar et al. "Numerical stabilization of Biot's consolidation model by a perturbation on the flow equation." In: *International Journal for Numerical Methods in Engineering* 75.11 (2008), pp. 1282–1300. DOI: 10.1002/nme.2295.

[225] Joshua A. White and Ronaldo I. Borja. "Stabilized low-order finite elements for coupled solid-deformation/fluid-diffusion and their application to fault zone transients." In: *Computer Methods in Applied Mechanics and Engineering* 197.49 (2008), pp. 4353–4366. ISSN: 0045-7825. DOI: 10.1016/j.cma.2008.05.015.

[226] P. Mira et al. "A new stabilized enhanced strain element with equal order of interpolation for soil consolidation problems." In: *Computer Methods in Applied Mechanics and Engineering* 192.37 (2003), pp. 4257–4277. ISSN: 0045-7825. DOI: 10.1016/S0045-7825(03)00416-X.

[227] WaiChing Sun et al. "A stabilized assumed deformation gradient finite element formulation for strongly coupled poromechanical simulations at finite strain." In: *International Journal for Numerical and Analytical Methods in Geomechanics* 37.16 (2013), pp. 2755–2788. DOI: 10.1002/nag.2161.

[228] Ross A. Stirling et al. "Modelling the deterioration of the near surface caused by drying induced cracking." In: *Applied Clay Science* 146 (2017), pp. 176–185. ISSN: 0169-1317. DOI: 10.1016/j.clay.2017.06.003.

[229] P. N. Hughes et al. "Full-scale testing to assess climate effects on embankments." In: *Proceedings of the Institution of Civil Engineers - Engineering Sustainability* 162.2 (2009), pp. 67–79. DOI: 10.1680/ensu.2009.162.2.67.

[230] Stephanie Glendinning et al. "Construction, management and maintenance of embankments used for road and rail infrastructure: implications of weather induced pore water pressures." In: *Acta Geotechnica* 9.5 (Oct. 2014), pp. 799–816. ISSN: 1861-1133. DOI: 10.1007/s11440-014-0324-1.

[231] R.N. Tollenaar et al. "Observations on the desiccation and cracking of clay layers." In: *Engineering Geology* 230 (2017), pp. 23–31. ISSN: 0013-7952. DOI: 10.1016/j.enggeo.2017.08.022.

[232] George W. Scherer. "Theory of Drying." In: *Journal of the American Ceramic Society* 73.1 (1990), pp. 3–14. DOI: 10.1111/j.1151-2916.1990.tb05082.x.

[233] Jian-Ying Wu and Vinh Phu Nguyen. "A length scale insensitive phase-field damage model for brittle fracture." In: *Journal of the Mechanics and Physics of Solids* 119 (2018), pp. 20–42. ISSN: 0022-5096. DOI: 10.1016/j.jmps.2018.06.006.

[234] Tushar Kanti Mandal et al. "Fracture of thermo-elastic solids: Phase-field modeling and new results with an efficient monolithic solver." In: *Computer Methods in Applied Mechanics and Engineering* 376 (2021), p. 113648. ISSN: 0045-7825. DOI: 10.1016/j.cma.2020.113648.

[235] M. Ambati et al. "Phase-field modeling of ductile fracture." In: *Computational Mechanics* 55.5 (May 2015), pp. 1017–1040. ISSN: 1432-0924. DOI: 10.1007/s00466-015-1151-4.

[236] C. Miehe et al. "Phase field modeling of fracture in multi-physics problems. Part II. Coupled brittle-to-ductile failure criteria and crack propagation in thermo-elastic–plastic solids." In: *Computer Methods in Applied Mechanics and Engineering* 294 (2015), pp. 486–522. ISSN: 0045-7825. DOI: 10.1016/j.cma.2014.11.017.

[237] Christian Miehe et al. "Phase field modeling of ductile fracture at finite strains: A variational gradient-extended plasticity-damage theory." In: *International Journal of Plasticity* 84 (2016), pp. 1–32. ISSN: 0749-6419. DOI: 10.1016/j.ijplas.2016.04.011.

[238] Ritukesh Bharali et al. "A micromorphic phase-field model for brittle and quasi-brittle fracture." In: *Computational Mechanics* (Aug. 2023). ISSN: 1432-0924. DOI: 10.1007/s00466-023-02380-1.

[239] A. Mesgarnejad et al. "A variational approach to the fracture of brittle thin films subject to out-of-plane loading." In: *Journal of the Mechanics and Physics of Solids* 61.11 (2013), pp. 2360–2379. ISSN: 0022-5096. DOI: 10.1016/j.jmps.2013.05.001.

[240] Emilio Martínez-Pañeda et al. "A phase field formulation for hydrogen assisted cracking." In: *Computer Methods in Applied Mechanics and Engineering* 342 (2018), pp. 742–761. ISSN: 0045-7825. DOI: 10.1016/j.cma.2018.07.021.

[241] Tymofiy Gerasimov et al. "A non-intrusive global/local approach applied to phase-field modeling of brittle fracture." In: *Advanced modeling and simulation in engineering sciences* 5.1 (2018), pp. 1–30. DOI: 10.1186/s40323-018-0105-8.

[242] Fredrik Larsson et al. "Computational homogenization of uncoupled consolidation in micro-heterogeneous porous media." In: *International Journal for Numerical and Analytical Methods in Geomechanics* 34.14 (2010), pp. 1431–1458. DOI: 10.1002/nag.862.

[243] Carl Sandstrom and Fredrik Larsson. "Variationally Consistent Homogenization of Stokes flow in porous media." In: *International Journal for Multiscale Computational Engineering* 11.2 (2013), pp. 117–138. ISSN: 1543-1649. DOI: 10.1615/IntJMultCompEng.2012004069.

[244] Mikael Öhman et al. "Computational homogenization of liquid-phase sintering with seamless transition from macroscopic compressibility to incompressibility." In: *Computer Methods in Applied Mechanics and Engineering* 266 (2013), pp. 219–228. ISSN: 0045-7825. DOI: 10.1016/j.cma.2013.07.006.

[245] Ralf Jänicke et al. "A poro-viscoelastic substitute model of fine-scale poroelasticity obtained from homogenization and numerical model reduction." In: *Computational Mechanics* (Jan. 2020). ISSN: 1432-0924. DOI: 10.1007/s00466-019-01808-x.

[246] Nele Pollmann et al. "Diffuse interface modeling and variationally consistent homogenization of fluid transport in fractured porous media." In: *European Journal of Mechanics - A/Solids* 84 (2020), p. 104067. ISSN: 0997-7538. DOI: 10.1016/j.euromechsol.2020.104067.

[247] Nele Pollmann et al. "Modeling and computational homogenization of chloride diffusion in three-phase meso-scale concrete." In: *Construction and Building Materials* 271 (2021), p. 121558. ISSN: 0950-0618. DOI: 10.1016/j.conbuildmat.2020.121558.

[248] Kenneth Runesson et al. "Computational homogenization of mesoscale gradient viscoplasticity." In: *Computer Methods in Applied Mechanics and Engineering* 317 (2017), pp. 927–951. ISSN: 0045-7825. DOI: 10.1016/j.cma.2016.11.032.

[249] Erik Svenning et al. "On computational homogenization of microscale crack propagation." In: *International Journal for Numerical Methods in Engineering* 108.1 (2016), pp. 76–90. DOI: 10.1002/nme.5220.

[250] Erik Svenning et al. "Two-scale modeling of fracturing solids using a smeared macro-to-micro discontinuity transition." In: *Computational Mechanics* 60.4 (Oct. 2017), pp. 627–641. ISSN: 1432-0924. DOI: 10.1007/s00466-017-1426-z.

[251] Adam Sciegaj et al. "On a volume averaged measure of macroscopic reinforcement slip in two-scale modeling of reinforced concrete." In: *International Journal for Numerical Methods in Engineering* 121.8 (2020), pp. 1822–1846. DOI: 10.1002/nme.6288.

[252] Adam Sciegaj et al. "Upscaling of three-dimensional reinforced concrete representative volume elements to effective beam and plate models." In: *International Journal of Solids and Structures* 202 (2020), pp. 835–853. ISSN: 0020-7683. DOI: 10.1016/j.ijsolstr.2020.07.006.

[253] Vinh Tu et al. "Variationally consistent homogenization of electrochemical ion transport in a porous structural battery electrolyte." In: *European Journal of Mechanics - A/Solids* 98 (2023), p. 104901. ISSN: 0997-7538. DOI: 10.1016/j.euromechsol.2022.104901.

[254] D.R. Rollin et al. "Upscaling of chemo-mechanical properties of battery electrode material." In: *International Journal of Solids and Structures* 281 (2023), p. 112405. ISSN: 0020-7683. DOI: 10.1016/j.ijsolstr.2023.112405.

[255] Elias Börjesson et al. "Variationally consistent homogenisation of plates." In: *Computer Methods in Applied Mechanics and Engineering* 413 (2023), p. 116094. ISSN: 0045-7825. DOI: 10.1016/j.cma.2023.116094.

[256] Vinh Phu Nguyen et al. "On the existence of representative volumes for softening quasi-brittle materials – A failure zone averaging scheme." In: *Computer Methods in Applied Mechanics and Engineering* 199.45 (2010), pp. 3028–3038. ISSN: 0045-7825. DOI: 10.1016/j.cma.2010.06.018.

[257] F. Larsson et al. "Computational homogenization based on a weak format of micro-periodicity for RVE-problems." In: *Computer Methods in Applied Mechanics and Engineering* 200.1 (2011), pp. 11–26. ISSN: 0045-7825. DOI: 10.1016/j.cma.2010.06.023.

[258] Ritukesh Bharali et al. "Computational aspects of the weak micro-periodicity saddle point problem." In: *PAMM* 20.1 (2021), e202000259. DOI: 10.1002/pamm.202000259.

[259] R De Borst et al. "Fundamental issues in finite element analyses of localization of deformation." In: *Engineering computations* 10.2 (1993), pp. 91–121. DOI: 10.1108/eb023897.

[260] J. W. Gunnink et al. "Glare Technology Development 1997–2000." In: *Applied Composite Materials* 9.4 (July 2002), pp. 201–219. ISSN: 1573-4897. DOI: 10.1023/A:1016006314630.

[261] P. Soltani et al. "Studying the Tensile Behaviour of GLARE Laminates: A Finite Element Modelling Approach." In: *Applied Composite Materials* 18.4 (Aug. 2011), pp. 271–282. ISSN: 1573-4897. DOI: 10.1007/s10443-010-9155-x.

[262] O. van der Sluis et al. "Overall behaviour of heterogeneous elastoviscoplastic materials: effect of microstructural modelling." In: *Mechanics of Materials* 32.8 (2000), pp. 449–462. ISSN: 0167-6636. DOI: 10.1016/S0167-6636(00)00019-3.

[263] Kenjiro Terada et al. "Simulation of the multi-scale convergence in computational homogenization approaches." In: *International Journal of Solids and Structures* 37.16 (2000), pp. 2285–2311. ISSN: 0020-7683. DOI: 10.1016/S0020-7683(98)00341-2.

[264] Frédéric Feyel. "Multiscale FE2 elastoviscoplastic analysis of composite structures." In: *Computational Materials Science* 16.1 (1999), pp. 344–354. ISSN: 0927-0256. DOI: 10.1016/S0927-0256(99)00077-4.

[265] Ritukesh Bharali et al. "A robust monolithic solver for phase-field fracture integrated with fracture energy based arc-length method and under-relaxation." In: *Computer Methods in Applied Mechanics and Engineering* 394 (2022), p. 114927. ISSN: 0045-7825. DOI: 10.1016/j.cma.2022.114927.

[266] Ritukesh Bharali. *rbharali/openFE2: First beta release of multi- scale code*. Version v.1.0-beta. Jan. 2021. DOI: 10.5281/zenodo.4463345.

[267] Daniele Boffi et al. *Mixed finite element methods and applications*. Vol. 44. Springer, 2013. ISBN: 978-3-642-36519-5. DOI: 10.1007/978-3-642-36519-5.

[268] Douglas N Arnold et al. "A stable finite element for the Stokes equations." In: *Calcolo* 21.4 (1984), pp. 337–344. DOI: 10.1007/BF02576171.